CHARACTERISATION OF THE DEFORMATION MECHANISMS IN HCP METALS BY COMBINED USE OF X-RAY IMAGING AND DIFFRACTION TECHNIQUES

A THESIS SUBMITTED TO THE UNIVERSITY OF MANCHESTER
FOR THE DEGREE OF DOCTOR OF PHILOSOPHY
IN THE FACULTY OF ENGINEERING AND PHYSICAL SCIENCES

2015

By
Laura Nervo
School of Materials

I certify that I have read this thesis and that in my opinion it is fully adequate, in scope and in quality, as a thesis for the degree of Doctor of Philosophy.

Prof. Michael Preuss
(Principal Advisor)

I certify that I have read this thesis and that in my opinion it is fully adequate, in scope and in quality, as a thesis for the degree of Doctor of Philosophy.

Prof. Robert Cernik

I certify that I have read this thesis and that in my opinion it is fully adequate, in scope and in quality, as a thesis for the degree of Doctor of Philosophy.

Prof. Jean-Yves Buffière

Approved for the University Committee on Graduate Studies.

Dean of Graduate Studies & Research

Table of Contents

Word Count: 39002

List of Tables

List of Figures

Abstract

CHARACTERISATION OF THE DEFORMATION MECHANISMS IN HCP METALS BY COMBINED USE OF X-RAY IMAGING AND DIFFRACTION TECHNIQUES

Laura Nervo

A thesis submitted to the University of Manchester
for the degree of Doctor of Philosophy, 2015

We envisage a fundamental study of the physical mechanisms (dislocation slip versus deformation twinning) involved in plastic deformation of hexagonal close-packed (HCP) metals like titanium and magnesium. A novel combination of X-ray imaging and diffraction techniques, termed X-ray diffraction contrast tomography (DCT), will be used to investigate details of the deformation process in the bulk of polycrystalline specimen. DCT provides access to the position, 3D shape, (average) orientation and elastic strain tensor of grains in polycrystalline sample volumes containing up to 1000 grains and more.
Ultimately, an extension of the X-ray DCT technique is associated with a section topography methodology on the same instrument. This combination enables the measurement of local orientation and elastic strain tensors inside selected bulk grains. A very preliminary study of this approach is carried out on a magnesium alloy, underlying the current limitations and possible improvements of such approach.
In this thesis, the data acquisition and analysis procedures required for this type of combined characterisation approach have been developed. The work is supported by the use of neutron diffraction, for an in-situ loading experiment, and two-dimensional EBSD, for the initial microstructure of the materials and cross-validation of the results obtained with the X-ray DCT technique.

Declaration

No portion of the work referred to in this thesis has been submitted in support of an application for another degree or qualification of this or any other university or other institute of learning.

Copyright

List of Abbreviations

3DXRD	3D X-ray diffraction
APS	advanced photon source
ART	algebraic reconstruction technique
ASTRA	All Scale Tomographic Reconstruction Antwerp
BCC	body-centered cubic
CCD	charge-coupled device
CPFEM	crystal plasticity finite element model
CRSS	critical resolved shear stress
CSL	coincident site lattice
CT	computed tomography
DAXM	differential aperture X-ray microscopy
DCT	diffraction contrast tomography
EBSD	electron backscatter diffraction
EDM	electro-discharge machining
EPSRC	Engineering and Physical Science Research Council
ESRF	European Synchrotron Radiation Facility
FCC	face-centered cubic
FReLoN	Fast Readout Low Noise
GND	geometrically necessary dislocation
GUI	graphical user interface

HCP	hexagonal close-packed
HEDM	high energy diffraction microscopy
ILL	Institut Laue-Langevin
IPF	inverse pole figure
PF	pole figure
RCI	rocking curve imaging
RSS	resolved shear stress
SALSA	Strain Analyser for Large and Small scale engineering Applications
SIRT	simultaneous iterative reconstruction technique
XRD	X-ray diffraction

Acknowledgements

First and foremost I want to thank my advisors Michael Preuss and Wolfgang Ludwig. It has been an honour to be their Ph.D. student. They both have taught me, both consciously and by example, how good experimental physics and material science are done. I appreciate all their contributions of time, ideas, and funding to make my Ph.D. experience productive and stimulating.
I would like to thank the ILL and ESRF institutions in Grenoble (France), who have allocated beam time to this project. Furthermore, thanks to the scientists at these facilities who have given their time to help me, in particular the staff of the ID11 and ID18F beam lines of the ESRF and the staff of the SALSA beam line of the ILL.
The members of the graintracking group have contributed immensely to my personal and professional time at the ESRF (Grenoble, France). A special thanks goes to Andrew King, for sharing so many of the experiments and for his excellent support and patience, to Arnas Fitzner, for providing samples and EBSD data, and to Péter Reischig and Nicola Viganò, for their important contribution to the DCT code. I am particularly indebted to Henry Proudhon, who helped me with the python code for the 3D rendering of grains.
I gratefully acknowledge the funding sources that made my Ph.D. work possible. The project was funded by the Engineering and Physical Science Research Council (EPSRC) [grant number EP/F020910/1] and by the European Synchrotron Radiation Facility (ESRF). I was honoured to be a Graduate Student of the University of Manchester, even my time spent in Manchester was very short, since I was based full-time at the ESRF.
My time at Grenoble was made enjoyable in large part due to the many friends and groups that became a part of my life. Loredana, Erminia, Beatrice and MariAngeles in particular deserve special mention for their friendship, moral support and affection.
Lastly, I would like to thank my family for all their love and encouragement. For my mother Liliana and my brother Roberto who raised me with an unlimited love and supported me in all my pursuits. Thank you.

"You have not truly understood something
until when you are not able to explain it to your grandmother."

Albert Einstein

"The joy of physics isn't in the results,
but in the search itself."

Dennis Overbye

Dedicated to my mother Liliana and my brother Roberto

Chapter 1

Introduction

Materials science and engineering is a field broadly based in chemistry, physics, and the engineering sciences. The field is concerned with the design, manufacture, and use of all classes of materials (including metals, ceramics, semiconductors, polymers, and biomaterials), and with energy, environmental, health, economic, and manufacturing issues relating to materials.

Materials science emphasises the study of the structure of materials and the relations between properties and structures in materials. Almost all the properties of materials can be modified in significant ways by changing the chemical composition, the arrangement of the atoms or molecules in crystalline or amorphous configurations, and the size, shape and orientation of the crystals or other macroscopic units of a solid.

To understand how the useful properties of a material can be modified, it is necessary to understand the fundamental relationships between structure (often the microstructure) and properties and how the structure can be changed and controlled by the various chemical, thermal, mechanical, or other processes to which a material is subjected during manufacture and in use.

Deformation of polycrystalline materials has been an active topic of research for more than 70 years (TAYLOR, 1938), as the scientific community has come to realise that deformation occurs within grains as well as amongst grains. The study of polycrystalline engineering materials on the length scale of individual grains is important for understanding their properties and behaviour during such deformation.

Over the past ten years considerable effort has been put into the development of novel three-dimensional diffraction techniques for mapping grain structures in polycrystalline materials, and these new tools offer new insights into deformation problems.

There are two main sets of techniques that aim at a real space description of

polycrystalline materials, in terms of three-dimensional shapes and orientations of all grains present in the illuminated sample volume. The first type of techniques is point scanning techniques like diffraction tomography (BLEUET *et al.*, 2009; STOCK, 2008) or the polychromatic Laue micro-diffraction technique and its extension into 3D via differential aperture X-ray microscopy (DAXM) (LARSON *et al.*, 2002), where three-dimensional information is obtained by scanning the sample and an analyser wire, relative to a point focused beam. 3D grain maps produced by this first type of 3D scanning techniques offer access to local orientation, phase and strain information, but are typically restricted to small sample volumes because of limitations in scan speed.
The second set of techniques are variants of the monochromatic beam, rotating crystal method, typified by 3D X-ray diffraction (3DXRD) microscopy (ODDERSHEDE *et al.*, 2010, 2012; POULSEN, 2012; SØRENSEN *et al.*, 2012) or high energy diffraction microscopy (HEDM) (LI *et al.*, 2012). 3DXRD produces 3D maps of the grains, visualising their position, orientation and elastic strain at the same time, using an extended beam of monochromatic radiation. Strain and orientation are usually averaged over each grain, with some exceptions (LI and SUTER, 2013; REISCHIG, 2008). 3DXRD experiments can be further sub-divided into near-field approaches and far-field approaches or combinations of both. Near-field diffraction imaging techniques aim at resolving 3D grain shapes (LI and SUTER, 2013; LUDWIG *et al.*, 2009a; REISCHIG *et al.*, 2013; SCHMIDT, 2010; SUTER *et al.*, 2006) and employ high resolution X-ray imaging detectors with pixels smaller than the grain size. Far-field approaches, on the other hand, employ a low resolution detector with pixels comparable or bigger than the grain size, in which case the morphology of grains is neglected.

X-ray diffraction contrast tomography (DCT) (JOHNSON *et al.*, 2008; LUDWIG *et al.*, 2009b; REISCHIG *et al.*, 2013) is a variant of the 3DXRD microscopy technique enabling simultaneous reconstruction of the 3D microstructure (shape and orientation) in suitable polycrystalline materials, along with the absorption map of the specimen. The X-ray DCT provides access to the 3D shape, orientation and elastic strain state of the individual grains from polycrystalline sample volumes containing up to a few thousand grains.

Since the absorption properties of matter are strongly dependent on the energy of the radiation, an X-ray spectrum passing through an object gets distorted. In general, low energy photons are absorbed more strongly than high energy photons, and the average energy of the spectrum shifts towards higher values, i.e. beam hardening effect. In conventional computed tomography (CT), beam hardening effects in the two dimensional images propagate to the 3D reconstruction, giving rise to artefacts that

can seriously impair the quality of the image. Recently, new detector systems have been developed, such as the Medipix readout chip for semiconductor pixel sensors, with the ability to record spectral information. This information can be exploited to reduce beam hardening effects and achieve material decomposition in X-ray CT, called spectral CT. Since different colours can be associated to the different materials that are recognised, spectral CT is often referred to as colour CT (SCHIOPPA, 2014).

It is clear that grains are not homogeneous, and that a complete understanding of material behaviour will involve understanding the sub-structures within individual grains. By combining the X-ray DCT and the X-ray section topography methodologies (LUDWIG *et al.*, 2010; SIMONS *et al.*, 2015), one can obtain a comprehensive description of the microstructure at the micrometre length scale. Section topography is used to reveal sub-grain structures, and enables strain and local orientation measurements.

The aim of the work presented in this thesis is the characterisation of deformation mechanisms in polycrystalline materials by means of X-ray imaging and diffraction techniques, i.e. X-ray DCT, neutron diffraction and section topography. All these techniques were combined to better describe the microstructure in selected polycrystalline materials at the micrometre level. The materials used for this study have a hexagonal crystal structure. Materials with hexagonal close-packed (HCP) crystal structure are highly sensitive to crystallographic texture due to their low symmetry. However, there is a lack of sufficient information regarding the microstructural evolution during deformation of HCP materials. Textured materials, where there is a tendency for certain preferred orientations, exhibit anisotropic mechanical properties. During deformation processing, well organised dislocation structures tend to form. Among the processing conditions, strain level is highly influential in transforming a random dislocation substructure into an aligned and developed one.

Plasticity in polycrystalline HCP materials involves a variety of deformation mechanisms, including substantial twinning activity. Thus, a modelling approach that can assess the impact of the grain anisotropy and its effects with respect to the aggregate is necessary. Additionally, any model has to account for the orientation changes during twinning and its effect on texture evolution and hardening response. The ultimate aim of studying HCP materials is the use of the experimental results in the crystal plasticity finite element model (CPFEM) (MARIN and DAWSON, 1998; ROTERS, 2005).

1.1 Structure of the thesis

A general introduction to the diffraction principles and different sources used for diffraction measurements is given in chapter 2.
Chapter 3 explains the deformation mechanisms in HCP materials, followed by a brief description of the HCP metals studied in this work, describing their properties and applications.
The experimental methodologies and a short outline of the material preparation are described in chapter 4.
Chapter 5 deals with my specific development of software tools needed for the data analysis.
Chapters 6–8 deal with my work on the characterisation of the deformation mechanisms in polycrystalline materials.
Chapter 6 compares and cross-validates indexing results obtained from two variants of 3DXRD, the X-ray DCT as an instance of a near-field method and conventional 3DXRD as a representative of the far-field diffraction method. The material used for this comparison was a polycrystalline commercially pure titanium (CP Ti) grade 2 sample and the data were analysed using two different software packages.
In chapter 7 the onset of twinning is studied in a binary Ti-4wt.%Al alloy, using two different diffraction techniques, neutron diffraction and X-ray DCT. The samples were first compressed and the activation of $\{10\bar{1}2\}\ \langle\bar{1}011\rangle$ tensile twins was followed in-situ by means of neutron diffraction.
In chapter 8 twinning mechanisms operational during plastic deformation in AZ31 Mg alloys is investigated, using a combination of the X-ray DCT technique and section topography.
Finally, chapter 9 summarises the main results from this work and outlines possible directives for a future work.

Chapter 2

Literature review: diffraction

An important aspect of this thesis is the characterisation of the deformation mechanisms in polycrystalline materials. The measurements are made during compression of samples made from materials with hexagonal close-packed (HCP) crystal structure, by using different diffraction techniques: X-ray diffraction contrast tomography (DCT), neutron diffraction and X-ray section topography. In this chapter an overview of the fundamental principles of X-ray and neutron diffraction is given.

Diffraction is a scattering phenomenon that can occur when a wave interacts with periodically arranged scattering centres (CULLITY and STOCK, 2001). For instance, if the periodic array of atoms in a crystal is irradiated with a monochromatic X-ray beam. Since X-rays are electromagnetic radiations, they can be described, at a large distance from the source, in terms of plane waves, with appropriate wave vectors.

2.1 Bragg's law of diffraction

We consider an X-ray wave falling on a crystal and a re-emitted (or scattered) X-ray wave. During an elastic scattering process, the magnitudes of the wave vectors of the two waves will be identical and equal to $1/\lambda$. Diffraction from an array of scattering centres can be described using Bragg's law. When radiation is scattered by a crystal, in phase or constructive interference only occurs along certain directions. Bragg's law states the essential condition, which must be met for diffraction to occur (CULLITY and STOCK, 2001). Bragg's law can be derived from a simple schematic illustration of radiation interacting with rows of atoms in a crystal, as shown in figure 2.1.

Incident radiation will only be diffracted (scattered in phase) if the path difference between scattered radiation by two successive planes is a integer number of wavelengths. For this condition to be met, the spacing between the planes of atoms

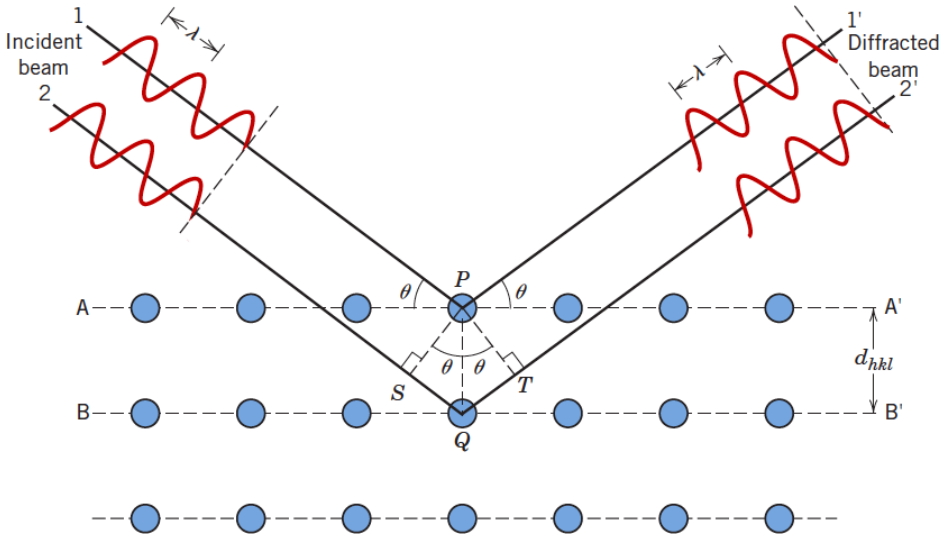

Figure 2.1: Schematic illustration of diffraction from the atoms in a crystal. The path difference between successive planes is an integer number of wavelengths, satisfying Bragg's law (CALLISTER JR, 2007, p. 68).

(d), the wavelength of the radiation (λ) and the diffraction angle (2θ) must be related as follows:

$$n\lambda = 2d\sin\theta \tag{2.1}$$

Equation (2.1) is known as Bragg's law. The integer n gives the order of diffraction from a given set of planes. It is usually omitted, and rather than considering second order diffraction from the (100) planes of a crystal, the diffraction is regarded as first order diffraction from the (200) planes, whether the (200) plane is real or fictitious (CULLITY and STOCK, 2001). Bragg's law is therefore most commonly written as:

$$\lambda = 2d\sin\theta \tag{2.2}$$

Diffraction may occur when Bragg's law is satisfied, and the normal to the diffracting planes bisects the incident and diffracted beams. The fact that the angle of incidence of the radiation on the diffracting planes equals the angle of scattering from the planes gives the process some resemblance to reflection. However, unlike reflection, diffraction involves scattering from all the atoms in a crystal, not just the surface, and diffraction of monochromatic radiation occurs only at specific angles, which satisfy Bragg's law. A further difference is that the intensity of the diffracted beam is very weak compared to the incident beam, whereas reflection is typically more efficient (CULLITY and STOCK, 2001).

The Bragg's law reduces to the formulation of the Laue equations, i.e. three conditions for incident waves to be diffracted by a crystal lattice, considering the elastic scattering condition $|\vec{k}_i|^2 = |\vec{k}_d|^2$ for a incident wave $\vec{k}_i$ and a diffracted wave

$\vec{k_d}$. The von Laue formulation of X-ray diffraction by a crystal says that diffraction peaks will be observed in directions that the rays scattered from all lattice points interfere constructively. A Laue diffraction peak, corresponding to a change in the wave vector $\Delta\vec{K} = \vec{k_d} - \vec{k_i}$ given by the reciprocal lattice vector $\vec{G}$, corresponds to a Bragg reflection from the plane family of the direct lattice planes perpendicular to $\vec{G}$. The order n of the Bragg reflection is just the length of $\vec{G}$ divided by the length of the shortest reciprocal lattice vector parallel to $\vec{G}$. The diffraction condition is $\Delta\vec{K} = \vec{k_d} - \vec{k_i} = \vec{g}^*_{hkl}$, where $\vec{G} = h\vec{a^*} + k\vec{b^*} + l\vec{c^*}$ (KITTEL, 2005).

2.1.1 Scattering by a unit cell

In materials, the atoms are not isolated but they are packed into crystals. Therefore, it is important to consider the coherent scattering from all the atoms making up the crystal. The fact that the atoms are arranged in a periodic array in space means that the scattered radiation is limited to definite directions and referred to as a set of diffracted beams. The directions of these beams are fixed by the Bragg's law. Assuming that the Bragg's law is satisfied, we wish to find the intensity of the diffracted beam by a crystal as a function of atom position. Since the crystal is the repetition of the fundamental unit cell, it is enough to consider the way in which the arrangement of atoms within a single unit cell affects the diffracted intensity. Thus, the waves scattered by individual atoms of a unit cell are not necessarily in phase except in the forward direction (CULLITY and STOCK, 2001).

The Bragg's law is a necessary but not sufficient condition for diffraction. Not all the crystal structures have primitive unit cells, i.e. atoms are only at unit cell corners, for which the Bragg's law defines a diffraction condition. Crystal structures with non-primitive unit cells have atoms at additional lattice sites (for further details see appendix B.2). These extra centres cause out-of-phase scattering to occur at certain Bragg angles. The result is that some reflections predicted by Bragg's law does not occur, i.e. certain sets of planes do not exist. They are called forbidden reflections (CALLISTER JR, 2007).

From an atom with coordinates (x,y,z) or fractional coordinates (u,v,w) equal respectively to $\left(\frac{x}{a}, \frac{y}{b}, \frac{z}{c}\right)$, the phase difference between the wave scattered by this atom and another atom at the origin, for the hkl reflection is:

$$\phi = 2\pi(hu + kv + lw) \tag{2.3}$$

These two waves may differ also in the amplitude if the two atoms are of different kinds. The amplitude of each wave is given by the atomic scattering factor f and the

scattered wave from one atom of coordinates (u,v,w) of equation (2.3) can then be expressed in the complex exponential form of equation (2.4):

$$Ae^{i\phi} = fe^{2\pi i(hu+kv+lw)} \tag{2.4}$$

The wave scattered by all the atoms of the unit cell is called structure factor (F) and it is expressed by equation (2.5).

$$F_N^{hkl} = \sum_{j=1}^{N} f_j e^{2\pi i(hu_j+kv_j+lw_j)} \tag{2.5}$$

where N is the number of the atoms in the unit cell. The intensity of the beam diffracted by all the atoms of the unit cell in a direction that satisfies the Bragg's law is proportional to $|F^2|$ and it is obtained by multiplying the expression of F given in equation (2.5) by its complex conjugate (CULLITY and STOCK, 2001).
The structure factors F and the atomic scattering factors f determine the selection/extinction rules for reflections in diffraction. The rules for the common conventional unit cells are displayed in table 2.1.

Table 2.1: Selection rules for common conventional unit cells.

Bravais lattice	**Allowed reflections**	**Forbidden reflections**
Primitive	Any h,k,l	None
Body-centered	$h+k+l=2n$ (even)	$h+k+l=2n+1$ (odd)
Face-centered	h,k,l all odd OR all even	h,k,l mixed odd/even
FCC Diamond	h,k,l all odd h,k,l all even AND $h+k+l=4n$	h,k,l mixed odd/even h,k,l all even AND $h+k+l\neq 4n$
Hexagonal	$h+2k\neq 3n$ AND l even	$h+2k=3n$ AND l odd

2.2 Diffraction from a polycrystalline sample

When a single crystal is irradiated with monochromatic radiation, it will produce a diffracted beam of radiation, which will arise from those crystal planes that satisfy Bragg's law. This radiation produces a diffraction pattern made up of spots. However, many metallic engineering materials are polycrystalline, made up of many small grains, each of which is a single crystal (HOLDEN, 1999). When a polycrystalline material is irradiated, the grains, which are correctly oriented, will produce diffracted beams. If the grain size is small enough with respect to the irradiated volume and the

orientations of the grains dispersed, we obtain many diffraction spots on the detector, which overlap and form diffraction rings (CULLITY and STOCK, 2001). The difference between the diffraction pattern obtained from a single crystal and a polycrystalline material is shown in figure 2.2.

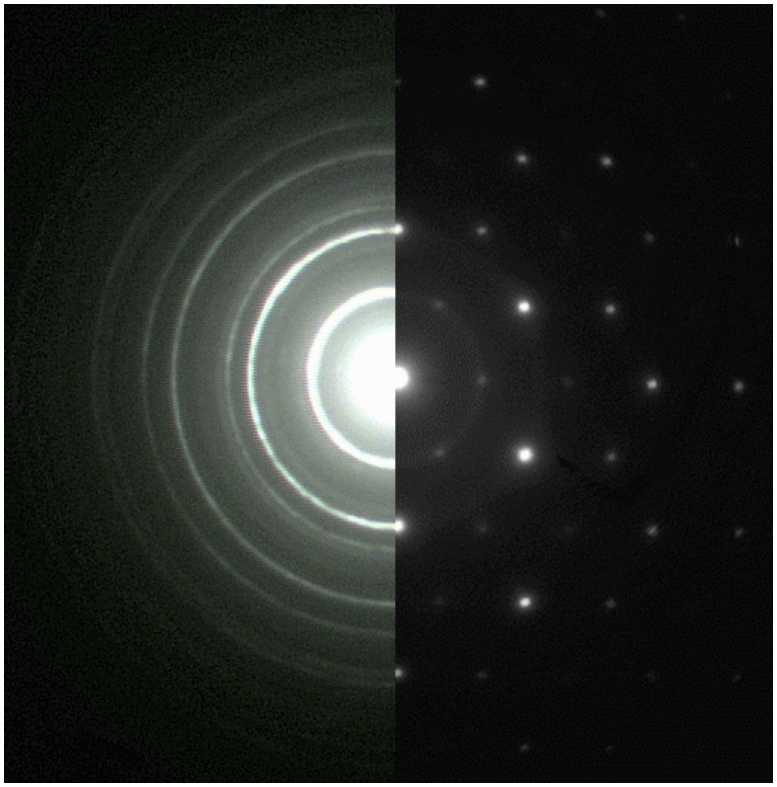

Figure 2.2: Diffraction pattern for polycrystalline (left) and single crystal (right) Cr2O3 (http://people.physics.anu.edu.au/~web107/research/highpage4.php)

The intensity of a given diffraction cone depends on multiple factors. The crystal structure determines both the intensity diffracted by a particular set of planes (structure factor) and the relative populations of different families of planes (multiplicity). Moreover, also the texture of a polycrystalline sample would affect the number of grains, which will be correctly oriented for diffraction from a particular family of crystal planes (CULLITY and STOCK, 2001; KRAWITZ, 2001).

2.3 Synchrotron X-rays

The physical principle of synchrotron radiation goes back to classical electrodynamics: an accelerated moving charge emits a spectrum of electromagnetic energy. The theory of synchrotron radiation and its application to crystallography have been discussed rather extensively in the literature (MEISEL, 1985). However, synchrotrons are not the only installations where we use X-rays to investigate

materials using diffraction. There are also simple equipments that can produce X-rays, making them available for laboratory use. The laboratory X-rays are described in section 2.5. Only a brief introduction of the synchrotron radiation theory and application will be given in this section.

If a charge e moves with velocity $\mathbf{u}$ and has an acceleration vector $\hat{\mathbf{u}}$, then the power radiated by the charge is given by:

$$P = \frac{e^2}{6\pi\varepsilon_0 c^3} \frac{\hat{u}^2 - (\mathbf{u} \times \hat{\mathbf{u}})^2/c^2}{(1 - u^2/c^2)^3} \tag{2.6}$$

where c is the speed of light in vacuum and ε_0 is the permittivity of free space. This general expression readily admits the basic ideal features of the synchrotron as a special case: a charge rotates in a circular orbit of radius R with speed $\mathbf{u}$ caused by a strong magnetic field perpendicular to the plane of the orbit, and orbits with a constant circular frequency ω. At any instant the velocity vector $\mathbf{u}$ is tangential to the orbit and the acceleration vector $\hat{\mathbf{u}}$ is perpendicular to it. Hence, the magnitude of the vector product $(\mathbf{u} \times \hat{\mathbf{u}})$ reduces to $u\hat{u}$ and equation (2.6) can be rewritten, by considering $u \ll c$, as:

$$P = \frac{e^2 \hat{u}^2}{6\pi\varepsilon_0 c^3} \tag{2.7}$$

where P is the total instantaneous power radiated by a non-relativistic accelerated charge. Equation (2.7) is of importance in the description of the scattering of X-rays by electrons in a crystal, since relatively small speeds are involved.
If we introduce the definitions $\beta = u/c$, $\gamma = (1 - \beta^2)^{-1/2}$ and $\omega = u/R = c\beta/R$, equation (2.7) becomes:

$$P = \frac{e^2 c}{6\pi\varepsilon_0} \frac{\beta^4 \gamma^4}{R^2} \tag{2.8}$$

The total instantaneous power radiated by an electron accelerated in this way is therefore approximately proportional to the fourth power of the energy of the relativistic electron, as shown by equation (2.8).

Synchrotron X-rays sources

Second and third generation synchrotrons are optimised for the production of synchrotron radiation for the investigation of materials. The European Synchrotron Radiation Facility (ESRF) is an example of a third generation source. Electrons are accelerated to energies of 6.03 GeV using a booster synchrotron and maintained at this energy in a storage ring. Magnetic fields are used to guide the electrons around the ring. When accelerated radially by magnetic fields, these electrons emit synchrotron radiation, as shown in figure 2.3(a).

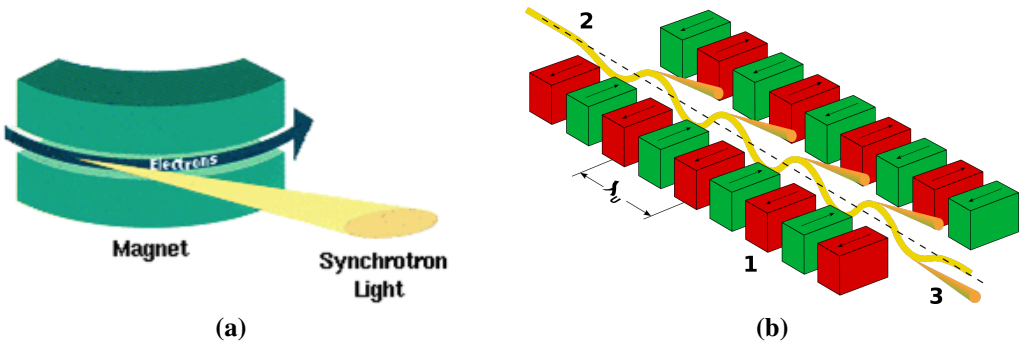

Figure 2.3: Synchrotron radiation from (a) a bending magnet and (b) an undulator (http://en.wikipedia.org/wiki/Synchrotron_radiation).

A bending magnet device applies a uniform field to the electrons. Insertion devices (wigglers or undulators) use a spatially oscillating magnetic field and can be set on straight sections of the electron beam between bending magnets. Bending magnets and wiggler devices emit a continuous spectrum of photon energies (BARUCHEL *et al.*, 2000). In figure 2.3(b), the principle of an undulator is illustrated. It consists of a periodic dipole magnet structure (1: magnet). The static magnetic field is alternating along the length of the undulator with a wavelength $\lambda(u)$. An electron beam (2: electrons) traversing the periodic magnet structure is forced to undergo oscillations and radiate (3: radiation). The high energy of the stored electrons gives access to high photon energies (hundreds of keV) and very high radiation fluxes can be obtained (BARUCHEL *et al.*, 2000). A modern synchrotron source can deliver radiation with higher energies than a laboratory X-ray tube and with brilliance more than 10 orders of magnitude greater (KRAWITZ, 2001; WITHERS, 2003). In addition, synchrotron sources are capable of producing photon energies of well over 100 keV, which increases the penetration length of the radiation in engineering materials. The penetration length in titanium for synchrotron X-rays used for diffraction varies in the range of 1–13 mm for energies from 40–150 keV. The typical path length, i.e. the distance needed to the intensity to fall by 1/e, varies in the range of 7–30 mm (WITHERS, 2003).

The wavelength of a photon (λ, in Å) is related to its energy (E, in keV) by the relationship described in BRANDES and BROOK (1992):

$$\lambda = \frac{12.3975}{E} \tag{2.9}$$

Therefore, photons with higher energies have shorter wavelengths, thus they diffract from crystal planes at lower diffraction angles (2θ). At low angles the efficiency of scattering of photons from the electrons surrounding atoms is increased, by giving stronger diffracted signals (KRAWITZ, 2001).

2.4 X-ray absorption

Further understanding of the electronic transitions in atoms can be gained by considering also the interaction of X-rays and atoms. When X-rays encounter matter, they are partly transmitted and partly absorbed. Experiments show that the fractional decrease of the intensity I of an X-ray beam when it passes through any homogeneous material is proportional to the traversed distance x, equation (2.10):

$$-\frac{\Delta I}{I} = \mu \Delta x \tag{2.10}$$

where μ is the linear absorption coefficient and it depends on the material considered, its density and the wavelength of the X-ray beam. Equation (2.10) can be rewritten after integrating over Δx as:

$$I = I_0 e^{-\mu x} \tag{2.11}$$

where I_0 is the X-ray beam incident intensity and I is the intensity of the transmitted beam after passing through a thickness x. The linear absorption coefficient μ is proportional to the density ρ, which means that μ/ρ is a constant of the material and independent of its physical status: this quantity is usually called mass absorption coefficient (KRAWITZ, 2001). Equation (2.11) can be rewritten as:

$$I = I_0 e^{-\left(\frac{\mu}{\rho}\right)\rho x} \tag{2.12}$$

The penetration length is the reciprocal of μ and it is defined as the thickness of material that causes the initial intensity I_0 to be reduced by a factor of e. This quantity is used to describe the penetration of radiation in materials (KING, 2005).

2.5 Laboratory X-rays

Since X-rays are part of the electromagnetic radiation and the investigation of materials using X-ray diffraction can be done with wavelengths in the range 0.5–2.5 Å, X-rays can be produced also by simple equipments to allow its use in a laboratory.

2.5.1 Laboratory X-ray sources

In-house or laboratory sources will produce X-rays using either an evacuated tube (figure 2.4) or a rotating anode (figure 2.5). X-ray tubes consist of a filament that acts as a cathode. Electrons are emitted by the glowing cathode and accelerated by a high negative potential (normally 30–50 kV) across the vacuum towards the anode, which

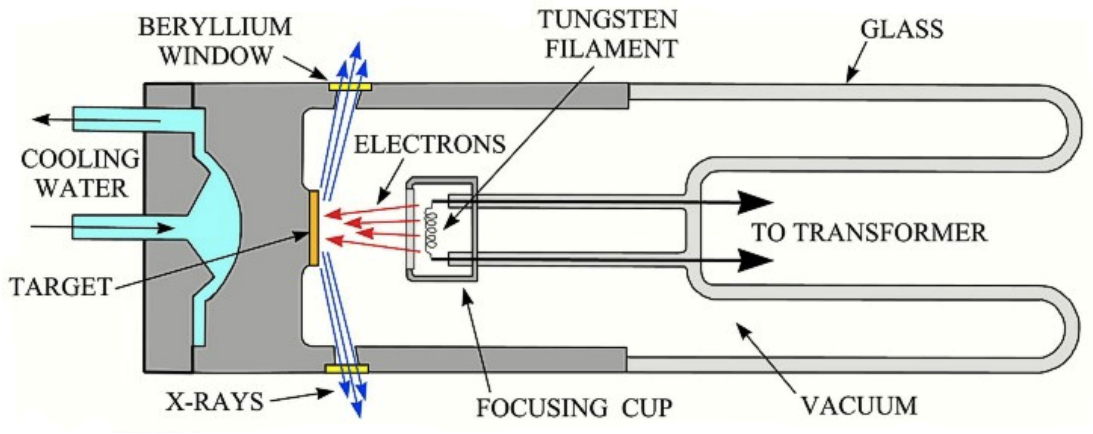

Figure 2.4: Schematic representation of an X-ray tube (http://pubs.usgs.gov/of/2001/of01-041/htmldocs/images/xrdtube.jpg).

consists of a metal target made of a characteristic material. As the electron beam impacts the anode, the high kinetic energy of the electrons is converted during deceleration into X-rays producing a continuous spectrum consisting of *bremsstrahlung* ("braking radiation") and emission lines characteristic for electronic transitions caused in the anode material. The characteristic X-ray emissions, which are important for crystallography, have an intensity that is several orders of magnitude higher than the *bremsstrahlung* and they are characteristic of the target material (CULLITY and STOCK, 2001).

If an incoming electron collides with a target atom, and knocks a low energy electron out of the atom, the atom is left in a high energy state. Another electron from a higher energy level in the atom will fall into the vacancy to reduce its energy. This transition involves a specific energy change, so a photon of characteristic energy is emitted. These characteristic peaks are labelled (K, L, M, etc) according to the energy level from which the electron is ejected. The K_α and K_β components of the X-rays emission are cut out from the *bremsstrahlung* and other emission lines by filters, monochromators or X-ray mirrors, and the resulting monochromatic X-rays are collimated and focused onto the crystals. Most laboratory X-ray equipment uses monochromatic beams of this type. Most of the kinetic energy of the incident electrons is converted into heat, which must be removed by cooling the target (CULLITY and STOCK, 2001).

Since X-ray tube is less than 1% efficient in producing X-rays and X-ray diffraction by crystals is far less efficient than this, it follows that the intensities of the diffracted X-ray beams are extremely low. Constant efforts are made to increase the intensity, finding one possible solution of using a rotating-anode tube. When X-rays are produced by a rotating anode, the cathode and anode are housed under vacuum, in which the anode target rotates at high speed to efficiently distribute and dissipate the

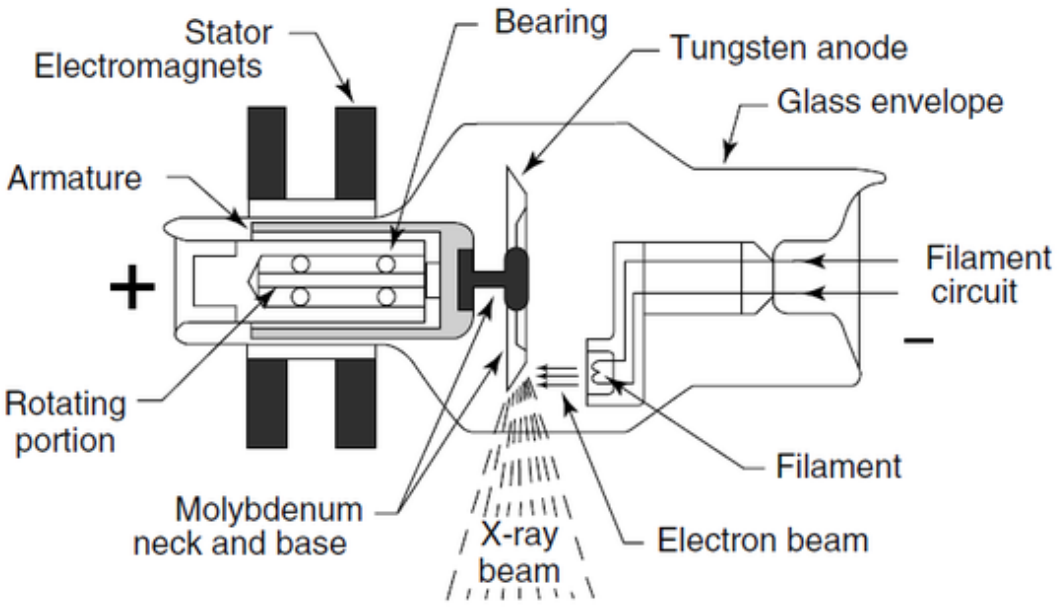

Figure 2.5: Simplified X-ray tube with a rotating anode and a heated filament (HENDEE and RITENOUR, 2003).

heat. In this way fresh target metal is continuously brought in the focal-spot area and allows a greater power input, without an excessive heating of the anode. The shafts rotate through vacuum-tight seals in the tube housing. Such tubes can operate at a power level 5–10 times higher than a fixed-focus tube, reducing then the exposure time (CULLITY and STOCK, 2001).

2.5.2 Laboratory X-ray properties

Laboratory X-rays are a useful tool for the investigation of materials by diffraction. X-rays are scattered from the electrons surrounding atomic nuclei. As the number of electrons per atom increases with increasing atomic number, the penetration length ($1/\mu$) of X-rays falls, being the linear absorption coefficient μ proportional to the atomic number. The penetration of X-rays increases with photon energy and, since the photon energies are relatively low for laboratory X-rays, their penetration in engineering materials is limited. The radiation typically used to investigate titanium (Cu-K_α) has a wavelength of 1.54 Å, corresponding to a photon energy of about 8 keV: the penetration length in titanium is only about 10 µm. Therefore, measurements using laboratory X-rays can only involve a radiation path-length in titanium of a few tens of microns, limiting the technique to surface measurements in reflection geometry (KING, 2005).

2.6 Thermal neutrons

Thermal neutrons can be used to make diffraction measurements in materials. They are neutrons at equilibrium with room temperature atoms and they have quite different properties to X-ray photons, which means different information can be obtained to complement measurements made using synchrotron X-rays.

2.6.1 Thermal neutron sources

Two different types of neutron source are commonly available for research of this kind: reactor sources and spallation sources, which have different advantages for diffraction experiments. Reactor sources produce neutrons from the controlled fission of heavy elements in a nuclear reactor.
Neutrons are uncharged, this allows them to penetrate deep in the target and close to the nuclei. The nuclear cross section of uranium-235 (U-235) for slow thermal neutrons is about 1000 barns, while for fast neutrons it is in the order of 1 barn [1]. Therefore, thermal neutrons are more likely to cause uranium-235 to fission than to be captured by uranium-238 (U-238). If at least one neutron from the U-235 fission strikes another nucleus and causes it to fission, then the chain reaction will continue. The energy released in the fission process, which is primarily in the form of the kinetic energy of the fission fragments, heats the water that serves both as a neutron moderator (i.e. it slows down the fission neutrons to thermal energies), and as a heat transfer fluid. The chain reaction is controlled by rods of neutron-absorbing material inserted into the core. The thermal energy is removed from the core by the water to an external thermal-energy converter. Collisions between neutrons and the moderator atoms bring the neutron energies into thermal equilibrium. The neutrons passing out of the moderator have a Maxwellian distribution of energies (KRAWITZ, 2001). Typically, a monochromator is then used to select a single neutron wavelength from the beam to use for diffraction measurements (WITHERS, 2001).

In contrast to reactor sources, spallation sources do not employ a self sustaining fission reactor. Instead, neutrons are released by the collision of high energy particles with a heavy metal target (BRYANT, 1996). At the ISIS spallation source (http://www.isis.stfc.ac.uk/), protons are accelerated by a synchrotron to energies of 800 MeV, which collide with a tantalum target. Each proton releases around 15 neutrons from the target. The proton beam consists of a 50 Hz series of pulses, rather than a continuous current. Therefore, the neutrons are released in

[1] A barn (symbol *b*) is a unit of area, originally used in nuclear physics for expressing the cross sectional area of nuclei and nuclear reactions. A barn is defined as 10^{-28} m^2 (100 fm^2) and is approximately the cross-sectional area of a uranium nucleus.

pulses. The neutrons are moderated by passing them through hydrogenous material (CH_4, H_2O, H_2). This reduces most of the neutrons to thermal energies while maintaining a sharply defined pulse time structure (JOHNSON and DAYMOND, 2003; WITHERS, 2001). The thermal neutrons travel at velocities comparable to the speed of sound in air (JOHNSON and DAYMOND, 2003). Because the neutrons in a single pulse all leave the target within a very short time, the time taken for each neutron to travel from the source to a detector can be used to determine its speed, and hence its wavelength (JOHNSON and DAYMOND, 2003; WITHERS, 2001). The penetration length in titanium for thermal neutrons used for diffraction is 17 mm and the typical path length is 40 mm. The given length is the distance needed to the intensity to fall by 1/e (WITHERS, 2003).

2.6.2 Thermal neutron properties

Neutrons are atomic particles with no charge and a mass of about 2000 times greater than an electron. Unlike photons, they are not scattered by electrons, but instead by the nuclei of atoms (KRAWITZ, 2001). The effect of this is that neutron scattering is equally effective at all scattering angles, while the scattering efficiency of X-rays falls off rapidly as the scattering angle is increased (FINNEY and TOMKINSON, 1990; KRAWITZ, 2001). Another important difference is that the scattering of neutrons is much weaker than X-rays for most engineering materials, and has an irregular dependence on atomic number (FINNEY and TOMKINSON, 1990).
Therefore, neutron penetration lengths are usually longer than those of synchrotron radiation, and measurements can be made through materials with greater thickness. Additionally, elements with large atomic numbers are not necessarily highly attenuating, while useful scattering can occur from light atoms such as hydrogen (FINNEY and TOMKINSON, 1990). These characteristics mean that thermal neutrons, which have wavelengths of the order of the spacing of atomic planes, have significant penetration lengths. Therefore, measurements can be made deep inside engineering materials at diffraction angles (2θ) close to 90° (PIRLING, 2000).

To achieve similar penetration lengths and effective scattering with synchrotron radiation requires high energy radiation, with short wavelengths and hence low diffraction angles (often 5–10°). This diffraction geometry means that at a given point in a component there are often particular strain components, which are difficult to measure without requiring an excessive path length, unless the component is sectioned in some way. In contrast, the near-90° 2θ diffraction angle achievable with neutron diffraction is often a more flexible tool for strain measurements in real components, particularly if the measurement of three orthogonal strain components is required (HUGHES *et al.*, 2006).

The penetration of neutrons often allows the incident and diffracted beams of radiation to be oriented so that the desired strain component is measured directly, with the diffracting planes perpendicular to the strain direction. The crystallographic plane spacing (d) is then determined using Bragg's law (equation (2.1)), and comparing the measured value to an unstrained plane spacing (d_0), elastic strain (ε) can be calculated as described above, using equation (2.13) (WITHERS, 2001):

$$\varepsilon = \frac{d - d_0}{d_0} \tag{2.13}$$

2.7 Differences between neutron and synchrotron X-ray diffraction (XRD)

Thermal neutrons and high energy synchrotron radiation have significantly different characteristics. Both are penetrating enough to make strain measurements through tens of millimetres of titanium. Therefore, subsurface elastic strain can be measured directly, without layer removal or sectioning of the sample. In materials with larger atomic mass, the penetration of synchrotron radiation falls significantly. Neutron penetration follows no clear trend with atomic mass. Therefore, it may be more suitable for measurements in materials with high atomic mass, or when light and heavy nuclei are both present in a crystal (KRAWITZ, 2001).

Synchrotron X-ray diffraction (XRD) typically involves a low diffraction angle ($2\theta \approx 5$–10°), while neutron diffraction involves a near-90° diffraction angle. Therefore, the gauge volume defined during a neutron strain measurement has an essentially rectangular cross section in the scattering plane, whereas a synchrotron gauge volume is often highly elongated. This has implications for the spatial resolution of strain measurements when different strain components are measured. The low diffraction angle associated with synchrotron radiation may lead to difficulties in measuring certain strain directions in some sample geometries. For example, if a sample geometry has the form of a wide flat plate, there will be certain strain components, which are difficult to reach without either an excessive path length (due to the low diffraction angle) or poor spatial resolution (due to the elongated gauge volume). These factors mean that neutron diffraction can sometimes be a more flexible tool for strain measurement in real engineering components (PIRLING, 2000). However, the very high radiation fluxes resulting from synchrotron sources mean that measurements can often be made orders of magnitude quicker than with neutron radiation. Typical counting times per measurement may be only a few seconds with synchrotron X-ray diffraction, compared to an hour or more for a neutron diffraction measurement.

Chapter 3

Literature review: deformations in metals

3.1 Crystallographic structure of metals

The majority of common metals have either a face-centered cubic (FCC), body-centered cubic (BCC) or a hexagonal close-packed (HCP) structure. The three different structures are represented by the unit cells shown in figure 3.1 and the difference between these structures is the building block. Different cells lead to different physical properties of the bulk metals, such as density, deformation processes, alloying behaviour, and much more (CALLISTER JR, 2007).

Hexagonal close-packed (HCP) unit cell

Planes and directions of the hexagonal lattice can be described with the Miller-Bravais indices related to a coordinate system of three basal vectors $\langle a_i \rangle$ and the longitudinal axis $\langle c \rangle$. Even if metals tend to crystallise in these perfect organised structures, stacking faults and dislocations appear to be extremely frequent and play a crucial role in the deformation behaviour of metals. A detailed description of deformation mechanisms in metals will be given in section 3.2.
Hexagonal close-packed planes are of the $\{0001\}$ family of which there is only one equivalent type. The atomic arrangement and directions of HCP planes are of the $\langle 2\bar{1}\bar{1}0 \rangle$ family and there are three for each $\{0001\}$ plane. The packing of planes in HCP structures can be described as follows: if the first layer at the bottom of the unit cell is the position A, the second layer of three atoms in the centre of the unit cell is the position B. The third layer, i.e. the top plane of the unit cell, is again the position A. So HCP crystals have a stacking sequence of ABABA. The ideal c/a ratio is 1.633, required for a perfect packing of spheres. Magnesium has the nearest c/a ratio to the perfect number with 1.624, while in α titanium the lattice parameters of the HCP

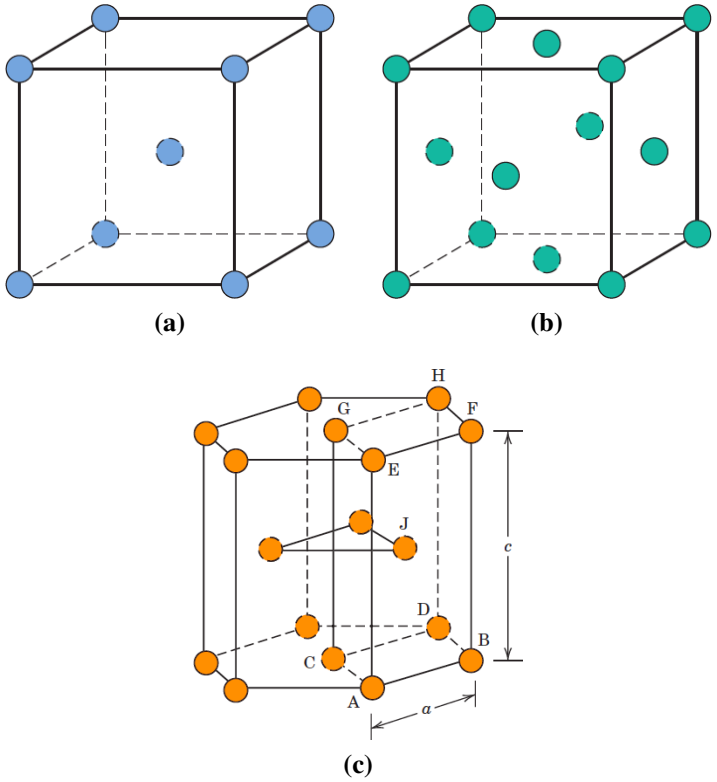

Figure 3.1: Crystallographic structure of metals: (a) Body-Centered Cubic, (b) Face-Centered Cubic and (c) Hexagonal Close-Packed (CALLISTER JR, 2007, Chapter 3).

crystal structure ($\langle a \rangle$ = 2.951 Å and $\langle c \rangle$ = 4.678 Å) give a c/a ratio of 1.5857 (LEYENS and PETERS, 2003, Chapter 1).

3.2 Slip mechanism

Deformation of metals may be of two natures, elastic and plastic. Elastic deformation corresponds to pure lattice stretching and is fully reversible as the applied load is released. Plastic deformation instead is irreversible since a residual deformation remains after the load is removed, and is controlled by slip of dislocations on specific crystallographic planes and in specific directions, which is triggered by mechanical shear loading.

Plastic deformation corresponds to the motion of large numbers of dislocations. An edge dislocation moves in response to a shear stress applied in a direction perpendicular to its line; the mechanics of dislocation motion are represented in figure 3.2. Let the initial extra half-plane of atoms be plane A. When the shear stress is applied, as indicated in figure 3.2(a), plane A is forced to the right; this in turn pushes the top halves of planes B, C, D, and so on, in the same direction. If the applied shear stress is of sufficient magnitude, the interatomic bonds of plane B are

severed along the shear plane, and the upper half of plane B becomes the extra half-plane as plane A links up with the bottom half of plane B, as shown in figure 3.2(b).

This process is subsequently repeated for the other planes, such that the extra half-plane, by discrete steps, moves from left to right by successive and repeated breaking of bonds and shifting by interatomic distances of upper half-planes. Before and after the movement of a dislocation through some particular region of the crystal, the atomic arrangement is ordered and perfect; it is only during the passage of the extra half-plane that the lattice structure is disrupted. Ultimately this extra half-plane may emerge from the right surface of the crystal, forming an edge that is one atomic distance wide; this is shown in figure 3.2(c).

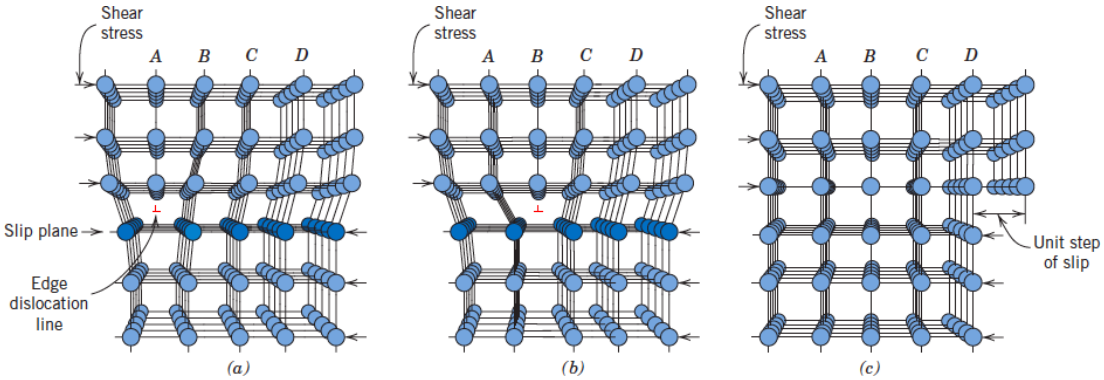

Figure 3.2: Atomic rearrangements that accompany the motion of an edge dislocation as it moves in response to an applied shear stress. (a) The extra half-plane of atoms is labelled A. (b) The dislocation moves one atomic distance to the right as A links up to the lower portion of plane B; in the process, the upper portion of B becomes the extra half-plane. (c) A step forms on the surface of the crystal as the extra half-plane exits (CALLISTER JR, 2007, p. 176). Adapted from GUY (1976).

The process by which plastic deformation is produced by dislocation motion is termed slip; the crystallographic plane along which the dislocation line traverses is the slip plane, as indicated in figure 3.2. Macroscopic plastic deformation simply corresponds to permanent deformation that results from the movement of dislocations, or slip, in response to an applied shear stress. A given combination of a crystallographic plane and crystallographic direction is defined as a slip system. The slip system depends on the crystal structure of the metal and is such that the atomic distortion, that accompanies the motion of a dislocation, is at a minimum. For a particular crystal structure, the slip plane is the plane that has the most dense atomic packing – that is, has the greatest planar density. The slip direction corresponds to the direction, in this plane, that is most closely packed with atoms – that is, has the highest linear density. This form of plastic deformation is particularly true at low homologous temperatures,

while at high homologous temperatures additional mechanisms like grain-boundary sliding for example may take place (CALLISTER JR, 2007).
Slip systems are defined via a plane and a direction in which, and along which, a dislocation may move, respectively, as subjected to external loading. Slip occurs in densely or close packed planes, where a lower shear stress/energy is required (CALLISTER JR, 2007). In FCC crystals, the usual slip system are the family $\{111\}$ $\langle 110\rangle$. There are four sets of octahedral $\{111\}$ planes and each of which has three $\langle 110\rangle$ directions. Consequently, there are 12 physically different slip systems. In BCC crystals, there are not close-packed planes but slip can occur in the plane of the greatest atomic density for planes, such as $\{110\}$, $\{112\}$ and $\{123\}$, always in the $\langle 111\rangle$ directions. The number of slip systems available are 12, 12 and 24 respectively, which gives a total of 48 slip systems for BCC crystals. In HCP crystals, the number of different families of deformation modes is high, however, HCP crystals generally have few active modes, as shown in figure 3.3 and listed in table 3.1 (CALLISTER JR, 2007).

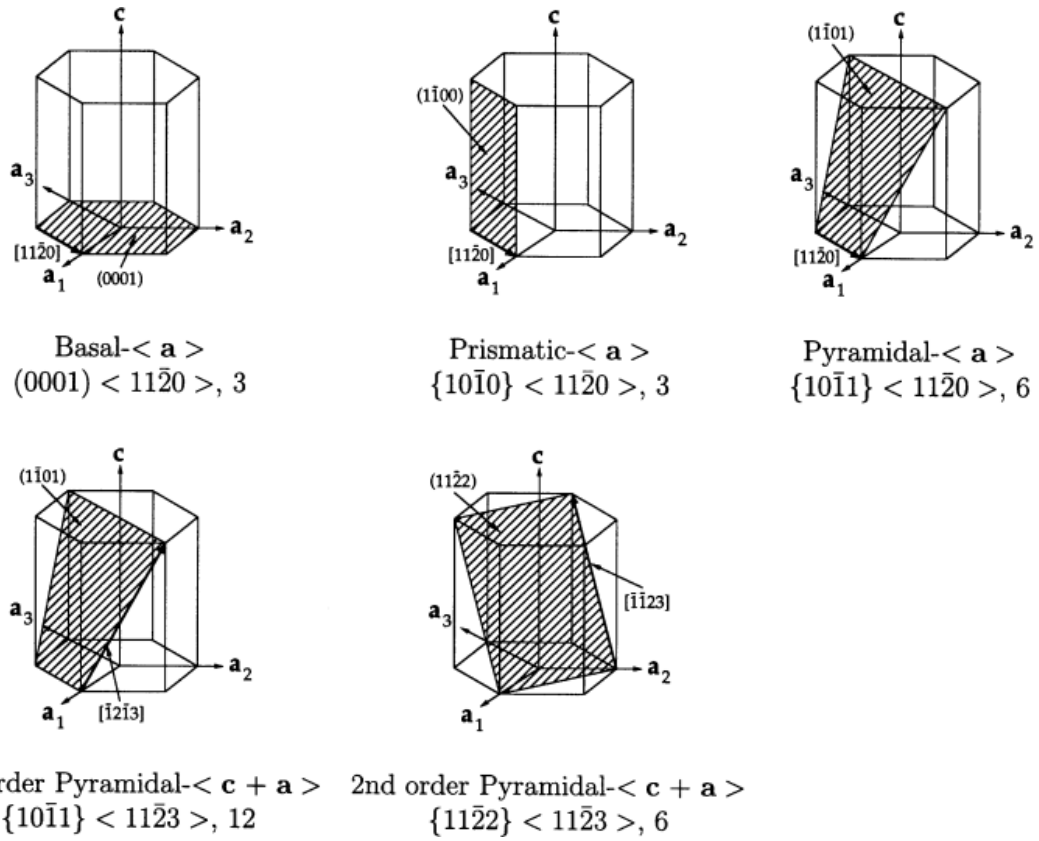

Figure 3.3: Basal $\langle a\rangle$, prismatic $\langle a\rangle$, pyramidal $\langle a\rangle$ slip systems, and first- and second-order pyramidal $\langle c+a\rangle$ slip systems in HCP crystals: grey surfaces represent slip and twinning planes; black bold vectors represent slip directions (BALASUBRAMANIAN and ANAND, 2002).

The restricted number of available slip systems in HCP crystals, due to the low

symmetry of the hexagonal lattice, usually makes the accommodation of arbitrary strains through dislocation slip difficult. It becomes especially difficult if the number of independent slip systems is less than five, which have been shown to be the minimum needed to undergo homogeneous deformation by crystallographic slip in polycrystalline materials (VON MISES, 1928). For this reason, twinning is often an additional deformation mode in HCP crystals, which allows for deformation in the $\langle c \rangle$ axis direction (PARTRIDGE, 1967).

The relative displacement of the two crystal halves resulting in the remaining plastic deformation is called Burgers vector (**b**) and its magnitude is one atomic distance on the example shown in figure 3.2(c). The nature of dislocations in a hexagonal lattice may be regrouped in three families, $\langle a \rangle$ slip, $\langle c \rangle$ slip and $\langle c+a \rangle$ slip, with respective Burgers vectors (slip directions) of lengths a, c and $\sqrt{c^2+a^2}$. Which of these slip systems gets activated depends among other factors on the aspect ratio c/a (GRAFF, 2008).

Table 3.1: Deformation slip systems in HCP crystals (ZAEFFERER, 2003).

Mode	plane	direction	multiplicity
Basal $\langle a \rangle$	$\{0001\}$	$\langle 11\bar{2}0 \rangle$	3
Prismatic $\langle a \rangle$	$\{10\bar{1}0\}$	$\langle 11\bar{2}0 \rangle$	3
Pyramidal $\langle a \rangle$	$\{10\bar{1}1\}$	$\langle 11\bar{2}0 \rangle$	6
Pyramidal $\langle c+a \rangle$ 1st ord	$\{10\bar{1}1\}$	$\langle 11\bar{2}3 \rangle$	12
Pyramidal $\langle c+a \rangle$ 2nd ord	$\{11\bar{2}2\}$	$\langle 11\bar{2}3 \rangle$	6

3.2.1 The Schmid's law

A further explanation of slip is simplified by treating the process in single crystals, then making the appropriate extension to polycrystalline materials. As mentioned previously, dislocations move in response to shear stresses applied along a slip plane and in a slip direction. Even though an applied stress may be pure tensile (or compressive), shear components exist at all but parallel or perpendicular alignments to the stress direction. These are termed resolved shear stresses, and their magnitudes depend not only on the applied stress, but also on the orientation of both slip plane and direction within that plane (CALLISTER JR, 2007).

Let ϕ represent the angle between the normal to the slip plane and the applied stress direction, and λ the angle between the slip and stress directions, as indicated in

figure 3.4. It can then be shown that for the resolved shear stress (RSS), indicated with τ_R, is:

$$\tau_R = \cos\lambda\cos\phi\,\sigma = m\,\sigma \tag{3.1}$$

where σ is the applied stress ($\sigma = F/A$, figure 3.4) and m is the Schmid factor and its range goes from 0 to 0.5. The relation expressed in equation (3.1) is usually called the Schmid's law. Since it is not always the case that the tensile axis, the slip plane normal, and the slip direction lie in the same plane, it follows that $\phi + \lambda \neq 90°$.

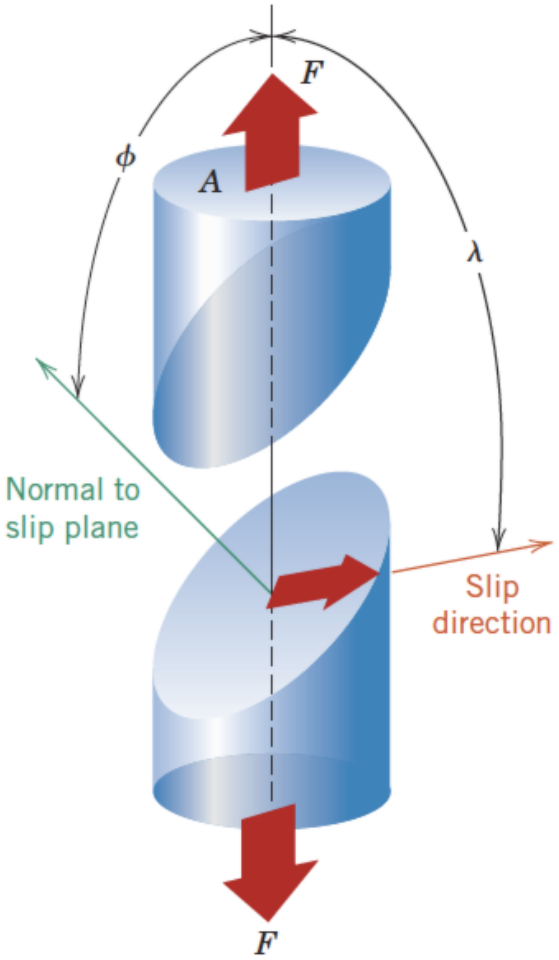

Figure 3.4: Geometrical relationships between the tensile axis, slip plane, and slip direction used in calculating the RSS for a single crystal (CALLISTER JR, 2007, p. 182).

A metal single crystal has different operating slip systems. The RSS normally differs for each one because the orientation of each slip system relative to the stress axis also differs. However, one slip system is generally oriented most favourably – that is, has the largest RSS, $\tau_R(\max)$:

$$\tau_R(\max) = (\cos\lambda\cos\phi)_{\max}\,\sigma \tag{3.2}$$

In response to an applied tensile or compressive stress, slip in a single crystal commences on the most favourably oriented slip system when the RSS reaches some critical value, termed the critical resolved shear stress (CRSS) (PIEHLER, 2009; SCHMID, 1924). It represents the minimum shear stress required to initiate slip, and it is a property of the material, determining when yielding occurs. The single crystal plastically deforms or yields when $\tau_R(\max) = \tau_{CRSS}$ and the magnitude of the applied stress required to initiate yielding (i.e., the yield strength σ_Y) is:

$$\sigma_Y = \frac{\tau_{CRSS}}{(\cos\lambda\cos\phi)_{max}} \tag{3.3}$$

where τ_{CRSS} is the critical resolved shear stress. The minimum stress necessary to introduce yielding occurs when a single crystal is oriented such that $\phi = \lambda = 45°$ under these conditions,

$$\sigma_Y = 2\tau_{CRSS} \tag{3.4}$$

For polycrystalline materials, slip occurs within each grain along the slip systems that are most favourably oriented with the applied stress; furthermore, during deformation, grains change their shape in such a manner that coherency at the grain boundaries is maintained (CALLISTER JR, 2007).

For most metallic materials, elastic deformation persists only to strains of about 0.005 (0.5%). As the material is deformed beyond this point, the stress σ is no longer proportional to the strain ε (Hooke's law, $\sigma = E\varepsilon$), and permanent, non-recoverable, or plastic deformation occurs.

Figure 3.5 plots schematically the tensile stress-strain behaviour into the plastic region for a typical metal. The transition from elastic to plastic is a gradual one for most metals; some curvature results at the onset of plastic deformation, which increases more rapidly with rising stress (CALLISTER JR, 2007).

From an atomic perspective, plastic deformation corresponds to the breaking of bonds with original atom neighbours and then reforming bonds with new neighbours as large numbers of atoms or molecules move relative to one another; upon removal of the stress they do not return to their original positions. The mechanism of this deformation is different for crystalline and amorphous materials. For crystalline solids, deformation is accomplished by means of a process called slip, which involves the motion of dislocations, as discussed in section 3.2.

Most structures are designed to ensure that only elastic deformation will result when a stress is applied. A structure or component that has plastically deformed, or experienced a permanent change in shape, may not be capable of functioning as intended. It is therefore desirable to know the stress level at which plastic deformation

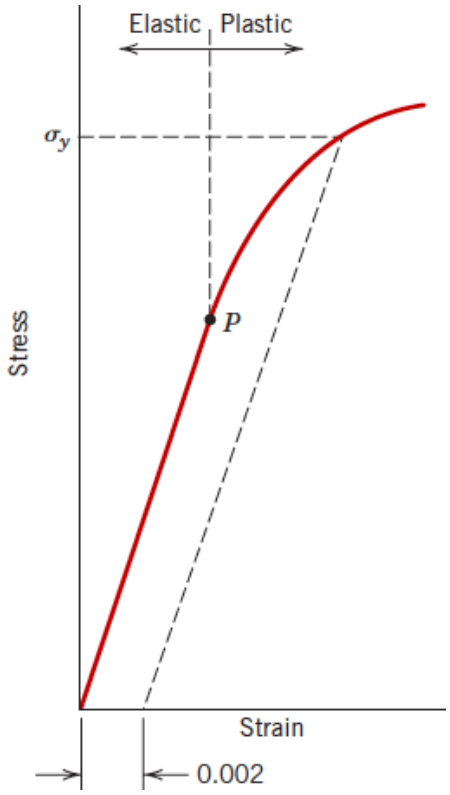

Figure 3.5: Typical stress-strain behaviour for a metal showing elastic and plastic deformations, the proportional limit *P*, and the yield strength σ_Y as determined using the 0.002 strain offset method (CALLISTER JR, 2007, p. 143).

begins, or where the phenomenon of yielding occurs. For metals that experience this gradual elasticplastic transition, the point of yielding may be determined as the initial departure from linearity of the stress-strain curve; this is sometimes called the proportional limit, as indicated by point *P* in figure 3.5. In such cases the position of this point may not be determined precisely. As a consequence, a convention has been established wherein a straight line is constructed parallel to the elastic portion of the stressstrain curve at some specified strain offset, usually 0.002 (0.2%). The stress corresponding to the intersection of this line and the stress-strain curve as it bends over in the plastic region is defined as the yield strength (σ_Y). This is demonstrated in figure 3.5. Of course, the unit of yield strength is MPa (CALLISTER JR, 2007).

For those materials having a non-linear elastic region, use of the strain offset method is not possible, and the usual practice is to define the yield strength as the stress required to produce some amount of strain (e.g., $\varepsilon = 0.005$). The magnitude of the yield strength for a metal is a measure of its resistance to plastic deformation. Yield strengths may range from 35 MPa for a low strength aluminium to over 1400 MPa for high-strength steels (CALLISTER JR, 2007).

3.3 Mechanical twinning

Under some circumstances limited plastic deformation may occur in BCC and HCP metals by mechanical twinning. Normally, twinning is important to the degree that accompanying crystallographic reorientations makes the slip process more favourable (CALLISTER JR, 2007). To date, twin nucleation criteria in metals with HCP crystal structure are still not understood. Many studies have shown that the most common slip mode in hexagonal titanium is $\{10\bar{1}0\}\ \langle 1\bar{2}10\rangle$ prismatic slip (BRIDIER *et al.*, 2005; YOO, 1981; ZAEFFERER, 2003). However, non prismatic slip and deformation twinning are necessary to achieve significant plastic deformation in polycrystalline titanium, because the $\{10\bar{1}0\}\ \langle 1\bar{2}10\rangle$ prismatic slip mode alone is not sufficient to accommodate an arbitrary plastic strain, which requires five independent slip systems (KOCKS, 1970), according to the von Mises criterion (VON MISES, 1928). Mechanical twinning is a deformation mode controlled by mechanical shear loading like slip and it occurs on a definite crystallographic plane and in a specific direction that depend on crystal structure, corresponding to a sudden reorientation of a small distinct volume of the crystal lattice. For example, for BCC metals, the twin plane and direction are (112) and [111], respectively.

Slip and twinning deformations are compared in figure 3.6 for a single crystal that is subjected to a shear stress τ. Slip ledges are shown in figure 3.6(a), the formation of which was described in section 3.2; for twinning, the shear deformation is homogeneous (figure 3.6(b)). These two processes differ from each other in several respects. First, for slip, the crystallographic orientation above and below the slip plane is the same both before and after the deformation; for twinning, there will be a reorientation across the twin plane. In addition, slip occurs in distinct atomic spacing multiples, whereas the atomic displacement for twinning is less than the interatomic separation (CALLISTER JR, 2007).

The planes of symmetry, twin planes, separate the twinned region from the not-twinned regions of the crystal lattice. Whether mechanical twinning is triggered by a critical shear stress τ, as dislocation slip is, remains an open question. This deformation mode may occur in most crystals but HCP metals are particularly subjected to twinning, especially at low homologous temperatures. In HCP metals, the twinning systems can be activated by either tension or compression of the $\langle c\rangle$ axis, depending on whether the deformation results in an elongation or a shortening of the $\langle c\rangle$ axis orientation (GRAFF, 2008).

Twinning can be the predominant deformation mechanism for plastic deformation in some hexagonal metals, such as Mg alloys, especially when most of the grains have their $\langle c\rangle$ axis aligned with the uniaxial deformation axis, which is often called a 'hard' orientation (AYDINER *et al.*, 2009; BHATTACHARYYA *et al.*, 2009; BROWN *et al.*,

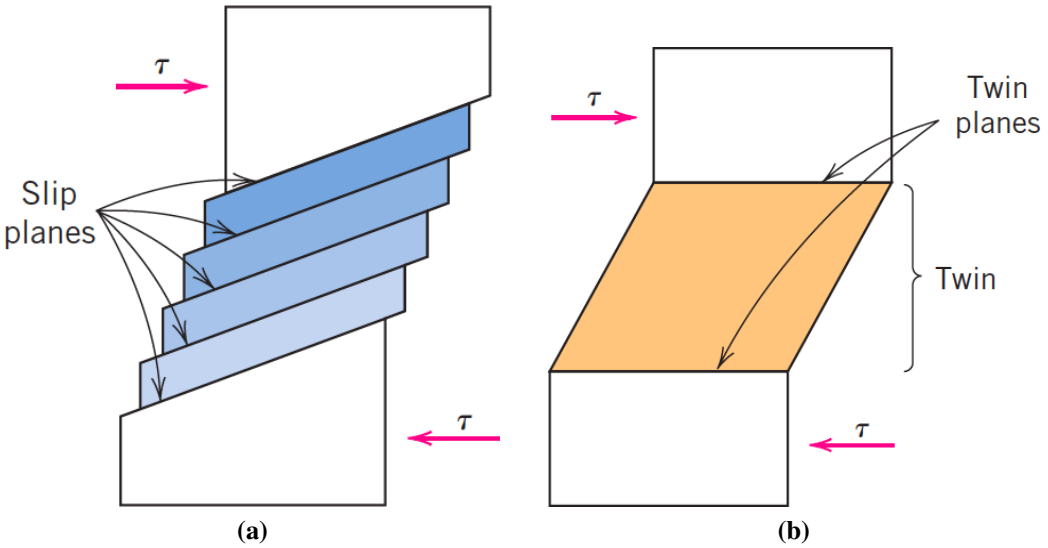

Figure 3.6: For a single crystal subjected to a shear stress, (a) deformation by slip; (b) deformation by twinning (CALLISTER JR, 2007, p. 187).

2005; CLAUSEN *et al.*, 2008; EL KADIRI and OPPEDAL, 2010). Mechanical twinning is also very important as a deformation mechanism in titanium alloys, where recent works have shown that in Ti-6Al-4V some grains reorient completely by mechanical twinning at modest strains (BRITTON *et al.*, 2010; COGHE *et al.*, 2012; PRAKASH *et al.*, 2010; PREUSS *et al.*, 2010).

The available twin systems for hexagonal titanium are listed in table 3.2. A description of the $K-\eta$ notation is given in appendix B.8.

Table 3.2: Deformation twinning modes in hexagonal titanium (BOZZOLO *et al.*, 2010; CHRISTIAN and MAHAJAN, 1995) using the $K-\eta$ notation adopted by BILBY and CROCKER (1965, p. 242).

Mode	K_1	η_1	**angle – axis**	**shear strain**
Tensile Type I	$\{10\bar{1}2\}$	$\langle\bar{1}011\rangle$	$85°\ \langle11\bar{2}0\rangle$	0.171
Tensile Type II	$\{11\bar{2}1\}$	$\langle\bar{1}\bar{1}26\rangle$	$35°\ \langle1\bar{1}00\rangle$	0.629
Compression Type I	$\{11\bar{2}2\}$	$\langle11\bar{2}\bar{3}\rangle$	$65°\ \langle\bar{1}100\rangle$	0.221
Compression Type II	$\{10\bar{1}1\}$	$\langle\bar{1}012\rangle$	$54°\ \langle\bar{1}2\bar{1}0\rangle$	0.101

The amount of bulk plastic deformation from twinning is normally small relative to that resulting from slip. However, the real importance of twinning lies with the accompanying crystallographic reorientations; twinning may place new slip systems in orientations that are favourable relative to the stress axis such that the slip process can now take place, or vice versa.

3.3.1 $\{10\bar{1}2\}\ \langle\bar{1}011\rangle$ tensile twin

Among the four deformation twinning modes that have been reported in table 3.2, at room temperature, the predominant twinning mode in hexagonal titanium is the $\{10\bar{1}2\}\ \langle\bar{1}011\rangle$ tensile twin (BHATTACHARYYA *et al.*, 2009; BILBY and CROCKER, 1965; BOZZOLO *et al.*, 2010; SALEM *et al.*, 2003; YOO *et al.*, 2002), which corresponds to a rotation of 85° around the $\langle 11\bar{2}0\rangle$ axis, as represented in 2D in figure 3.7.

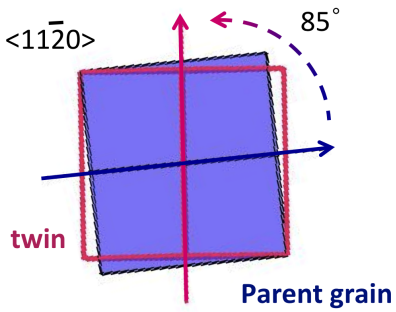

Figure 3.7: Schematic view of the $\{10\bar{1}2\}\ \langle\bar{1}011\rangle$ tensile twin: the $\langle c\rangle$ axis is rotated of 85° around one of the $\langle a\rangle$ axis ($\langle 11\bar{2}0\rangle$) common to both the twin and the parent. The direction of the rotation axis $\langle 11\bar{2}0\rangle$ points perpendicular outside the paper.

3.3.2 Slip transfer parameter

Statistical analysis of twin nucleation in hexagonal metals such as Mg and Zr has shown that twin activation does not necessary follow the traditional Schmid's law (section 3.2.1), meaning that in some cases the twin variant that forms is not the one with the highest Schmid factor (BEYERLEIN *et al.*, 2010; CAPOLUNGO *et al.*, 2009; TOMÉ *et al.*, 2011). The principle question that needs to be addressed is whether twin nucleation has a simple CRSS or more complex criterion. For example, grain neighbourhood is expected to play an important role as twinning results in significant local shear strain that needs to be accommodated. Consequently, Schmid factors calculated using the global stress state (e.g., uniaxial compression or tension) may not accurately represent the true RSS on twin systems.

In addition to this, dislocations in the grain boundaries have been found playing an important role on the twin nucleation, in terms of the relationships between the stress state in the parent grain and dislocation reactions at the grain boundary, which have been recently investigated in commercially pure titanium (CP Ti) grade 1 (WANG *et al.*, 2010a,b, 2011, 2013), together with the free surface relaxation and non-Schmid stress effects on twin nucleation (BARRETT *et al.*, 2012). The slip activity in a neighbouring grain leading to the twin nucleation was shown to be significant using

electron backscatter diffraction (EBSD) observations in WANG *et al.* (2010b). Twin to twin shear transfer across grain boundaries was also observed, particularly in boundaries with misorientation angles lower than 30° (WANG *et al.*, 2010a).
These correlations were quantified using a slip transfer parameter that is purely geometric and that was first introduced by LUSTER and MORRIS (1995) based on the observations of CLARK *et al.* (1992). The Luster-Morris parameter for slip transfer is defined as:

$$m' = \cos\kappa \cos\psi \tag{3.5}$$

where κ is the angle between the slip directions and ψ is the angle between the operating slip plane normals. This mechanism is illustrated in figure 3.8 and it is one of the several mechanisms by which twins accommodate heterogeneous deformation among the neighbouring grains.
This parameter can be referred to (i) geometric correlation between two observed slip systems in neighbouring grains that have correlated traces ("S+S"), (ii) prismatic slip traces in a 'soft' grain located next to a 'hard' grain correlated to tensile twin activity in the neighbouring 'hard' grain ("S+T") or (iii) the case of twinned grains that showed correlated twinning activity across an impinged boundary in samples with predominantly 'hard' orientations ("T+T").

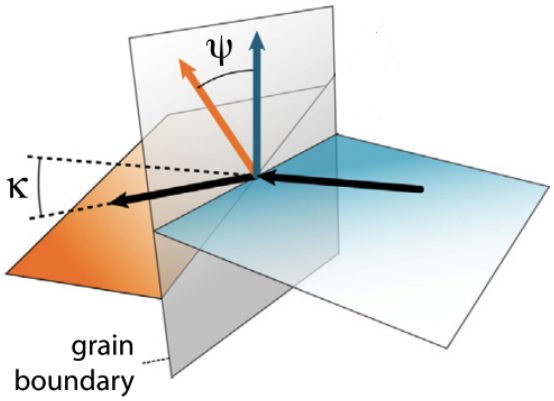

Figure 3.8: Geometry of slip transfer across a grain boundary. Horizontal (orange and blue) planes signify slip or twinning planes on either side of the boundary (BIELER *et al.*, 2014a).

3.4 Studied materials

The materials studied in this thesis are metals with a hexagonal unit cell, such as α titanium and magnesium. In this chapter a short description of their physical and chemical properties is given, followed by a brief overview of the production process and their applications.

3.4.1 Titanium

Titanium (Ti, atomic number 22) is a lustrous transition metal with a silver colour, low density and high strength. It is highly resistant to corrosion in sea water, aqua regia and chlorine. Titanium was discovered by William Gregor in 1791 in Cornwall, Great Britain. The element occurs within a number of mineral deposits and it is found in almost all living things, rocks, water bodies, and soils (*Encyclopædia Britannica*, 2006). The two most useful properties of the metal are corrosion resistance and the highest strength-to-density ratio of any metallic element (DONACHIE, 1988). In its unalloyed condition, titanium is as strong as some steels, but less dense (BARKSDALE, 1968).

As metallic element, titanium is recognised for its high strength-to-weight ratio (*Columbia Encyclopedia*, 2000). It is a strong metal with low density that is quite ductile, especially in an oxygen-free environment (*Encyclopædia Britannica*, 2006), lustrous, and metallic-white in colour (STWERTKA, 2002). The relatively high melting point (more than 1650 °C) makes it useful as a refractory metal. It is paramagnetic and has fairly low electrical and thermal conductivity (*Encyclopædia Britannica*, 2006).

Commercial (99.2% pure) grades of titanium have ultimate tensile strength of about 434 MPa, equal to that of common, low-grade steel alloys, but are less dense. Titanium is 60% more dense than aluminium, but more than twice as strong (BARKSDALE, 1968).

Certain titanium alloys achieve tensile strengths of over 1400 MPa (DONACHIE, 1988). However, titanium loses strength when heated above 430 °C (BARKSDALE, 1968).

Titanium is fairly hard, non-magnetic and a poor conductor of heat and electricity. Like those made from steel, titanium structures have a fatigue limit, which guarantees longevity in some applications (STWERTKA, 2002). Titanium alloys have lower specific stiffness than in many other structural materials such as aluminium alloys and carbon fibre. The metal is a dimorphic allotrope whose HCP α phase changes into a BCC (lattice) β phase at 882 °C (BARKSDALE, 1968).

Like aluminium and magnesium metal surfaces, titanium metal and its alloys oxidise immediately upon exposure to air. Nitrogen acts similarly to give a coating of the nitride. Titanium readily reacts with oxygen at 1200 °C in air, and at 610 °C in pure oxygen, forming titanium dioxide (*Columbia Encyclopedia*, 2000). It is, however, slow to react with water and air, as it forms a passive and oxide coating that protects the bulk metal from further oxidation (*Encyclopædia Britannica*, 2006).

Titanium exhibits excellent resistance to corrosion. It is almost as resistant as platinum, capable of withstanding attack by dilute sulphuric and hydrochloric acids as

well as chloride solutions, and most organic acids. Melting is only possible in an inert atmosphere or in a vacuum. At 550 °C, it combines with chlorine (LIDE, 2005). It also reacts with the other halogens and absorbs hydrogen (KREBS, 2006). Titanium is one of the few elements that burns in pure nitrogen gas, reacting at 800 °C to form titanium nitride, which reduces the integrity of the assembly welds and lead to joint failure (FORREST, 1981).
Titanium is always bonded to other elements in nature. As it is the ninth-most abundant element in Earth's crust (0.63% by mass) (BARKSDALE, 1968) and the seventh-most abundant metal, it is present in most igneous rocks and in sediments derived from them (as well as in living things and natural bodies of water) (*Encyclopædia Britannica*, 2006). It is widely distributed and the total reserves of titanium are estimated to exceed 600 million tonnes (*United States Geological survey*, 2012).

The processing of titanium metal occurs in 4 major steps (DONACHIE, 1988): (i) reduction of titanium ore into "sponge", a porous form; (ii) melting of sponge, or sponge plus a master alloy to form an ingot; (iii) primary fabrication, where an ingot is converted into general mill products such as billet, bar, plate, sheet, strip, and tube; (iv) secondary fabrication of finished shapes from mill products. Because it cannot be readily produced by reduction of its dioxide (STWERTKA, 2002), titanium metal is obtained by reduction of $TiCl_4$ with magnesium metal, the Kroll Process (LIDE, 2005). The complexity of this batch process explains the relatively high market value of titanium (BARKSDALE, 1968).
About 50 grades of titanium and titanium alloys are designated and currently used, although only a couple of dozen are readily available commercially (DONACHIE, 1988). The ASTM International recognizes 31 grades of titanium metal and alloys, of which grades 1 through 4 are commercially pure (unalloyed). These four are distinguished by their varying degrees of tensile strength, as a function of oxygen content, with grade 1 being the most ductile (i.e. it has the lowest tensile strength with an oxygen content of 0.18%), and grade 4 the least (i.e. it has the highest tensile strength with an oxygen content of 0.40%) (EMSLEY, 2001). The remaining grades are alloys, each designed for specific purposes, be it ductility, strength, hardness, electrical resistivity, creep resistance, resistance to corrosion from specific media, or a combination thereof (*Annual Book of ASTM Standards*, 1998; *Annual Book of ASTM Standards*, 2006). The metal can be machined using the same equipment and via the same processes as stainless steel (BARKSDALE, 1968).

Titanium is used in steel as an alloying element (ferro-titanium) to reduce grain size and as a deoxidizer, and in stainless steel to reduce carbon content (*Encyclopædia Britannica*, 2006). Titanium is often alloyed with aluminium (to refine grain size),

vanadium, copper (to harden), iron, manganese, molybdenum, and with other metals (HAMPEL, 1968). Applications for titanium mill products (sheet, plate, bar, wire, forgings, castings) can be found in industrial, aerospace, recreational, and emerging markets. Powdered titanium is used in pyrotechnics as a source of bright-burning particles.
Titanium can be alloyed with iron and molybdenum, among other elements, to produce strong, lightweight alloys for automotive, agri-food, military, industrial process (chemicals and petrochemicals, desalination plants, pulp, and paper), aerospace (jet engines, missiles, and spacecraft), medical prostheses, orthopaedic implants, dental and orthodontic instruments and files, dental implants, mobile phones, sporting goods, jewellery, and other applications (*Encyclopædia Britannica*, 2006).

In this work we have used the commercially pure titanium grade 2 and the Ti-4wt.%Al alloy.

3.4.2 Magnesium

Magnesium (Mg, atomic number 12) is a grey-white lightweight metal, with two-thirds the density of aluminium. Since magnesium is less dense than aluminium, this alloy is prised for its properties of lightness combined with strength (SILLEKENS and HORT, 2013).
Magnesium has a hexagonal close-packed (HCP) crystal structure with the nearest c/a ratio (i.e. 1.624) to the ideal 1.633 c/a ratio. It damages slightly when exposed to air, although, unlike the other alkaline metals, an oxygen-free environment is unnecessary for storage because magnesium is protected by a thin layer of oxide that is fairly impermeable and difficult to remove. The free metal burns with a characteristic brilliant-white light, making it a useful ingredient in flares (DREIZIN *et al.*, 2000). Magnesium reacts with water at room temperature, allowing the production of energy and run a magnesium-based engine. Magnesium also reacts exothermically with most acids, such as hydrochloric acid (HCl). As with aluminium, zinc, and many other metals, the reaction with HCl produces the chloride of the metal and releases hydrogen gas. Magnesium has both the lowest melting and the lowest boiling points of any of the alkaline earth metals, at 923 K and 1363 K, respectively (http://www.ptable.com/#Property/State).

Magnesium is the ninth most abundant element in the universe (HOUSECROFT and SHARPE, 2008). It is synthesised in large, ageing stars from the sequential addition of three helium nuclei to a carbon nucleus. When such a star explodes as a supernova, much of its magnesium is expelled into the interstellar medium, where it can be

recycled into new star systems. Consequently, magnesium is the eighth most abundant element in the Earth's crust (RAILSBACK, 2008) and the fourth most common element in the Earth (below iron, oxygen and silicon), making up 13% of the planet's mass and a large fraction of the planet's mantle. It is the third most abundant element dissolved in seawater, after sodium and chlorine (FLOOR, 2006). Magnesium is the eleventh most abundant element by mass in the human body. Its ions are essential to all cells, since they interact with polyphosphate compounds such as ATP, DNA, and RNA. Hundreds of enzymes require magnesium ions to function. Magnesium compounds are used medicinally as common laxatives, antacids (e.g., milk of magnesia), and to stabilise abnormal nerve excitation or blood vessel spasm such as in eclampsia. Magnesium is the metallic ion at the centre of chlorophyll, and it is a common additive to fertilizers (`http://www.mg12.info/`).

Magnesium is a highly flammable metal, especially when powdered or shaved into thin strips. It is, however, difficult to ignite in mass or bulk. Once ignited, it is difficult to extinguish, being able to burn in nitrogen, carbon dioxide and water. This property was used in incendiary weapons used in the fire-bombing of cities in the Second World War, the only practical civil defence being to smother a burning flare under dry sand to exclude the atmosphere. When burning in air, magnesium produces a brilliant-white light that includes strong ultraviolet. Thus, magnesium powder (flash powder) was used as a source of illumination in the early days of photography and in the manufacture of fireworks and marine flares, where a brilliant white light is required. Flame temperatures of magnesium and magnesium alloys can reach 3100 °C, although flame height above the burning metal is usually less than 300 mm (DREIZIN *et al.*, 2000).

China is the dominant supplier of magnesium, with approximately 80% of the world market share. China is almost completely reliant on the silico-thermic Pidgeon process to obtain the metal (*China magnesium Corporation*, 2013). Magnesium was first extracted by Sir Humphry Davy in 1808 (DAVY, 1808) and, in 1852, Robert Bunsen constructed a small laboratory cell for the electrolysis of fused $MgCl_2$ (BALL, 1956; HOY-PETERSEN, 1990). Commercial production commenced in Germany in 1886 but had reached only $\sim$ 10 tonnes worldwide by 1900. This jumped to more than 3000 tonnes by the last year of the First World War, only to fall to 330 tonnes in 1920. Production in 1939 was 32000 tonnes and, under the impetus of the Second World War, it again increased nearly tenfold only to fall again in the late 1940s. Production during the last decade has been close to 250000 tonnes/year (CLOW, 1992).

Historically, magnesium was one of the main aerospace construction metals and was used for German military aircraft as early as the First World War and extensively for

German aircraft in the Second World War. The Germans coined the name ”Elektron” for magnesium alloy, still used today. The application of magnesium in the commercial aerospace industry was generally restricted to engine-related components, due either to perceived hazards with magnesium parts in the event of fire or to corrosion. Currently, the use of magnesium alloys in aerospace is increasing, mostly driven by the increasing importance of fuel economy and the need to reduce weight (AGHION and BRONFIN, 2000). The development and testing of new magnesium alloys continues, notably Elektron 21, which has successfully undergone extensive aerospace testing for suitability in engine and internal and airframe components (BRONFIN, 2007).

Magnesium is the third-most-commonly-used structural metal, following iron and aluminium. It has been called the lightest useful metal by HARAN (2011). The main applications of magnesium are, in order: component of aluminium alloys, in die-casting (alloyed with zinc) (AVEDESIAN and BAKER, 1999), to remove sulphur in the production of iron and steel, and the production of titanium in the Kroll process (AMUNDSEN *et al.*, 2002).
Alloyed with zinc to produce the zinc sheet used in photoengraving plates in the printing industry, dry-cell battery walls, and roofing (AVEDESIAN and BAKER, 1999). As a metal, this element’s principal use is as an alloying additive to aluminium with these aluminium-magnesium alloys being used mainly for beverage cans, sports equipment such as golf clubs, fishing reels, and archery bows and arrows. Specially, high-grade car wheels of magnesium alloy are called ”mag wheels”, although the term is often more broadly misapplied to include aluminium wheels. Many car and aircraft manufacturers have made engine and body parts from magnesium.
Magnesium compounds, primarily magnesium oxide (MgO), are used as a refractory material in furnace linings for producing iron, steel, non-ferrous metals, glass, and cement. Magnesium oxide and other magnesium compounds are also used in the agricultural, chemical, and construction industries. Magnesium oxide from calcination is used as an electrical insulator in fire-resistant cables (LINSLEY, 2011).
Pharmaceutical preparations of magnesium are used to treat magnesium deficiency and hypomagnesemia, as well as eclampsia (EUSER and CIPOLLA, 2009). Usually in lower dosages, magnesium is commonly included in dietary mineral preparations, including many multivitamin preparations.

In this work we have used the Mg-3% Al-1% Zn (AZ31) alloy.

Chapter 4

Experimental methods

4.1 Material and processing

For the purpose of the research presented in this thesis, three different materials were used: commercially pure titanium grade 2, Ti-4Al alloy and AZ31 magnesium alloy.

4.1.1 Commercially pure titanium (CP Ti)

A commercially pure titanium (CP Ti) grade 2 sample was provided by Richard Moat and João Quinta da Fonseca (from the University of Manchester, UK). The sample has a diameter of about 700 µm and a length of about 1 mm and its chemical composition of the CP Ti grade 2 is given in table 4.1.

Table 4.1: Chemical composition of the CP Ti grade 2: the wt.% for the maximum values for each elements are given (http://www.cartech.com/dynamet/).

C	N	O	Fe	H	other	Ti
0.10	0.03	0.250	0.30	0.015	0.40	bal.

The microstructure of the CP Ti grade 2 material was provided by Arnas Fitzner (former University of Manchester), figure 4.1. The average grain size of the studied sample is 40.5 µm, measured by electron backscatter diffraction (EBSD).

4.1.2 Ti-4Al alloy

200 g binary Ti-4Al (i.e. 4wt.%) alloy buttons were double melted in a tungsten arc furnace under inert gas atmosphere. This was followed by beta forging at 1100 °C at the TIMET - Savoie research facility in Witton, UK. The measured chemical composition of the alloy is given in table 4.2. Subsequently, the buttons were cross-rolled in bar shape ($14 \times 14 \times 260$ mm) on a "2 high Robertson mill" (WHA

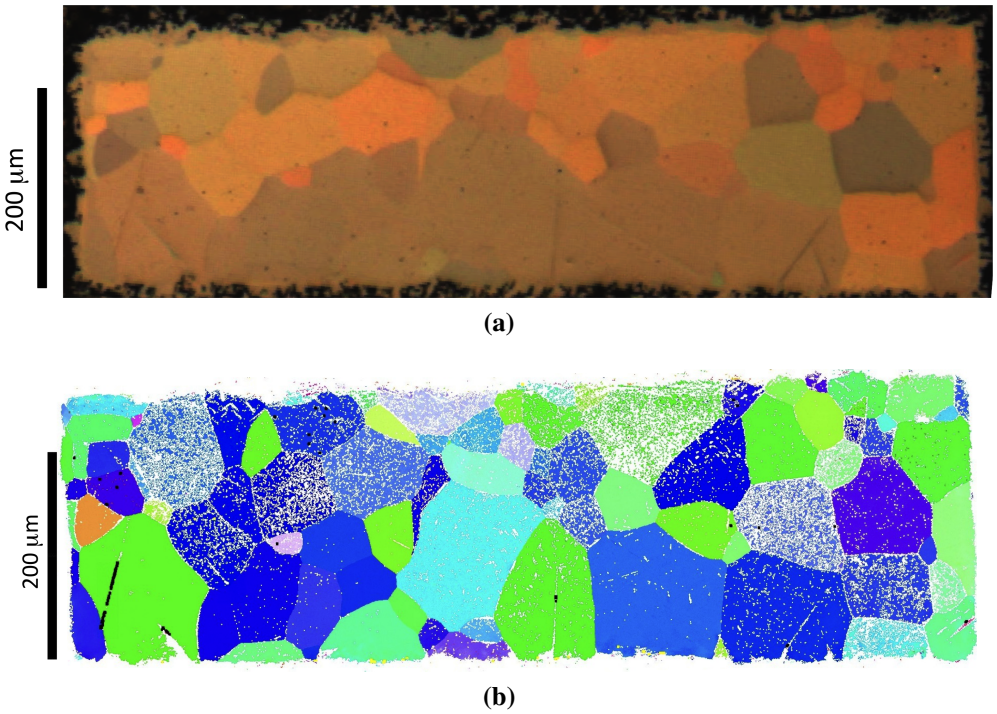

Figure 4.1: Microstructure of the material represented in terms of (a) optical micrograph with filter and (b) grain orientation map recorded by EBSD.

Robertson & Co Ltd) at 870 °C followed by a recrystallization (RX) heat treatment at 993 °C (30 °C below the beta transus temperature) in a tube furnace under Argon shielding for 5 hours followed by air-cooling. The raw material was provided by Arnas Fitzner (former University of Manchester), from which three samples with a diameter of 5 mm and length of 12.35 mm each were cut by electro-discharge machining (EDM) with the cylinder axis parallel to the original rolling direction (RD).

Table 4.2: Chemical composition of the Ti-4Al alloy, measured by TIMET - Savoie using inductively coupled plasma mass spectrometry on a HORIBA Ultima2 for metallic elements, and on a HORIBA EIMA 820V for C and on a LECO EF-400 for O and N (http://www.timet.com).

Al	C	N_2	O_2	Ti
3.9 wt.%	50 ppm	23 ppm	778 ppm	bal.

The lattice parameters and the c/a ratio were determined at the neutron spallation source ISIS, Chilton, UK. They are $\langle a \rangle$ = 2.935 Å and $\langle c \rangle$ = 4.678 Å giving a c/a ratio of around 1.5938 (FITZNER *et al.*, 2014). The average grain size of the studied samples is 73 µm, which was measured by using the linear intercept method (FITZNER *et al.*, 2014). The {0002} pole figure and the initial microstructure of the

Ti-4Al raw material are provided by Arnas Fitzner (former University of Manchester), figure 4.2.

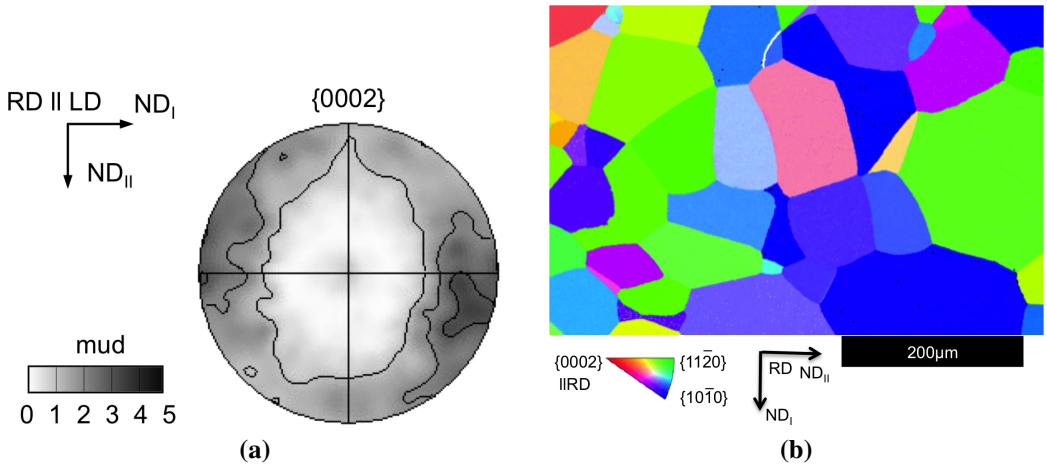

Figure 4.2: Initial microstructure of the material represented in terms of (a) {0002} pole figure and (b) grain orientation map recorded by EBSD.

4.1.3 AZ31 Mg alloy

An extruded Mg-3% Al-1% Zn (AZ31) magnesium sample was provided by Gugliermo Requena from TU Vienna. The sample has a diameter of 600 µm and a length of about 1 mm, and it was annealed for 8 hours at 500 °C. It was inserted into a glass capillary and mounted in a loading device, illustrated in figure 4.3, which is equipped with a load cell and connected to a computer controller to monitor the load applied on the sample. The loading rig, made of a glass capillary of 0.7 mm inner diameter, contains two pistons to hold the sample in-between. One of the pistons is fixed (glued into the capillary) whereas the other can be displaced by means of a thread with a pitch of 0.25 mm per full turn.

4.2 In-situ loading using neutron diffraction

The experiment was performed at the Strain Analyser for Large and Small scale engineering Applications (SALSA) beam line of the Institut Laue-Langevin (ILL) in Grenoble, France (HUGHES *et al.*, 2006; PIRLING *et al.*, 2006) on a Ti-4Al alloy. The experimental setup is shown in figure 4.4. The two-dimensional position sensitive micro-strip detector has an active area of 80×80 mm^2 with 256×256 channels. The angle covered by each channel is 0.02° at a sample-detector distance of one metre. Two-dimensional data are integrated to produce a one-dimensional diffraction peak

Figure 4.3: Loading rig used at the beam line ID18F of the ESRF during the experiment on AZ31 Mg specimens.

profile covering 5°, in which the $\{0002\}$ and $\{10\bar{1}1\}$ peaks are visible, and fitted using a Gaussian function.

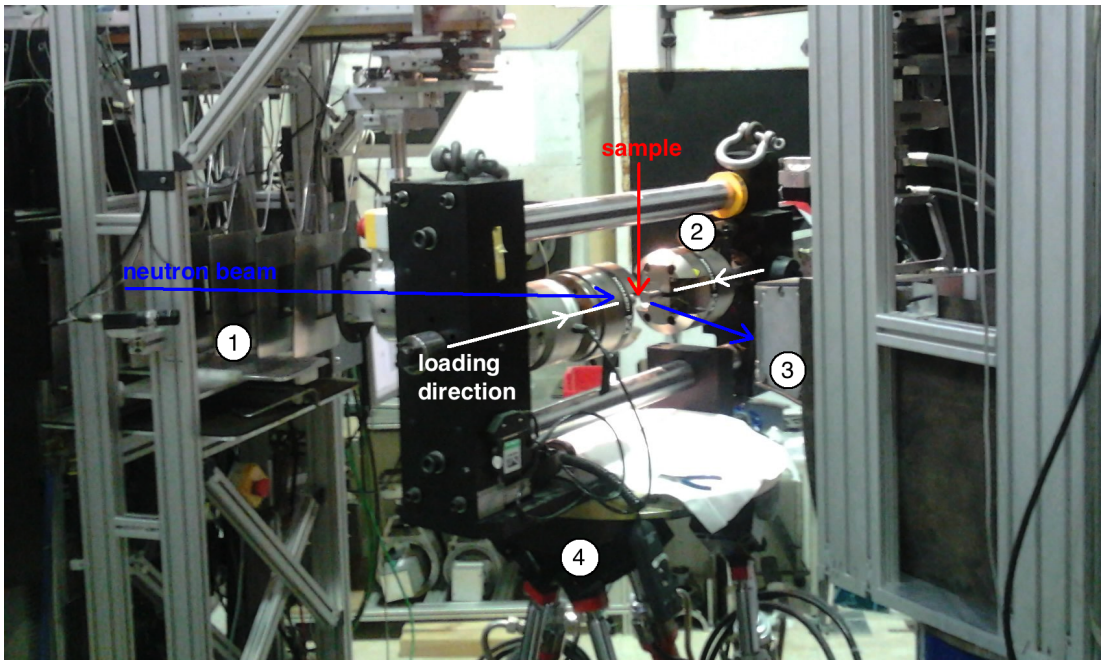

Figure 4.4: Experimental setup for the in-situ loading experiment of Ti-4Al alloy at the SALSA beam line at the ILL. The setup is composed by (1) the collimator/slits of the neutron incoming beam; (2) the stress-rig whose axis is parallel to the sample rolling direction; (3) the two-dimensional micro-strip detector and (4) the hexapod.

The material used in this experiment is the Ti-4Al alloy, which texture is such that the $\langle c \rangle$ axis of the grains tend to be oriented perpendicular to the cylinder axis. Each sample was placed in the stress-rig with the longitudinal direction of the sample aligned with the scattering vector of $\{0002\}$ planes. In this configuration, the angle

between the incoming neutron beam and the detector normal is about $2\theta = 40.5°$, at the given wavelength of $\lambda = 1.62$ Å. By monitoring the $\{0002\}$ peak intensity it is possible to follow the activation of $\{10\bar{1}2\}\ \langle\bar{1}011\rangle$ tensile twin as shown in figure 4.5. One sample was loaded in-situ and characterised by neutron diffraction, reaching a plastic deformation of about 7%. Two other samples were deformed up to the onset of deformation twinning and then cut by EDM to extract smaller cylindrical samples of 400 µm diameter and 3 mm length for the X-ray diffraction contrast tomography (DCT) measurement, section 4.3. These small samples share the same cylinder axis as the sample from which they were extracted.
The aim of this experiment was to capture the initial stage of twinning in the Ti-4Al alloy and then continue the analysis by means of the X-ray DCT.

4.3 Diffraction Contrast Tomography (near-field analysis)

The X-ray DCT (JOHNSON *et al.*, 2008; KING *et al.*, 2008, 2011; LUDWIG *et al.*, 2008, 2009a,b; REISCHIG *et al.*, 2013) is a variant of the 3D X-ray diffraction (3DXRD) microscopy technique (LI and SUTER, 2013; ODDERSHEDE *et al.*, 2010, 2012; POULSEN, 2004, 2012; SCHMIDT, 2010; SØRENSEN *et al.*, 2012; SUTER *et al.*, 2006) enabling simultaneous reconstruction of the 3D microstructure visible in X-ray attenuation contrast and the 3D grain microstructure (shape and orientations) in suitable polycrystalline materials. The technique shares a common experimental setup with conventional synchrotron radiation X-ray micro-tomography. The sample is placed on a rotation stage and irradiated by an extended, parallel and monochromatic synchrotron X-ray beam. For the case of polycrystalline materials, each of the grains will pass through Bragg diffraction alignments multiple times during the sample rotation, producing diffracted beams. Beams diffracted at small angles will be captured on the detector system that covers an area substantially bigger than the sample. In the absence of significant orientation and strain gradients inside the grains, the diffracted beams will form two-dimensional spots that can be treated as parallel projections of the diffracting grain. The analysis of Friedel pairs of these diffraction spots allows one to determine the crystallographic orientation and 3D shape of the grains in the sample (LUDWIG *et al.*, 2009b, 2010; REISCHIG *et al.*, 2013).

The principal steps of the image processing can be summarised as follows:
1. Acquisition. A stack containing several thousand diffraction images are acquired during a continuous rotation movement of the sample over 360°. The volume may

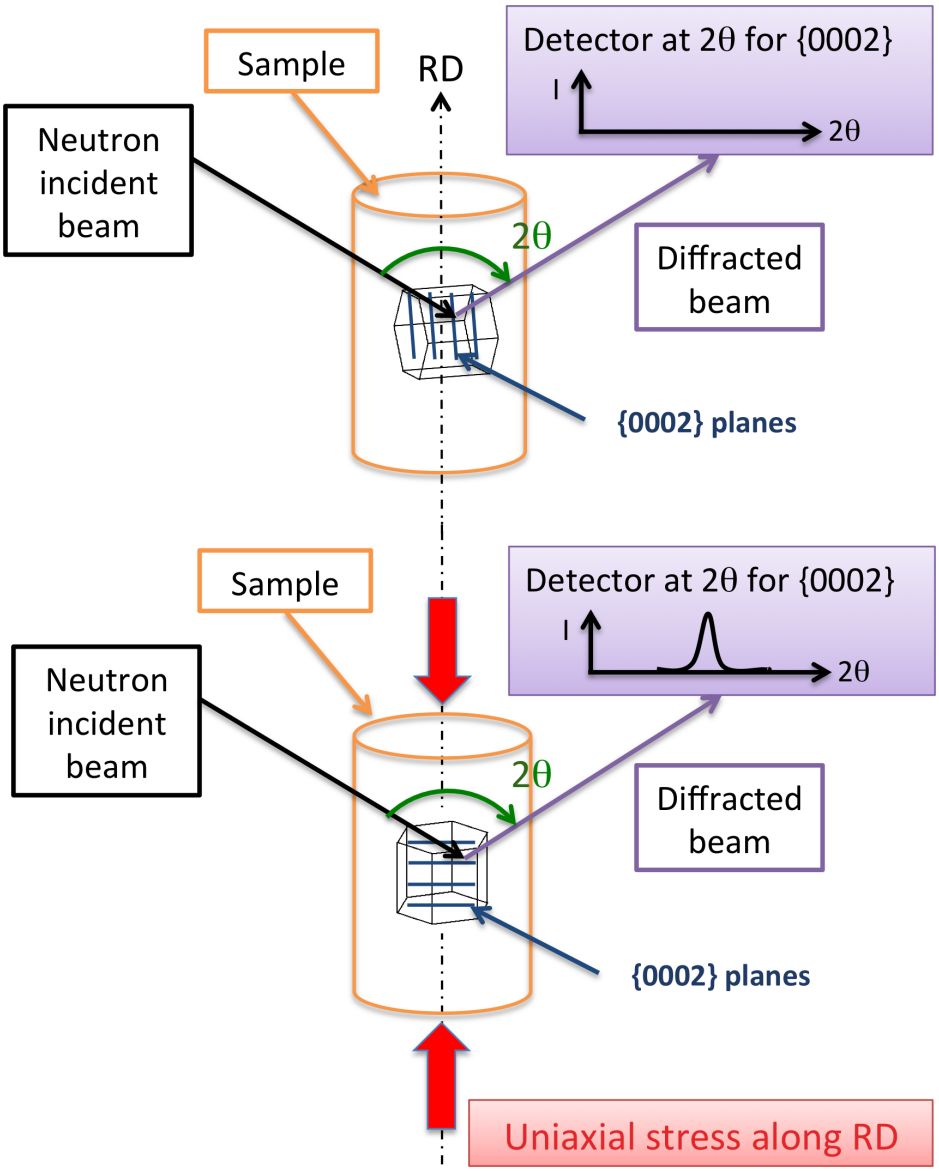

Figure 4.5: Activation of the $\{10\bar{1}2\}\ \langle\bar{1}011\rangle$ tensile twin during compression along the rolling direction (RD), where a grain with the $\langle c\rangle$ axis oriented almost perpendicular to the loading direction is rotated of 85° by the uniaxial applied load, resulting in the $\langle c\rangle$ axis to be aligned with the RD.

contain up to 100.000 diffraction *blobs* (i.e. 3D diffraction volumes), part of which may extend over several consecutive images.

2. Segmentation. Consecutive images of the 3D diffraction *blobs* are summed and segmented into 2D diffraction spots using methods based on thresholds and connectivity search. At this step all the information about the spots is stored in a database (centre-of-mass position, intensity, area, etc...).

3. Pair matching. From an axial symmetry consideration, a grain that diffracts for an angular position ω diffracts at ω + 180° (*hkl* and $\overline{hkl}$ reflections). These are called *Friedel pairs* of diffraction spots and they are detected by using a combination of

spatial and crystallographic criteria. Once a spot pair is detected, the diffraction angles that describe the geometry of the diffraction event (plane normal, scattering vector) can be calculated.

4. Indexing. The detected *Friedel pairs* are sorted into sets belonging to the same grain. Both spatial and crystallographic consistency criteria are checked. The diffracted beams arising from a grain have to intersect at the grain position and the angle between the scattering vectors has to reflect the crystal symmetry. Typically, several tens of diffraction spots can be identified per grain and the (average) grain orientation and elastic strain tensor can be determined.

5. Grain reconstruction. In the absence of strong orientation and strain gradients within a grain, the diffraction spots can be considered as parallel projections of the grain from which they arise. These projections are used to reconstruct the 3D grain shape using algebraic reconstruction techniques (ARTs) (GORDON *et al.*, 1970). This algorithm allows the reconstruction of 3D shapes from a limited number of projections. Each grain is reconstructed individually.

6. Absorption contrast tomogram. The direct beam projection images recorded during the scan are used to reconstruct the absorption contrast tomogram of the sample by a conventional filtered back-projection reconstruction. The 3D tomogram obtained can be superimposed on the 3D grain map determined by X-ray DCT.

7. Volume assemble. After thresholding the 3D grain volume, the binarised 3D grain volumes are assembled into the common sample volume. The assembly of all the reconstructed grains produces the 3D grain microstructure of the sample.

Multiple diffraction of the X-rays throughout the crystal that is nearly perfect can give rise to successive interferences with other diffracted rays. This process was described by Ewald as dynamical theory of diffraction during the early part of the 20^{th} century, in which the diffracted intensity is proportional to just the magnitude of the structure factor.

In practice, dynamic effects are relatively rare because most crystals are not perfect but consist of slightly mis-oriented ”mosaic” blocks as in the final diagram below. Therefore, when an imperfect crystal is subjected to an X-ray beam only a small fraction of the mosaic blocks will be exactly at the Bragg condition and capable of diffracting. As the crystal is rotated slightly, some mosaic blocks will move away from the Bragg condition while others will move towards it. So during a complete angular scan, the full diffracting power of the crystal will still be measurable, but obviously the mosaic spread will lead to a broadening of the diffraction peaks, without affecting excessively the diffraction pattern. The mosaic blocks in effect break up the links between the different parts of the diffracting crystal so that the multiple interference effects of the dynamic case do not occur.

The experimental setup for the standard X-ray DCT at the beam line ID11 of the ESRF is represented schematically in figure 4.6.

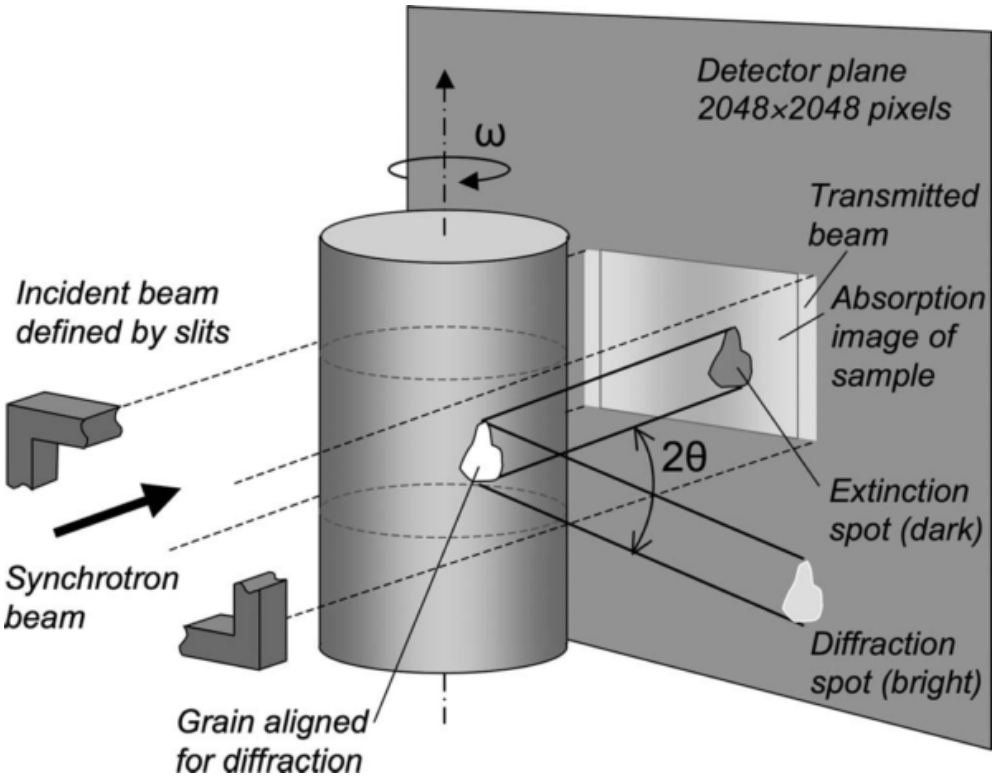

Figure 4.6: X-ray DCT experimental setup at the beam line ID11 of the ESRF, Grenoble, France (LUDWIG *et al.*, 2009b).

A monochromatic beam is produced by a bent Si (111) Laue-Laue double-crystal monochromator, with a relative bandwidth $\Delta\lambda/\lambda \approx 10^{-3}$. The diffraction images are recorded on a Fast Readout Low Noise (FReLoN) charge-coupled device (CCD) camera (LABICHE *et al.*, 2007), positioned normal to the incident beam, downstream from the sample. The CCD camera has an array of 2048×2048 pixels and it is coupled via visible light microscope optics to a transparent luminescent screen, with a field of view of 2.87×2.87 mm^2. This detector, used for the near-field approach, is placed at a sample-detector distance of about 4–7 mm and will be referred to as the near-field or in-line detector. 7200 images are recorded during a 360° rotation of the sample, with an exposure time in the range 0.15–1 second, giving scan duration of 2.5 hours. The sample must have a diameter of 500–700 µm and usually a length of 1–3 mm, to fit in the DCT geometry.

The coordinate system is defined such that the X-ray beam is along the laboratory X direction the Z direction is vertical, upwards from the origin, and the Y direction is consistent with a right-handed system. The laboratory reference system is defined by

three unit vectors $\mathbf{X}, \mathbf{Y}, \mathbf{Z}$ in the 3D Cartesian space, with components shown in equation (4.1).

$$\begin{aligned} X &= (1,0,0) \\ Y &= (0,1,0) \\ Z &= (0,0,1) \end{aligned} \tag{4.1}$$

The rotation axis of the sample is right-handed and parallel with the sample z-axis. The sample coordinate system rotates around the z-axis and it coincides with the laboratory coordinate system when the rotation angle ω is equal to zero. The rotation angle ω describes the sample rotation counter clockwise if we look at it from the top. Coordinates (U,V) on the detector have the origin in the point (0,0) on the top left corner of the camera (being the camera and looking into the beam). Two unit vectors $\mathbf{U}, \mathbf{V}$, defined in equation (4.2), represent the directions on the detector.

$$\begin{aligned} U &= (0,1,0) \\ V &= (0,0,-1) \end{aligned} \tag{4.2}$$

Three experiments were performed using the X-ray DCT technique:

1. Characterisation of a polycrystalline CP Ti grade 2 sample using two variants of 3DXRD: (i) X-ray diffraction contrast tomography (DCT) as an instance of a near-field method and (ii) conventional 3DXRD as a representative of the far-field diffraction method. The aim of this experiment was a comparison between near-field and far-field indexing approach for the characterisation of a polycrystalline CP Ti sample. The far-field analysis is described in section 4.4. Both approaches are frequently used at beam line ID11 of the ESRF.
2. Characterisation of deformation twinning in a Ti-4Al alloy, which was previously loaded in-situ and characterised by neutron diffraction at the ILL. This experiment was performed at beam line ID11 of the ESRF. An absorber was inserted between the sample and the detector to attenuate the transmitted beam without affecting the diffracted beams and preventing the saturation area illuminated by the direct beam. This allows the integration time per image to be increased, in order to increase the intensity in the diffraction spots, improving the detection of weak spots (i.e. the ones related to thin twin lamellae).
3. Section topography at high diffraction angles ($2\theta \approx 90^\circ$) on AZ31 Mg alloys. This experiment was performed at the beam line ID18F of the ESRF. The high diffraction angle geometry requires a vertical detector configuration with a horizontal rotation axis (parallel to the Y direction) as described in section 4.5.

4.4 3D X-ray diffraction (far-field analysis)

The experimental setup for the far-field approach is illustrated in figure 4.7. A CCD camera has a fibre-optic coupling (COAN *et al.*, 2006), which gives an effective pixel size of 48.5 µm/pixel and a field of view of 99.3×99.3 mm^2. It was placed 205 mm from the sample and was used for the acquisition of far-field diffraction data. 7200 images were recorded during a 360° rotation of the sample, with an exposure time of 0.1 seconds, giving a scan duration of 27 minutes.

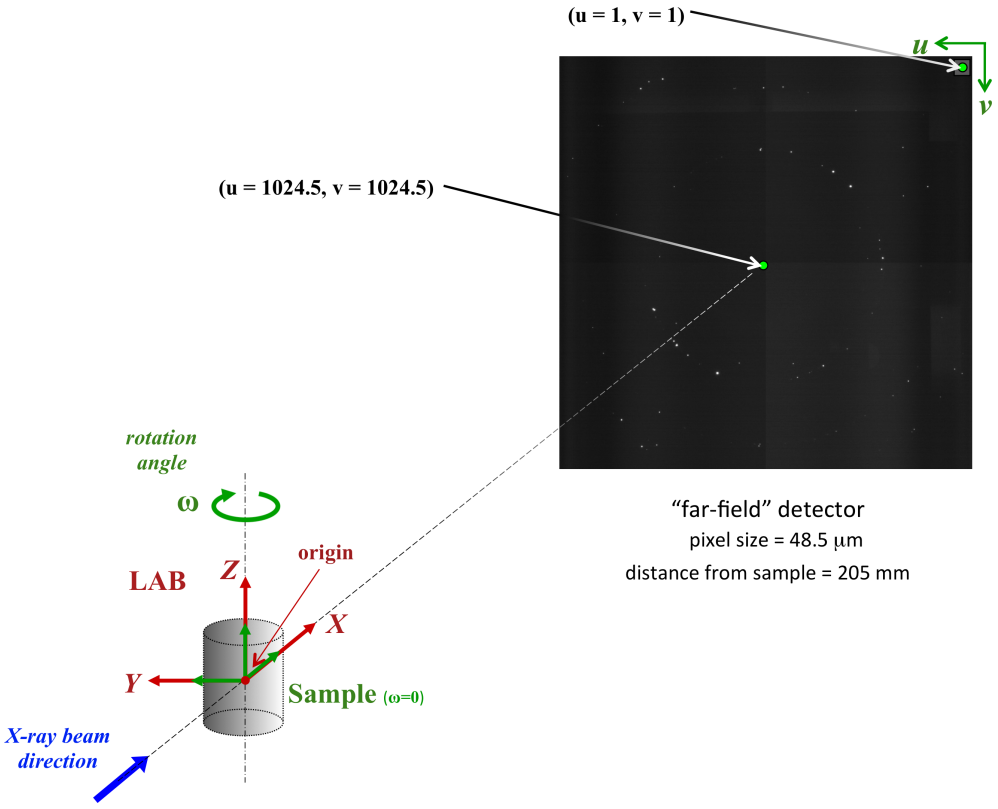

Figure 4.7: Experimental setup for the far-field approach at beam line ID11 of the ESRF, Grenoble, France.

The far-field configuration has a reduced sensitivity to unwanted translational (e.g. thermal) drifts of the setup leading to more accurate observations of diffraction angles. The large effective pixel size also means that it can use a thicker scintillator screen without degrading the resolution. Consequently, it has a higher sensitivity than the near-field detector and the counting times are one or two orders of magnitude faster. Given the higher sensitivity, it is generally believed that smaller grains can be detected. As explained later, the actual range of detectable grain sizes may be determined by the dynamic range of the detector system.

The far-field data were analysed using ImageD11, part of the FABLE package (http://sourceforge.net/projects/fable/). The principal steps of the image processing can be summarised as follows (WRIGHT, 2005):

1. Peaksearching in raw two-dimensional images.

2. Post-processing peaksearch output to obtain final merged peaks and filtering.

3. Calibration of sample-detector distance/beam centre.

4. Indexing.

5. Refinement of the diffraction geometry, grains and crystal translations and filtering to zap out any dubious peaks.

4.5 X-ray section topography

The experiment was performed at the beam line ID18F of the ESRF using a monochromatic beam produced by a Si (111) Bragg-Bragg double-crystal monochromator (14.4 keV, relative energy bandwidth $\Delta\lambda/\lambda \approx 10^{-4}$). The sample rotation axis is right-handed and parallel with the laboratory Y direction. The sample coordinate system rotates around this axis.
A compression rig (see section 4.1.3) hosting the cylinder shaped sample was mounted on the rotation stage such that the sample and the loading axis were aligned with the rotation axis. The X-ray DCT and section topography acquisitions were carried out consecutively, without changing the sample mounting or the beam defining slit settings.
X-ray diffraction topography allows visualising in a non-destructive way distortion fields in crystals caused by defects, defect distributions, or microscopic deformation. It is possible to provide a quantitative analysis of the lattice distortions, strain and local orientation measurements at the sub-grain level (HÄRTWIG *et al.*, 2002).

The experiment was divided into two parts: (i) an X-ray DCT experiment was performed with "full" beam illumination and horizontal rotation axis; (ii) from one of the grains of the DCT reconstruction on the in-line detector, selected diffraction images corresponding to pinhole and section topography experiments were taken only on the vertical detector.
In the first part the detector was an ATMEL FReLoN with an effective pixel size of 3.5 µm/pixel and a sample-detector distance of 4.3 mm. The scan was performed over a 360° continuous rotation with 0.05° rotation steps.
For the second part, absorption masks were placed in the incoming beam to produce two configurations (figure 4.8): (i) the "line" beam profile illuminating a 7 µm-thick slice of the sample, parallel to the rotation axis; (ii) a periodic array of "pencil" beams with period 50 µm and individual sections of about 7×7 µm^2. The diffraction images

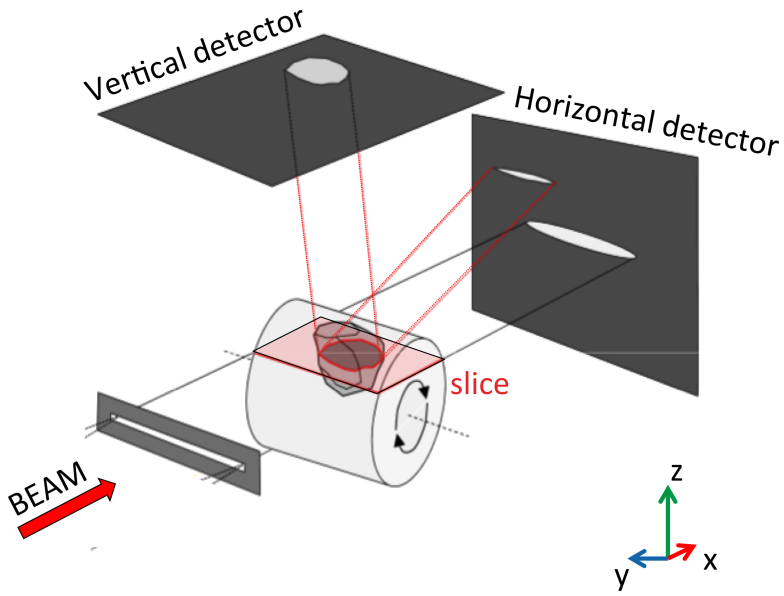

(a) "Line" beam illumination

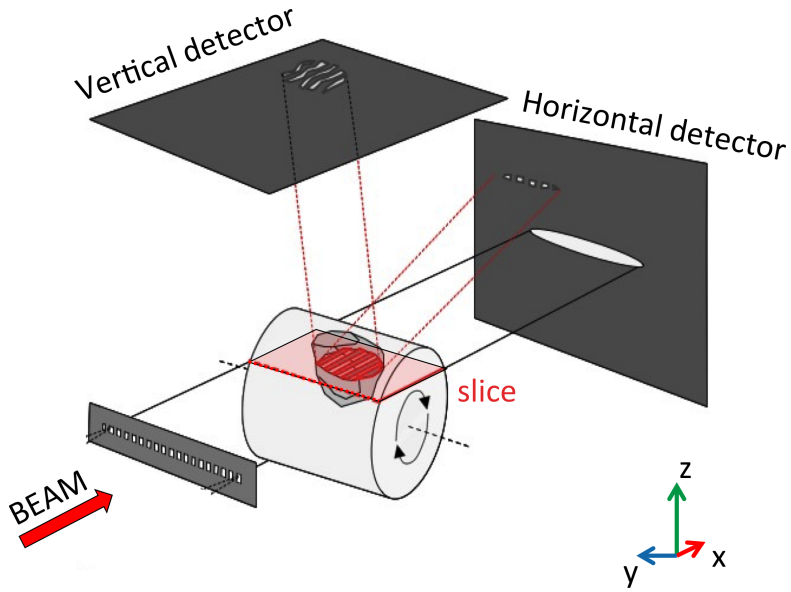

(b) "Pencil" beam illumination

Figure 4.8: Experimental setup with two detectors (horizontal and vertical) with an absorption mask that provides (a) the "line" beam illumination or (b) the "pencil" beam illumination of the sample. The irradiated section of the grain is projected almost perpendicularly ($2\theta \approx 90°$) onto the detector plane. An horizontal (in-line) detector on which the section appears compressed as it diffracts is also shown for comparison (REISCHIG *et al.*, 2013).

were recorded on a FReLoN E2V camera, placed above the sample at about 2.3 mm distance, containing 2048×2048 pixels and an effective pixel size of 1.5 µm/pixel.

In this configuration, it is possible to look into single grains in more detail, revealing the presence of sub-grain structures like slip bands and twins. For an undeformed

grain, one observes 2D sections of the grain and one can construct 3D volumes without tomographic reconstruction by stacking slices (section topography). Without having a reference on the vertical detector, we need to use single crystal scan using the in-line detector for the alignment of the vertical detector. Thus, the indexed reflections from a Ge single crystal on the vertical detector were used to fit the position of the vertical detector.

In a grain mapping experiment, one has the choice between different illumination modes ("full" beam versus "line" beam versus "pencil" beam) and detector positions (in-line (horizontal) detector versus vertical detector). In figure 4.8 "line" beam illumination is compared to the "pencil" beam illumination. Normally the forward scattering geometry with the detector normal to the incident beam direction is used. The choice of this standard acquisition geometry is natural for experiments on macroscopic, absorbing samples, where the use of high X-ray energies is mandatory and scattering at high 2θ angles is weak.
However, most materials of technological relevance have grain sizes below 30 µm and therefore require ultimate detector resolution when characterised with full field imaging techniques. In order to limit the probability of spot overlap, the sample dimensions need to be scaled accordingly (typically less than 20 grains through the diameter of the sample) and therefore in many materials one may then work at X-ray energies below 25 keV. This is a practical prerequisite for observation of reflections at high scattering angles, which improve sensitivity for elastic strain and orientation determination inside grains, which can be of interest for characterisation of deformation progress in materials.
In the characterisation of deformation in materials, the use of the X-ray DCT combined with the section topography could potentially increase the orientation resolution and elastic strain sensitivity by acquiring diffracted beams at 2θ diffraction angles close to 90° (LUDWIG *et al.*, 2010).
Three selected reflections of the biggest grain, intersecting the vertical detector close to the centre, were selected and seven "pencil" beam scans were performed for each reflection and its corresponding Friedel pair. Each image was integrated over a ω range of 1.5°, covering the angular range of the reflection curve with an integration time of 7.5 seconds. Seven "pencil" beam scans were needed to illuminate the whole slice by shifting the grid along the rotation axis direction (1:6 duty cycle).

Chapter 5

Development of software tools

In the following chapter, the software tools and graphical user interfaces (GUIs) that I have developed are described. Those tools have been used mostly for the data analysis of the experiments introduced in chapter 4 and then explained in detail in chapters 6–8. The main language used is MATLAB, with some scripts written in Python. The scripts referenced in this chapter are included (entirely or headings only) in appendix C.
The development of software tools was carried out in various domains:

- Calculation of the crystallographic reflections and symmetry operators using FABLE (section 5.1),
- Identification of twins (section 5.2),
- Importing data from far-field 3D X-ray diffraction (3DXRD) experiments into the DCT code (section 5.3),
- Development of a simple GUI to visualise the indexed grains using the representation of the unit cell (section 5.4),
- Development of a GUI where to select and visualise diffraction spots assigned to a grain after the forward simulation (section 5.5),
- Improvement and extension of an existing GUI, adding functionalities as the use of several colour maps for the reconstructed volume, the 3D grain visualisation and rendering, the texture analysis, the Schmid factor and slip transfer parameter calculations (section 5.6).

5.1 Calculation of the crystallographic reflections and symmetry operators using FABLE

The calculation of the symmetry operators in the DCT code was initially restricted to cubic and hexagonal crystal systems. We have generalised the calculation of the

reflections and the symmetry operators to all the available space groups. For this purpose we have used the *xfab* module in FABLE (http://sourceforge.net/projects/fable/), where the calculation of the unique set of reflections is based on the algorithm described in LE PAGE and GABE (1979).

The list of symmetry operators are computed given a space group or a crystal system and they are saved into text files that are read in MATLAB. The symmetry operators for hexagonal crystal systems are reported here below. The symmetry operators for all the crystal systems are reported in appendix B.1.

$$\begin{pmatrix} 1 & 0 & 0 \\ 0 & 1 & 0 \\ 0 & 0 & 1 \end{pmatrix} \quad \begin{pmatrix} 0.5 & 0.866 & 0 \\ -0.866 & 0.5 & 0 \\ 0 & 0 & 1 \end{pmatrix} \quad \begin{pmatrix} -1 & 0 & 0 \\ 0 & 1 & 0 \\ 0 & 0 & -1 \end{pmatrix}$$

$$\begin{pmatrix} -0.5 & -0.866 & 0 \\ 0.866 & -0.5 & 0 \\ 0 & 0 & 1 \end{pmatrix} \quad \begin{pmatrix} 0.5 & -0.866 & 0 \\ 0.866 & 0.5 & 0 \\ 0 & 0 & 1 \end{pmatrix} \quad \begin{pmatrix} -0.5 & -0.866 & 0 \\ -0.866 & 0.5 & 0 \\ 0 & 0 & -1 \end{pmatrix}$$

$$\begin{pmatrix} -0.5 & 0.866 & 0 \\ -0.866 & -0.5 & 0 \\ 0 & 0 & 1 \end{pmatrix} \quad \begin{pmatrix} 0.5 & 0.866 & 0 \\ 0.866 & -0.5 & 0 \\ 0 & 0 & -1 \end{pmatrix} \quad \begin{pmatrix} -0.5 & 0.866 & 0 \\ 0.866 & 0.5 & 0 \\ 0 & 0 & -1 \end{pmatrix}$$

$$\begin{pmatrix} -1 & 0 & 0 \\ 0 & -1 & 0 \\ 0 & 0 & 1 \end{pmatrix} \quad \begin{pmatrix} 0.5 & -0.866 & 0 \\ -0.866 & -0.5 & 0 \\ 0 & 0 & -1 \end{pmatrix} \quad \begin{pmatrix} 1 & 0 & 0 \\ 0 & -1 & 0 \\ 0 & 0 & -1 \end{pmatrix}$$

The list of the unique reflections for Ti-4Al with $\lambda = 0.309$ Å for synchrotron X-rays is reported here below:

```
h k l sin(theta)/lambda2 1 0 0.520452        2 1 4 0.673539
1 0 0 0.196712         2 1 1 0.531313        2 2 0 0.681431
0 0 2 0.213767         1 1 4 0.546692        3 1 0 0.709256
1 0 1 0.223874         2 1 2 0.562642        2 2 2 0.714174
1 0 2 0.290503         1 0 5 0.569470        3 1 1 0.717264
1 1 0 0.340716         2 0 4 0.581005        1 1 6 0.726190
1 0 3 0.376181         3 0 0 0.590137        3 0 4 0.728729
2 0 0 0.393424         3 0 1 0.599738        3 1 2 0.740770
1 1 2 0.402223         2 1 3 0.611299        2 1 5 0.745970
2 0 1 0.407685         3 0 2 0.627660        2 0 6 0.752362
0 0 4 0.427533         0 0 6 0.641300        1 0 7 0.773611
2 0 2 0.447749         2 0 5 0.663614        3 1 3 0.778370
1 0 4 0.470617         1 0 6 0.670791        4 0 0 0.786849
2 0 3 0.507542         3 0 3 0.671623
```

The corresponding list of the first three reflections for Ti-4Al using the symmetry operators is reported here below:

```
h k l sin(theta)/lambda0 0 -2 0.213767        0 -1 1 0.223874
0 -1 0 0.196712        0 0 2 0.213767         0 1 -1 0.223874
-1 0 0 0.196712        -1 0 -1 0.223874       1 -1 -1 0.223874
1 -1 0 0.196712        -1 1 -1 0.223874       0 1 1 0.223874
-1 1 0 0.196712        -1 0 1 0.223874        1 0 -1 0.223874
1 0 0 0.196712         0 -1 -1 0.223874       1 -1 1 0.223874
0 1 0 0.196712         -1 1 1 0.223874        1 0 1 0.223874

...
```

The reference functions in the DCT code for the calculation of the reflections are:

- *zUtil_Cryst/gtCrystCalculateReflections.m*
- *zUtil_Cryst/gtCrystCalculateSymmetryOperators.m*

5.2 Identification of twins

The X-ray diffraction contrast tomography (DCT) analysis process starts with the preprocessing of the collected images at the beam line and ends with the reconstructed grains, which are reconstructed individually and then assembled in the sample volume (see section 4.3). When assembling grains it may occur that some of them overlap, totally or partially, producing a conflict. During this operation, if two grains overlap, the orientations of the grains in conflict are compared using the coincident site lattice (CSL) value and the Brandon criterion (BONNET *et al.*, 1981; BOZZOLO *et al.*, 2010).
The relation between the number of lattice points in the unit cell of a CSL and the number of lattice points in a unit cell of the generating lattice is called Σ (Sigma); it is the unit cell volume of the CSL in units of the unit cell volume of the elementary cells of the crystals. Grains close to CSL misorientations can still be considered CSL boundaries. A grain boundary is considered to be a CSL type Σ if the misorientation from the exact coincidence relationship γ_m (measured in degrees) satisfies the Brandon criterion shown in equation (5.1):

$$\gamma_m = \frac{15}{\sqrt{\Sigma}} \tag{5.1}$$

The CSL values built-in in the DCT code for cubic and hexagonal close-packed (HCP) crystal lattices are reported in tables 5.1 and 5.2.

Table 5.1: CSL values for cubic crystal systems.

Σ	**angle** (γ_Σ)	{**hkl**}	**axis cart** ($\mathbf{u}_\Sigma$)	γ_m
3	60.0	1 1 1	0.577 0.577 0.577	8.660
5	36.9	1 0 0	1 0 0	6.708
7	38.2	1 1 1	0.577 0.577 0.577	5.669
9	38.9	1 1 0	0.707 0.707 0	5.000
11	50.5	1 1 0	0.707 0.707 0	4.522
13	22.6	1 0 0	1 0 0	4.160
13	27.8	1 1 1	0.577 0.577 0.577	4.160

Table 5.2: CSL values for hexagonal crystal systems. (*) X axis convention is used.

Σ	**angle** (γ_Σ)	{**hkil**}	(*)**axis cart** ($\mathbf{u}_\Sigma$)	γ_m
7	21.8	0 0 0 1	0 0 1	5.629
7	64.6	1 0 $\bar{1}$ 0	0.866 0.5 0	5.590
11	35.1	1 0 $\bar{1}$ 0	0.866 0.5 0	4.502
11	84.8	2 $\bar{1}$ $\bar{1}$ 0	1 0 0	4.482
13	27.8	0 0 0 1	0 0 1	4.144
13	57.4	2 $\bar{1}$ $\bar{1}$ 0	1 0 0	4.129
13	76.7	1 0 $\bar{1}$ 0	0.866 0.5 0	4.113
17	40.1	2 $\bar{1}$ $\bar{1}$ 0	1 0 0	3.627
17	79.8	3 $\bar{1}$ -2 0	0.982 0.189 0	3.617
19	13.2	0 0 0 1	0 0 1	3.432
19	65.1	10 $\bar{5}$ $\bar{5}$ 3	0.982 0 0.185	3.423
19	87.0	1 0 $\bar{1}$ 0	0.866 0.5 0	3.414
23	55.6	1 0 $\bar{1}$ 0	0.866 0.5 0	3.121
23	72.3	2 $\bar{1}$ $\bar{1}$ 0	1 0 0	3.114
23	86.3	10 0 $\bar{1}$0 3	0.855 0.494 0.161	3.108

If a grain is a twin candidate, the misorientation between the two grains must fulfil the conditions for the angle γ and the axis $\mathbf{u}$ expressed in equation (5.2):

$$\begin{aligned} \text{abs}(\gamma - \gamma_\Sigma) &< \gamma_m \\ \text{abs}(\arccos(\mathbf{u} \cdot \mathbf{u}_\Sigma)) &< \gamma_m \end{aligned} \tag{5.2}$$

The shared volume fraction between two grains is the volume in common between those grains divided by the volume of the biggest grain among the two considered. In the case of a twinned grain, this fraction should be greater than 0.5 because the twin normally grows inside the parent grain (being part of the grain that has been reoriented). Sometimes it happens that the twin grows at the surface of the parent grain and it is also possible that it has not been reconstructed correctly. In this latter case, the shared volume fraction can be very small or zero, even if both grains (parent grain and twin) satisfy the orientation conditions requested by equation (5.2). Thus, a manual checking of all the identified twins or grains in conflicts is recommended.

In the process of assembling grains, it is possible to select one twin type and hide the others, providing the corresponding Σ value. For hexagonal crystal systems, the two existing conventions for defining the crystal reference system are taken into account and, by default, the X convention is used, i.e. the X crystallographic axis is parallel to $\langle 2\bar{1}\bar{1}0 \rangle$.
An example of the twin identification output in a Ti-4Al volume is shown below, selecting the $\{10\bar{1}2\}\ \langle\bar{1}011\rangle$ tensile twin, with misorientation angle γ of 85 $^\circ$ and misorientation axis **u** parallel to $\langle 11\bar{2}0 \rangle$ axes.

```
*** PHASE 1 *** Selected {10-12}<-1011> tensile twin (CSL: 11.b) ***
Found twin  52 for grainID  28 with mis_angle 85.23 degrees
(shared volume fraction 0.88)
Found twin  41 for grainID  15 with mis_angle 85.44 degrees
(shared volume fraction 0.91)
Found twin  73 for grainID  55 with mis_angle 85.10 degrees
(shared volume fraction 0.96)
Found twin  94 for grainID  40 with mis_angle 85.24 degrees
(shared volume fraction 0.77)
Found twin  68 for grainID  17 with mis_angle 85.10 degrees
(shared volume fraction 0.98)
Found twin 113 for grainID  61 with mis_angle 85.32 degrees
(shared volume fraction 0.87)
Found twin  95 for grainID  32 with mis_angle 85.73 degrees
(shared volume fraction 0.87)
Found twin  71 for grainID  16 with mis_angle 85.59 degrees
(shared volume fraction 0.89)
Found twin 125 for grainID  50 with mis_angle 85.33 degrees
(shared volume fraction 0.76)
Found twin 123 for grainID  42 with mis_angle 85.27 degrees
(shared volume fraction 0.88)
```

```
Found twin  89 for grainID  17 with mis_angle 84.79 degrees
(shared volume fraction 0.97)
Found twin 145 for grainID 110 with mis_angle 85.29 degrees
(shared volume fraction 0.84)
Found twin 160 for grainID 111 with mis_angle 85.57 degrees
(shared volume fraction 0.88)
Found twin  87 for grainID  8 with mis_angle 85.62 degrees
(shared volume fraction 0.03)
Found twin 107 for grainID  4 with mis_angle 85.92 degrees
(shared volume fraction 0.48)
Found twin 147 for grainID  16 with mis_angle 85.14 degrees
(shared volume fraction 0.11)
Found twin 144 for grainID  67 with mis_angle 85.26 degrees
(shared volume fraction 0.28)

Check POSSIBLE twin  44 for grainID  2 with mis_angle 88.41 degrees
(shared volume fraction 0.00)
Check POSSIBLE twin  50 for grainID  47 with mis_angle 76.53 degrees
(shared volume fraction 0.00)
Check POSSIBLE twin  77 for grainID  28 with mis_angle 60.27 degrees
(shared volume fraction 0.02)
Check POSSIBLE twin  81 for grainID  25 with mis_angle 80.02 degrees
(shared volume fraction 0.01)
Check POSSIBLE twin  69 for grainID  16 with mis_angle 36.54 degrees
(shared volume fraction 0.08)
Check POSSIBLE twin 111 for grainID  48 with mis_angle 79.01 degrees
(shared volume fraction 0.00)
Check POSSIBLE twin 111 for grainID  61 with mis_angle 37.25 degrees
(shared volume fraction 0.01)
Check POSSIBLE twin 108 for grainID 103 with mis_angle 74.53 degrees
(shared volume fraction 0.00)
Check POSSIBLE twin 132 for grainID  3 with mis_angle 87.35 degrees
(shared volume fraction 0.00)
Check POSSIBLE twin 137 for grainID  75 with mis_angle 54.65 degrees
(shared volume fraction 0.02)
Check POSSIBLE twin 165 for grainID  49 with mis_angle 57.08 degrees
(shared volume fraction 0.38)
Check POSSIBLE twin 171 for grainID  40 with mis_angle 35.31 degrees
(shared volume fraction 0.20)
```

```
Hidden twin  85 for grainID  15: {11-21}<11-26> tensile twin

Grains in conflict: grain  59 and  20 - mis_angle 4.27 degrees
(shared volume fraction 0.01)
Grains in conflict: grain 120 and 104 - mis_angle 2.52 degrees
(shared volume fraction 0.03)
Grains in conflict: grain 156 and  17 - mis_angle 2.28 degrees
(shared volume fraction 0.11)
Grains in conflict: grain 165 and 126 - mis_angle 2.09 degrees
(shared volume fraction 0.22)
Grains in conflict: grain 166 and 126 - mis_angle 3.88 degrees
(shared volume fraction 0.06)
```

The reference function of the DCT code for the twin identification is:

- *5_reconstruction/GtAssembleVol3D.m::calculatePhaseVolumeTwins*

5.3 Importing data from far-field 3DXRD experiments into the DCT code

Sometimes it is the case that various experiments are performed on the same sample, resulting in different types of data from different techniques. At the end the main issue is how to use all the available data, finding a way to combine and cross-validate the results.
A specific case is introduced in chapter 6, where near-field and far-field 3DXRD data from a polycrystalline CP Ti sample containing more than 1500 grains have been analysed using two different software packages. The near-field data have been acquired using the X-ray DCT technique and analysed using the DCT code (http://sourceforge.net/projects/dct/); the far-field data have been acquired using the far-field 3DXRD technique and analysed using the ImageD11 (http://sourceforge.net/p/fable/wiki/imaged11/), part of the FABLE project.
The work that has been done allows the conversion of the far-field data into near-field data, handling correctly the different geometries of the experiment and making possible a comparison of the grain properties (position, orientation and size). The grain size is computed from the measured intensity of the diffracted peaks. We have developed a routine to read in MATLAB the output from FABLE and then, using the same geometry, to compare the two types of data as described in chapter 6.

The FABLE parameter file used for this analysis for the material description, experimental geometry and detector type is reported here:

```
cell__a 2.9518
cell__b 2.9518
cell__c 4.689
cell_alpha 90.0
cell_beta 90.0
cell_gamma 120.0
cell_lattice_[P,A,B,C,I,F,R] P
chi 0.0
cosine_tol 0.002
distance 205324.70768
ds_tol 0.008
eta_range 0.0
fit_tolerance 0.2
hkl_tol 0.02
max_grains 2000
min_bin_prob 1e-05
minpks 60
no_bins 10000
o11 1
o12 0
o21 0
o22 1
omegasign 1.0
ring_1 6
ring_2 2
t_x 0.0
t_y 0.0
t_z 0.0
tilt_x 0.00044576791848
tilt_y -0.00767352759395
tilt_z -0.00410647550274
uniqueness 0.5
wavelength 0.3099625
wedge -0.0202613006997
y_center 1002.89148361
y_size 48.5
z_center 1032.96000657
```

```
z_size 48.5
```

An example of output file from ImageD11 indexing routine for a grain is:

```
#translation: 170.674 211.389 244.885
#name 259:peaks_t100_s_cleaned.flt
#intensity_info sum_of_all = 965216.655696 ,
middle 70 from 0.000000 to 180.000000 in tth:
median = 12149.408181 , min = 2370.248608 , max = 26053.761383 ,
mean = 12856.252608 , std = 7340.169631 , n = 70
#npks 74
#Rod 0.723821 0.538484 -0.167791
#UBI:
1.31913112 0.956139329 2.46147586
0.712128933 1.18149885 -2.60913363
-3.35935608 3.22462965 0.545372354
```

All the indexed grains are then plotted using the Pyhon script *plotImageD11map.py* from FABLE, figure 5.1(a). Grains are coloured according to the number of assigned peaks. The equivalent plot in MATLAB, after having converted the ImageD11 data into DCT data, is shown in figure 5.1(b), coloured according to the inverse pole figure (IPF) of the sample z-axis and plotted using the script described in section 5.4. The reference functions of the DCT code for converting the far-field data into the DCT code are:

- *zUtil_Taper/gtTaperReadParFile.m*
- *zUtil_Taper/gtTaperReadMapFile.m*
- *zUtil_Taper/gtTaperReadFltFile.m*
- *zUtil_Taper/gtTaperUpdateGrains.m*

5.4 A simple GUI for visualising the indexed grains

After having indexed all the grains, in order to check the results it is necessary to visualise the indexed grains in the sample, looking at their position, orientation and size. For this purpose a GUI that displays grains using a unit cell representation was created, currently built-in for cubic and hexagonal crystal systems only. In general, if the crystal system is not hexagonal, the cubic unit cell representation is used.
As an example, the twinned grains (edges) and the twins (faces) of a Ti-4Al alloy are shown in figure 5.2.

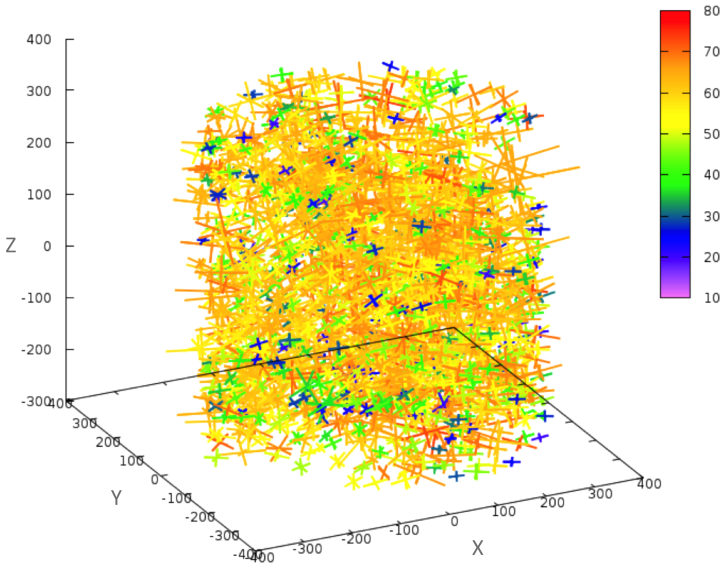

(a)

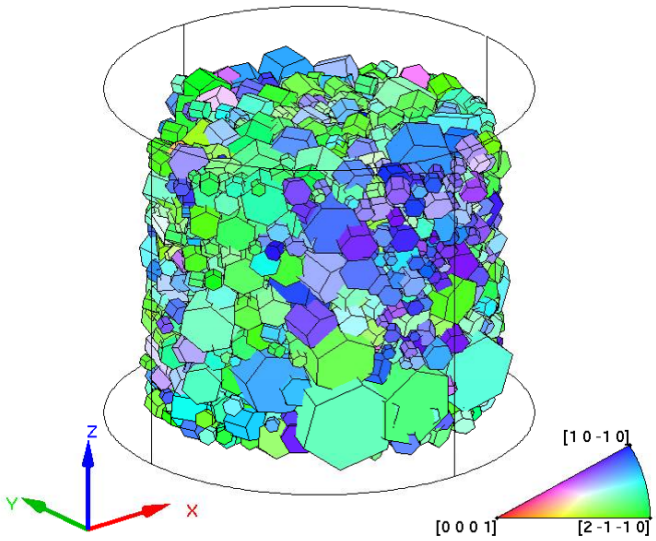

(b)

Figure 5.1: (a) Grains plotted using Python script *plotImageD11map.py* from FABLE and coloured according to the number of assigned peaks; (b) Grains plotted using the DCT code and coloured according to the IPF along the sample z-axis. The two plots do not have the same axes view.

The grains are positioned in the sample envelope (black cylinder) and oriented according to their orientation, coloured by the IPF along the sample z-axis and scaled according to their volume, estimated from the total measured intensity of the diffraction spots assigned to the grains.

In the left panel buttons allow rotating the figure (**Rotate 3D ON**), zooming in (**Zoom IN**) and zooming out (**Zoom OUT**), showing/hiding all the grains (**Hide grains**), showing/hiding the sample envelope (**Hide sample**), showing/hiding the axis (**Hide axes**), toggling the transparency of the grains from edges-only to flat surfaces (**Toggle**

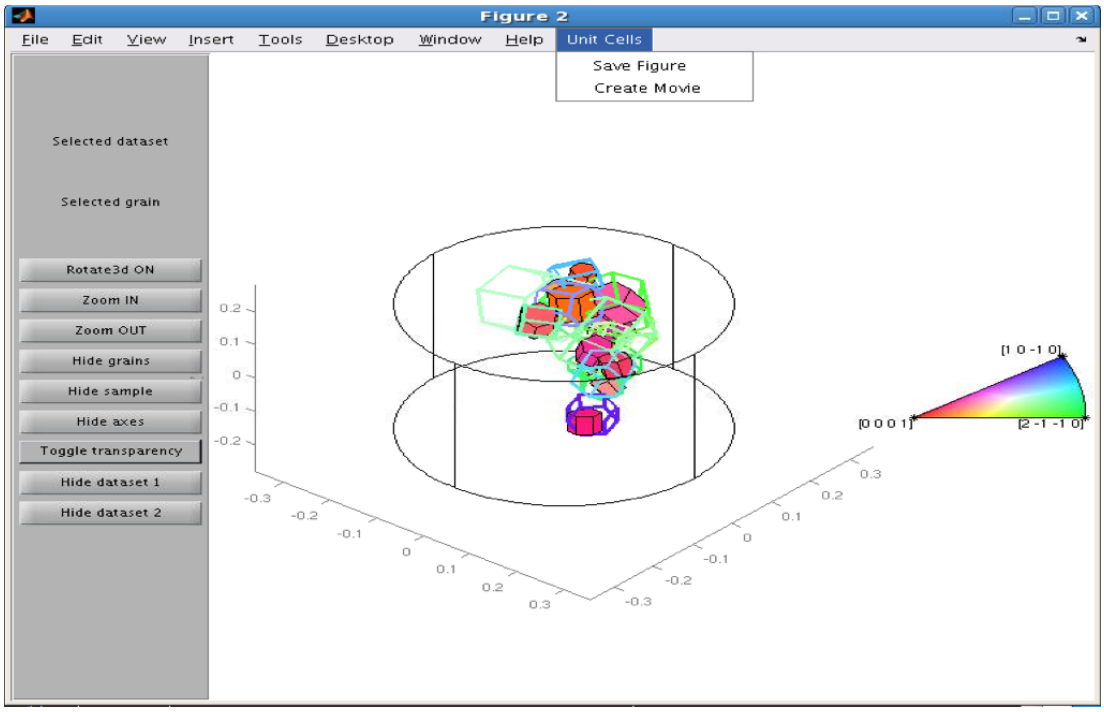

Figure 5.2: A simple GUI for displaying the indexed grains: twinned grains and their twins of a Ti-4Al sample with 171 grains are shown. IPF-Z colour map is used.

transparency) and showing/hiding each dataset (**Hide dataset 1**, **Hide dataset 2**). Each grain in the sample envelope has a context menu (i.e. it is activated by a right click of the mouse) with additional options as displaying the grain information (ID, orientation, position, RGB colour, . . .), saving the grain information in the workspace and toggling the transparency for the selected grain.
In the figure menu, there is a **Unit Cells** menu with the options to save the figure (**Save Figure**) and to create a movie while rotating around the sample z-axis (**Create Movie**).
The reference function of the DCT code for the displaying of the indexed grains is:

- *6_rendering/gtDrawGrainUnitCells.m*

5.5 Forward simulation GUI

After having indexed all the grains in a polycrystalline material, the typical number of diffraction spots ('difspot' or reflection) assigned to a grain may vary between 10 to 80, depending on the experimental geometry, crystallographic orientation, the position of the grain in the sample, the grain size and the spot quality, in terms of intensity and shape. Normally the number of assigned reflections is not equal to the total number of available reflections on the detector.

In order to increase the number of the reflections assigned to a grain, it can be useful to simulate all the reflections on the detector using the available symmetry operators for the current crystal system and using the orientation and position of the grain in the sample. After this simulation, it is possible to look for 'missing' intensity at the predicted spot positions directly in the raw images. This process is called forward simulation and it follows the indexing step in the DCT analysis process as explained in LUDWIG *et al.* (2009b) and REISCHIG *et al.* (2013). As explained above, the forward simulation allows finding additional diffraction spots that can be included into the diffraction stack used in the grain reconstruction. Moreover, it enables to verify the validity of those that have been selected using search criteria on spot position, intensity, spot bounding box dimensions. Thus, the diffraction spots are sorted in six categories (flags), to better handle their selection for the reconstruction algorithm:

1. No intensity found in raw images
2. Intensity found in raw images but no segmented spot at this position
3. Segmented intensity not matching search criteria
4. Diffraction spot matching search criteria
5. Diffraction spot that has been indexed as a Friedel pair during the indexing step
6. Spot claimed by another grain (conflict)

By default, the selected reflections are from categories 4 and 5, which correspond to the reflections matching the search criteria and those indexed as Friedel pairs. With this in mind, a GUI allowing the visualisation and the selection of the reflections assigned to a grain after the forward simulation has been built and it is shown in figure 5.3, as an example for a Ti-4Al sample.

The figure is divided into three parts: left panel (red), central panel (blue) and right panel (green). For clarity each component of the GUI is numbered.
In the red panel, there are (1) the brightness-contrast slider, (2) the **Candidate Search** panel where the spot information is displayed when clicking on a point on the image and (3) the **Tolerances** panel with the tolerances used for the intensity search in the raw images and for the search of segmented spots when clicking on the image. **U** and **V** are the coordinates on the detector and **om** is the sample rotation angle (ω), which corresponds to the image number **W**:

$$\mathbf{W} = \omega/\omega_{\text{step}} \tag{5.3}$$

where ω_{step} is the step size of the sample rotation around the z-axis in degrees (typically in the range 0.05–0.1°).
In the green panel there are (4) the *full* image that displays all the spots assigned to the grain and all the forward simulated spots together, without taking into account the

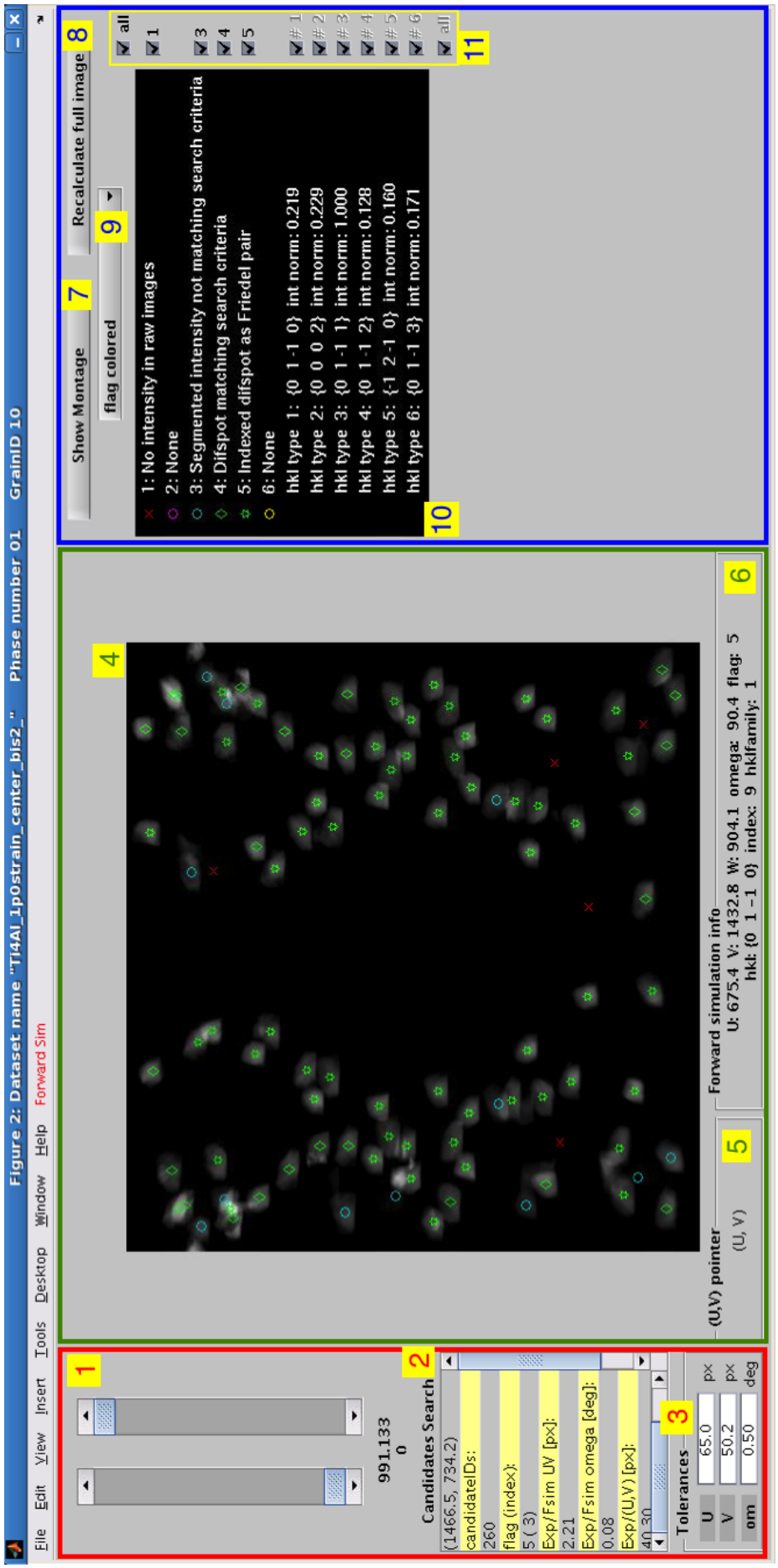

Figure 5.3: Forward simulation GUI for grain 10 (phase 1) from a Ti-4Al sample using a colour map according to the diffraction spot flag.

image number; (5) the **(U,V) pointer** panel displays the coordinates of the pointer on the image and (6) the **Forward simulation info** panel the information on the forward simulated spot if clicked.
In the blue panel, there are: (7) the **Show Montage** button for building a montage of the diffraction spots (a grid where to visualise the images of the selected spots, sorted by omega angle, i.e. the sample rotation angle) and (8) the **Recalculate full Image** button for calculating the *full* image using only the selected categories on the right (11). On the right side (blue panel) there is also a pop up menu (9) where to select the used colour map for the simulated spots that can be coloured according to the flags (i.e. the categories, figure 5.3), the omega angle (figure 5.4) or the *hkl* family (figure 5.5). All the six categories (flags) and the available *hkl* families are listed in the legend (10), with the corresponding check box to select/deselect each of them (11).
When right-clicking on a forward simulated spot, a context menu appears with options for performing the intensity search in the raw images and displaying the new segmented spot in a separate window.
The reference function of the DCT code for the visualisation of the forward simulation results is:

- *zUtil_ForwardSim/gtShowFsim.m*.

5.6 Building a GUI for twinning analysis

Since the main goal of this thesis is the characterisation of deformation twinning in polycrystalline materials, the necessity of having tools for the identification and visualisation of twins has become primary. As already described in section 5.2, a tool for the automatic identification of twins has been created, and the selection of only one twin type is now possible. Once the twins are identified, they are visualised in the sample volume and they are handled as grains. An existing GUI for the visualisation of the reconstructed volume has been improved and extended to perform the twinning analysis. The elements that were added to the existing GUI (see the function *GtGrainsManager.m* of the DCT code) are highlighted using coloured rectangles, as shown in figure 5.6. The left panel contains three main regions: customising the colour map (red), switching from the built-in colour maps (yellow) and performing a texture analysis (green).
The reference function of the DCT code for the twinning analysis is:

- *zUtil_Twins/GtTwinAnalysis.m*.

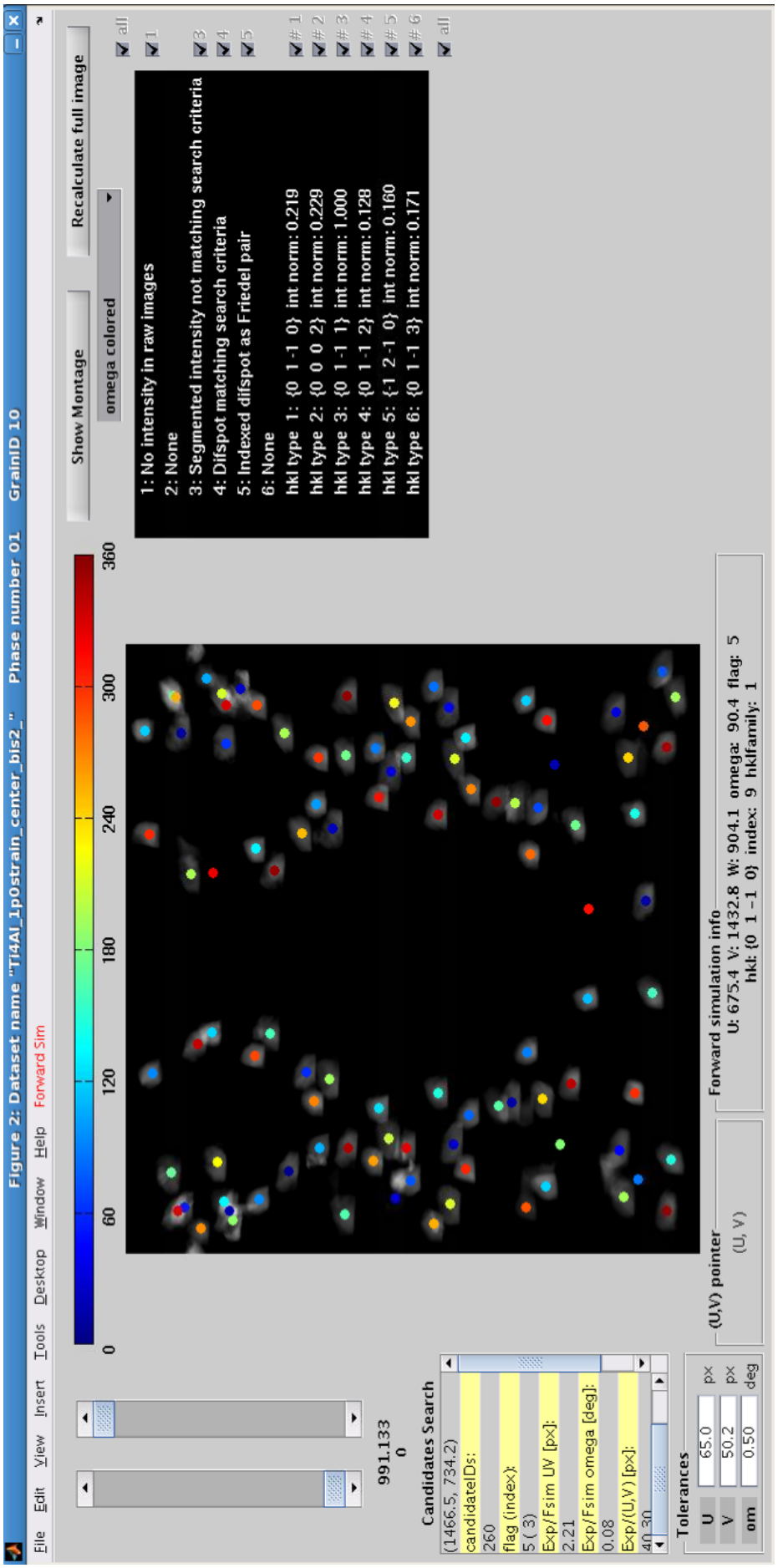

Figure 5.4: Forward simulation GUI for grain 10 (phase 1) from a Ti-4Al sample using a colour map according to the omega angle (ω, see figure 4.1).

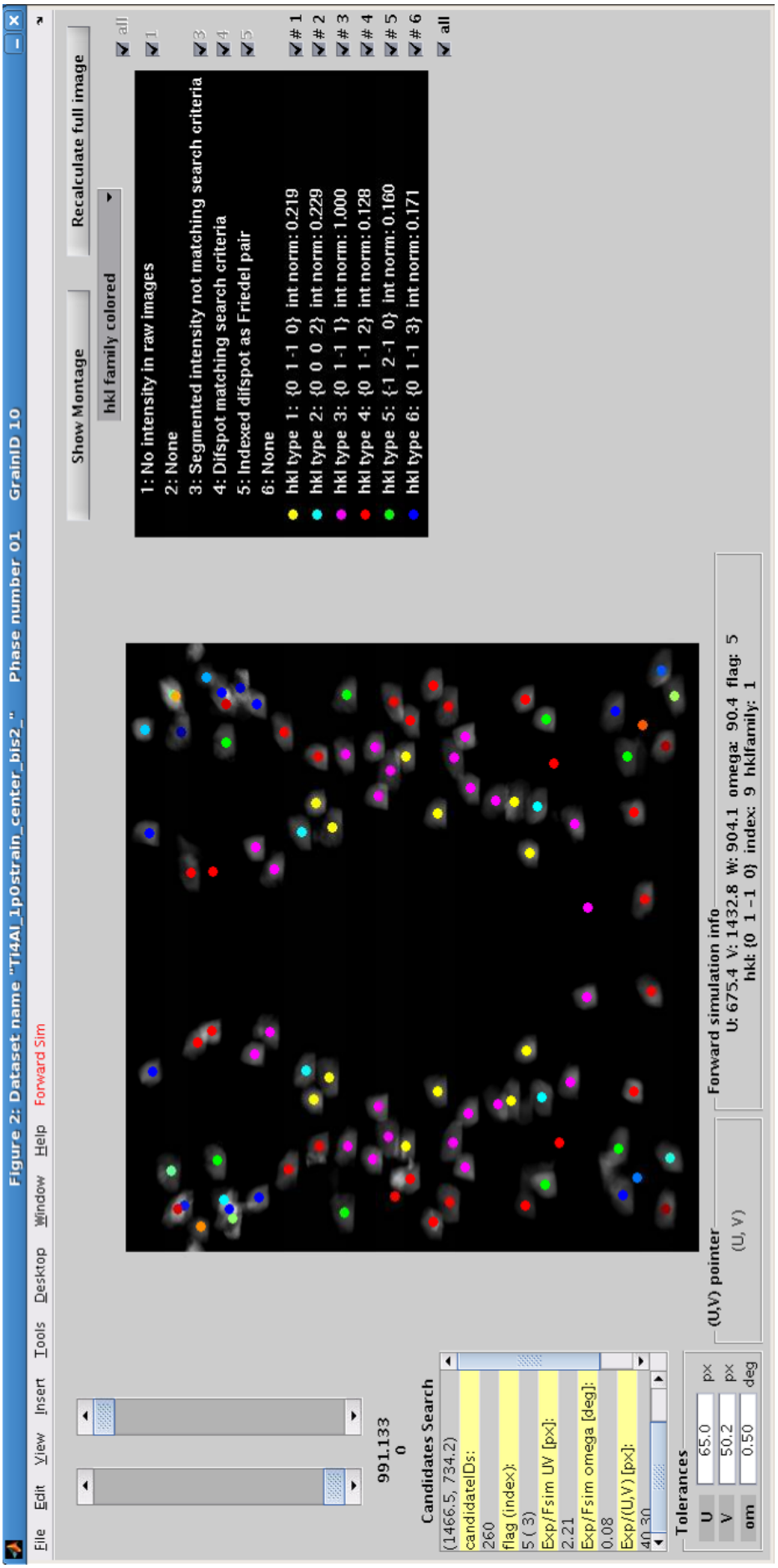

Figure 5.5: Forward simulation GUI for grain 10 (phase 1) from a Ti-4Al sample using a colour map according to the *hkl* families.

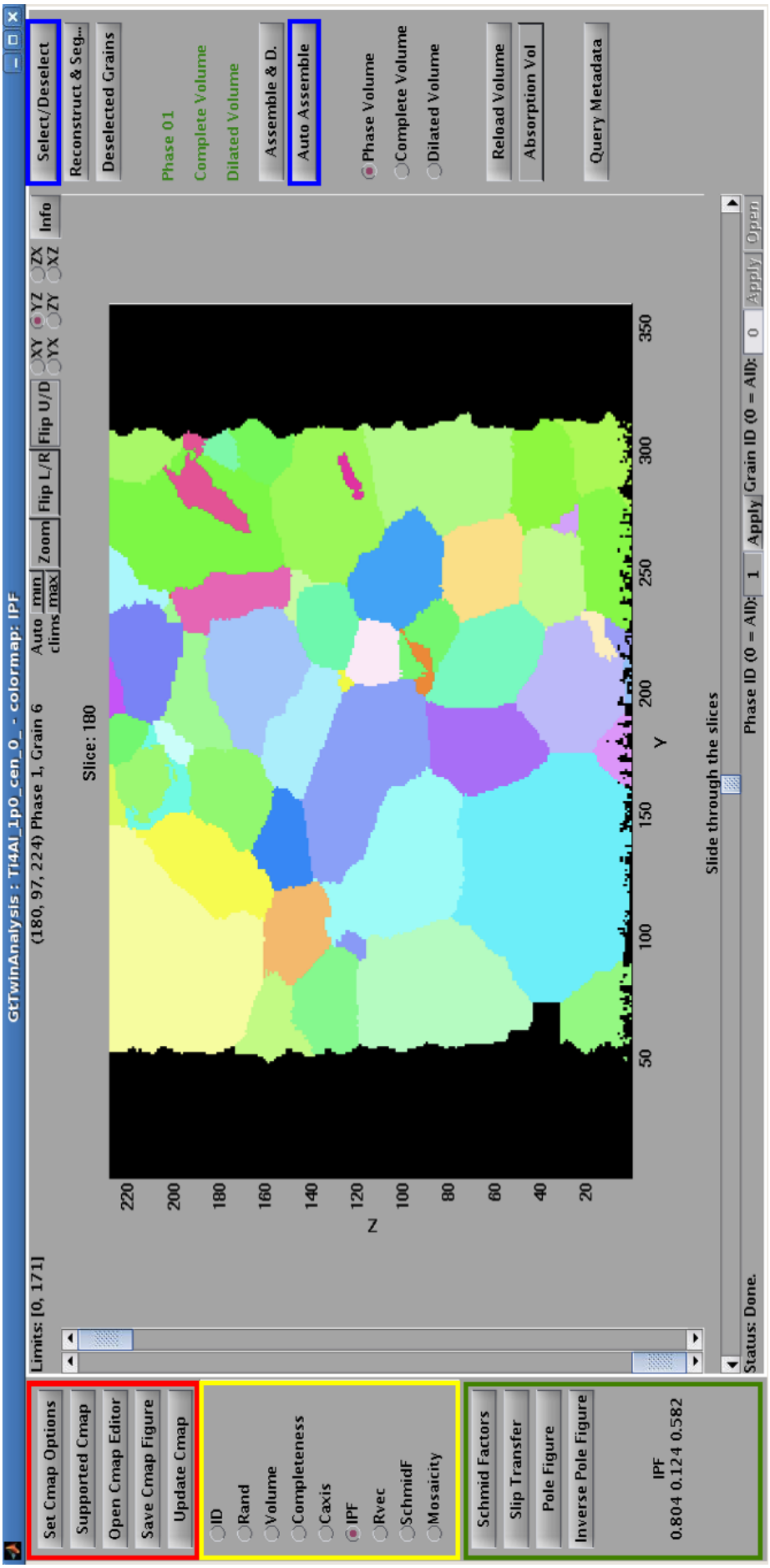

Figure 5.6: Twinning analysis GUI: the highlighted parts were added to the existing GUI.

5.6.1 The red panel: customising the colour map

The components of the red panel of figure 5.6 are:

- **Set Cmap Options** to set general options for the colour map (i.e. background and conflict colours, figure 5.7)
- **Supported Cmaps** to choose graphically one of the supported colour maps given in both grey and RGB colour spaces (figure 5.8)
- **Open Cmap Figure** to open a new figure where to visualise the current volume slice, the colour bar (or colour map key) with the support of useful control buttons to adjust the colours (figures 5.9(a) and 5.9(b))
- **Save Cmap Figure** to save the current figure using an automatic file name
- **Update Cmap** to update/change the options of the current colour map (figures 5.11–5.13)

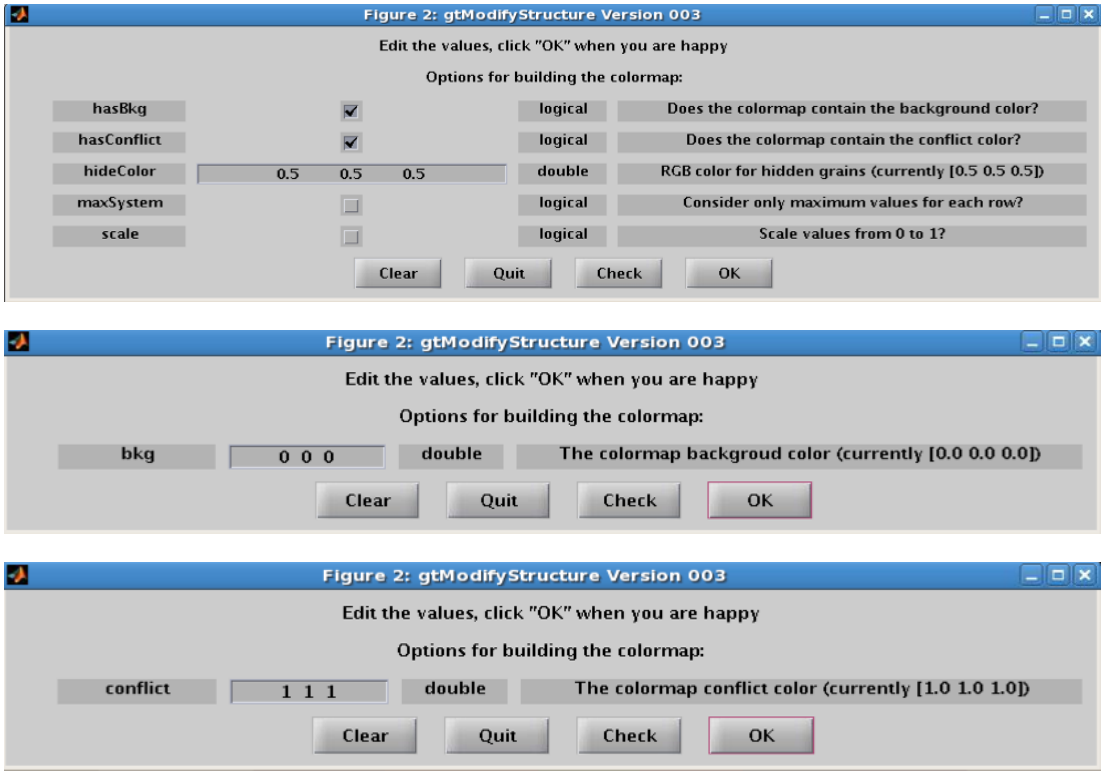

Figure 5.7: General settings for the colour map

5.6.2 The yellow panel: choosing one of the built-in colour maps

The yellow panel of figure 5.6 contains a check box list to switch between the built-in colour maps. The different colour maps are divided into two categories:

(A) Each colour is defined by a scalar value (R, G and B colour components are proportional to this scalar value).

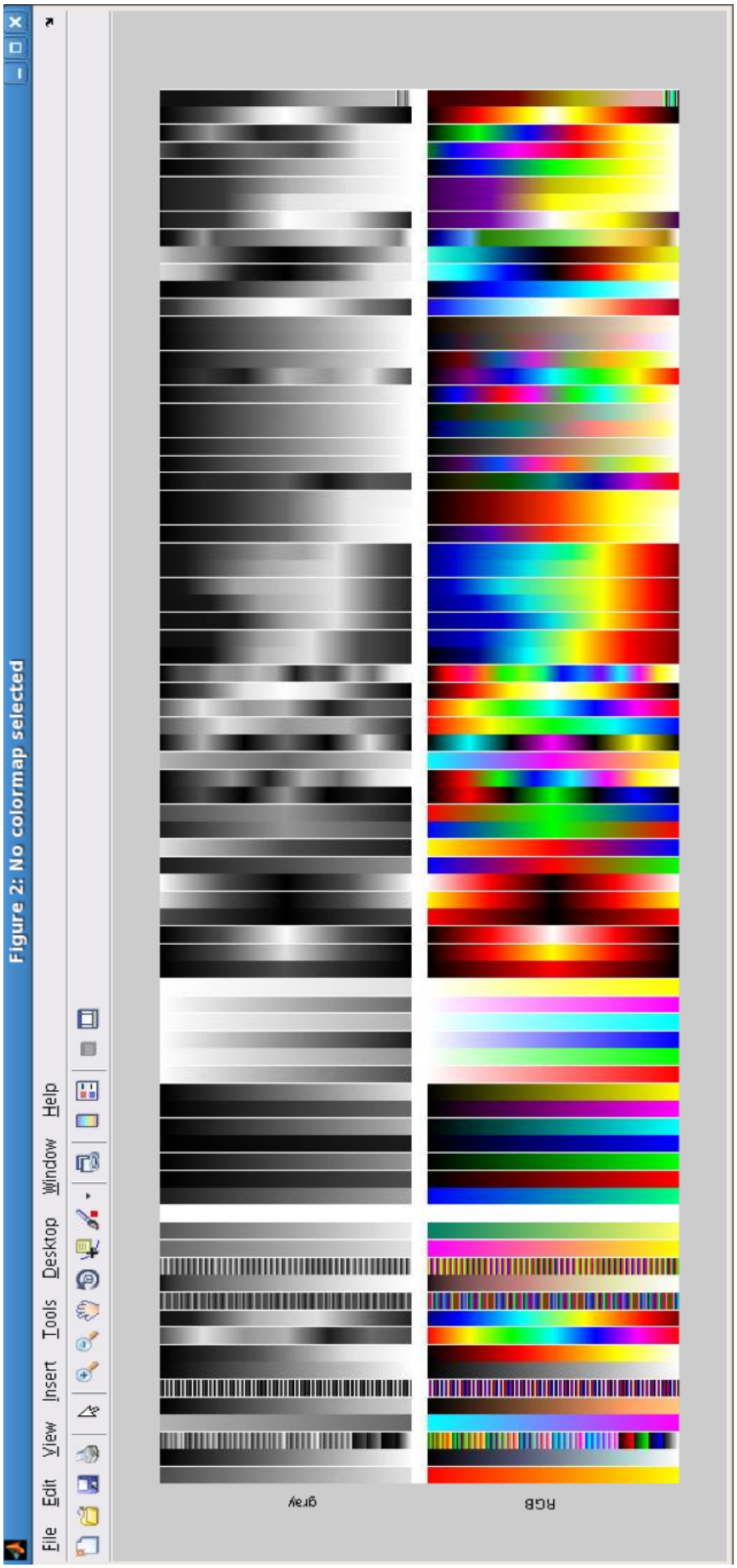

Figure 5.8: GUI to choose one of the supported colour maps for the "indexed" colour maps, i.e. ID, Volume, Completeness, Schmid factor (SchmidF) and Mosaicity.

Figure 5.9: (a) Control buttons for an "indexed" colour map, i.e. ID, Volume, Completeness, Schmid factor (SchmidF) and Mosaicity; (b) Control buttons for a "vectorised" colour map, i.e. IPF, Caxis and Rvec.

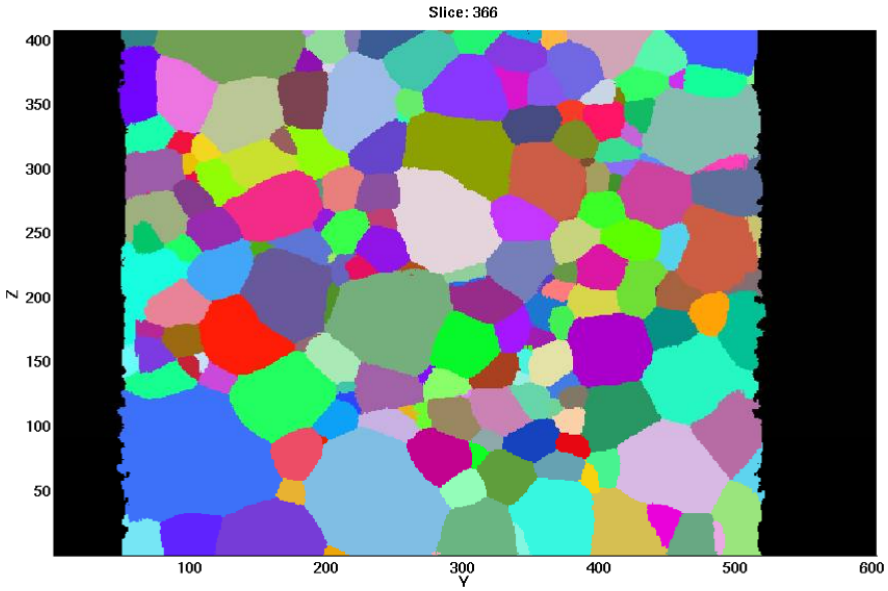

Figure 5.10: Random colour map

- ID, unique identification number (figure 5.14)
- VOLUME, grain volume (figure 5.15)
- COMPLETENESS, fraction of the assigned reflections over the simulated reflections (figure 5.16)

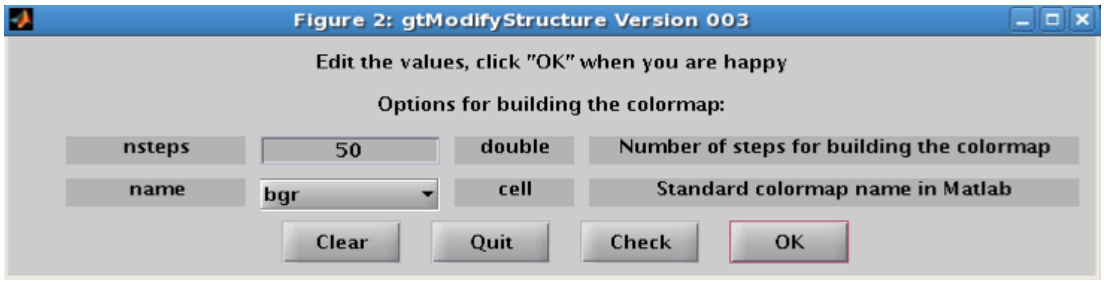

(a)

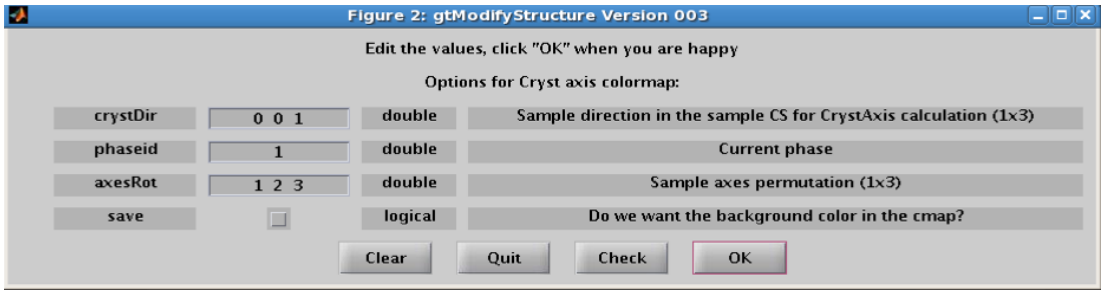

(b)

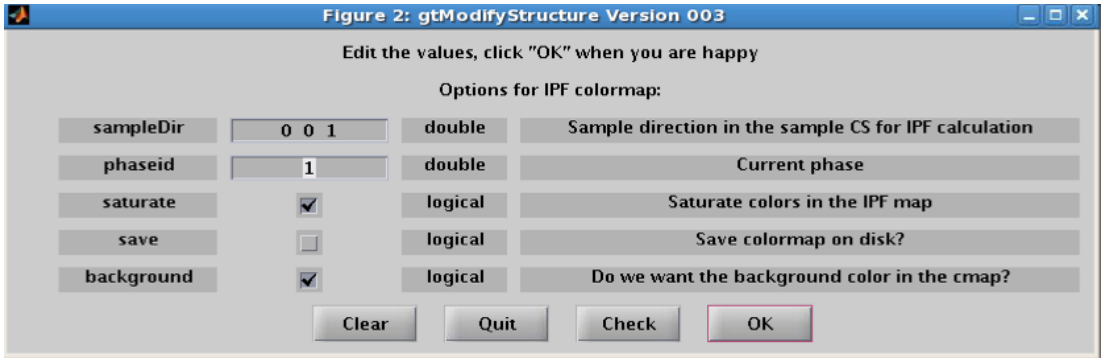

(c)

Figure 5.11: (a) General options for updating either the ID, Volume, Completeness, Schmid factor (SchmidF) and Mosaicity colour maps; (b) Specific options for updating the Crystallographic axis colour map (Caxis) and (c) Specific options for updating the IPF colour map.

- SCHMIDF, Schmid factors given a loading direction and a slip plane/direction (figure 5.20)
- MOSAICITY, omega spread (i.e. sample rotation angle) of the diffraction spots assigned to a grain (figure 5.21)

(B) Each colour is defined by a vector (R, G and B colour components are proportional respectively to the X,Y and Z vector components).

- RAND*, random (figure 5.10)
- CAXIS**, direction of a crystallographic axis in the sample reference system (figure 5.17)

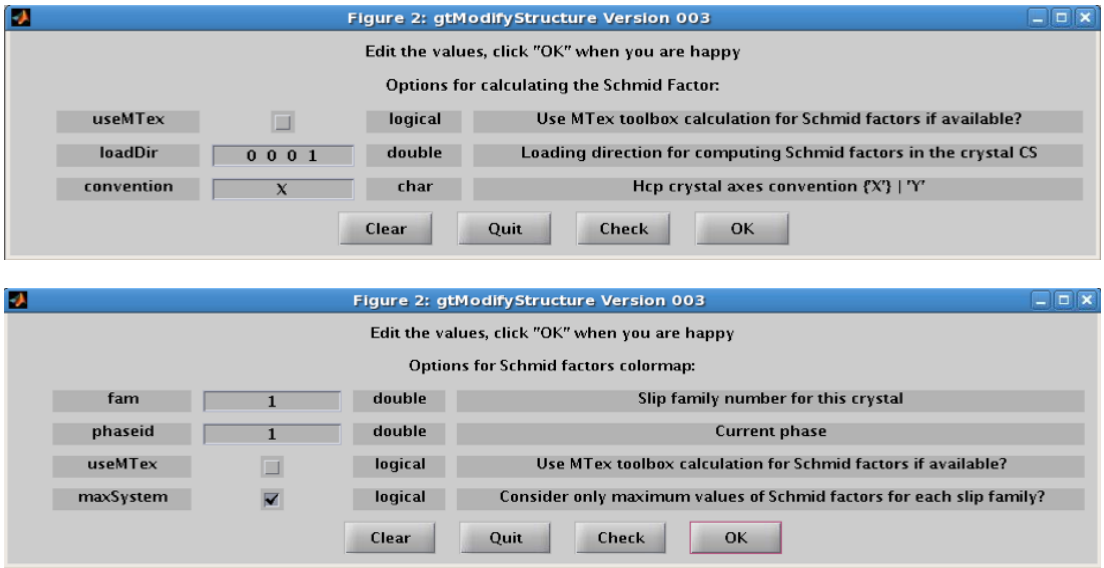

Figure 5.12: Specific options for updating the Schmid factor colour map

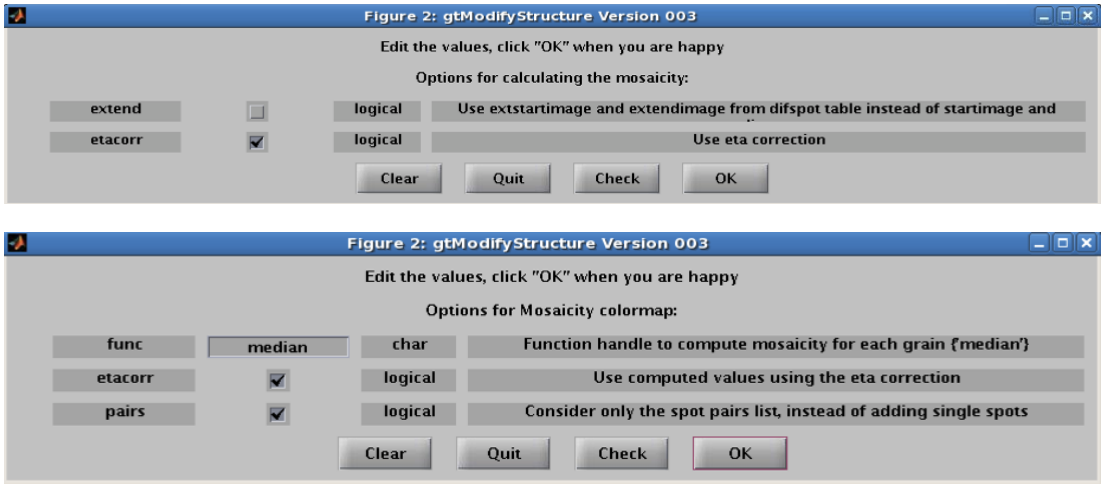

Figure 5.13: Specific options for updating the Mosaicity colour map

- IPF**, direction of a sample axis in the crystal reference system (figure 5.18)
- RVEC**, Rodrigues vector (figure 5.19)

The random colour map (*) does not have any colour map key. Colour maps marked with (**) have a specific colour map key. The others have a standard colour bar as colour map key, chosen among the supported colour maps of figure 5.8. An example for each colour map is given in figures 5.14–5.21 using the CP Ti sample analysed in chapter 6 with 1755 grains.

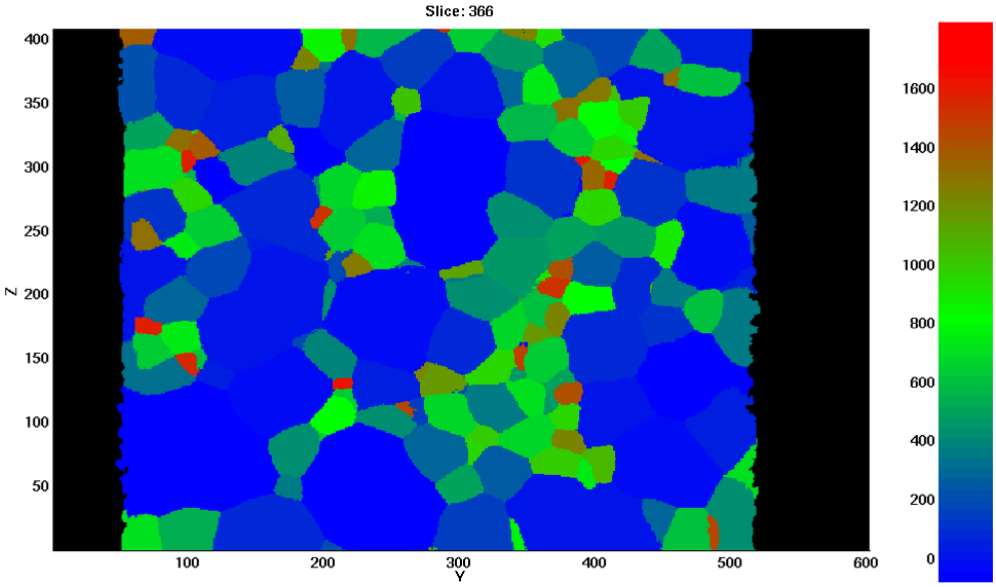

Figure 5.14: ID colour map

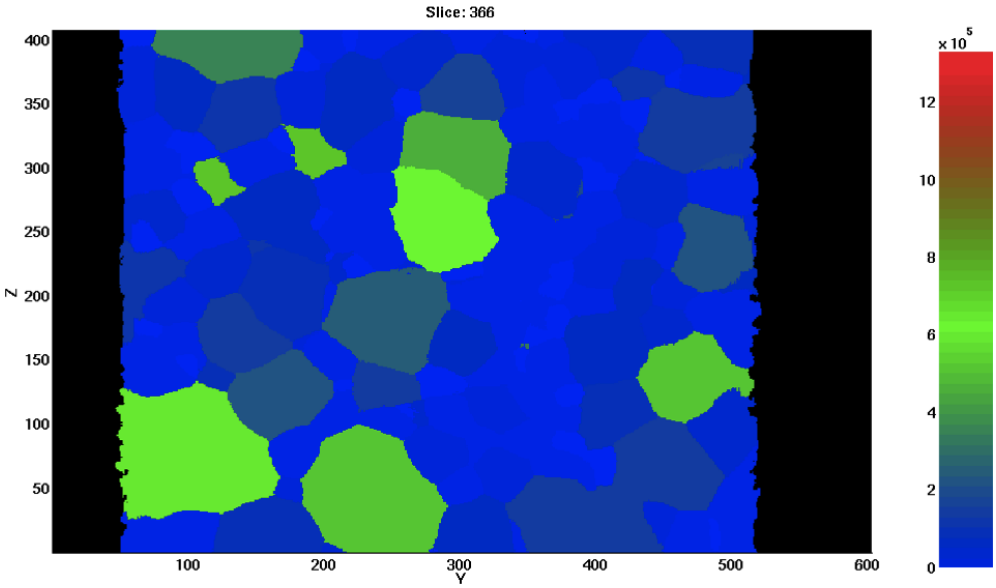

Figure 5.15: Volume colour map

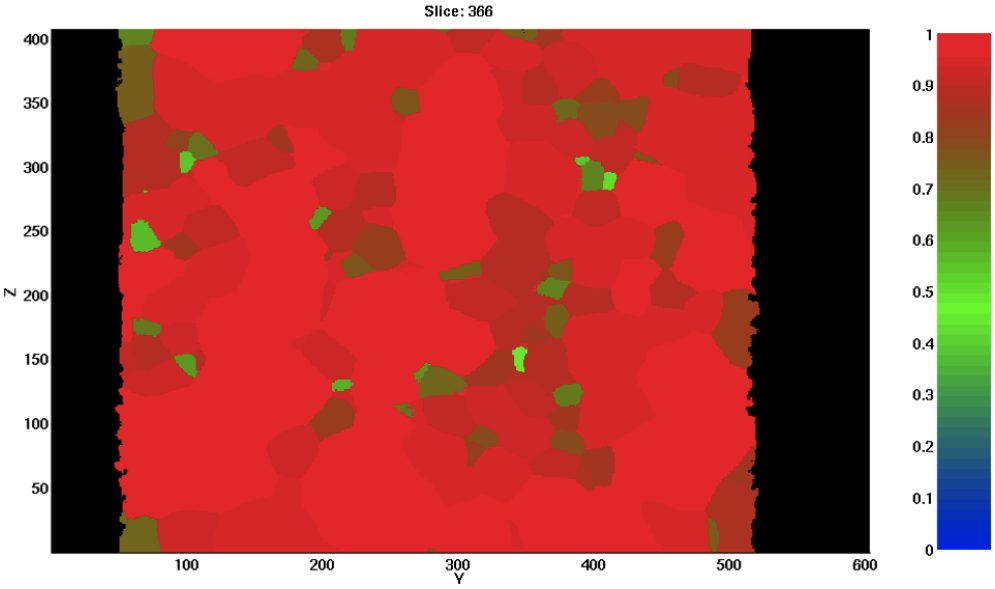

Figure 5.16: Completeness colour map

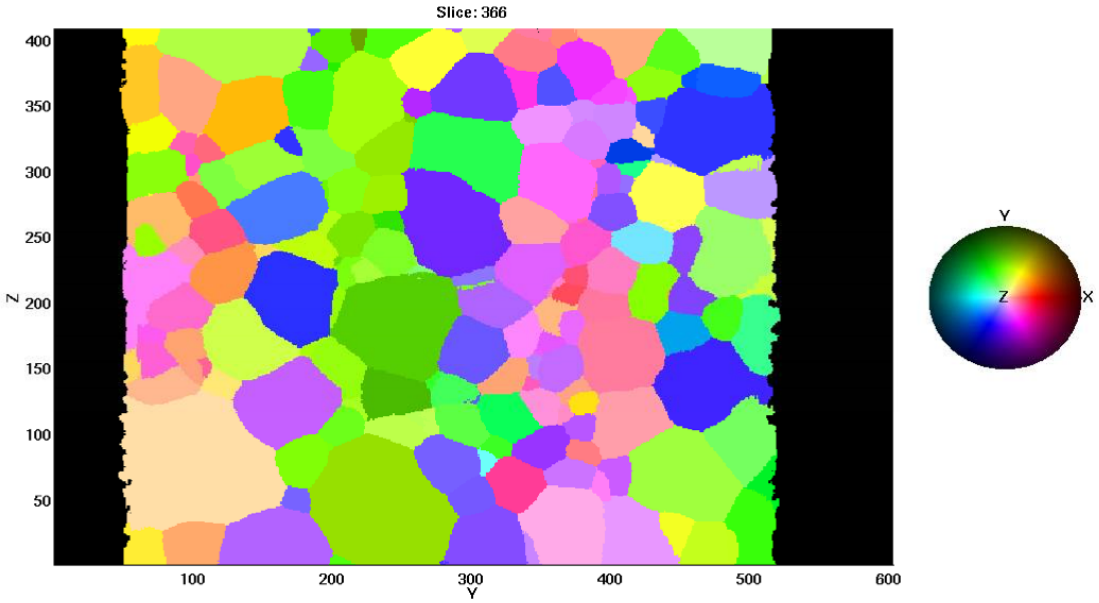

Figure 5.17: Crystallographic axis colour map for the $\langle 0001 \rangle$ direction.

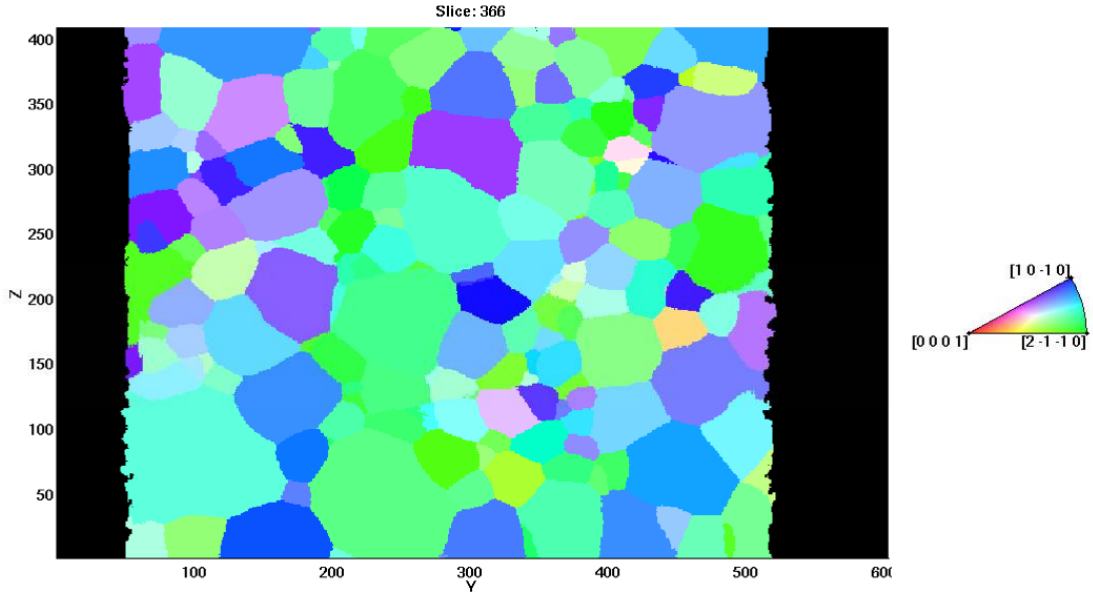

Figure 5.18: IPF colour map along the sample z-axis

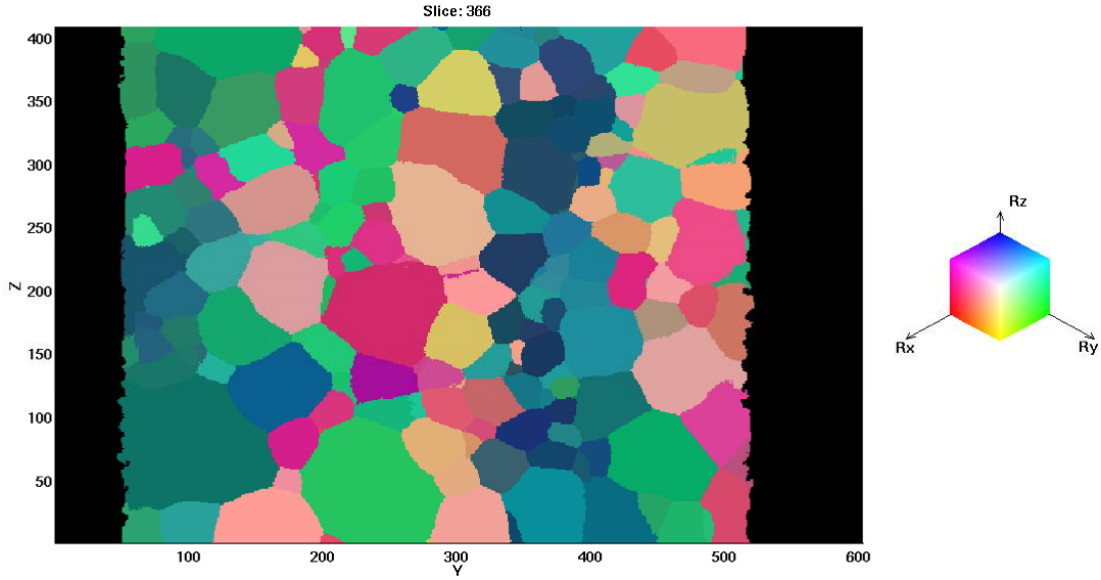

Figure 5.19: Rodrigues vector colour map

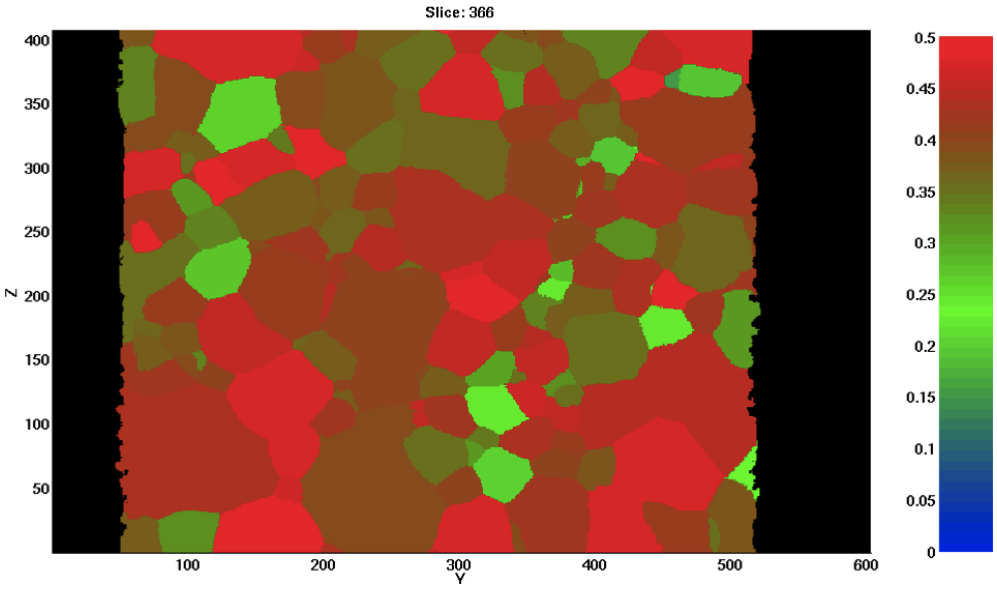

Figure 5.20: Schmid factor colour map for tensile twin: the loading direction is the sample z-axis, the twin plane is $\{10\bar{1}2\}$ and the twin direction is $\langle 11\bar{2}0\rangle$.

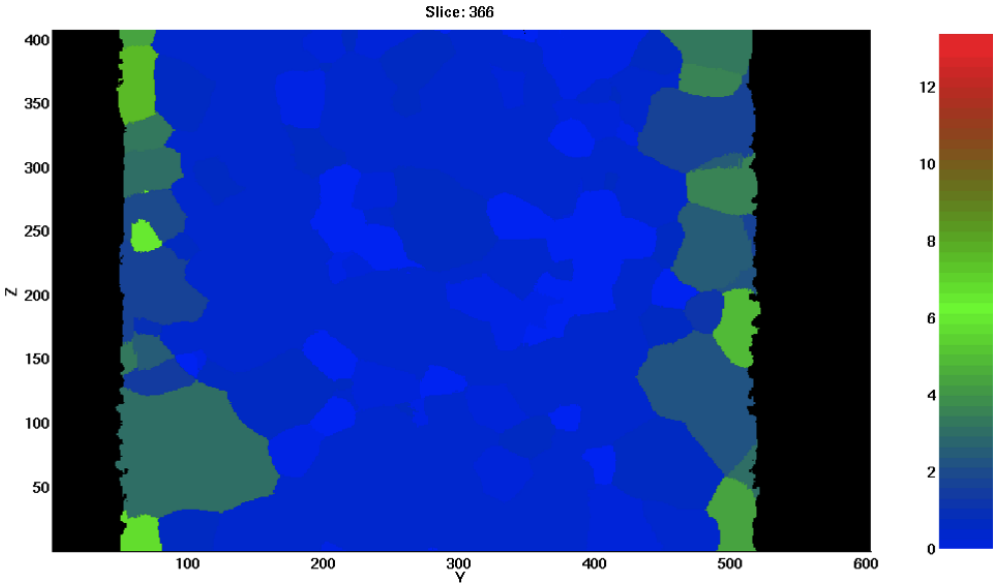

Figure 5.21: Mosaicity colour map

5.6.3 The green panel: texture analysis

The green panel of figure 5.6 contains buttons for the texture analysis:

- **Schmid Factors** to calculate the Schmid factor (*m*) (figure 5.22)
- **Slip Transfer** to calculate the slip transfer parameter (*m'*) between a list of grains and their neighbourhood (figure 5.23)

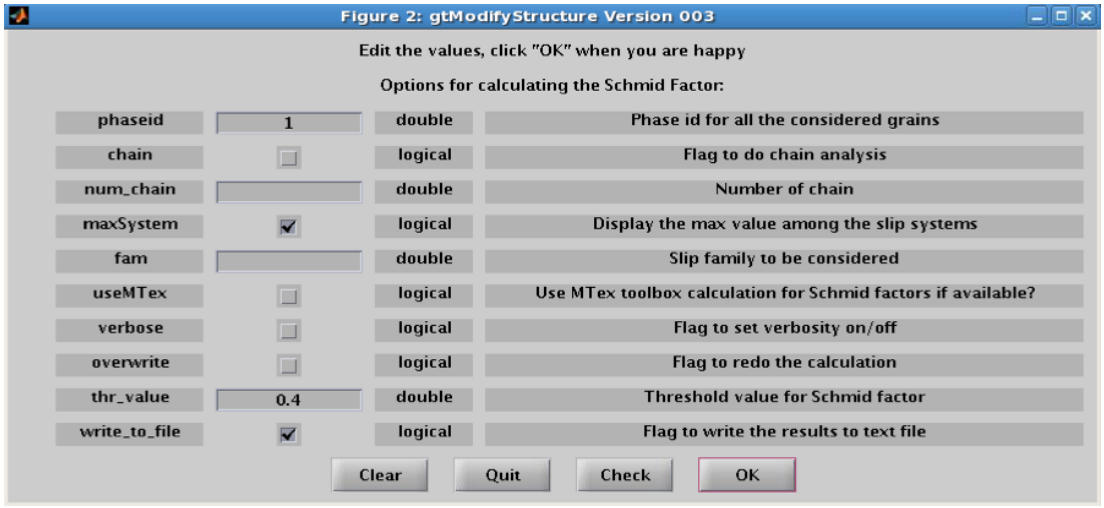

Figure 5.22: Options for the calculation of the Schmid factor *m*

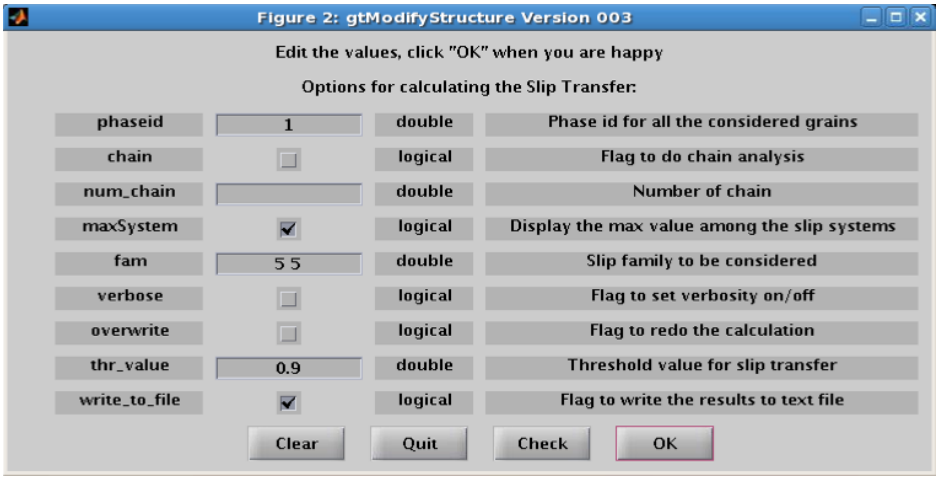

Figure 5.23: Options for the calculation of the slip transfer parameter *m'*

- **Pole Figure** to calculate the pole figure (figures 5.25 and 5.26(a))
- **Inverse Pole Figure** to calculate the inverse pole figure (figures 5.24 and 5.26(b))
- A text area where the current colour map value is visualised when moving the mouse on a grain in the sample volume.

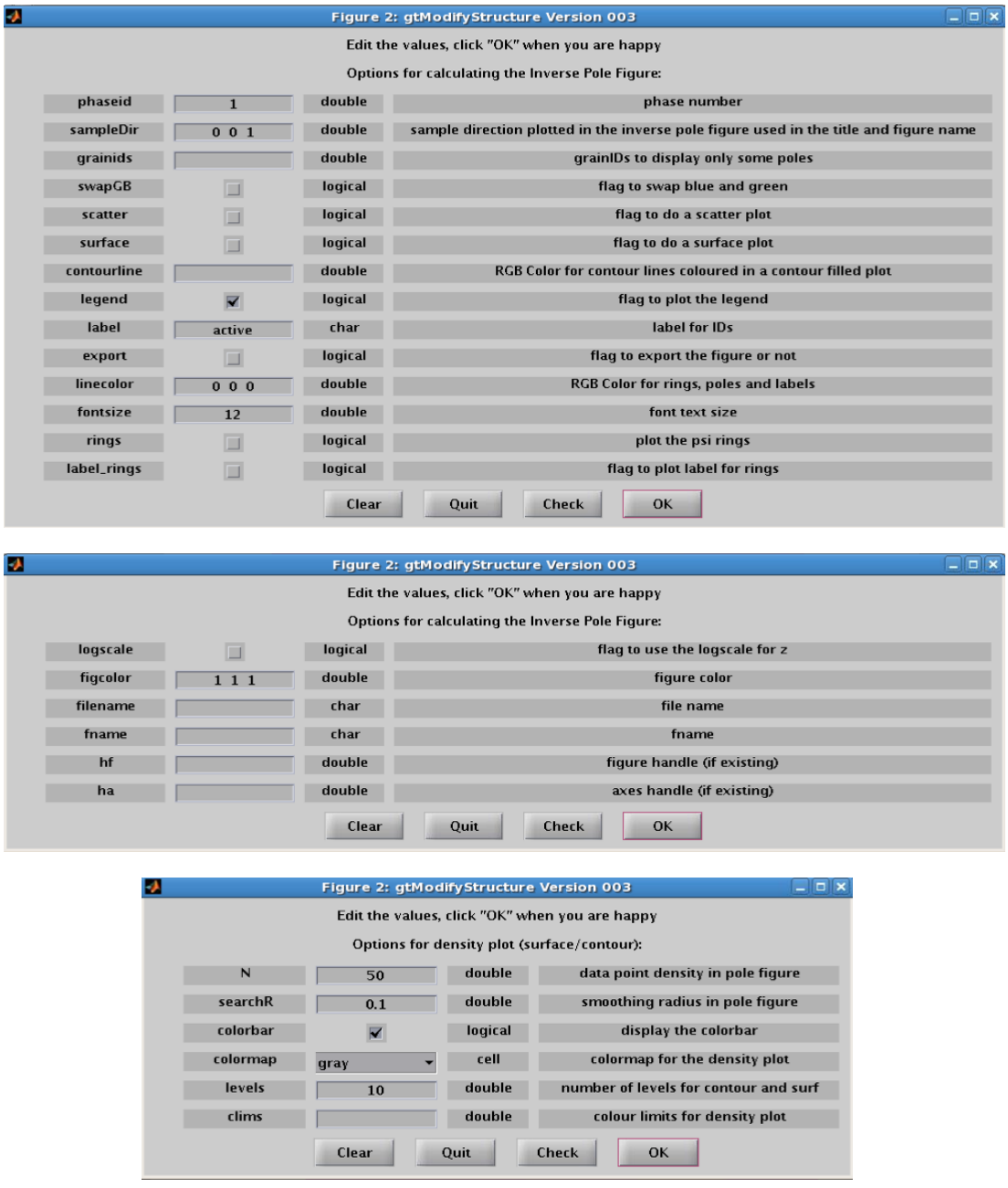

Figure 5.24: Options for the calculation of the inverse pole figure (IPF).

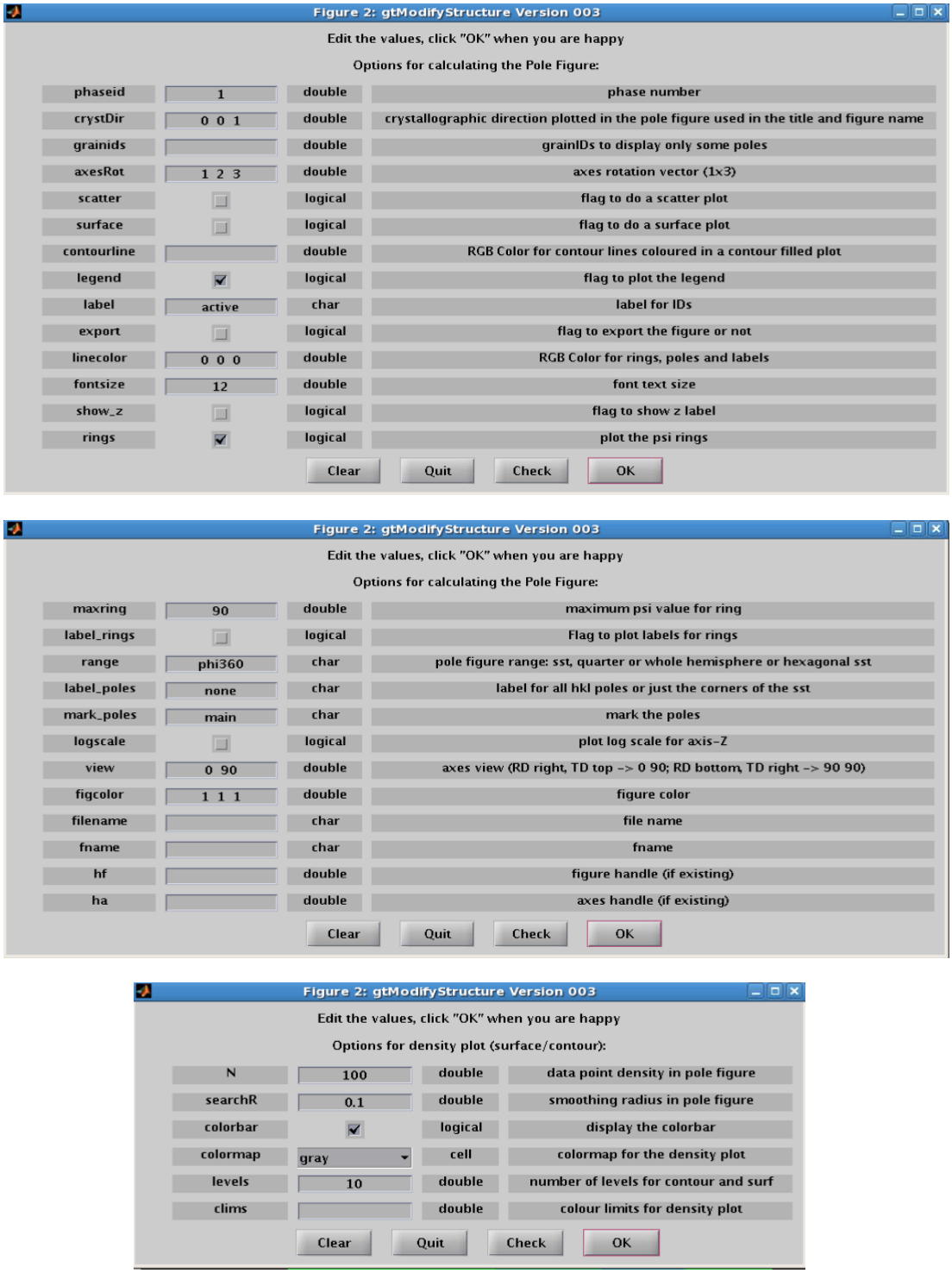

Figure 5.25: Options for the calculation of the pole figure (PF).

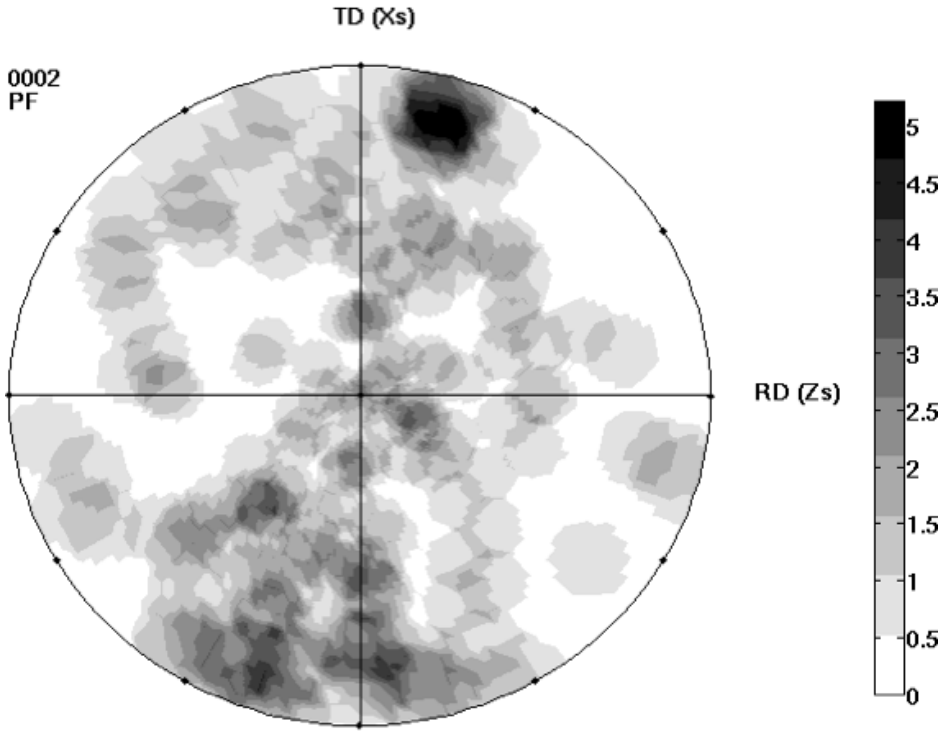

(a)

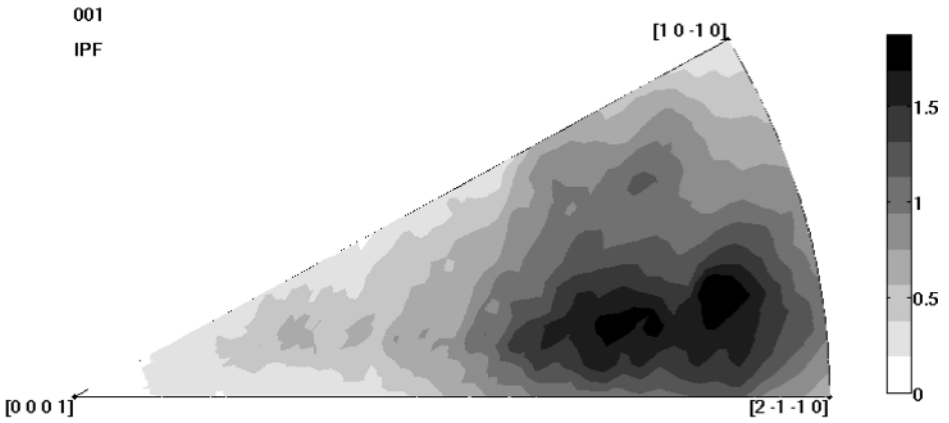

(b)

Figure 5.26: (a) {0002} pole figure and (b) {001} inverse pole figure for a Ti-4Al sample loaded along the rolling direction (RD).

5.6.4 The blue buttons: grains selection and volume assembling

The right panel of figure 5.6 contains two new functionalities:

1. **Select/Deselect** to select/deselect grains in the volume (figure 5.27) and visualise the selected grains in the GUI (figure 5.28)
2. **Auto Assemble** to automatically assemble the volume and reload the colour map, without going through the steps of assembling and dilating the volume.

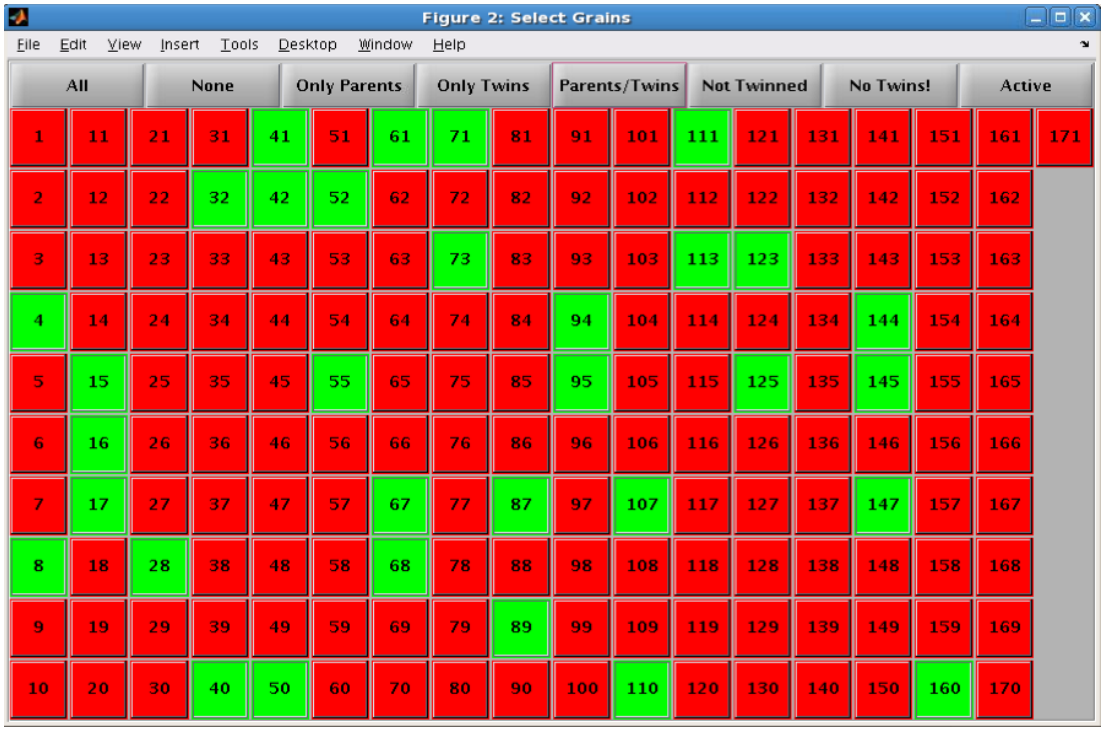

Figure 5.27: GUI for selecting/deselecting grains in the volume: pre-defined lists are available using the buttons on the top. In this example twinned grains and twins are selected.

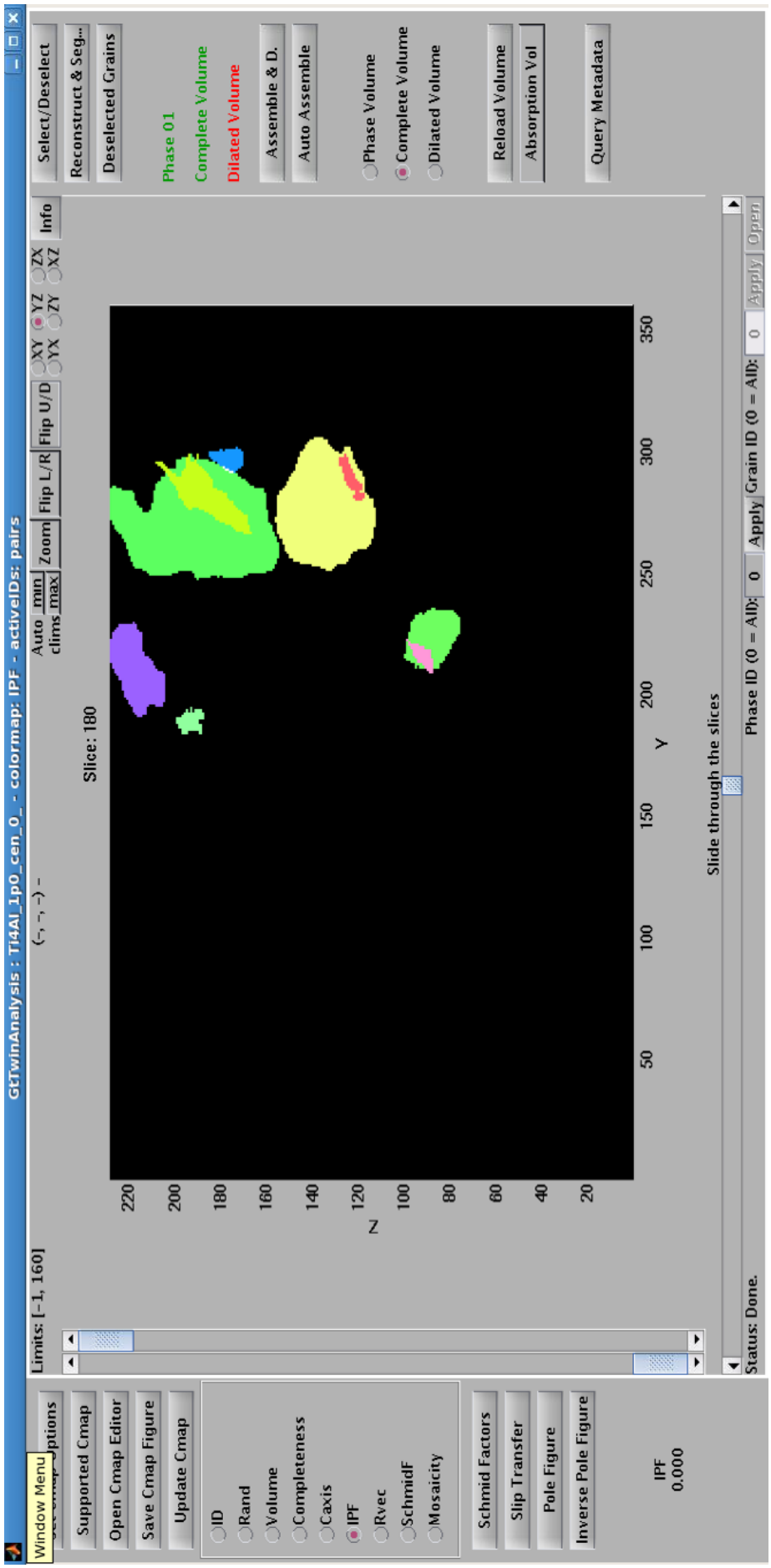

Figure 5.28: Sample volume slice shown in figure 5.6 after having selected only the twinned grains and twins of figure 5.27.

Chapter 6

Results I: Comparison between a near-field and a far-field indexing approach for characterisation of a polycrystalline sample volume containing more than 1500 grains

Abstract

A comparison of the performance of X-ray diffraction tomography, a near-field diffraction technique, and a far-field diffraction technique for indexing X-ray diffraction data of polycrystalline materials has been carried out by acquiring two sets of diffraction data from the same polycrystalline sample volume. Both approaches used in this study are variants of the three-dimensional X-ray diffraction (3DXRD) methodology, but they rely on different data collection and analysis strategies. Previous attempts for assessing the quality of 3DXRD indexing results from polycrystalline materials have been restricted to comparisons with two-dimensional electron backscatter diffraction cross sections containing a limited number of grains. In the current work, the relative performance of two frequently used polycrystalline-material indexing algorithms is assessed, comparing the indexing results obtained from a three-dimensional sample volume containing more than 1500 grains. The currently achievable accuracy of three-dimensional grain maps produced with these algorithms has been assessed using a statistical analysis of the measurement of the size, position and orientation of the grains in the sample. The material used for this comparison was a polycrystalline commercially pure titanium (CP Ti) grade 2 sample, which has a hexagonal close packed crystal structure. The

comparison of the two techniques shows good agreement for the measurements of the grain position, size and orientation. Cross-validation between the indexing results shows that about 99% of the sample volume has been indexed correctly by either of these indexing approaches. The remaining discrepancies have been analysed and the strengths and limitations of both approaches are discussed.

6.1 Introduction

Over the past ten years considerable effort has been put into the development of novel three-dimensional diffraction techniques for mapping grain structures in polycrystalline materials. There are two main sets of techniques that aim at a real space description of polycrystalline materials, in terms of three-dimensional shapes and orientations of all grains present in the illuminated sample volume.

The first type of techniques is point scanning techniques like diffraction tomography (BLEUET *et al.*, 2009; STOCK, 2008) or the polychromatic Laue micro-diffraction technique and its extension into 3D via differential aperture X-ray microscopy (DAXM) (LARSON *et al.*, 2002), where three-dimensional information is obtained by scanning the sample and an analyser wire, relative to a point focused beam. 3D grain maps produced by this first type of 3D scanning techniques offer access to local orientation, phase and strain information, but are typically restricted to small sample volumes because of limitations in scan speed.

The second set of techniques are variants of the monochromatic beam, rotating crystal method, typified by 3D X-ray diffraction (3DXRD) microscopy (ODDERSHEDE *et al.*, 2010, 2012; POULSEN, 2012; SØRENSEN *et al.*, 2012) or high energy diffraction microscopy (HEDM) (LI *et al.*, 2012). 3DXRD produces 3D maps of the grains, visualising their position, orientation and elastic strain at the same time, using an extended beam of monochromatic radiation. 3DXRD experiments can be further sub-divided into near-field approaches and far-field approaches or combinations of both. Near-field diffraction imaging techniques aim at resolving 3D grain shapes (LI and SUTER, 2013; LUDWIG *et al.*, 2009a; REISCHIG *et al.*, 2013; SCHMIDT, 2010; SUTER *et al.*, 2006) and employ high resolution X-ray imaging detectors with pixels smaller than the grain size. Far-field approaches, on the other hand, employ a low resolution detector with pixels comparable or bigger than the grain size, in which case the morphology of grains is neglected.

The term 3DXRD has in the past been used for both, near-field and far-field diffraction experiments and sometimes both detector configurations are used

simultaneously. We will use the term "conventional 3DXRD" as referring to the more frequently used far-field 3DXRD acquisition geometry.

One of the main difference between the near-field and far-field acquisition geometries is that in the near-field configuration spatial and angular information are mixed and scattering vectors cannot directly be derived from the measurement of the position of a diffraction spot on the detector. Near-field indexing approaches are therefore typically based on one of the following principles, resolving the ambiguity arising from the unknown grain centre of mass position: (i) voxel-wise forward modelling (SUTER *et al.*, 2006), (ii) ray tracing over several detector positions (LAURIDSEN *et al.*, 2001) or (iii) identification of Friedel pairs (LUDWIG *et al.*, 2009b).

Indexing from far-field diffraction data can be based on the same three principles, but in many practical cases approximate grain orientations can be identified using scattering vectors, directly derived from diffraction spot positions (neglecting the precession of the grain around the rotation axis). Both, grain position and orientation are then refined in a subsequent processing step.

Given the complexity of diffraction patterns arising from sample volumes containing 1000 grains and more, the precision or validity of indexing results obtained by any of the above-mentioned approaches is not trivial to evaluate from a single experiment.

The aim of the current study is to compare and cross-validate indexing results obtained from two variants of 3DXRD, frequently used at beam line ID11 of the European Synchrotron Radiation Facility (ESRF): (i) X-ray diffraction contrast tomography (DCT) as an instance of a near-field method and (ii) conventional 3DXRD as a representative of the far-field diffraction method. The data were analysed respectively using the DCT code (`http://sourceforge.net/projects/dct/`) and ImageD11 software (`http://sourceforge.net/projects/fable/`).

In section 6.2 we describe the sample preparation (section 6.2.1) and experimental setup (section 6.2.2) and briefly recall the principle of the polycrystalline materials indexing algorithms used in this study. We then proceed with a quantitative analysis in section 6.2.3 and cross-validation of the indexing results obtained with both approaches (section 6.3). In section 6.4 we discuss strengths and limitations of both approaches and analyse in some more detail the discrepancies observed in the experimental results.

6.2 Experimental procedure

6.2.1 Sample preparation and mounting

The experiment has been performed on a cylindrical sample of commercially pure titanium with an average grain size of 40.5 μm as determined by electron backscatter diffraction (EBSD). The material was thermo-mechanically processed and re-crystallised at 650 °C for 3 hours in an Argon atmosphere in order to produce grains with a low intergranular orientation spread followed by 1 °C/min cooling. A sample with a diameter of 700 μm was cut by electro-discharge machining (EDM) with the cylinder axis parallel to the original rolling direction (RD). The cylindrical sample was placed into a small loading rig, with an external compressive load of 15 N along the sample and rotation axis, equivalent to 39 MPa of average normal stress across the cross section. As the yield strength of CP Ti grade 2 is about one order of magnitude higher than the applied stress (HOLT *et al.*, 1996; WELSCH *et al.*, 1993), the sample was only deformed elastically.
The compression device was designed to suit the space constraints of the near-field acquisition geometry, with typical sample-detector distance in the range 3-10 mm. It also allows irradiation of the entire gauge volume during a 360° rotation.

6.2.2 Experimental setup

The experiment was performed at the beam line ID11 of the ESRF (VAUGHAN *et al.*, 2010) using a monochromatic beam produced by a bent Si (111) Laue-Laue double-crystal monochromator (40 keV, relative energy bandwidth $\Delta\lambda/\lambda \approx 10^{-3}$). The experimental setup is represented schematically in figure 6.1. The coordinate system is defined such that the X-ray beam is along the laboratory X direction [100], the Z direction is vertical, upwards from the origin [001], and the Y direction [010] is consistent with a right-handed system. The rotation axis of the sample is right-handed and parallel with the Z-axis. The sample coordinate system rotates around the Z-axis and it coincides with the laboratory coordinate system when the rotation angle ω is equal to zero. A compression rig hosting the cylinder shaped sample was mounted on the rotation stage such that the sample and the loading axis were aligned with the rotation axis. The near-field and far-field acquisitions were carried out consecutively, without changing the sample mounting or the beam defining slit settings.

Two Fast Readout Low Noise (FReLoN) charge-coupled device (CCD) cameras (LABICHE *et al.*, 2007) were used for this experiment, positioned normal to the incident beam, downstream from the sample. Both the CCD cameras have an array of 2048×2048 pixels. The first is coupled via visible light microscope optics to a

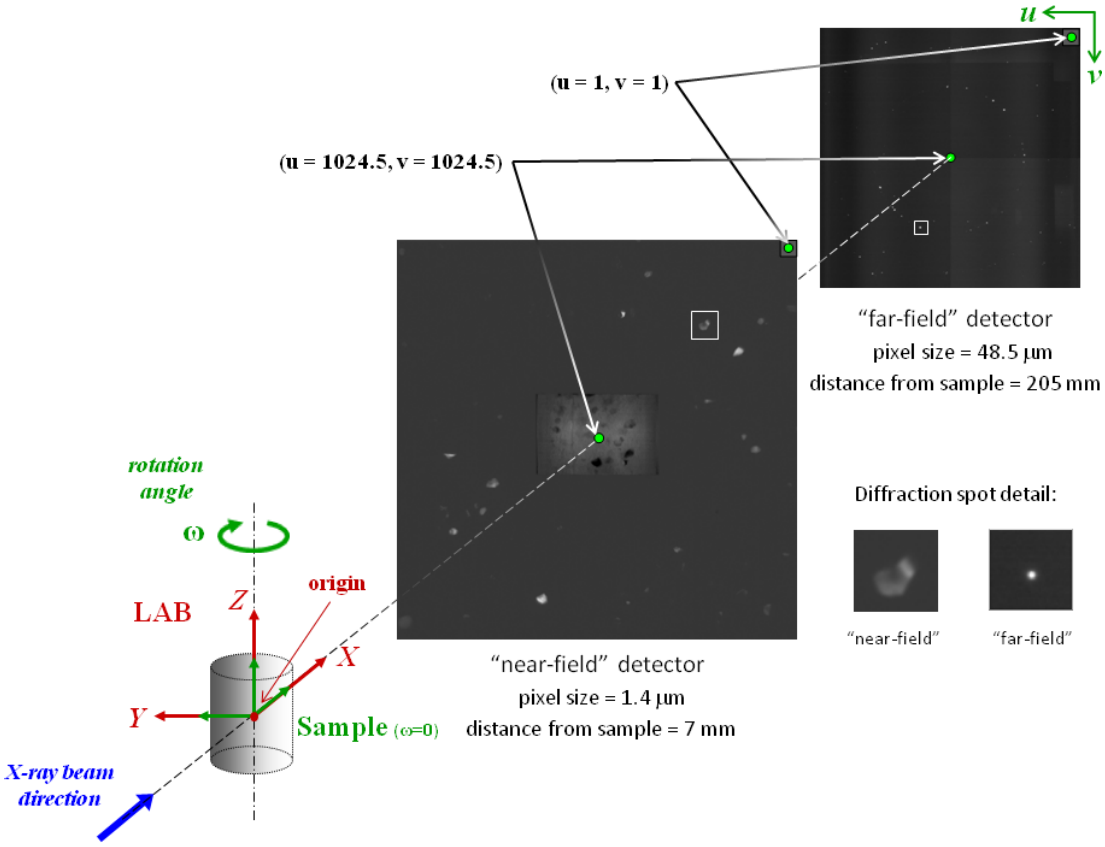

Figure 6.1: Experimental setup with high resolution near-field and low resolution far-field detectors and vertical rotation axis configuration at beam line ID11 of the ESRF, Grenoble, France.

transparent luminescent screen, giving an effective pixel size of 1.4 µm/pixel and a field of view of 2.87×2.87 mm^2. This detector, used for the near-field approach, was placed at a sample-detector distance of 7 mm and will be referred to as the near-field detector. 7200 images were recorded during a 360° rotation of the sample, with an exposure time of 1 second, giving scan duration of 2.5 hours.

The second CCD camera has a fiber-optic coupling (COAN *et al.*, 2006), which gives an effective pixel size of 48.5 µm/pixel and a field of view of 99.3 x 99.3 mm^2. It was placed 205 mm from the sample and was used for the acquisition of far-field diffraction data. 7200 images were recorded during a 360° rotation of the sample, with an exposure time of 0.1 second, giving scan duration of 27 minutes.

The far-field detector cannot spatially resolve grain shape due to its larger pixel size and working distance. However, this configuration has a reduced sensitivity to unwanted translational drifts of the setup leading to more accurate observations of diffraction angle. The large effective pixel size also means that it can use a thicker scintillator screen without degrading the resolution. Consequently, it has a higher sensitivity than the near-field detector – hence the counting times are one or two

orders of magnitude faster, and it is generally believed that smaller grains can be detected.

6.2.3 Data analysis

The data analysis of the near-field and far-field diffraction data has been carried out using two different software packages. In both cases the data processing involves some basic steps like determination (fitting) of the global experimental parameters (in particular detector position and tilts), correction of spatial distortions of the detector system and background correction, which are followed by segmentation of connected pixel neighbourhoods (peak search) of the recorded diffraction spots.
Generally speaking, the task of indexing polycrystalline materials diffraction data corresponds to assigning scattering vectors to grains of origin. In the case of far-field diffraction data the scattering vectors can to first approximation be derived from diffraction spot positions, whereas in the case of near-field data an intermediate processing step is required, due to the coupling of spatial and angular information in diffraction spot centre-of-mass positions. In the case of the near-field data, which were analysed using the DCT code (http://sourceforge.net/projects/dct/), the latter problem is solved exploiting the symmetry of Friedel pairs (see section 6.4.1 for more details on this aspect).

An automated matching procedure working on diffraction spot metadata (i.e. spot position, aspect ratio, size and intensity) identifies Friedel pairs of diffraction spots observed at 180° offset in sample rotation. Each Friedel pair defines a (diffracted) beam trajectory through the sample volume from which the direction of the scattering vector can be derived. The actual indexing routine carries out a systematic search among these spot pairs and tries to identify mutually consistent groups of pairs, using a combination of real space (proximity of beam trajectories in real space) and crystallographic constraints (valid inter-planar angles). Grains with at least 5 assigned pairs (out of 40 expected) were accepted in the current study. For materials with negligible intergranular orientation spread, the diffraction spots assigned to a grain can be treated as an approximation of parallel projections of the grain. This enables 3D reconstruction of the grain shape by means of a three-dimensional simultaneous iterative reconstruction technique. The complete procedure is described in detail in LUDWIG *et al.* (2009b) and REISCHIG *et al.* (2013).

For the far-field data the ImageD11 software was used, which is part of FABLE, an open-source software package complete with a graphical user interface, with options for use of parallel computing, complete with documentation and a developers' corner (http://sourceforge.net/projects/fable/).

ImageD11 indexes grain orientations from diffraction spots by first assigning spots to powder *hkl* rings for the known unit cell. The scattering vectors between pairs of spots in selected rings are then compared to those which are expected based on the unit cell and *hkl* indices for the rings. When a pair of spots with a consistent angle between them is located they are used to compute an orientation matrix and this matrix is used to compute *hkl* indices for all observed scattering vectors. A large number of trial orientation matrices are produced in this way and those which are retained are decided according to the number of spots which are found to have integer *hkl* values within a tolerance value. A large number of spots found with integer *hkl* values are assumed to indicate a correct orientation. These matrices are later refined together with the grain positions after all grains have been located and each peak has been assigned to the grain which gives the best fit (rather than the first grain found).

The choice of tolerance parameters for assigning spots to *hkl* rings and whether or not to accept *hkl* indices as "close enough" to being integers depends on the precision of the experimental data and the density of peaks in the data. The tolerance should be large enough to accept a correct peak, but small enough to reject peaks which are just coincidentally close to expected positions. If the tolerance is too large or the number of peaks is too low then the algorithm can produce false orientations, but this is usually obvious provided some grains are indexed correctly, as the true orientations should fit many more peaks with smaller errors. When the sample size is large in comparison to the detector pixel size and the number of grains is also large then the peak shifts due to the unknown grain positions are enough to completely mix up which peak belongs to which grain. The software overcomes this problem by assuming a particular position inside the sample prior to computing scattering vectors etc and using a tolerance value which is as small as would be expected for a point like sample. To map out the volume of the sample an algorithm simply loops over a 3D grid inside the sample volume assuming point like sample from each point. The number of peaks, tolerance values and grid step are all chosen by the user to best match their experimental conditions. In this work grains were accepted if they indexed at least 18 out of 100 spots on the detector on average, and a *hkl* tolerance of 0.02 was used.

The software packages used to analyse the two datasets are both open source, and are available to visiting users at the ESRF on the beam line ID11. For the case of materials with small intergranular orientation spread and limited texture, both programs are able to index several thousands of grains in a single dataset. The limitation on the number of grains is given by the requirement to locate well separated diffraction spot positions on the 2D detector. Electro-discharge machining cutting process often produces a "re-cast" layer in the sample surface. In this analysis we

have observed a distinct population of "re-cast" grains close to the surface layer. It is possible that the cutting process has deformed some grains intersecting the surface and so they result in being harder to index, with increased errors.
A number of alternative software packages for indexing grains from far-field diffraction data exist (BERNIER *et al.*, 2011; LAURIDSEN *et al.*, 2001; MOSCICKI *et al.*, 2009; SCHMIDT, 2005, 2014; SHARMA *et al.*, 2012; SØRENSEN *et al.*, 2012). Fitting modules like *FitAllB* (ODDERSHEDE *et al.*, 2010) also perform a 12-parameter fit for each grain of the centre-of-mass grain positions, orientations and elastic strain tensors including error estimation and outlier rejection. This may be of interest for a future strain analysis on the same material, with a particular attention to the characterisation of the grain resolved stresses.

6.3 Comparison of results

Both datasets have been analysed using the respective software packages (DCT and ImageD11). In both cases, around 1750 grains have been identified, and their position, size and crystallographic orientation calculated. In the case of DCT, the 3D grain shapes have also been reconstructed. The following sections report specific details of the indexing results accessible with both methods.

6.3.1 Crystallographic texture

The grain indexing results were used to plot pole figures in order to represent the crystallographic texture of the sample, as shown in figure 6.2. The $\{0002\}$ and $\{11\bar{2}0\}$ pole figures are chosen to represent the texture of this material. The density is calculated by considering poles in a radius of 0.1 rad (5.73°) of a given direction, which acts as a smoothing parameter.

6.3.2 Grain unit cell representation

A second, qualitative way for comparison of indexing results on a grain-by-grain basis is shown in figure 6.3 where all the indexed grains are represented as hexagonal prisms, enabling easy identification of the crystal orientation. The differences between the two results are small but detectable to the human eye. Looking carefully at the top and bottom surfaces, one may notice a few missing grains or small differences in grain size and position.
For completeness, the spatially resolved grain map of all the grains, reconstructed from the near-field data is shown in figure 6.4. In this figure the asymmetric shape of

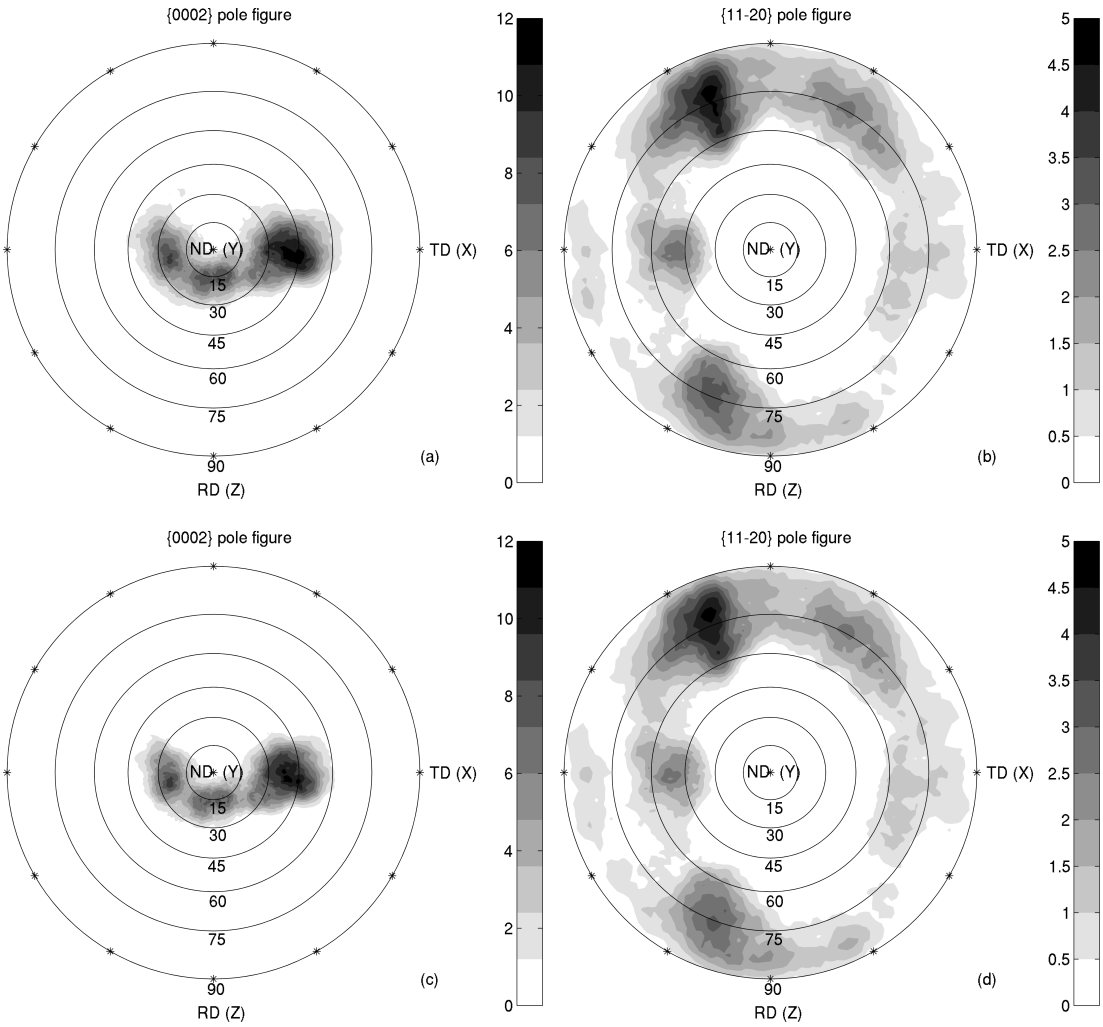

Figure 6.2: Texture analysis of the data is presented calculating the pole figures: in the top line they are computed from the near-field data, $\{0002\}$ pole figure on the left (a) and $\{11\bar{2}0\}$ pole figure on the right (b). In the bottom line the pole figures are computed from the far-field data, $\{0002\}$ on the left (c) and $\{11\bar{2}0\}$ on the right (d). The sample reference system is indicated with the rolling direction (RD), the transversal direction (TD) and the normal direction (ND), which are respectively parallel to the sample z-axis, x-axis and y-axis. The angles ψ and ϕ describe the pole figure: ψ is the angle between the pole and the ND direction. It goes from 0° to 90°. ϕ is the rotation around ND starting from the positive RD direction to the pole, for a right-handed rotation. It goes from 0° to 360°. Rings are drawn for ψ values from 15° to 90°.

the sample (a result of the electro discharge machining), which can be confirmed by absorption tomography, is very clear.

The next sections in the paper analyse these differences and similarities in depth, comparing the distribution of grain size, position and orientation of the same grains found in both datasets.

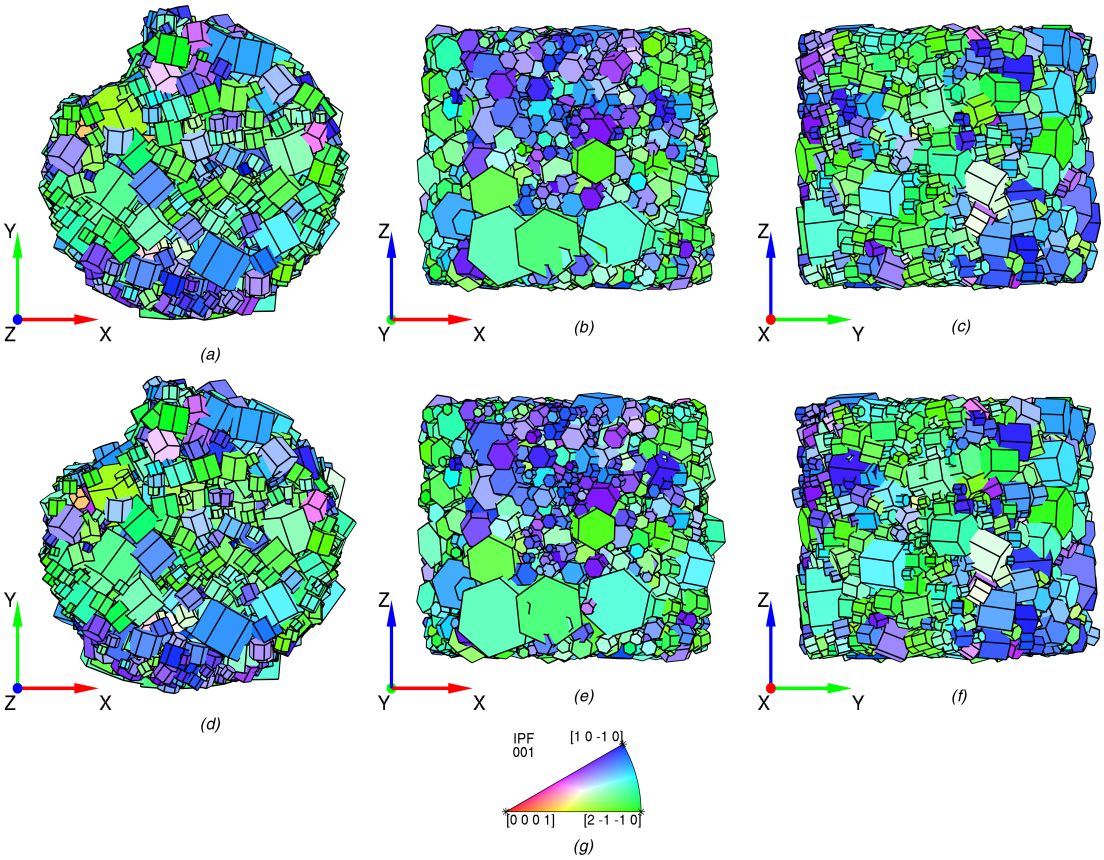

Figure 6.3: Representation of the grains using hexagonal unit cells. Each unit cell is defined by the corresponding grain centre and scaled according to its size (calculated from the average intensity of diffraction spots assigned to a grain). (g) Orientation colour coding given by the IPF relative to the sample Z-axis (IPF-Z). (a), (b) and (c) are relative to the near-field data. (d), (e) and (f) are relative to the far-field data. Three projections are shown: (a) and (d) XY plane, (b) and (e) XZ plane, (c) and (f) YZ plane.

6.3.3 Indexing results comparison and grain size calculation

Firstly, a comparison of the two techniques regarding number of indexed grains revealed 1755 and 1743 for the near-field and the far-field data, respectively. For the grain size calculation we assume proportionality between the grain volume (V_{grain}) and the average integrated intensity (Int) determined from all diffraction spots which have been assigned to this grain. With this assumption an estimate of absolute grain volume (V_{grain}) can be calculated using equation (6.1), where $\sum$Int stands for the sum of average intensities of all indexed grains and V_{sample} corresponds to the illuminated sample volume:

$$V_{grain} = \frac{\text{Int}}{\sum \text{Int}} V_{sample} \tag{6.1}$$

.

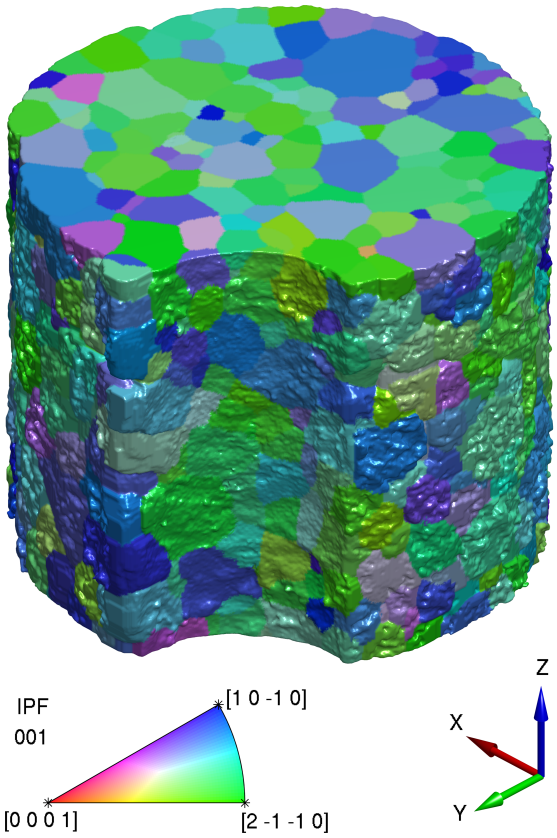

Figure 6.4: Grain map of the reconstructed sample volume from the near-field data using DCT. The grains are coloured according to the IPF-Z map. The represented volume is about half of the real sample volume.

An absolute measure of the illuminated sample volume (V_{sample} = 0.209 mm^3) was obtained from the tomographic reconstruction of the transmission images recorded during the near-field scan, and was not feasible with only the far-field scan.
In order to define an equivalent grain size, the grain volume (V_{grain}) was approximated using hexagonal prism as shape (side length r, height h) and setting the h/r ratio to the c/a ratio for pure titanium (1.5857), as expressed in equation (6.2):

$$V_{grain} = \frac{3}{2}\sqrt{3}\left(\frac{\mathrm{h}}{\mathrm{r}}\right)\mathrm{r}^3 \tag{6.2}$$

Note that diffraction spots from a grain typically show a spread of intensities caused by (i) differences in diffraction conditions (i.e. structure factor and Lorentz factor), (ii) attenuation of the incoming and diffracted beam in the sample (absorption, extinction) as well as (iii) spatial and temporal inhomogeneities in the incoming beam profile. These factors will affect the accuracy of the absolute volume estimate obtained with equation (6.1), but can be expected to yield similar estimates when applied to near-field and far-field diffraction data from the same sample. In many practical cases only contribution from (i) can be corrected, whereas (ii) and (iii) are unknown or not easily accessible. In order to assess the error related to the simplified

volume estimate used in equation (6.1), a comparison of grain volumes obtained with this approach (V_{int}) and volumes calculated from the grain map obtained by tomographic reconstruction (V_{tomo}) has been carried out using equation (6.3).

$$\Delta V = |V_{int} - V_{tomo}| \qquad \sigma_{\Delta V} = \sqrt{\sigma^2_{V(Int)} + \sigma^2_{V(tomo)}} \tag{6.3}$$

This comparison indicates average volume (size) errors of order of 10^3 µm^3 (1 µm) for grains close to the average grain size (40.5 µm) in the sample. Similar volume errors were observed when accounting for structure and Lorentz factors in the calculation of the average intensities (Int). This in turn seems to indicate that contributions from (ii) and (iii) dominate the error in the calculation of the absolute grain volume according to equation (6.1), at least in the conditions used for this experiment.

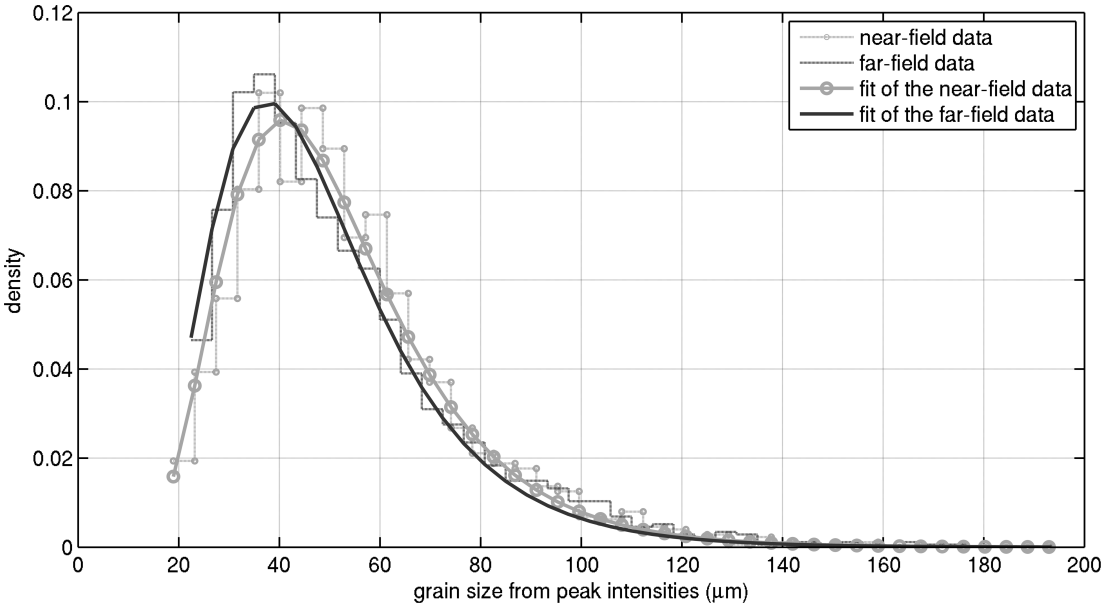

Figure 6.5: Grain size distribution is shown for both the near-field and far-field data (dash lines). The grain size distribution is fitted with a lognormal distribution (solid lines).

Figure 6.5 compares the grain size of the indexed grains of the two datasets. The agreement between the measurements of the grain size is almost perfect, suggesting a lognormal distribution of the grain size, described by the following equation:

$$f(S;\mu,\sigma) = \frac{1}{S\sigma\sqrt{2\pi}} \exp \frac{-[\ln(S)-\mu]^2}{2\sigma^2} \tag{6.4}$$

where S is the grain size, μ and σ are respectively the mean and the standard deviation of the corresponding normal distribution. For a more quantitative comparison, a fit was performed using the expected lognormal grain size distribution (solid lines in figure 6.5), which yields mean values for the two distributions of 51.8 µm and

48.7 μm with standard deviations of 21.7 μm and 21.3 μm respectively for near-field and far-field data. Both techniques enabled identification of grains down to around 20 μm. However, the far-field methodology shows a slightly higher frequency at the small end compared to the near-field measurement technique, suggesting that on average the far-field technique allows indexing smaller grains than the near-field technique, even though there is no significant difference in minimum detected grain size with the acquisition conditions used in this study.

Given the higher detective quantum efficiency of the far-field detector, the latter result is at first sight surprising – one could have expected a spectrum with tails extending down to the (sub-) micron grain size. However, the exposure time of CCD based diffraction detectors has to be adjusted such that only a small fraction of the diffraction spots reach the saturation level beyond which streaking artefacts ("blooming" of the CCD) deteriorate the quality of the diffraction images. The intensity *per pixel* scales with the third power of the grain size for grain dimensions smaller than the detector pixel size and continues to increase linearly for grain dimensions bigger than the detector pixel size. In the latter case the integrated diffraction spot intensity is spread over neighbouring pixels and the contribution received by a single pixel corresponds to a grain sub-volume scaling linearly with the equivalent size of the grain. The ratio between the strongest and weakest *per pixel* intensities which have been segmented from the far-field data is of order $DR_{ff} = 4000$ (limited by the dynamic range achievable in a single CCD exposure) and about $DR_{nf} = 30$ (limited by counting time) on the near-field detector. Given the different scaling behaviour for near-field and far-field pixel intensities, this resulted in a similar minimum grain size detection limit of order of 10 μm in both cases. We conclude that the grain size distribution depicted in figure 6.5 is truncated and that smaller grains are present in the sample but could not be detected with the acquisition conditions used in the experiment.

6.3.4 Matching datasets

The next step in the comparison was to identify to which level the two sets of results agree on individual grains in terms of grain position, size and orientation. In order to match the grains between the two scans, the following criteria were considered: the distance between the centres of mass must be smaller than the product of a factor (*distf*) and the grain size, the misorientation angle must be smaller than a maximum allowed angle (*angle*) and the grain size ratio between the two compared grains from the two scans must differ by less than a given ratio (*ratio*). In summary the criteria

were chosen as shown in equation (6.5).

$$\begin{aligned} distf &= 0.4 \\ angle &= 2.3^\circ \\ ratio &= 2 \end{aligned} \tag{6.5}$$

Using those tolerances the number of matched grains is 1465, i.e. about 84% of all the indexed grains for both techniques were matched. In the following comparison only the matched grains are taken into account, meaning only those grains indexed from DCT that can be identified amongst the indexed grains from ImageD11 and vice versa.

6.3.4.1 Matching datasets: grain position

The first variable studied during this comparison between the matched grains is the position, calculated from the indexing procedure for both techniques. The position of the grains is compared, considering the three components separately as shown in figure 6.6. It is observed that the Z component is the most accurate, with a standard deviation of 2.7 µm, whilst the X and Y components have a larger error, respectively of 6.5 µm and 6.8 µm. The larger error in X and Y can be explained as follows.

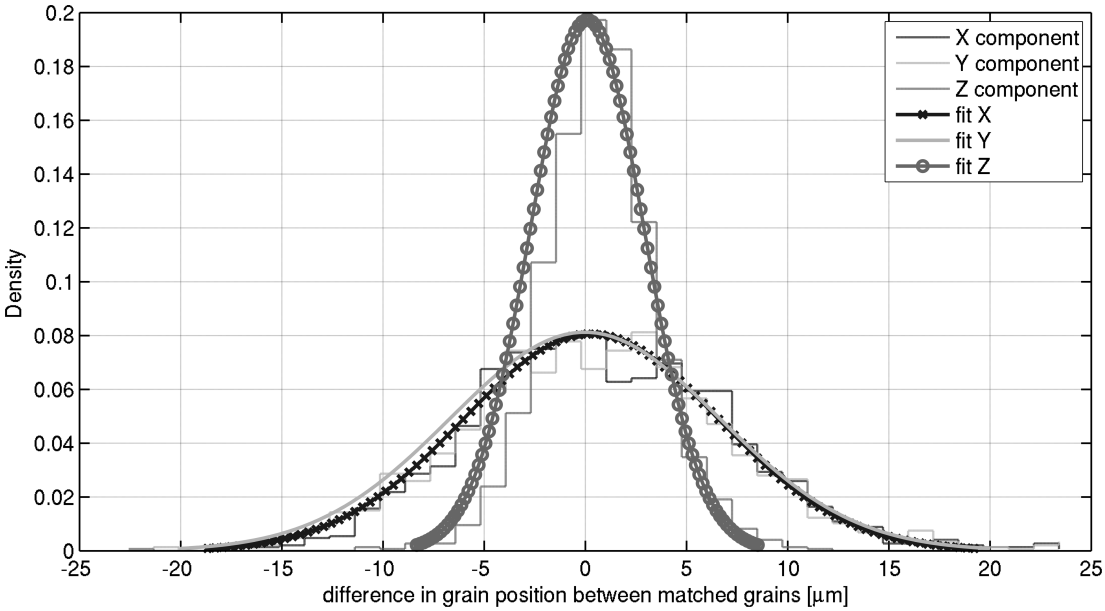

Figure 6.6: Difference in grain position between near-field and far-field data, considering only the matched grains. The total number of points is 1465. The three components are shown with different colours and markers. A normal fit is performed for each component.

In the current experimental setup (see figure 6.1) the sample z-axis is parallel with the rotation axis. Therefore, the grain Z position is constant during data acquisition whereas the X and Y positions precess around the Z axis which in turn leads to systematic shifts of the spot positions on the detector. Given the low diffraction angles used in these measurements ($2\theta < 12°$), the vertical shift of the spot position on the detector has a reduced amplitude or sensitivity ($\tan 2\theta \approx 0.2$) which in turn leads to slightly less accurate position estimates in the XY plane. Furthermore, mechanical imperfections of the rotation stage (wobble and eccentricity) contribute particularly to the error in the XY plane. While it is not possible to compare the absolute errors of the two methods from this comparison, it can be expected that the near-field detector provides higher positional accuracy and the deviations are mostly due to the larger errors from the far-field dataset.

6.3.4.2 Matching datasets: grain size

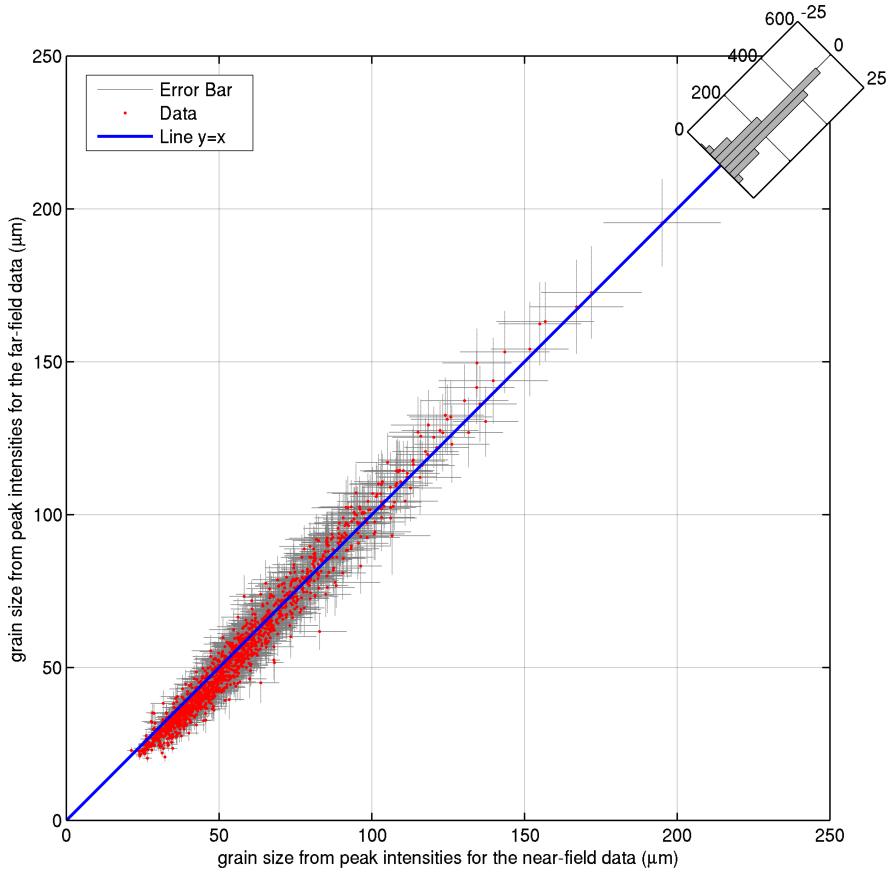

Figure 6.7: Grain size comparison between near-field and far-field data, considering only the matched grains. The total number of points is 1465. The grain size is calculated from the average intensity measured for each grain. The distribution of the deviations from y = x is shown in the top-right histogram.

The grain sizes determined in the two scans are shown plotted against each other in figure 6.7, considering only the matched grains. One can see that all the grains stay close to the y = x line, indicating a good agreement between the measurements. A slight difference in the distribution of the grains in the two parts separated by the diagonal is visible, especially for grains below 50 µm of equivalent size. The distribution of those deviations is shown in the top-right histogram, which gives a mean value of 2.9 µm and a standard deviation of 11 µm. The smaller grains appear to be larger in the DCT results in comparison to ImageD11. This difference might arise from differences in the algorithms for measuring the peak intensities. In DCT, the peak tail cut-off is scaled by the peak height but in ImageD11 the same threshold is used for all spots, so that weak peaks are systematically underestimated.

6.3.4.3 Matching datasets: grain orientation

The misorientation is the difference in crystallographic orientation between two grains (or crystals), expressed as the smallest rotation between two coordinates systems. One coordinate system can be superimposed onto the other by rotating it by an angle around the common axis. Because it is an axis of rotation, the direction is the same in both the coordinate systems. Considering the orientation matrix g of equation (6.6), which can be described by the axis/angle pair (RANDLE, 1992), one can extract the misorientation angle (γ) and the components of the rotation axis (u, v, w) as explained in MAINPRICE *et al.* (1993):

$$g = \begin{pmatrix} g_{11} & g_{12} & g_{13} \\ g_{21} & g_{22} & g_{23} \\ g_{31} & g_{32} & g_{33} \end{pmatrix} \tag{6.6}$$

$$\gamma = \cos^{-1}\left[1/2\left(g_{11} + g_{22} + g_{33} - 1\right)\right] \tag{6.7}$$

$$u = \frac{g_{23} - g_{32}}{2\sin\gamma} \qquad v = \frac{g_{31} - g_{13}}{2\sin\gamma} \qquad w = \frac{g_{12} - g_{21}}{2\sin\gamma} \tag{6.8}$$

Figure 6.8 presents a histogram of the misorientation for the matched grains, taking the same grain in the two datasets and computing the difference in orientation for each of them. A very close agreement between the measured orientations of the indexed grains for the two datasets can be observed. In this comparison a misorientation up to 2.3° is allowed between matched grains. The histogram shows a maximum at around 0.03°, which is of the order of magnitude of the rotation increment used in the scans (0.05°) and the angular extent of a pixel seen from the sample position (approximately 0.012°).

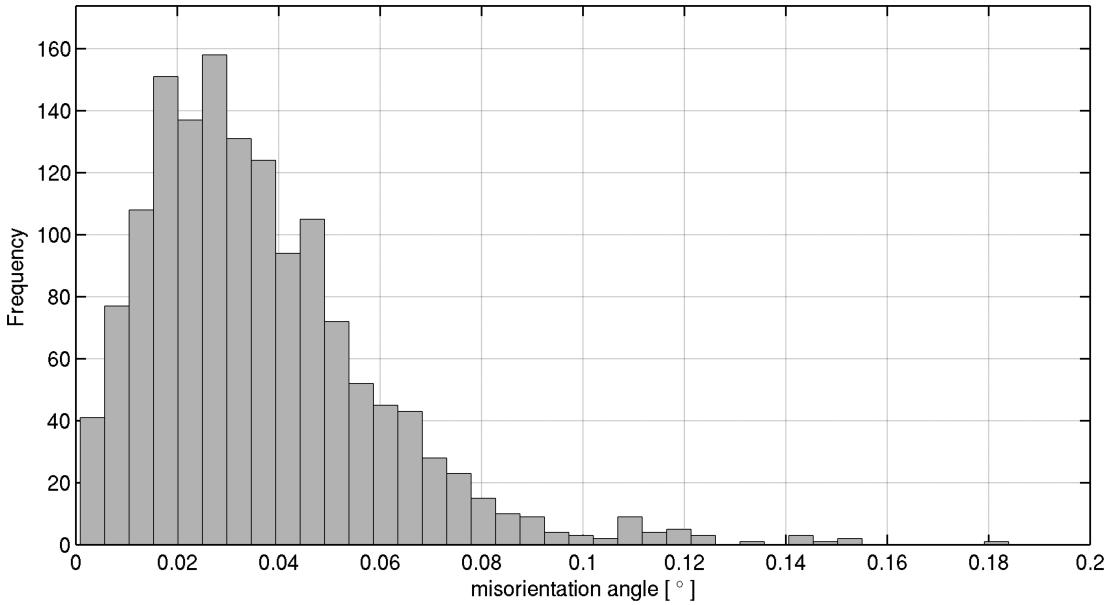

Figure 6.8: Misorientation angle distribution between near-field and far-field data, considering only the matched grains. The total number of points is 1465.

6.3.4.4 Matching datasets: further analysis

For the current analysis, it was possible to match 1465 grains using a given set of tolerances, which corresponds to 84% of the indexed grains in each dataset, leaving about 300 unmatched grains. Adjusting the tolerances can reduce the number of unmatched grains. The analysis presented suggests that the measurements of grain size and crystallographic orientation are very reliable, and the most significant variations are seen in the calculated grain positions. The far-field detector has a pixel size of 48.5 μm/pixel, about 35 times bigger than the pixel size of the near-field detector (1.4 μm/pixel). Consequently, the far-field measurement is not very sensitive to the grain position, but instead delivers improved accuracy in the angular measurements of scattering vectors. In the present analysis the relative distance tolerance was used to match grains, which means that the position of a grain can have an error, which is normalised by the actual grain size.
Alternatively one can consider the absolute distance between two grains measured in micrometres as an alternative to the relative distance. Figure 6.9 plots the number of matched grains as a function of the tolerance in respect of relative and absolute distance between grain centres.

One can increase the number of matched grains by changing the criteria, at the risk of introducing false matches or “multiple” matches, cases in which a grain in one dataset can be matched to more than one grain in the other dataset. In this analysis the multiple matches are not taken into account and only the “unique” cases are considered: if a multiple match occurred, it is discarded and removed from the list of

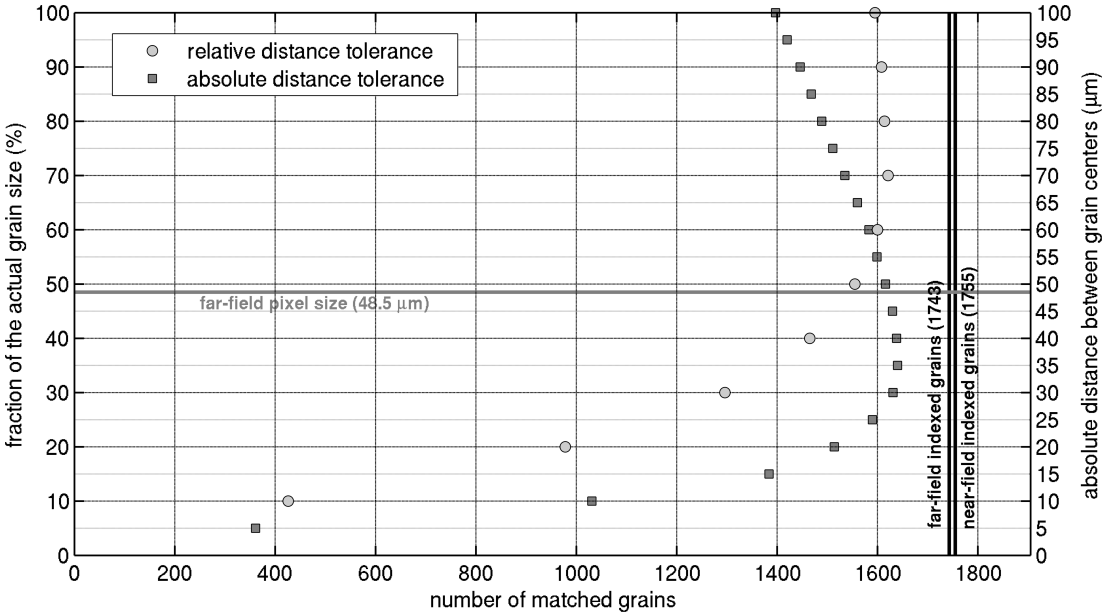

Figure 6.9: Maximum allowed distance between centres to match grains between near-field and far-field data. The absolute distance tolerance goes from 5 µm to 100 µm (squares). The relative distance tolerance, scaled to the grain size, goes from 0.1 to 1 (circles). Two vertical lines indicate the total number of indexed grains for both datasets, while the horizontal line indicates the far-field detector pixel size.

matched grains. By choosing a relative tolerance of 50% of the actual grain size, more than 1600 grains can be matched and the number of unmatched grains is reduced to 91 and 71 for near-field and far-field data, respectively. This corresponds to about 0.7% of the sample volume. Note that the analysis already includes the grains at the bottom of the gauge volume, which are partially irradiated and where the irradiation may slightly change during the scan due to drifts of the setup, resulting in larger expected errors. The unmatched grains populate typically the lower end of the grain size distribution (see red circles in figures 6.10 and 6.11). Since these grains are close to the detection limit and represent only a small fraction of the volume, we prefer to take a conservative approach and discard them from the analysis.

6.4 Discussion

6.4.1 Differences between the DCT and the ImageD11 indexing procedures

The precession of a grain around the rotation axis leads to systematic shifts in the diffraction spot positions recorded on the detector. In order to transform spot positions into scattering vectors, these shifts have to be taken into account in the indexing

procedure. In the case of far-field data analysed using ImageD11, the problem is solved by dividing the sample into smaller sub-regions (a few times the effective pixel size) and repeating the indexing procedure on the set of scattering vectors computed according to the current position of the sub-volume. The actual grain positions and orientation matrices are refined subsequently by means of a simplex fitting procedure.

In the case of near-field data analysed using the DCT code, the transformation from diffraction spot positions into scattering vectors is based on the concept of Friedel pairs. The position of the *hkl* and $\overline{hkl}$ reflections observed at 180° offset in rotation allow for precise determination of the scattering vectors, independent of the grain position (LUDWIG *et al.*, 2009b). The DCT indexing procedure uses both, spatial (i.e. the size of diffraction spot pairs and the distance between the diffraction beam path) and crystallographic criteria (angle between the scattering vectors), for assigning Friedel pairs of diffraction spots to a given grain. The algorithm performs a combined search, taking these criteria simultaneously into account. The grain position is defined as the point minimising the distance to the diffracted beam trajectories calculated from the Friedel pairs assigned to the grain. The diffracted beam trajectories are calculated for a Friedel pair from the intensity-weighted centres of mass positions of its two diffraction spots.

Since centre of mass positions of sharp diffraction spots on a far-field detector can be determined with higher accuracy and since sample drifts or mechanical error motions of up to a few microns are negligible compared to the pixel size, the accuracy of scattering vectors determined from far-field diffraction data is in general superior to the one obtained from near-field data. As a consequence, the individual grain elastic strain tensors (ODDERSHEDE *et al.*, 2010) can be determined with about one order of magnitude better resolution compared to the results obtained from near-field diffraction data (REISCHIG *et al.*, 2013).
As stated earlier, the near-field, high resolution approach allows a 3D reconstruction of the sample volume at the micrometre level, as shown in figure 6.4. One might argue that with the help of such a voxelized representation it should be possible to recognise erroneous indexing results (in particular missing grains) by visual inspection of the 3D grain volume. Although this is true for bigger grains, previous work on comparison of 2D grain maps produced with X-ray DCT and EBSD (SYHA *et al.*, 2013) shows that it remains difficult to reliably identify indexing problems related to grains at the lower end of the size spectrum.

Given the large pixel size of the diffraction detector, 3D shape reconstruction of the grains contained in the sample volume is not possible using the far-field diffraction data acquired in this study. However, one could perform a Voronoi or Laguerre

tessellation of the 3D volume containing the grain centres, using only the information of grain position and size. Because no grain shape information is available in this case, such a reconstruction can contain significant errors in terms of grain connectivity (neighbours) and grain boundary structure. An assessment of the accuracy of 3D grain shapes reconstructions determined from such tessellation procedures can be found in LYCKEGAARD *et al.* (2011).

Both algorithms can index datasets containing up to a few thousand grains, when applied to well re-crystallized polycrystalline materials with limited intergranular orientation spread. The presence of grain sub-structures and texture leads to breakup of diffraction spots. This increases the probability of diffraction spot overlap and will increase the probability of diffraction spot mis-assignment and false indexing. With deformed samples the increased size of a diffraction spot on the detector leads to a reduction in the number of individual spots, which can be resolved and used for indexing.

Alternative approaches exist for indexing near-field diffraction data, particularly if these data have been acquired with a line-focus (1D) illumination of the sample (POULSEN *et al.*, 2001). Forward modelling algorithms such as the one described in SUTER *et al.* (2006) and LI and SUTER (2013) perform a systematic search over orientation space and both, an orientation and a confidence indicator can be assigned to each voxel in the sample volume. It has been shown that this type of reconstruction algorithms can deal with samples having undergone significant plastic deformation (LI *et al.*, 2012; WEST *et al.*, 2009). It would be interesting in the future to compare this class of "forward modelling" algorithms with the approaches presented in this work.

6.4.2 Unmatched grains

For future users of polycrystalline materials indexing software, it is important to be aware of limitations and understand the origins of unmatched grains, which have been indexed in only one of the two scans. These may arise because one of the indexing routines fails to detect a real grain or because an algorithm falsely identifies a grain, which does not in fact exist. A useful measure of confidence in the indexing of a grain is its completeness. The completeness is the number of the indexed reflections from a grain as a fraction of the theoretical number of reflections that should be observed with the given setup. The theoretically expected number of reflection varies slightly between different grains as it depends on the grain orientation and position. For this prediction, all reflections on the detector are assumed to be detected, even though the weak diffractions signals may be under the detection limit. The average number of

expected reflections per grain for the near-field and far-field acquisition geometries used in this study was about 80 and 150, respectively.

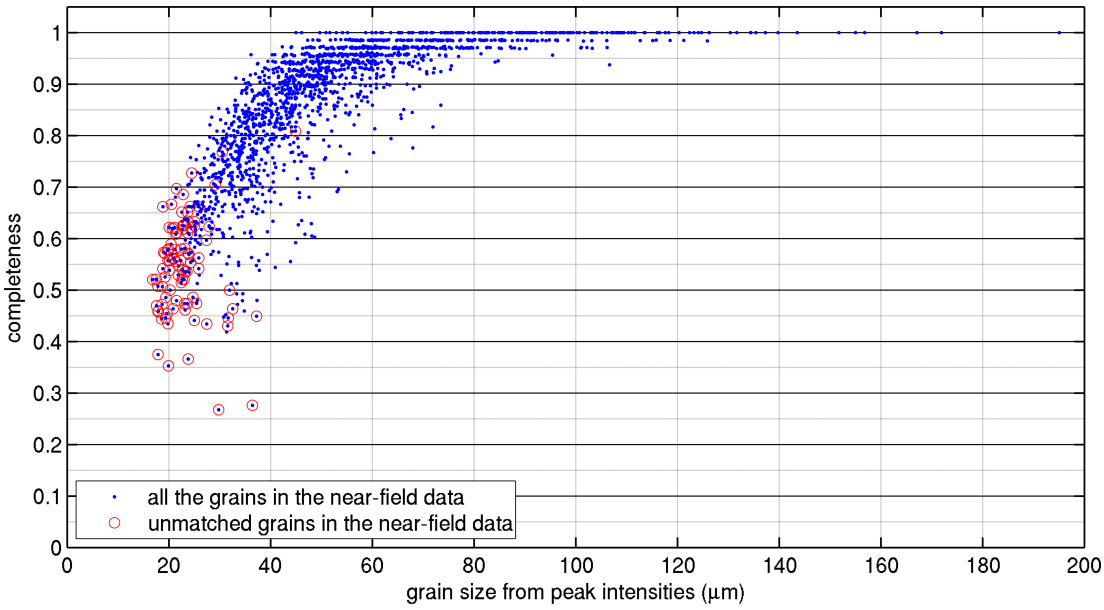

Figure 6.10: Completeness values for near-field data as a function of the grain size. The circles indicate the grains that have not been matched.

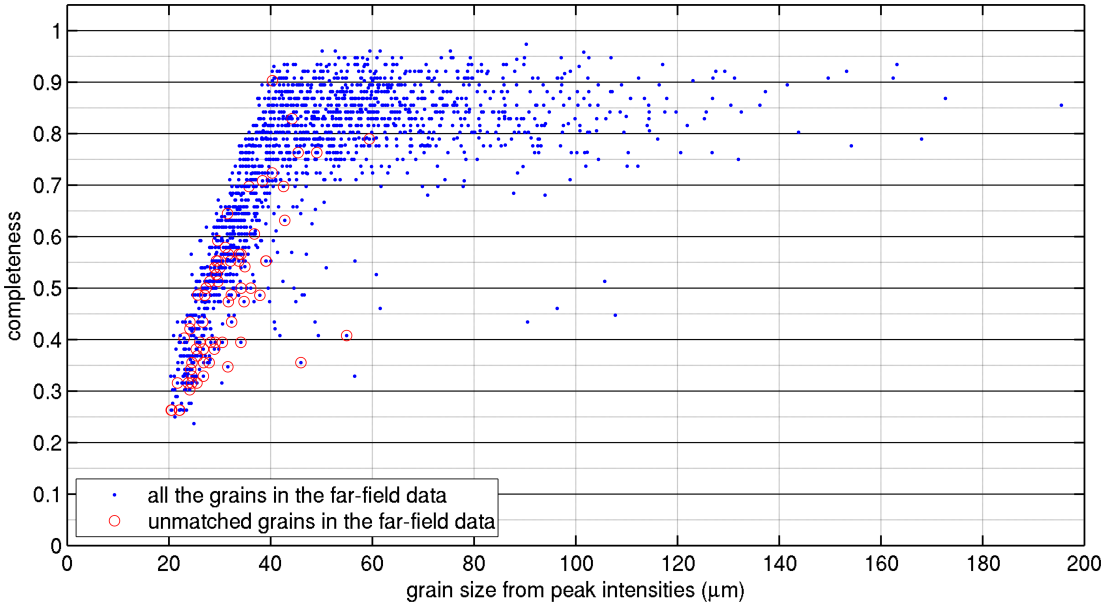

Figure 6.11: Completeness values for far-field data as a function of the grain size. The circles indicate the grains that have not been matched.

Figures 6.10 and 6.11 plot the completeness as a function of the grain size for the near-field and far-field datasets, respectively. Unmatched grains are marked with circles in each figure. From figure 6.10 one can state that all the near-field unmatched grains have a grain size lower than 40 µm, while for the far-field unmatched grains

(see figure 6.11) there is not such a strong systematic relationship with grain size and completeness. The presence of unmatched grains of relatively large size and with high completeness in the far-field data suggests either a false indexing result from the ImageD11 analysis code, or that the DCT algorithm has failed to find these particular orientations. An alternative scenario is that the matching code has discarded a low angle grain boundary where two grains are seen on the far-field detector but only a single grain on the near-field detector.

To better understand the remaining discrepancies, a simulation was carried out to analyse the number of reflections from one dataset which could have been assigned to the unmatched missing grains in the other dataset. As a first step, the positions of reflections on the far-field detector were computed from the position and orientation of the 91 unmatched grains in the DCT dataset. Then a nearby measured peak on the far-field detector was associated with each simulated reflection, where their distance was within a tolerance limit derived from previous indexing results. As a last step, the associated peaks were categorised according to whether or not they had been indexed as a reflection of a grain in the far-field data. The results are shown in figure 6.12 for all the grains, ordered by size.
For a large fraction of these grains the number of reflections, which could be attributed on the far-field detector, is below 18, which is the number of reflections on the far-field detector to accept a grain. This may indicate either that they are false "positives" or that the spot intensities are close to the detection limit of the far-field data set acquired in this study. Moreover, 78.7% of the reflections assigned to the new grains have not been indexed before.
The same procedure was repeated by simulating reflections on the near-field detector from the 71 unmatched grains in the far-field data. The results are shown in figure 6.13. The number of assigned reflections on near-field detector is fairly constant and relatively high, also for the smallest grains. This in turn suggests that the DCT has failed for some reason to index those grains, which are real. Moreover, 98.3% of the reflections assigned to the new grains have not been indexed before.

Observing the results from the forward simulation shown in figures 6.12 and 6.13, one can draw the conclusion that there are some remaining uncertainties in the indexing procedures, both for DCT and ImageD11. These uncertainties mostly concern small grains and it is difficult to provide objective criteria for classification of these cases into valid or erroneous indexing results, since, at least for the smaller grains, the low completeness values may be due to insufficient counting statistics.
The methods of indexing presented and discussed in this paper are inverse indexing approaches based on a systematic search through a list of scattering vectors identified by some sort of image segmentation or peak search algorithm. The main advantage of

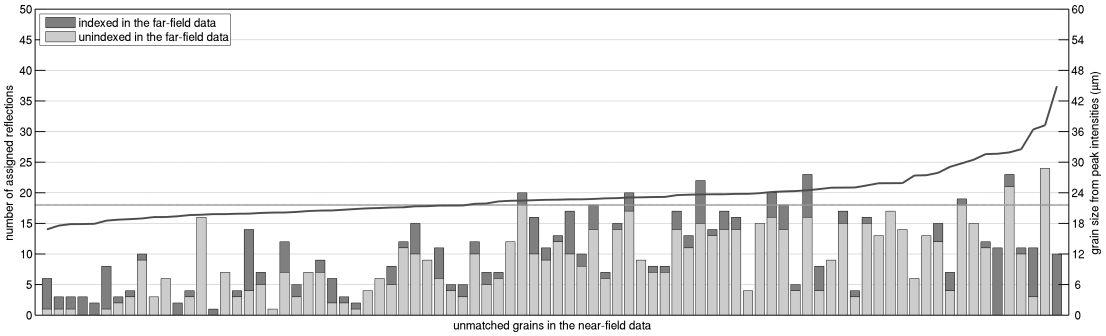

Figure 6.12: Number of peaks on the far-field detector assigned to the unmatched grains in the near-field data shown as a bar graph. The peaks are categorised as "indexed" if they had been assigned to a grain in the far-field data, or "unindexed" otherwise. The number of reflections required on the far-field detector to accept a grain is indicated with a horizontal line. The grains are ordered by grain size, which is plotted as a continuous line according to the axis on the right.

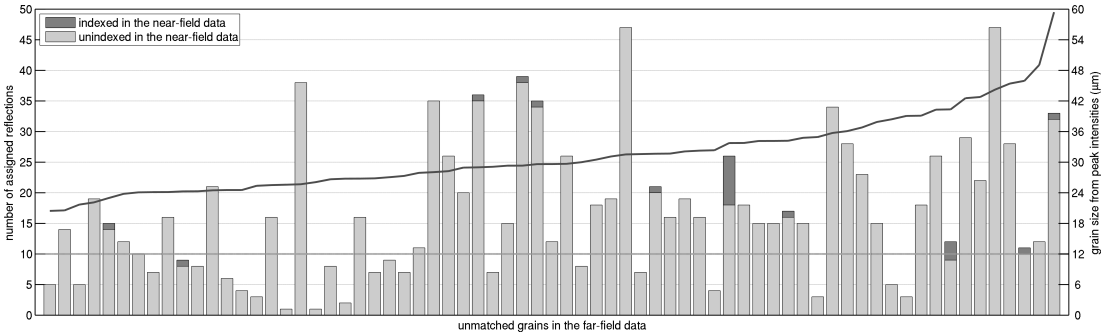

Figure 6.13: Number of peaks on the near-field detector assigned to the unmatched grains in the far-field data shown as a bar graph. The peaks are categorised as "indexed" if they had been assigned to a grain in the near-field data, or "unindexed" otherwise. The number of reflections required on the near-field detector to accept a grain is indicated with a horizontal line. The grains are ordered by grain size, which is plotted as a continuous line according to the axis on the right.

this approach is speed (a few minutes for indexation of up to several thousand grains). However, it is well known that this concept has limitations in the case of strongly textured or plastically deformed materials, since the concept of a grain described by a single orientation will no longer hold and diffraction spots start to overlap and to break up into sub peaks, spread out dominantly along the azimuth direction of the Debye-Scherrer rings.

6.4.3 Routes for improvement of indexing routines

The indexing procedures discussed in this paper do not include systematic, predictable intensity variations of the diffraction signals (i.e. structure and Lorentz

factor, self-absorption and extinction) assigned to a grain. Adding such an additional constraint could be used for outlier rejection and would help to reduce the number of erroneous spot assignments. This functionality is available in the FitAllB code (ODDERSHEDE *et al.*, 2012).
Since diffraction spots that have been erroneously assigned to a grain are removed from the list of available spots, the completeness of grains processed at a later stage of the indexing procedure may be deficient. This is due to the fact that diffraction spots assigned to a "wrong" grain could belong to another "good" grain, which would be process later in the process. This problem could be alleviated by running the indexing procedure on different instances of the spot metadata, sorted in a different way. Last but not least, spots assigned to grains with poor quality of fit indicators could be kept in the list of spots available for indexation of new grains. In case of multiple assignments, those spots would be assigned to the grain yielding the smallest error. This last case is currently under development in the DCT code.

Spot overlaps are generally not well accounted for in any procedure where a single spot is matched to a single grain. The centre of mass position for the far-field data will be dominated by the stronger signal from the larger grain, which leads the spot to be assigned to that grain. Allowing spots to be assigned to multiple grains and down-weighting them when they are overlapped would improve the overall accuracy.

6.5 Conclusions

In the present paper, results are presented for indexing about 1750 grains in a polycrystalline titanium sample. The analysis focuses on the comparison of indexing results obtained with the DCT and ImageD11 software package representing near-field and far-field techniques, respectively. Near-field and far-field notations are not relative to the optical distinction between Fresnel and Fraunhofer diffraction. They only concern the difference between the sample-detector distance and the detector type used in both approaches.
The measurements of grain position, size and crystallographic orientation are analysed. An important aspect of the analysis is "matching" (cross-validation of indexing results), whereby the indexed grains from the near-field scan are associated with the respective indexed grains from the far-field scan. The two techniques deliver very similar results in terms of describing a polycrystalline aggregate and there is a good but not perfect agreement between the results from the two techniques.

The principle difference between the two techniques is the spatial resolution and the quantum efficiency of the detector systems employed. Consequently, near-field

acquisition schemes are more accurate in spatial resolution and can be used for reconstruction of spatially resolved grain maps, whereas far-field acquisition schemes are faster and provide more reliable angular resolution for scattering vectors. Discrepancies between both approaches are mainly observed in the lower tail of the grain size distribution. For the far-field data, the finite dynamic range of the diffraction detector limits the minimum detected grain size with a single exposure in the current study to about 20 µm, whereas for the near-field diffraction data the limitation is rather related to the poor quantum efficiency of the high resolution imaging system. Both algorithms can be used for fast indexing datasets containing up to a few thousand grains.

Experimentally it is possible to carry out these two experiments simultaneously, using the "3D" detector concept (OLSEN *et al.*, 2009). Here, a high resolution detector semi-transparent to X-rays is used (in which only a scintillator and 45° mirror are placed in the X-ray beam, with the microscope optics perpendicular), recording the diffraction signal on both detectors at the same time. Simply processing the two datasets independently would allow orientation to be transferred between the two programs, leading to a more complete overall picture. An algorithm, which matches the diffraction spots across the two datasets prior to indexing, should further improve the results by creating more accurate scattering vectors that are essentially free from the errors, due to the grain positions in the sample.

6.6 Acknowledgements

The authors are grateful for the help of Sébastien Petitdemange. We further acknowledge Richard Moat (former University of Manchester, UK), who provided the samples and for his assistance during the experiment. ESRF and its support staff are acknowledged for beam time on the beam line ID11. The project was supported financially by the Engineering and Physical Science Research Council in the UK (EP/F020910/1) and the ESRF.

The work presented in chapter 6 has been published as the following:
NERVO, L. *et al.* (2014), "Comparison between a near-field and a far-field indexing approach for characterization of a polycrystalline sample volume containing more than 1500 grains", *Journal of Applied Crystallography* **47** (4), pp. 1402–1416.

6.7 References

BERNIER, J. V. *et al.* (2011), "Far-field high-energy diffraction microscopy: a tool for intergranular orientation and strain analysis", *Journal of Strain Analysis for Engineering Design* **46** (7), pp. 527–547.

BLEUET, P. *et al.* (2009), "Towards synchrotron-based nanocharacterization", *Frontiers of Characterization and Metrology For Nanoelectronics* **1173**, ed. by SEILER, D. G. *et al.*, pp. 181–187.

COAN, P. *et al.* (2006), "Evaluation of imaging performance of a taper optics CCD 'FReLoN' camera designed for medical imaging", *Journal of Synchrotron Radiation* **13** (3), pp. 260–270.

DCT code, http://sourceforge.net/projects/dct/.

FABLE, http://sourceforge.net/projects/fable/.

HOLT, J. M. T., MINDLIN, H., and HO, C. Y. (1996), *Structural alloys handbook*, West Lafayette, IN, USA: CINDAS/Purdue University.

LABICHE, J.-C. *et al.* (2007), "The fast readout low noise camera as a versatile x-ray detector for time resolved dispersive extended x-ray absorption fine structure and diffraction studies of dynamic problems in materials science, chemistry, and catalysis", *Review of Scientific Instruments* **78** (9), p. 91301.

LARSON, B. C. *et al.* (2002), "Three-dimensional X-ray structural microscopy with submicrometre resolution.", *Nature* **415** (6874), pp. 887–890.

LAURIDSEN, E. M. *et al.* (2001), "Tracking: a method for structural characterization of grains in powders or polycrystals", *Journal of Applied Crystallography* **34** (6), pp. 744–750.

LI, S. F. and SUTER, R. M. (2013), "Adaptive reconstruction method for three-dimensional orientation imaging", *Journal of Applied Crystallography* **46** (2), pp. 512–524.

LI, S. F. *et al.* (2012), "Three-dimensional plastic response in polycrystalline copper via near-field high-energy X-ray diffraction microscopy", *Journal of Applied Crystallography* **45** (6), pp. 1098–1108.

LUDWIG, W. *et al.* (2009a), "New opportunities for 3D materials science of polycrystalline materials at the micrometre lengthscale by combined use of X-ray diffraction and X-ray imaging", *Materials Science and Engineering: A* **524** (1–2), pp. 69–76.

LUDWIG, W. *et al.* (2009b), "Three-dimensional grain mapping by x-ray diffraction contrast tomography and the use of Friedel pairs in diffraction data analysis", *Review of Scientific Instruments* **80** (3), p. 033905.

LYCKEGAARD, A. *et al.* (2011), "On the Use of Laguerre Tessellations for Representations of 3D Grain Structures", *Advanced Engineering Materials* **13** (3), pp. 165–170.

MAINPRICE, D., LLOYD, G. E., and CASEY, M. (1993), "Individual orientation measurements in quartz polycrystals: advantages and limitations for texture and petrophysical property determinations", *Journal of Structural Geology* **15** (9–10), pp. 1169–1187.

MOSCICKI, M *et al.* (2009), "Friedel-pair based indexing method for characterization of single grains with hard X-rays", *Materials Science and Engineering: A* **524** (12), pp. 64–68.

ODDERSHEDE, J. *et al.* (2010), "Determining grain resolved stresses in polycrystalline materials using three-dimensional X-ray diffraction", *Journal of Applied Crystallography* **43** (3), pp. 539–549.

ODDERSHEDE, J. *et al.* (2012), "Measuring the stress field around an evolving crack in tensile deformed Mg AZ31 using three-dimensional X-ray diffraction", *Acta Materialia* **60** (8), pp. 3570–3580.

OLSEN, U. L. *et al.* (2009), "Structured scintillators for X-ray imaging with micrometre resolution", *Nuclear Instruments and Methods in Physics Research Section A: Accelerators, Spectrometers, Detectors and Associated Equipment* **607** (1), pp. 141–144.

POULSEN, H. F. (2012), "An introduction to three-dimensional X-ray diffraction microscopy", *Journal of Applied Crystallography* **45** (6), pp. 1084–1097.

POULSEN, H. F. *et al.* (2001), "Three-dimensional maps of grain boundaries and the stress state of individual grains in polycrystals and powders", *Journal of Applied Crystallography* **34** (6), pp. 751–756.

RANDLE, V. (1992), *Microtexture Determination and Its Applications*, 1st ed., Institute of Materials.

REISCHIG, P. *et al.* (2013), "Advances in X-ray diffraction contrast tomography: flexibility in the setup geometry and application to multiphase materials", *Journal of Applied Crystallography* **46** (2), pp. 297–311.

SCHMIDT, S. (2005), GrainSweeper, http://fable.svn.sourceforge.net/svnroot/fable/GrainSweeper.

— (2010), GrainSpotter v. 0.82, http://fable.svn.sourceforge.net/svnroot/fable/GrainSpotter.

— (2014), "GrainSpotter: a fast and robust polycrystalline indexing algorithm", *Journal of Applied Crystallography* **47** (1), pp. 276–284.

SHARMA, H., HUIZENGA, R. M., and OFFERMAN, S. E. (2012), "A fast methodology to determine the characteristics of thousands of grains using three-dimensional X-ray diffraction. II. Volume, centre-of-mass position, crystallographic orientation and strain state of grains", *Journal of Applied Crystallography* **45** (4), pp. 705–718.

SØRENSEN, H. O. *et al.* (2012), "Multigrain crystallography", *Zeitschrift für Kristallographie* **227** (1), pp. 63–78.

STOCK, S. R. (2008), "Recent advances in X-ray microtomography applied to materials", *International Materials Reviews* **53** (3), pp. 129–181.

SUTER, R. M. *et al.* (2006), "Forward modeling method for microstructure reconstruction using x-ray diffraction microscopy: Single-crystal verification", *Review of Scientific Instruments* **77** (12), p. 123905.

SYHA, M. *et al.* (2013), "Validation of three-dimensional diffraction contrast tomography reconstructions by means of electron backscatter diffraction characterization", *Journal of Applied Crystallography* **46** (4), pp. 1145–1150.

VAUGHAN, G. B. M. *et al.* (2010), "The extension of ID11 for nanoscale and hierarchical characterization", in: *RisøInternational Symposium on Materials Science*, vol. 31, Roskilde, Denmark, pp. 457–476.

WELSCH, G, BOYER, R, and COLLINGS, E. W. (1993), *Materials Properties Handbook: Titanium Alloys*, ASM International.

WEST, S. S. *et al.* (2009), "Direct non-destructive observation of bulk nucleation in 30% deformed aluminum", *Scripta Materialia* **61** (9), pp. 875–878.

Chapter 7

Results II: A study of deformation twinning in a Titanium alloy by X-ray Diffraction Contrast Tomography

Abstract

A specimen of Ti-4Al deformed in-situ to about 0.7% compressive strain using neutron diffraction, and showing early stages of twinning, has been investigated in 3D using synchrotron X-ray diffraction contrast tomography (DCT). A small test piece was extracted from the compression samples containing about 400 grains of which almost 60 grains were identified to have twinned predominantly by $\{10\bar{1}2\}\ \langle\bar{1}011\rangle$ tensile twinning. In order to consider possible twin nucleation criteria, non-twinned grains of similar orientation to the twinned grains were compared against the family of twinned grains. Such comparison highlights that the twinned grain family has a grain size distribution shifted to a higher mean value than the corresponding family of grains that has not twinned. An initial neighbourhood analysis did not reveal any significant differences of the two grain families. However, complex twin chains and clusters were identified forming a slightly imperfect network demonstrating the importance of the 3D analysis. Analysis of the parent grain orientations within those chains/clusters using the Luster-Morris parameter revealed a significantly higher propensity of prismatic $\langle a\rangle$ slip transfer compared to the neighbourhood of the non-twinned grain family while no difference was observed for the likelihood of twin shear transfer. The findings suggest that grain chains/clusters with high ability of prismatic $\langle a\rangle$ slip activity and slip transfer does promote formation and clustering of twins, which is likely associated with the build up of tensile intergranular strain along the $\langle c\rangle$ axis perpendicular to the loading direction recently suggested by crystal plasticity modelling (TIMÁR and QUINTA DA FONSECA, 2014).

7.1 Introduction

Metals with a hexagonal close-packed (HCP) crystal structure, such as Ti, Mg and Zr, are known to display easy $\langle a \rangle$ slip, either on the prismatic or basal plane. In the case of titanium, the most common slip mode is $\{10\bar{1}0\}\ \langle 1\bar{2}10 \rangle$ prismatic slip while pyramidal $\langle c+a \rangle$ slip has been observed but only in small fractions (BRIDIER *et al.*, 2005; YOO, 1981; ZAEFFERER, 2003). This is due to pyramidal $\langle c+a \rangle$ slip having a critical resolved shear stress (CRSS) at room temperature about 3-5 times higher than for prismatic $\langle a \rangle$ slip (GONG and WILKINSON, 2011; LEYENS and PETERS, 2003). However, plasticity that provides shear with a $\langle c \rangle$ component is necessary to achieve significant plastic deformation in polycrystalline titanium (YOO *et al.*, 2002). This is because the $\{10\bar{1}0\}\ \langle 1\bar{2}10 \rangle$ prismatic slip mode alone is not sufficient to accommodate an arbitrary plastic strain, which requires five independent slip systems (KOCKS, 1970), according to the von Mises criterion (VON MISES, 1928).
More recent work has demonstrated that plasticity in polycrystalline materials can be accommodated by fewer independent slip systems per grain (YOO, 1981) but, in the absence of easy slip including a $\langle c \rangle$ component, twinning is commonly observed in Ti and other metals with an HCP crystal structure. This is particularly the case during compression loading (ARMSTRONG *et al.*, 1962; BEYERLEIN and TOMÉ, 2010; CAPOLUNGO and BEYERLEIN, 2008; CHRISTIAN and MAHAJAN, 1995; HULL, 1961; MCCABE *et al.*, 2009; MEYERS *et al.*, 2001; STAROSELSKY and ANAND, 2003). For example, twinning can provide the majority of plastic deformation in Mg alloys, if the starting texture promotes grains ideally orientated for twinning but not for $\{0001\}\ \langle 1\bar{2}10 \rangle$ basal slip (AGNEW *et al.*, 2003, 2006; AYDINER *et al.*, 2009; BEYERLEIN *et al.*, 2010; BHATTACHARYYA *et al.*, 2009; BROWN *et al.*, 2005; CLAUSEN *et al.*, 2008; EL KADIRI and OPPEDAL, 2010).

In hexagonal titanium, four different twinning modes have been reported (CHRISTIAN and MAHAJAN, 1995). At room temperature, the predominant twinning mode is the $\{10\bar{1}2\}\ \langle \bar{1}011 \rangle$ tensile twin (BHATTACHARYYA *et al.*, 2009; BILBY and CROCKER, 1965; BOZZOLO *et al.*, 2010; CHUN *et al.*, 2005; SALEM *et al.*, 2003; SERRA and BACON, 1996; SONG and GRAY III, 1995b; THOMPSON and MILLARD, 1952; YOO *et al.*, 2002), which corresponds to a rotation of 85° around the $\langle 11\bar{2}0 \rangle$ axis. In some cases, this twin mode has been observed to result in almost complete grain reorientation after only modest levels of strain (BARNETT *et al.*, 2008; CAPOLUNGO *et al.*, 2009; CHICHILI *et al.*, 1998; COGHE *et al.*, 2012; LAHAIE *et al.*, 1992; PRAKASH *et al.*, 2010; PREUSS *et al.*, 2010).

Statistical analysis of twin nucleation in hexagonal metals has suggested that twin activation does not necessary follow the traditional Schmid law, meaning that in some

cases the twin variant that forms is not the one with the highest Schmid factor (BEYERLEIN *et al.*, 2010; CAPOLUNGO *et al.*, 2009; TOMÉ *et al.*, 2011). However, more recent work has demonstrated that once the local stress state is taken into account by the use of a crystal plasticity model, the twin variant selection follows the stress criterion (HONNIBALL *et al.*, 2015). The applied stress is expected to play an important role in twin nucleation, as discussed in YOO (1981) and MEYERS *et al.* (2001). In general, they state that the applied stress is proportional to the number of twins per unit of observed area, as found similarly in CHICHILI *et al.* (1998). This applied stress is an average resolved stress and is a rather crude approximation. To understand the increasing density of twins with increasing levels of applied stress there can be two scenarios: (i) the stress is considered as uniform field applied on an array of potential twin nucleation sites, in which the increasing levels of applied stress allow more sites to be activated; (ii) the critical stress for nucleation is met only at the most potent of the stress concentrations. When increasing the applied stress, more of the available stress concentrators provide stresses that attain the critical level. In most of the cases, the reality is most likely to correspond to a combination of these two scenarios.

Localised slip resulting in dislocation pile up at grain boundaries has also been found to play a role in twin nucleation, which has been recently investigated in commercially pure titanium grade 1 (WANG *et al.*, 2010a,b, 2011, 2013), together with the free surface relaxation and non-Schmid stress effects on twin nucleation (BARRETT *et al.*, 2012). The slip activity in a grain well aligned for prismatic $\langle a \rangle$ slip leading to twin nucleation in a neighbouring grain not well aligned for $\langle a \rangle$ type slip was shown to be significant when a tensile stress state was created (WANG *et al.*, 2010b). Twin to twin shear transfer across grain boundaries has also been observed, particularly in boundaries with misorientations lower than 30° (WANG *et al.*, 2010a). These correlations were quantified using the slip transfer parameter *m'*, which was first introduced by LUSTER and MORRIS (1995) based on observations by CLARK *et al.* (1992) and are described in section 7.2.4.

Numerous deformation studies on metals with a HCP crystal structure have used in-situ loading in combination with neutron diffraction to study intergranular strain evolution of various grain families (CAI *et al.*, 2009; DAYMOND and PRIESMEYER, 2002; DAYMOND *et al.*, 2007; KERR *et al.*, 2010; KORSUNSKY *et al.*, 2004; XU *et al.*, 2008). When carrying out compression loading such approach also enables easy detection of $\{10\bar{1}2\}\ \langle\bar{1}011\rangle$ twinning as the $\langle c \rangle$ axis tends to rotate into the loading direction, which is monitored by measuring the $\{0002\}$ integrated peak intensity. This method is particularly useful to compare twin activities and enables one to capture the moment of early twin formation.

Considering the importance of neighbourhood in relation of twinning, several synchrotron X-ray techniques might be of particular interest as they enable 3D analysis of polycrystalline materials non-destructively. Examples here are the differential aperture X-ray microscopy (DAXM) approach that was developed at the advanced photon source (APS) by a group from the Oak Ridge National Laboratory in USA (ICE and BARABASH, 2007; LARSON *et al.*, 2002; LIU and DUPONT, 2004; LIU *et al.*, 2005) and far-field 3D X-ray diffraction (3DXRD), which was first developed at Risø DTU in Denmark (LAURIDSEN *et al.*, 2001; POULSEN, 2004, 2012; POULSEN *et al.*, 1997, 2001).
X-ray DCT (LUDWIG *et al.*, 2009b; REISCHIG *et al.*, 2013) is a variant of the 3DXRD microscopy technique enabling simultaneous reconstruction of the 3D microstructure (shape and orientation) in suitable polycrystalline materials, along with the absorption map of the specimen. The X-ray DCT methodology provides access to the 3D shape, orientation and elastic strain state of the individual grains from polycrystalline materials fulfilling some conditions in terms of grain size and intergranular orientation spread.

In the present work the onset of twinning is studied in a binary Ti-4Al alloy, using two different diffraction techniques, neutron diffraction and X-ray DCT. Samples were first compressed and the activation of $\{10\bar{1}2\}\ \langle\bar{1}011\rangle$ tensile twins was followed in-situ by means of neutron diffraction.
Subsequently, small samples were extracted from the deformed samples (about 0.04% of the initial sample volume) at selected applied strains, and characterised using the X-ray DCT methodology to reveal the 3D grain structure, allowing a grain-by-grain study of the shape and location of twins. A statistical analysis was carried in which the parent grains of twins where grouped together and compared with similarly orientated grains that had not twinned. Comparisons were carried out regarding grain size, the general Schmid factor *m* (based on an uniaxial stress) (GUO *et al.*, 2014a) and slip transfer parameter *m'* (BIELER *et al.*, 2014a,b; GUO *et al.*, 2014b; WANG *et al.*, 2010b) across the grain boundaries. Finally, a search for possible clustering of twins was carried out and cluster neighbourhoods were again analysed.

7.2 Experimental procedure

7.2.1 Material preparation

For the purpose of this research, 200 g binary Ti-4Al (i.e. 4wt.%) alloy buttons were double melted in a tungsten arc furnace under inert gas atmosphere. This was followed by beta forging at 1100 °C at the TIMET - Savoie research facility in

Table 7.1: Chemical composition of Ti-4Al:

Al		C	N_2	O_2	Ti
3.9 wt.%	6.7 at.%	50 ppm	23 ppm	778 ppm	bal.

Witton, UK. The measured chemical composition of the alloy is given in table 7.1. Subsequently, the buttons were cross-rolled in bar shape ($14 \times 14 \times 260$ mm) on a "2 high Robertson mill" (WHA Robertson & Co Ltd) at 870 °C followed by a recrystallization (RX) heat treatment at 993 °C (30 °C below the beta transus temperature) in a tube furnace under Argon shielding for 5 hours followed by air-cooling. The lattice parameters and the c/a ratio were determined at the neutron spallation source ISIS, Chilton, UK. They are $\langle a \rangle$ = 2.935 Å and $\langle c \rangle$ = 4.678 Å giving a c/a ratio of around 1.5938 (FITZNER *et al.*, 2014). The average grain size of the studied samples is 73 µm, which was measured by using the linear intercept method (FITZNER *et al.*, 2014). The {0002} pole figure and the initial microstructure of the Ti-4Al raw material used in this analysis in shown in figure 7.1.

Three samples with a diameter of 5 mm and length of 12.35 mm each were cut by electro-discharge machining (EDM) with the cylinder axis parallel to the original rolling direction (RD). The texture of the material is such that the $\langle c \rangle$ axes of the grains tend to be oriented perpendicular to the cylinder axis, which promotes tensile twinning during compression loading as the $\langle c \rangle$ axis is strained in tension.

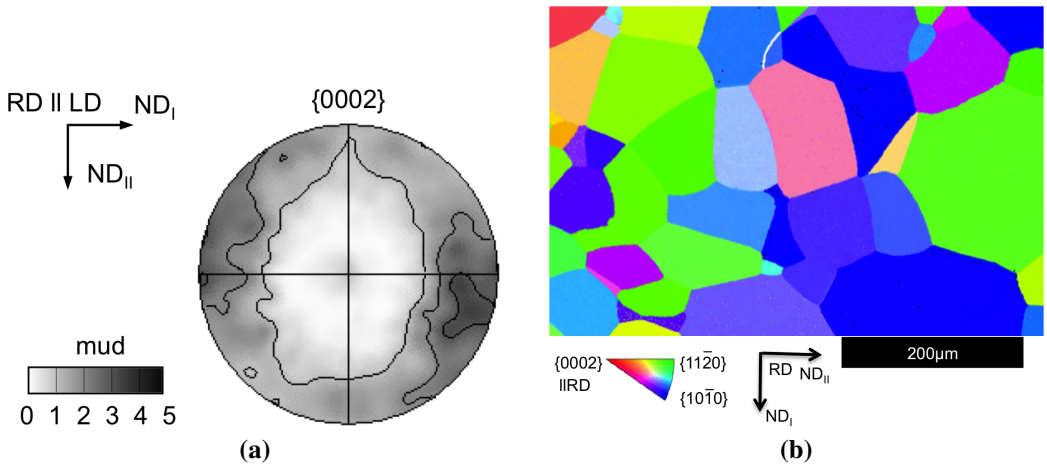

Figure 7.1: Initial microstructure of the material represented in terms of (a) {0002} pole figure and (b) grain orientation map recorded by EBSD.

7.2.2 In-situ loading using neutron diffraction

In the first part of the experiment, each sample was placed in a stress-rig based on the Strain Analyser for Large and Small scale engineering Applications (SALSA) beam line at the Institut Laue-Langevin (ILL) in Grenoble, France (HUGHES *et al.*, 2006; PIRLING *et al.*, 2006). It uses a thermal neutron beam with wavelength $\lambda = 1.62$ Å corresponding to a two-theta angle of 40.5° for the $\{0002\}$ reflection for Ti-Al alloy, which was measured in the loading direction. The two-dimensional position sensitive micro-strip detector has an active area of 80×80 mm^2 with 256×256 channels and was positioned in a way that the scattering vector $\mathbf{q}$ of the $\{0002\}$ reflection was parallel to the loading direction. The angle covered by each channel is 0.02° at a sample-detector distance of one metre. The 2D data were integrated to produce a one-dimensional diffraction peak profile covering 5°, in which the $\{0002\}$ and $\{10\bar{1}1\}$ peaks are visible, and fitted using a Gaussian function. Because of the poor neutron scattering properties of Ti the counting time per load step was 30 minutes in order to obtain a fittable $\{0002\}$ reflection. As the main concern was the plastic strain induced at each load step, the sample was placed in displacement control while acquiring the neutron diffraction data in order to avoid cold creep. The load increments were carried out using a strain rate of 0.004 s^{-1}.
Initially, a sample was deformed reaching a plasticity of about 6.4% and the evolution of the integrated intensity of the $\{0002\}$ reflection was monitored. Based on the initial observation, two more samples were deformed up to the onset of deformation twinning and cut subsequently by EDM to extract small cylindrical samples of 400 µm diameter and 3 mm length for the X-ray DCT measurement. These small samples share the same cylinder axis as the sample from which they were extracted.

7.2.3 Diffraction Contrast Tomography (DCT)

The second part of the experiment was performed at the beam line ID11 of the European Synchrotron Radiation Facility (ESRF) (Grenoble, France), using a monochromatic beam produced by a bent Si (111) Laue-Laue double-crystal monochromator (40 keV, wavelength $\lambda = 0.309$ Å, relative bandwidth $\Delta\lambda/\lambda \approx 10^{-3}$). The experimental setup is represented schematically in figure 7.2. A high resolution detector system consisting of a Fast Readout Low Noise (FReLoN) charge-coupled device (CCD) camera (LABICHE *et al.*, 2007) equipped with a scintillator screen and visible light microscope optic was used for this experiment, positioned normal to the incident beam, about 5 mm downstream from the sample. The detector has an array of 2048×2048 pixels with an effective pixel size of 1.4 µm/pixel and an active area of 2.87×2.87 mm^2. An absorber was inserted between the sample and the detector to attenuate the transmitted beam without affecting the diffracted beams. This allows the

integration time per image to be increased in order to improve the intensity particularly of weak diffraction spots (i.e. the ones related to this twin lamellae).

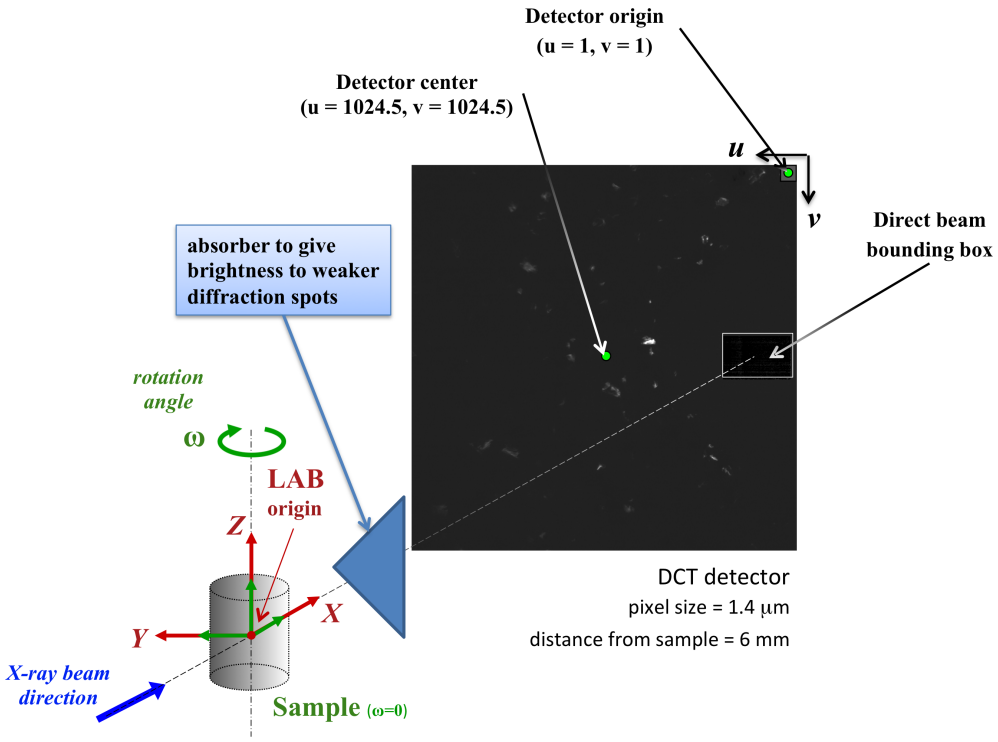

Figure 7.2: X-ray DCT experimental setup used at the beam line ID11 of the ESRF, Grenoble, France. The coordinate system is defined such that the X-ray beam is along the laboratory X direction, the Z direction is vertical, upwards from the origin and the Y direction is consistent with a right-handed system. The rotation axis of the sample is right-handed and parallel with the z-axis. The sample coordinate system rotates around the z-axis and it coincides with the laboratory coordinate system when the rotation angle ω is equal to zero.

7.2.4 Data analysis

The standard X-ray DCT analysis methodology has previously been described in detail (LUDWIG *et al.*, 2009b; REISCHIG *et al.*, 2013). A series of images (typically 3600–7200) are recorded while the sample is rotated through 360°. The background is subtracted from the images, leaving only the diffraction spot images. These are segmented, and metadata are recorded that describe the spots. The geometry of diffraction events is extracted using a Friedel pair geometry, based on identifying pairs of spots arising from the scattering vector and same grain, offset by 180° rotation of the sample. The Friedel pair construction reveals the diffraction angles and scattering vector associated with the diffraction event, and a path through the sample on which the grain must lie. Grain positions and orientations are identified by searching for

Friedel pairs that are spatially and crystallographically consistent. The grain shapes are then reconstructed using a simultaneous iterative reconstruction technique (SIRT) algorithm, using the diffraction spot images as grain projections. Subsequently, the grains shapes are assembled to produce a 3D grain map. Any overlapping or unassigned spaces in the 3D map are filled using a morphological dilation.

Twinned microstructures present a significant challenge for the DCT methodology. The plastic deformation associated with the applied strain tends to introduce mosaicity in the crystal lattice of the grains, blurring and distorting the diffraction spot shapes. In addition, the mechanical twins formed during compression have a characteristic thin plate-like shape and a small volume, particularly at the onset of twinning, which poses difficulties for several reasons. The low volume means that the spot intensities are generally low, and difficult to segment from the background. The high aspect ratio means that different diffraction spots arising from a twin may have very different shapes, depending on the diffracted beam direction (projection direction).

As a result, the number of reflections assigned to parents and twins can vary a lot, with the one for twins being typically significantly smaller than the one for parents. For the experimental conditions used in this study typical numbers of assigned reflections were around 10-15 for twins, compared to 60-70 for the parent grains. The integrated diffraction spots were assembled into a stack of projections (sinogram) and stored together with the parameters defining the projection geometry.

An iterative tomographic reconstruction process was performed using an implementation of the SIRT algorithm available in the All Scale Tomographic Reconstruction Antwerp (ASTRA) tomographic toolbox (PALENSTIJN *et al.*, 2011, 2013). The process assumes that all grains can be indexed in the volume and remaining gaps in this initial grain map are removed by dilating the existing grains until a space filling grain map is obtained.

X-ray DCT data were acquired for a couple of samples compressed to about 0.7% and to 1.5% plastic strain respectively. An absolute measure of the illuminated sample volume (V_{sample} = 0.0757 mm^3) was obtained from the tomographic reconstruction of the transmission images recorded during the scan. The sample strained to 1.5% displayed significant reconstruction artefacts owing to limitations of the 3D analysis code, based on a single (grain average) orientation in the iterative algebraic reconstruction process and has been omitted here. However, the volume of the sample deformed to 0.7% plastic strain was reconstructed successfully using the DCT code (`http://sourceforge.net/projects/dct/`). In order to identify the expected $\{10\bar{1}2\}\ \langle\bar{1}011\rangle$ tensile twins an automated search was carried out to identify grains overlapping in space and fulfilling the orientation requirements of any of the twinning

modes for hexagonal titanium and then the $\{10\bar{1}2\}\ \langle\bar{1}011\rangle$ tensile twinning mode was selected (the angle between the $\langle c\rangle$ axis of two grains must be 85° and the rotation axis parallel to one of the six $\langle 11\bar{2}0\rangle$ directions). The available slip systems and twin systems for HCP materials are listed in table 7.2.

Table 7.2: Deformation slip and twinning modes in hexagonal titanium (BOZZOLO *et al.*, 2010; CHRISTIAN and MAHAJAN, 1995; KOCKS *et al.*, 1998; WANG *et al.*, 2010b; YOO, 1981; ZAEFFERER, 2003). For the deformation twinning modes we are using the $K-\eta$ notation adopted by BILBY and CROCKER (1965, p. 242).

Slip mode	**plane**	**direction**	**multiplicity**	
Basal $\langle a\rangle$	$\{0001\}$	$\langle 11\bar{2}0\rangle$	3	
Prismatic $\langle a\rangle$	$\{10\bar{1}0\}$	$\langle 11\bar{2}0\rangle$	3	
Pyramidal $\langle a\rangle$	$\{10\bar{1}1\}$	$\langle 11\bar{2}0\rangle$	6	
Pyramidal $\langle c+a\rangle$ 1st ord	$\{10\bar{1}1\}$	$\langle 11\bar{2}3\rangle$	12	
Pyramidal $\langle c+a\rangle$ 2nd ord	$\{11\bar{2}2\}$	$\langle 11\bar{2}3\rangle$	6	
Twinning mode	K_1	η_1	**angle – axis**	**shear strain**
Tensile Type I	$\{10\bar{1}2\}$	$\langle\bar{1}011\rangle$	85° $\langle 11\bar{2}0\rangle$	0.171
Tensile Type II	$\{11\bar{2}1\}$	$\langle\bar{1}\bar{1}26\rangle$	35° $\langle 1\bar{1}00\rangle$	0.629
Compression Type I	$\{11\bar{2}2\}$	$\langle 11\bar{2}\bar{3}\rangle$	65° $\langle\bar{1}100\rangle$	0.221
Compression Type II	$\{10\bar{1}1\}$	$\langle\bar{1}012\rangle$	54° $\langle\bar{1}2\bar{1}0\rangle$	0.101

One particular point of interest in the analysis of the volume was the Luster-Morris parameter introduced in section 7.1, which can be used to describe relative alignment of neighbouring grains in respect of certain planes and directions. It is defined by equation (7.1) and illustrated schematically in figure 7.3.

$$m' = \cos\kappa\cos\psi \tag{7.1}$$

where ψ is the angle between two plane normals and κ is the angle between the associated slip/shear directions. Hence, *m'* = 1 indicates perfect alignment of two neighbouring grains for easy slip transfer across the grain boundary. In the present work the Luster-Morris parameter was considered for neighbouring grains aligned for prismatic to prismatic slip transfer and $\{10\bar{1}2\}\ \langle\bar{1}011\rangle$ twinning shear to $\{10\bar{1}2\}\ \langle\bar{1}011\rangle$ twinning shear transfer between neighbouring grains.

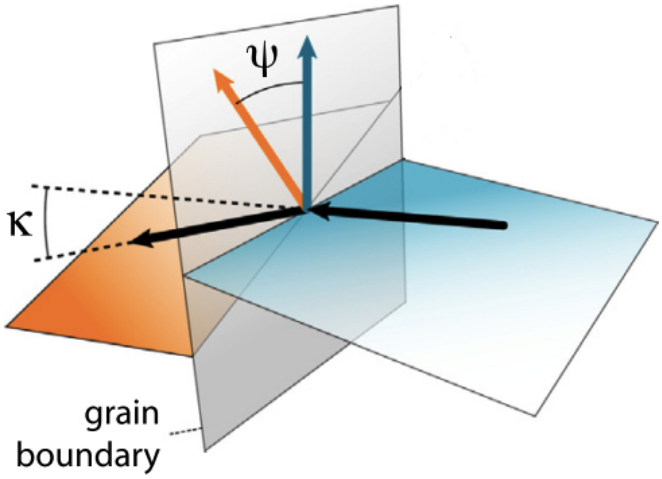

Figure 7.3: Schematic description of the Luster-Morris parameter showing horizontal (orange and blue) planes (slip or twinning planes) on either side of the boundary. ψ is the angle between plane normals and κ is the angle between specific directions (slip or twin shear) (BIELER *et al.*, 2014a).

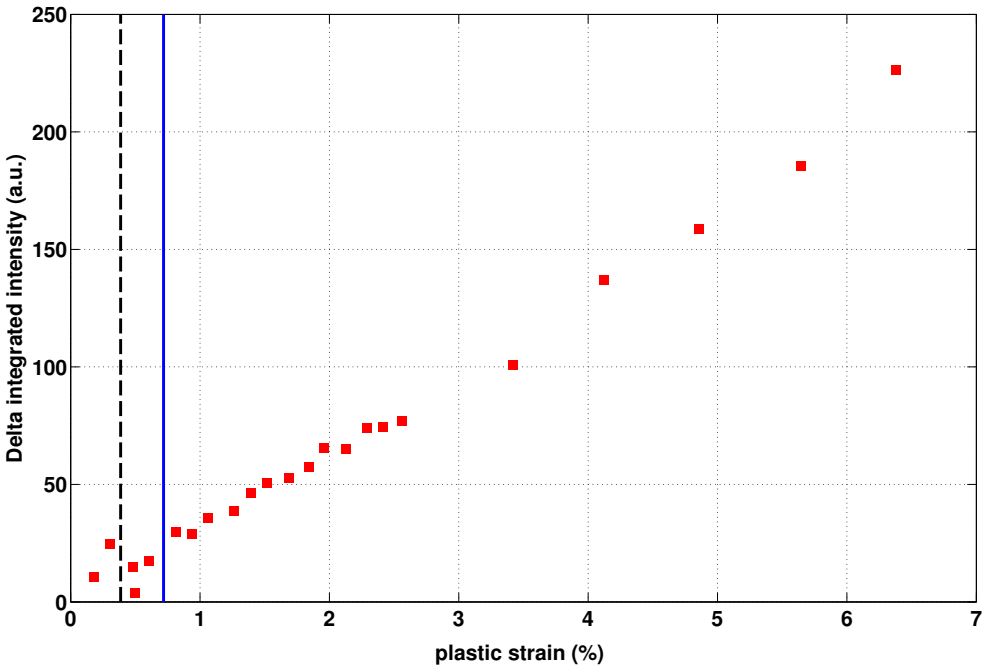

Figure 7.4: Change of {0002} integrated intensity as a function of plastic strain recorded during in-situ loading on SALSA, at the ILL, Grenoble. Early signs of twinning by slight increase of intensity can be seen just below 1%.

7.3 Results

Figure 7.4 displays the change of integrated intensity of the {0002} peak relative to the initial value monitored in the loading direction as a function of plastic strain. It can be seen that the integrated intensity does increase from about 0.4% plastic strain

(dashed line), which is indicative of $\{10\bar{1}2\}\ \langle\bar{1}011\rangle$ tensile twinning. Further, based on the evolution of the integrated intensity as a function of plastic strain, twinning activity appears constant over the tested range. Based on this observation, a second and third sample were compressed in-situ to 0.7% (blue line) and 1.5% plastic strain and neutron diffraction data confirmed early signs of twinning in both cases.

Both deformed samples were scanned using X-ray DCT but so far only the volume of the sample strained to 0.7% plastic strain has been reconstructed successfully. The reconstructed volume, together with the volume of the twinned grains only, is presented in figures 7.5(a) and 7.5(b). In both figures grains are coloured according to the inverse pole figure scheme with the sample loaded along (0001), figure 7.5(c).

The reconstructed grain volumes were dilated using a mask determined from absorption tomography in order to fill the empty spaces between the grains (a single grain dilation of maximum 7 μm has been used). The reconstructed sample volume, resulting from concatenation of 3 DCT scans, has resulted in a height of 0.77 mm and a volume of about 0.0757 mm^3. The total number of grains in the studied volume is 402, out of which 58 have twinned (some of them containing multiple twins) and 67 of the 70 indexed twins have been identified as $\{10\bar{1}2\}\ \langle\bar{1}011\rangle$ tensile twins (≈17% with respect to the total number of indexed grains).

The crystallographic orientations of the 402 grains are presented in form of an inverse pole figure map in figure 7.6(a), distinguishing between twinned grains, twins and grains that did not twin. It can be stated that the twinned grains (squares) are distributed uniformly in the region between $(10\bar{1}0)$ and $(2\bar{1}\bar{1}0)$ poles. Figure 7.6(a) also highlights that the studied volume contains plenty of grains without twins that are similarly orientated to the grains that have twinned. In order to compare twinned and non-twinned grains in a meaningful way, each twinned grain was paired with the most similarly orientated grain that had not twinned, as shown in figure 7.6(b). This was achieved by calculating a distance in the orientation space between individual twinned grains and non-twinned grains. The orientation space is defined by two angles, the azimuthal angle ϕ and the polar angle ψ, which both describe the inverse pole figure. In order to consider a non-twinned grain of similar crystallographic orientation to a twinned grain the distance d between a twinned grain with coordinates (ϕ_i, ψ_i) and a grain that had not twinned with coordinates (ϕ, ψ) had to satisfy:

$$d = \sqrt{(\phi_i - \phi)^2 + (\psi_i - \psi)^2} < 1.5^\circ \tag{7.2}$$

This tight criterion was chosen to ensure that single solutions could be found for each twinned grain. Following this procedure, 43 similarly oriented grains were found corresponding to twinned grains over a total of 58 twinned grains. Hence, 15% of the twinned grains could not be paired with a non-twinned grain.

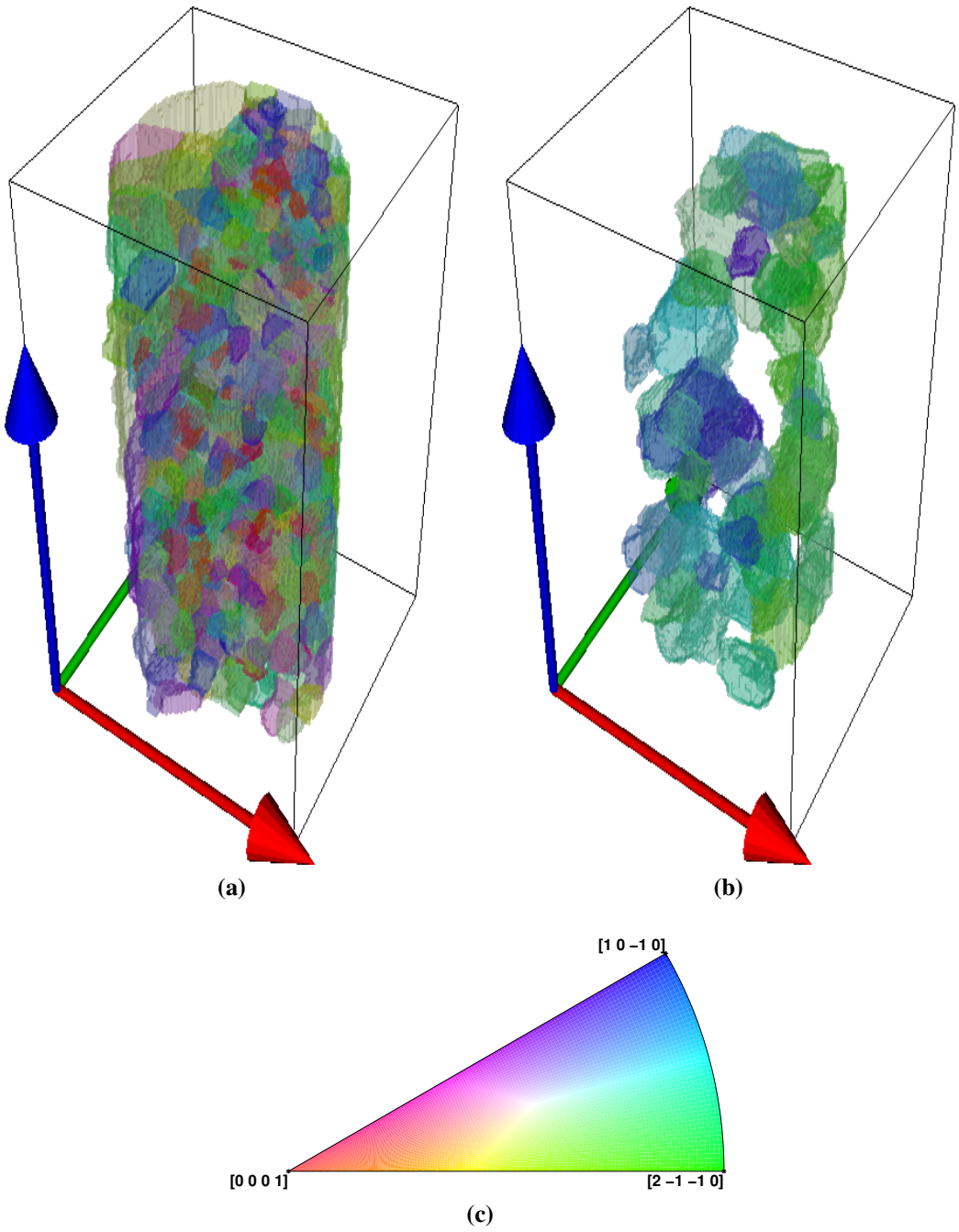

Figure 7.5: 3D grain map of the reconstructed sample volume coloured according to the IPF colour code for HCP materials (c). Full 3D grain maps of (a) all the grains and (b) only twinned grains are displayed.

The analysis of the twinned grains revealed that 96% of the characterised deformation twins in the sample were $\{10\bar{1}2\}\ \langle\bar{1}011\rangle$ tensile twins, i.e. 67 $\{10\bar{1}2\}\ \langle\bar{1}011\rangle$ tensile twins, one $\{11\bar{2}1\}\ \langle\bar{1}\bar{1}26\rangle$ tensile twin and two $\{11\bar{2}2\}\ \langle11\bar{2}\bar{3}\rangle$ compression twins. The distribution of the misorientation angle between the twinned grains and the $\{10\bar{1}2\}\ \langle\bar{1}011\rangle$ tensile twins is shown in figure 7.7 showing an average misorientation angle of 85.3°, which is 0.3° above the theoretical value for this type of twin in pure

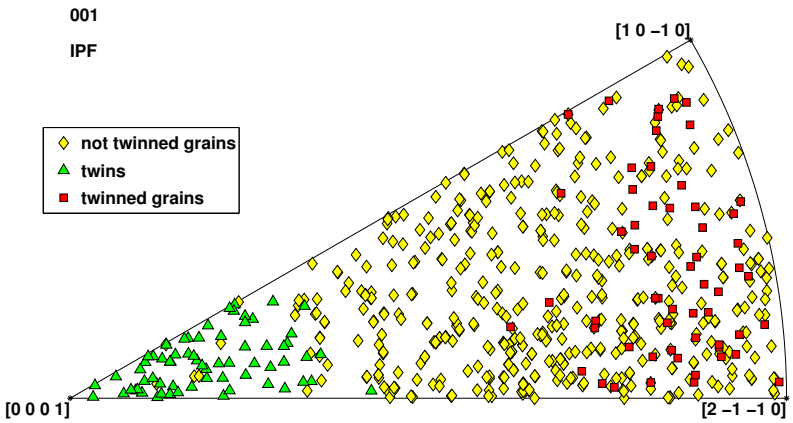

(a)

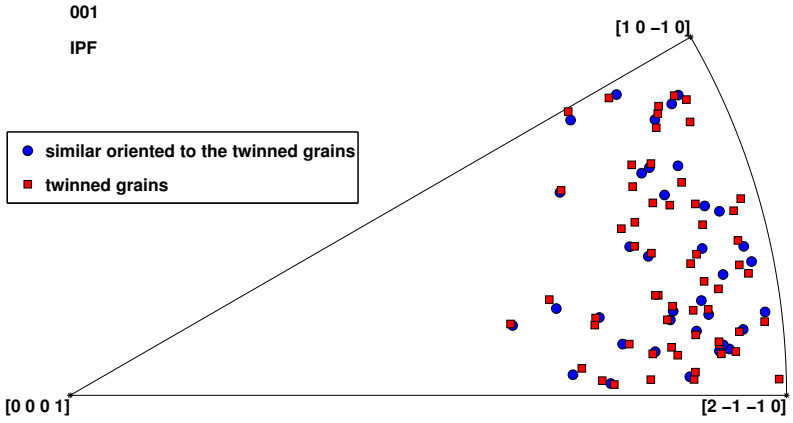

(b)

Figure 7.6: Inverse Pole Figure (IPF) representation of the grain orientations with respect to the sample loading direction (001). In (a), all grain and twin are shown while in (b) only the two grain families, i.e. the twinned grains and their corresponding non-twinned similar oriented grains are shown.

Ti, table 7.2.
In a first step of comparing the twinned grain family with the one that had not twinned but was of comparable crystallographic orientation, figure 7.8 compares the number of grain neighbours for the two different families in form of a cumulative plot.
This analysis immediately highlights that the twinned grains have in average a significantly higher number of grain neighbours than the related grain family that has not twinned yet. Following on from this observation, the grain volume for each grain has been computed directly from the reconstructed sample, before and after dilation, as shown in figures 7.9(a) and 7.9(b), respectively. It should be noted that the volume of a twinned grain combines the parent grain and the twin volume.

It can be noted that the difference of grain volume before and after dilation is not significant. Most importantly, the volume dilation does not appear to create artefacts justifying the use of the dilated volume for each grain as a measurement of the grain

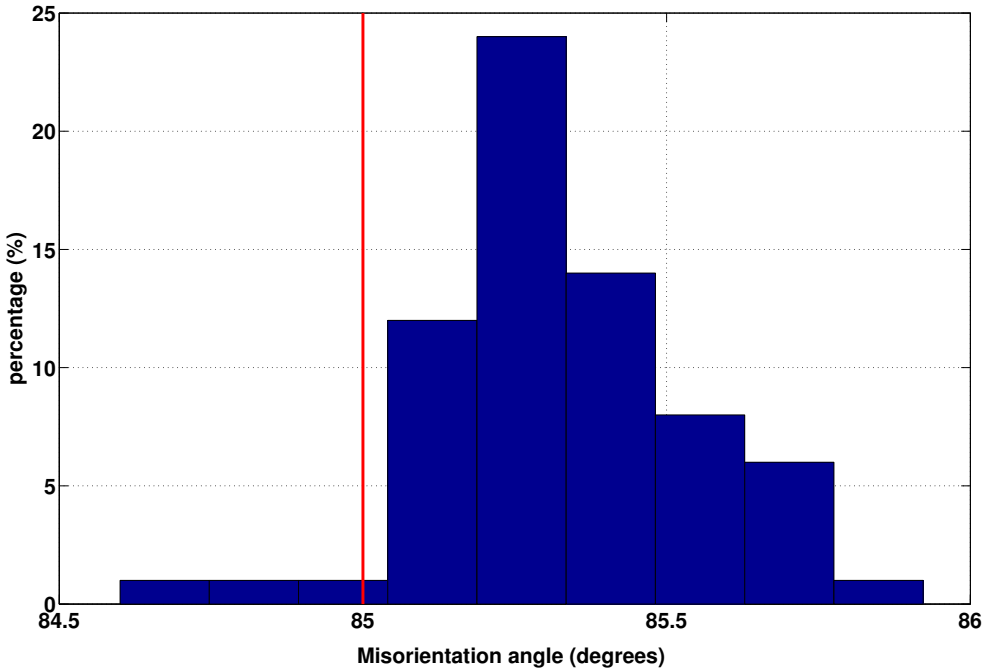

Figure 7.7: Misorientation angle between the twinned parent grains and their tensile twins. The red line indicates the theoretical value of the misorientation angle (85°) for $\{10\bar{1}2\}\ \langle\bar{1}011\rangle$ tensile twin.

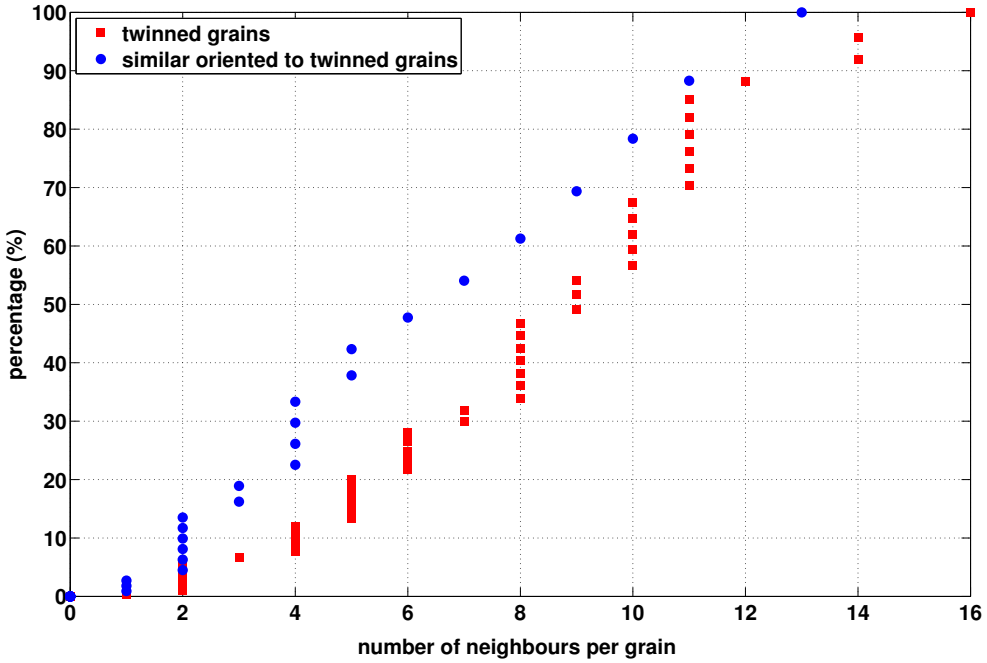

Figure 7.8: Cumulative plot of the number of neighbours per grain for the twinned grains (squares) and the similarly oriented grains to the twinned grains (circles). The neighbours are computed from the reconstructed and dilated sample volume (shown in figure 7.5(a)) and the surface grains have been removed from this calculation, in order to avoid any bias in the data.

volume. Consequently, figure 7.9(b) clearly demonstrates that the grain volume distribution of the twinned grain family is shifted to a larger volume than the grains without twins. Hence, the grain volume analysis suggests that during the very early stage of plasticity grain size is an important factor for twin nucleation and growth.

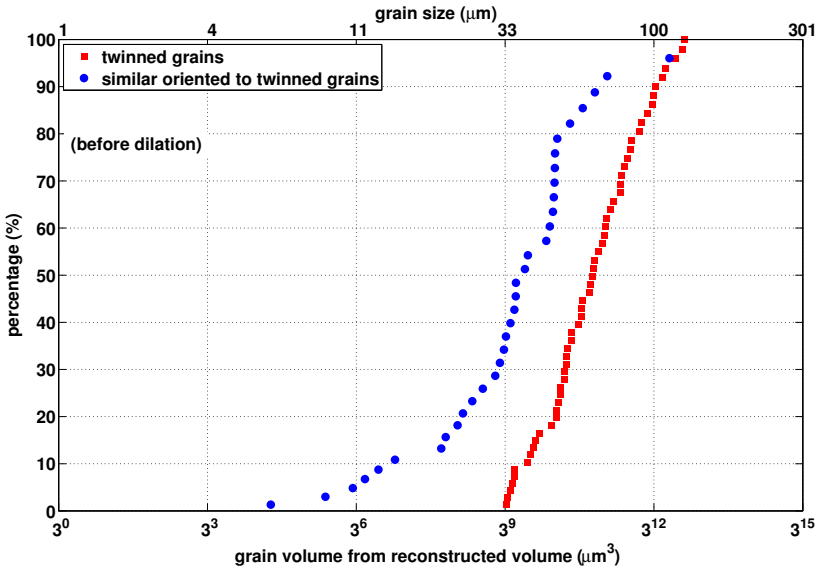

(a)

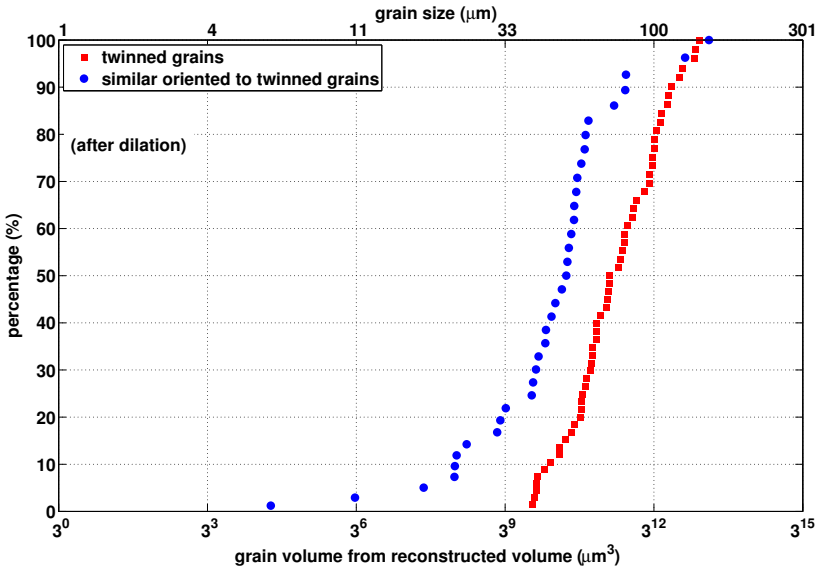

(b)

Figure 7.9: Cumulative plot of the grain volume for the twinned grains (squares) and the similarly oriented grains to the twinned grains (circles), calculated from the reconstructed volume: (a) before dilation and (b) after dilation. The grain size is the diameter of the equivalent sphere corresponding to the grain volume and it is shown in the upper horizontal axis. A log scale in base 3 is used for both the horizontal axes.

During the next stage, the grain neighbourhood of the two grain families was investigated in greater detail. First of all it is important to note that during

compression loading and considering the starting texture, the grains that are most likely to twin are also well aligned for deformation by prismatic $\langle a \rangle$ slip. Hence, a neighbourhood that displays a high Schmid factor of similar orientation is more likely to allow the twinning grain to build up a high dislocation density and large intergranular strains, i.e. large tensile strains along the $\langle c \rangle$ axis perpendicular to the compressive loading axis. Both these aspects could be considered to promote $\{10\bar{1}2\}$ $\langle\bar{1}011\rangle$ twin nucleation. Figure 7.10(a) plots the prismatic $\langle a \rangle$ slip Schmid factor distribution computed for the grain neighbourhood of both grain families. It can be seen that both grain families display a high fraction of grain neighbours well aligned for prismatic $\langle a \rangle$ slip but there is no noticeable difference in Schmid factor distribution between the two.
In addition, figure 7.10(b) exhibits the distribution of the transfer parameter *m'* for prismatic $\langle a \rangle$ slip computed from the neighbourhood of the two different grain families. It is noticeable that both grain families display a wide distribution of m but the analysis again does not yield a clear differentiation between the twinned grains and the grains that have not twinned yet after 0.7% plastic deformation.

It is also potentially important to consider the ability of the grain neighbourhood to accommodate the shear strain generated by a twin. This might be best accommodated by twin nucleation in a neighbouring grain and hence figure 7.11(a) plots the Schmid factor distribution for $\{10\bar{1}2\}$ $\langle\bar{1}011\rangle$ tensile twinning of the neighbourhood assuming a stress criterion for twinning while the transfer parameter m' for $\{10\bar{1}2\}$ $\langle\bar{1}011\rangle$ tensile twins is plotted in figure 7.11(b). Again, both neighbourhoods display a high fraction of neighbouring grains well aligned for $\{10\bar{1}2\}$ $\langle\bar{1}011\rangle$ tensile twinning but also an almost identical distribution. Further, both grain families show a relatively sharp distribution of very high m' values indicating that the grain neighbourhood is well aligned for shear transfer by $\{10\bar{1}2\}$ $\langle\bar{1}011\rangle$ tensile twinning. However, no distinction can be drawn between the two different grain families.
As a next step, a more detailed analysis of the position of the twinned grains was carried out within the studied volume with the purpose of identifying potential chains or clusters of twinned grains and perform a neighbourhood analysis on these.
Figure 7.5(b) had already indicated that twinned grains are not isolated, but they form chains/clusters very close to each other. The individual twin chains/clusters are rendered in figure 7.12(a) a using a different colour for each chain.

For clarity, figures 7.12(b)–7.12(f) also highlight each individual chain. As this search indicated predominantly clusters rather than chains, the exact identification presented some difficulties. In this case a given twinned grain can have more than two neighbouring twinned grains, which makes the rendering of the neighbourhood more difficult. Each cluster was defined by starting from a grain with only one neighbouring

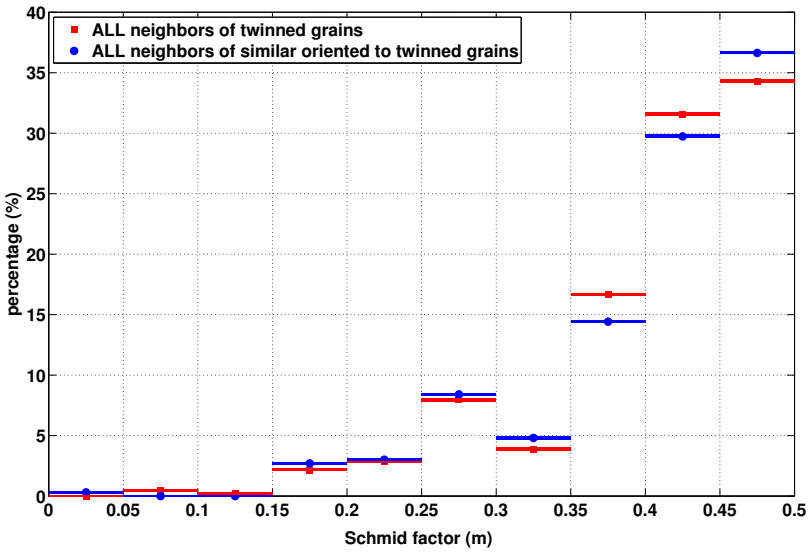

(a)

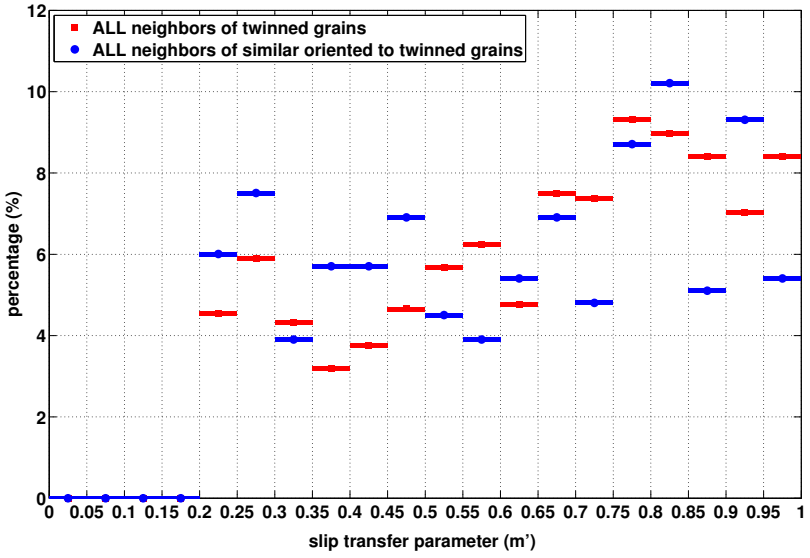

(b)

Figure 7.10: (a) Schmid factor *m* for prismatic slip and (b) slip transfer parameter *m'* for prismatic slip to prismatic slip has been calculated for all the neighbours of the twinned grains (squares) and the similarly oriented grains to the twinned grains (circles).

twinned grain and the rendering did proceed by choosing the grain with the lowest number of neighbours among the neighbouring twinned grains, in order to simplify the choice as much as possible. As such search needs to be carried out in 3D space the calculation and the identification of the clusters was very computing intensive. Among 58 twinned grains, 5 different clusters/chains were identified with the shortest cluster consisting of 6 twinned grains and the largest cluster containing 16 grains. In general, the twins linked up well within a cluster as demonstrated in

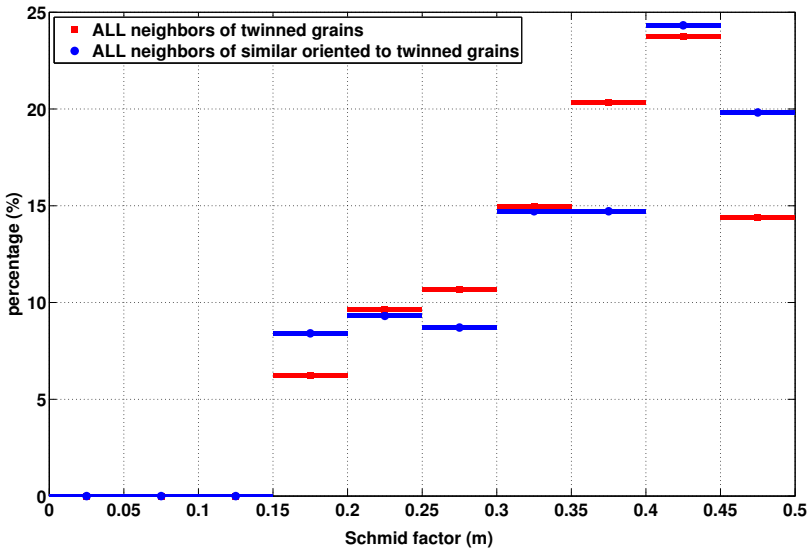

(a)

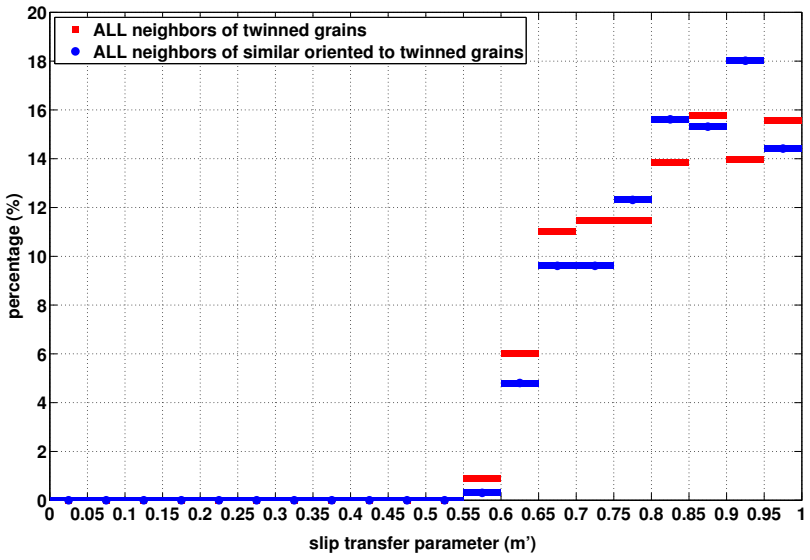

(b)

Figure 7.11: Distribution of (a) Schmid factor m for $\{10\bar{1}2\}\ \langle\bar{1}011\rangle$ tensile twinning of the neighbourhood and (b) slip transfer parameter m for $\{10\bar{1}2\}\ \langle\bar{1}011\rangle$ tensile twinning of the parent grain to $\{10\bar{1}2\}\ \langle\bar{1}011\rangle$ tensile twinning a neighbouring grain calculated for both grain families.

figures 7.12(b)–7.12(f). In addition, only one isolated twinned grain was identified. It is also worth noting that a careful analysis of all the clusters/chains revealed that they seem to have formed a slightly imperfect network, i.e. only small gaps are present between the clusters/chains. Finally, the transfer parameters for prismatic $\langle a\rangle$ slip and $\{10\bar{1}2\}\ \langle\bar{1}011\rangle$ tensile twinning were computed along those chains/clusters. The variation of these two transfer parameters is plotted along the longest chain consisting of 16 grains/twins in figure 7.13. It can be seen that m' for $\{10\bar{1}2\}\ \langle\bar{1}011\rangle$ tensile

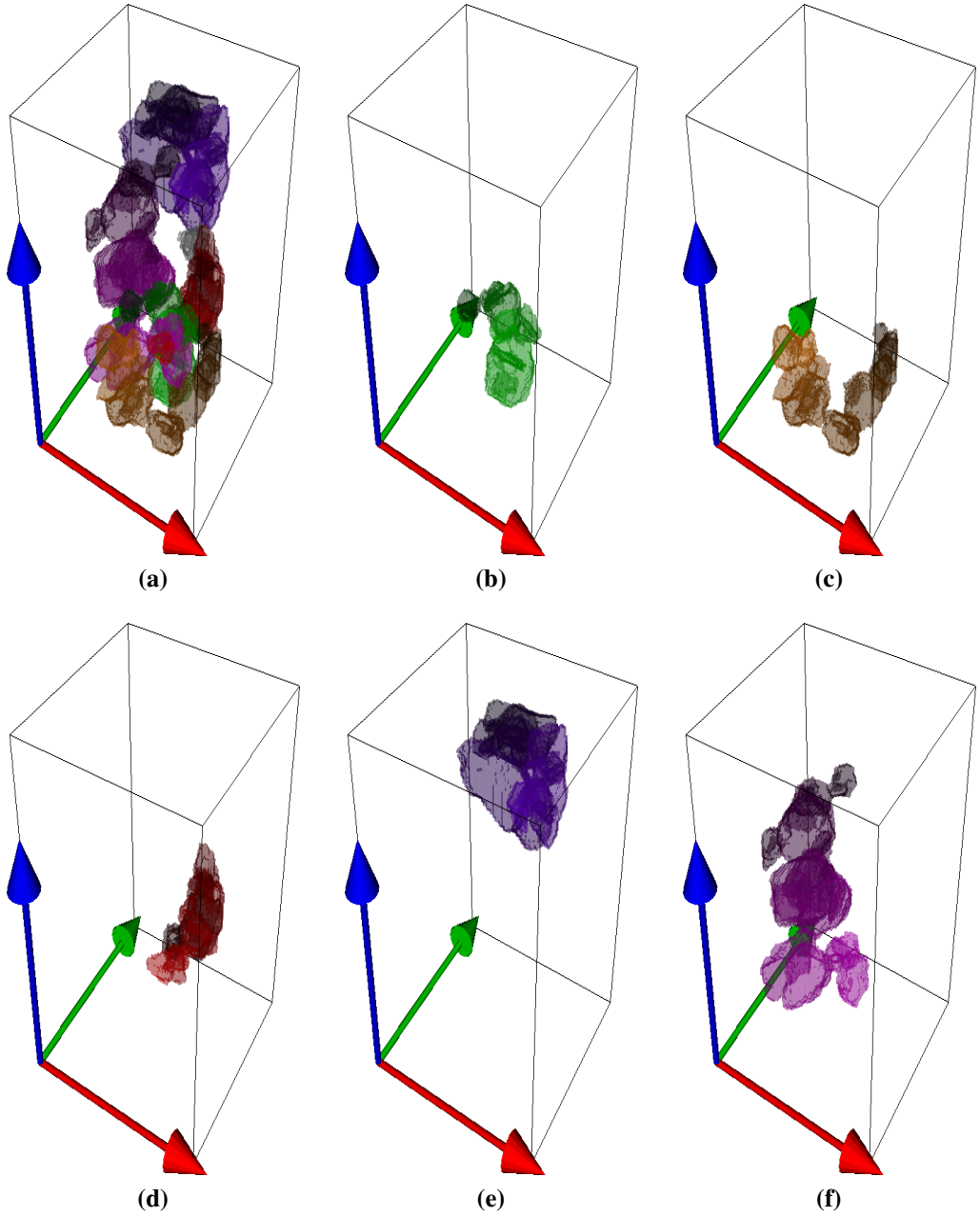

Figure 7.12: (a) 3D rendering of the identified chains of twinned grains. (b)–(f) Each chain is visualised with a different colour and displayed in a separate figure. The darkest colour has been assigned to the first grain of the chain.

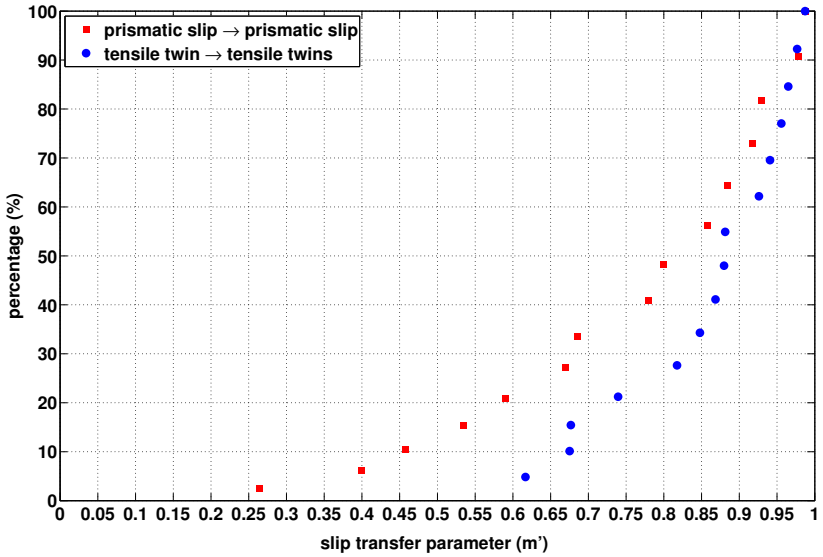

Figure 7.13: Slip transfer parameter *m'* along the longest chain for prismatic slip to prismatic slip (squares) and for tensile twin to tensile twin (circles).

twinning within the chain never drops below 0.6 while the transfer coefficient for prismatic $\langle a \rangle$ slip within the chain shows a few neighbours with a value around 0.25. The calculated values for the two transfer parameters and the two Schmid factors along each chain/cluster are reported in tables A.1–A.5.

Figures 7.14(a) and 7.14(b) display the distributions of both transfer coefficients computed from within the chains/clusters and compare them with the previously computed transfer coefficient between the twin-free grain family and their neighbourhood. It should be noted that the main difference here to figures 7.10(b) and 7.11(b) for the twinned grains is that now only the transfer coefficients within clusters/chains are calculated whereas before simply all neighbours of a twinned grains were considered in the calculation. Such more local comparison reveals that within clusters/chains the grains are particularly well aligned for transferring prismatic $\langle a \rangle$ slip showing significantly higher *m'* values compared to the twin-free grain family, figure 7.14(a). In contrast, the *m'* of $\{10\bar{1}2\}\ \langle\bar{1}011\rangle$ tensile twinning within twin clusters/chains remains very similar to the twin-free grain family, figure 7.14(b).

7.4 Discussion

The results presented here clearly demonstrate that X-ray based diffraction contrast tomography is an excellent tool to undertake detailed analysis of twinned grains and their neighbourhood. It should be kept in mind that twins are detected by capturing the diffraction spot signals of the twin. Clearly, in the case of very thin twins, there is

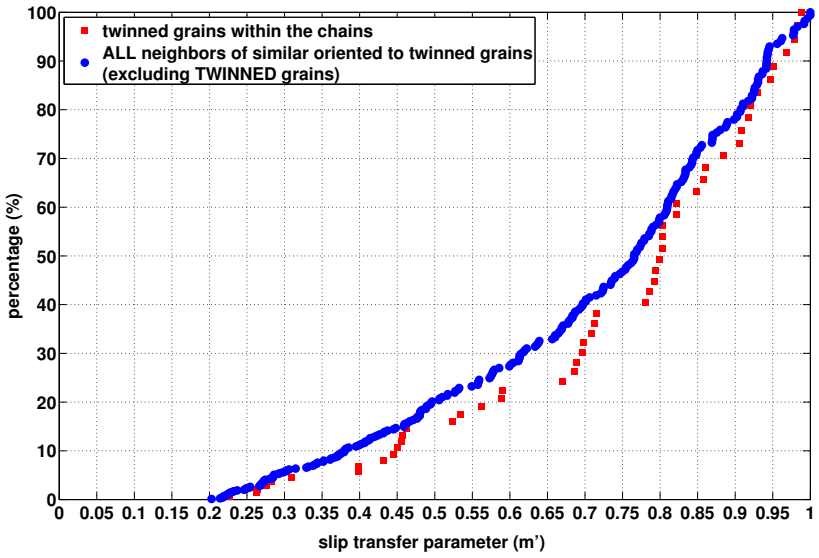

(a)

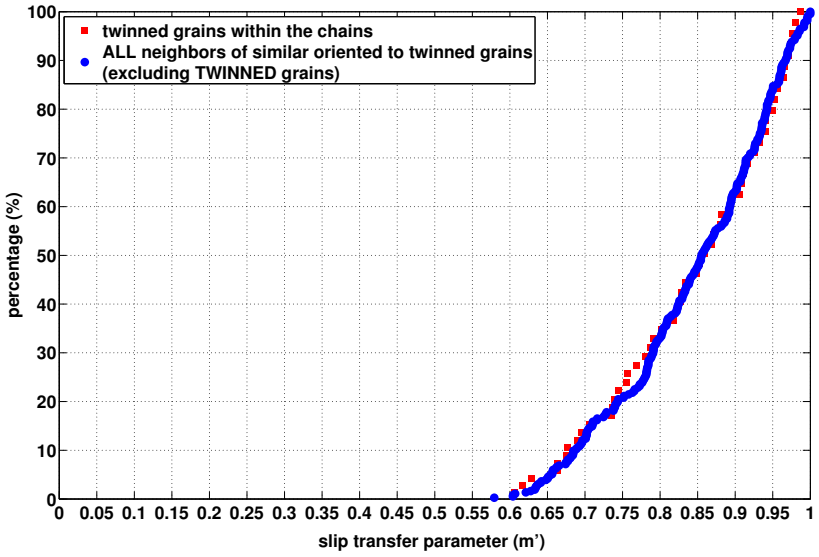

(b)

Figure 7.14: Distributions of transfer parameter m for (a) prismatic slip to prismatic slip and for (b) $\{10\bar{1}2\}\ \langle\bar{1}011\rangle$ tensile twin to $\{10\bar{1}2\}\ \langle\bar{1}011\rangle$ tensile twin for all the twinned grains of the chains (squares) and all the neighbours of the similarly oriented grains to the twinned grains (circles). The twinned grains are excluded from the neighbours of the similarly oriented grains.

a high possibility that a twin is missed in the analysis. The thinnest twin detected in the present case was about 14 μm wide for the thin twin face and occupied a volume of 1.2 10^3 μm^3. Hence, one might assume that the present analysis captures the twins that formed first and have grown to a size that has made them detectable. An important aspect of the present work is that a sufficient number of twins were captured to undertake a statistical analysis of the neighbourhood and compare with similarly orientated grains that had not twinned. This analysis reveals a number of important drivers for early twin formation and that there is a tendency for the formation of twin clusters and chains, which seem to develop into a twin network, section 7.3.

Regarding drivers for early twin formation, the 3D nature of the analysis has revealed the importance of grain size for early twin formation, figure 7.9. While positive grain size dependency of twinning has been reported previously for Mg (BARNETT *et al.*, 2004), Ti (STANFORD *et al.*, 2008) and Zr (CAPOLUNGO *et al.*, 2009), the present 3D analysis provides a very clear picture of the size dependency. It has been suggested previously that the root cause for less twin formation in the case of small grains is related to the twin boundary energy cost being relatively high compared to the plastic work induced by the twin (HOSFORD, 1993, p. 532). It has also been suggested that the size effect is simply related to a decrease in the number of twins with decreasing grain size (BARNETT, 2008).
This consideration assumes the importance of grain boundaries on twin nucleation. The true twin thickness has been found to be independent of grain size in magnesium and zirconium by Tomé and colleagues (BEYERLEIN *et al.*, 2010; CAPOLUNGO *et al.*, 2009) but strongly dependent on the grain size in titanium (OKAZAKI and CONRAD, 1973). Nevertheless, they found that the number of twins, in grains that did twin, increased with increasing grain size. Armstrong and Worthington (ARMSTRONG and WORTHINGTON, 1973) suggest that twinning is associated with micro-plasticity and high stress concentrations within local regions. As X-ray DCT might not capture the very early stage of twin formation, the observed grain size dependency could indicate easier growth of twins in comparatively large grains.

An important factor regarding twin nucleation is also the stress acting on the grains during mechanical loading. It has been demonstrated previously that compression loading of Ti and Zr, with similar starting textures as in the present case, first result in deformation by slip before twinning is observed (SONG and GRAY III, 1995a,b). In this configuration, it is the 'soft' grains, i.e. grains well aligned for prismatic $\langle a \rangle$ slip, which are prone to form $\{10\bar{1}2\}$ $\langle \bar{1}011 \rangle$ tensile twins in order to relief the tensile stress along the $\langle c \rangle$ axis generated in the transverse direction. It is also the configuration that tends to result in the highest twin activity when the material is deformed. Hence, one might argue that prismatic $\langle a \rangle$ slip activity is a critical

parameter in order to induce sufficiently large intergranular strain along the c-axis to nucleate $\{10\bar{1}2\}\ \langle\bar{1}011\rangle$ tensile twins.

It should be noted that in a polycrystalline aggregate, the level of plasticity experienced by a grain does not necessarily depend on the global but the local stress state. For instance, a grain well orientated for prismatic $\langle a\rangle$ slip in respect of the applied loading direction but surrounded by grains well aligned for pyramidal $\langle c+a\rangle$ slip (hard orientation) will be shielded and is unlikely to experience high levels of plasticity. In contrast, if neighbouring grains are well aligned for prismatic slip and prismatic $\langle a\rangle$ 'slip transfer' across grain boundaries is possible, high levels of plasticity are likely in those grains. This will produce high intergranular strains, which could be a driver for twin nucleation. For this reason, the prismatic $\langle a\rangle$ slip transfer analysis is of importance here. While a simple comparison of the neighbourhood of all twinned grains with the neighbourhood of a similarly orientated non-twinned grain family did not show any differences, figure 7.10(b), considering only twin clusters/chains clearly demonstrated a *m'*-value distribution shifted to higher values, figure 7.14(a). Hence, the evolution of twin chains or clusters seems to be guided by following a chain/cluster of grains that can be linked by high prismatic $\langle a\rangle$ slip *m'*-values, i.e. a cluster of parent grains being well aligned for deforming first by prismatic $\langle a\rangle$ slip.

In contrast, a similarly sophisticated analysis of the transfer coefficient for $\{10\bar{1}2\}\ \langle\bar{1}011\rangle$ tensile twinning did not display a difference of values computed from within twin chains/clusters compared to calculating the transfer coefficient distribution of the related twin-free grain family and their neighbourhood, figure 7.14(b). This is interesting as one might argue that a shift towards higher *m'*-values within twin clusters/chains would have emphasised the importance of twins nucleating twins in neighbouring grains by creating stress concentrations (Barnett *et al.*, 2012; Fernández *et al.*, 2013; Guo *et al.*, 2014a; Wang *et al.*, 2010a; Xin *et al.*, 2014). As this concept should be most effective when the shear strain of the twinned grain is of similar direction as the twin shear strain induced in the neighbouring grain, i.e. high *m'*-value, the observations in figure 7.14(b) suggest that this mechanism only plays a minor role in the formation of twins in a polycrystalline aggregate with the given crystallographic texture.

Finally, it is worth emphasising that the present observations are relevant for compression loading and that the situation during tensile loading will be a very different one as in such case the $\{10\bar{1}2\}\ \langle\bar{1}011\rangle$ tensile twins form in grains that are not well aligned for any easy $\langle a\rangle$ slip (Bieler *et al.*, 2014b).

7.5 Conclusions

A detailed analysis of a Ti-4Al sample compressed along the former rolling direction by only 0.7% plastic strain has been carried out first by using in-situ loading and neutron diffraction on SALSA, ILL, followed by X-ray Diffraction Contrast Tomography (DCT) on ID11, ESRF. The main purpose of this work was to study the onset of deformation twinning and consider the true grain neighbourhood in this 3D analysis in order to elucidate possible twin nucleation criteria. An important aspect of the analysis was to compare the family of twinned grains with a family of similarly orientated grains that had not twinned yet and identify key differences. The main findings can be summarised as follows:

- The neutron diffraction analysis enabled the early detection of $\{10\bar{1}2\}\ \langle\bar{1}011\rangle$ tensile twinning, which was seen after less than 1% plastic strain. A subsequent X-ray DCT analysis confirmed the dominance of $\{10\bar{1}2\}\ \langle\bar{1}011\rangle$ twins.
- The X-ray DCT analysis enabled the identification of almost 60 twinned grains with a few cases of multiple twins per grain within a sample volume of about 400 grains. It is important to note that it is possible that only twins that formed very early and have grown to an appreciable size were captured.
- A grain volume/size distribution analysis comparing twinned grains including the twin volume and similarly orientated grains that had not twinned revealed a clear shift towards a higher mean value in the case of the twinned grain family highlighting the importance of grain size on twin formation.
- An initial statistical analysis of the neighbourhood comparing the family of twinned grains with the crystallographically related non-twinned grain family did not reveal any significant differences.
- The 3D analysis revealed chains and clusters of twins that have also developed a slightly imperfect twin network. This suggests a strong neighbourhood effect.
- A Luster-Morris parameter analysis in respect of prismatic $\langle a\rangle$ slip and twin shear within chains/clusters and in comparison to the neighbourhood of the non-twinned grain family revealed that the twin clustering is most likely related to easy prismatic $\langle a\rangle$ slip transfer between the parent grains that form the chains/clusters of twins. In principle, this finding is in good agreement with TIMÁR and QUINTA DA FONSECA (2014), which predicts the formation of twin clusters and the role of $\langle a\rangle$ slip strain location in Mg. In contrast, easy shear transfer from $\{10\bar{1}2\}\ \langle\bar{1}011\rangle$ twins was not identified as important factor within the chains/clusters suggesting that twin nucleation by stress concentration from a neighbouring grain that has twinned is not a main driving force for twin formation.

Finally, it should be noted that the present observations are relevant for a compression experiment and that tensile loading is likely to give different results since in this case the twinning grain has a 'hard' orientation while during compression loading the twinning grain is in a 'soft' orientation in respect of slip.

7.6 Acknowledgements

The authors would like to thank Henry Proudhon (Mines Paristech, Paris, France), for his help with the 3D volume rendering using python scripts.
The authors are grateful to the SALSA beam line scientists for their experimental support as well as the ESRF for their beam time support. The project was supported financially by the Engineering and Physical Science Research Council (EPSRC) in the UK (EP/F020910/1) and the ESRF in Grenoble, France.

The work presented in chapter 7 will be submitted as the following:
NERVO, L. *et al.* (2015), "A study of deformation twinning in a Titanium alloy by X-ray Diffraction Contrast Tomography.", *Acta Materialia*, In progress.

7.7 References

AGNEW, S. R. *et al.* (2003), "Study of slip mechanisms in a magnesium alloy by neutron diffraction and modeling", *Scripta Materialia* **48**, pp. 1003–1008.

AGNEW, S. R., BROWN, D. W., and TOMÉ, C. N. (2006), "Validating a polycrystal model for the elastoplastic response of magnesium alloy AZ31 using in situ neutron diffraction", *Acta Materialia* **54**, pp. 4841–4852.

ARMSTRONG, R. W. and WORTHINGTON, P. J. (1973), "A Constitutive Relation for Deformation Twinning in Body Centered Cubic Metals", in: *Metallurgical Effects at High Strain Rates*, ed. by ROHDE, R. W. *et al.*, Boston, MA, USA: Springer US, pp. 401–414.

ARMSTRONG, R *et al.* (1962), "The plastic deformation of polycrystalline aggregates", *Philosophical Magazine* **7** (73), pp. 45–58.

AYDINER, C *et al.* (2009), "Evolution of stress in individual grains and twins in a magnesium alloy aggregate", *Physical Review B* **80** (2), p. 024113.

BARNETT, M. R. (2008), "A rationale for the strong dependence of mechanical twinning on grain size", *Scripta Materialia* **59** (7), pp. 696–698.

BARNETT, M. R. *et al.* (2004), "Influence of grain size on the compressive deformation of wrought Mg-3Al-1Zn", *Acta Materialia* **52**, pp. 5093–5103.

BARNETT, M. R. *et al.* (2008), "Non-Schmid behaviour during secondary twinning in a polycrystalline magnesium alloy", *Acta Materialia* **56** (1), pp. 5–15.

BARNETT, M. R., NAVE, M. D., and GHADERI, A. (2012), "Yield point elongation due to twinning in a magnesium alloy", *Acta Materialia* **60** (4), pp. 1433–1443.

BARRETT, C. D., EL KADIRI, H., and TSCHOPP, M. A. (2012), "Breakdown of the Schmid law in homogeneous and heterogeneous nucleation events of slip and twinning in magnesium", *Journal of the Mechanics and Physics of Solids* **60** (12), pp. 2084–2099.

BEYERLEIN, I. J. and TOMÉ, C. N. (2010), "A probabilistic twin nucleation model for HCP polycrystalline metals", in: *Proceedings of the Royal Society A: Mathematical, Physical and Engineering Sciences*, vol. 466, pp. 2517–2544.

BEYERLEIN, I. J. *et al.* (2010), "Statistical analyses of deformation twinning in magnesium", *Philosophical Magazine* **90** (16), pp. 2161–2190.

BHATTACHARYYA, D *et al.* (2009), "Origin of dislocations within tensile and compressive twins in pure textured Zr", *Acta Materialia* **57** (2), pp. 305–315.

BIELER, T. R. *et al.* (2014a), "Grain boundaries and interfaces in slip transfer", *Current Opinion in Solid State and Materials Science* **18** (4), pp. 212–226.

BIELER, T. R. *et al.* (2014b), "In Situ Characterization of Twin Nucleation in Pure Ti Using 3D-XRD", *Metallurgical and Materials Transactions A* **45** (1), pp. 109–122.

BILBY, B. A. and CROCKER, A. G. (1965), "The Theory of the Crystallography of Deformation Twinning", in: *Proceedings of the Royal Society of London. Series A: Mathematical, Physical and Engineering Sciences*, vol. 288, pp. 240–255.

BOZZOLO, N., CHAN, L., and ROLLETT, A. D. (2010), "Misorientations induced by deformation twinning in titanium", *Journal of Applied Crystallography* **43**, pp. 596–602.

BRIDIER, F, VILLECHAISE, P, and MENDEZ, J (2005), "Analysis of the different slip systems activated by tension in a α/β titanium alloy in relation with local crystallographic orientation", *Acta Materialia* **53** (3), pp. 555–567.

BROWN, D. W. *et al.* (2005), "Internal strain and texture evolution during deformation twinning in magnesium", *Materials Science and Engineering: A* **399** (1–2), pp. 1–12.

CAI, S *et al.* (2009), "Evolution of interphase and intergranular stresses in Zr2.5Nb during room temperature deformation", *Materials Science and Engineering: A* **501** (1–2), pp. 166–181.

CAPOLUNGO, L. and BEYERLEIN, I. J. (2008), "Nucleation and stability of twins in hcp metals", *Physical Review B* **78** (2), p. 024117.

CAPOLUNGO, L. *et al.* (2009), "Nucleation and growth of twins in Zr: A statistical study", *Acta Materialia* **57** (20), pp. 6047–6056.

CHICHILI, D. R., RAMESH, K. T., and HEMKER, K. J. (1998), "The high-strain-rate response of alpha-titanium: experiments, deformation mechanisms and modeling", *Acta Materialia* **46** (3), pp. 1025–1043.

CHRISTIAN, J. W. and MAHAJAN, S (1995), "Deformation Twinning", *Progress in Materials Science* **39** (1–2), pp. 1–157.

CHUN, Y. B. *et al.* (2005), "Effect of deformation twinning on microstructure and texture evolution during cold rolling of CP-titanium", *Materials Science and Engineering: A* **398** (1–2), pp. 209–219.

CLARK, W. A. T. *et al.* (1992), "On the criteria for slip transmission across interfaces in polycrystals", *Scripta Metallurgica et Materialia* **26** (2), pp. 203–206.

CLAUSEN, B *et al.* (2008), "Reorientation and stress relaxation due to twinning: Modeling and experimental characterization for Mg", *Acta Materialia* **56** (11), pp. 2456–2468.

COGHE, F *et al.* (2012), "Importance of twinning in static and dynamic compression of a Ti6Al4V titanium alloy with an equiaxed microstructure", *Materials Science and Engineering: A* **537**, pp. 1–10.

DCT code, http://sourceforge.net/projects/dct/.

DAYMOND, M. R. and PRIESMEYER, H. G. (2002), "Elastoplastic deformation of ferritic steel and cementite studied by neutron diffraction and self-consistent modelling", *Acta Materialia* **50**, pp. 1613–1626.

DAYMOND, M. R., PREUSS, M., and CLAUSEN, B (2007), "Evidence of variation in slip mode in a polycrystalline nickel-base superalloy with change in temperature from neutron diffraction strain measurements", *Acta Materialia* **55**, pp. 3089–3102.

EL KADIRI, H. and OPPEDAL, A. L. (2010), "A crystal plasticity theory for latent hardening by glide twinning through dislocation transmutation and twin accommodation effects", *Journal of the Mechanics and Physics of Solids* **58** (4), pp. 613–624.

FERNÁNDEZ, A *et al.* (2013), "Three-dimensional investigation of grain boundarytwin interactions in a Mg AZ31 alloy by electron backscatter diffraction and continuum modeling", *Acta Materialia* **61** (20), pp. 7679–7692.

FITZNER, A. *et al.* (2014), "The effect of Aluminium on twin activity in binary α-Ti", *Acta Materialia*, Submitted.

GONG, J. and WILKINSON, A. J. (2011), "A microcantilever investigation of size effect, solid-solution strengthening and second-phase strengthening fora prism slip in alpha-Ti", *Acta Materialia* **59** (15), pp. 5970–5981.

GUO, C. *et al.* (2014a), "Understanding of variant selection and twin patterns in compressed Mg alloy sheets via combined analysis of Schmid factor and strain compatibility factor", *Materials Science and Engineering: A* **609**, pp. 92–101.

GUO, Y, BRITTON, T. B., and WILKINSON, A. J. (2014b), "Slip bandgrain boundary interactions in commercial-purity titanium", *Acta Materialia* **76**, pp. 1–12.

HONNIBALL, P. *et al.* (2015), "Grain break-up during elevated temperature deformation of an HCP metal", *Metallurgical and materials transactions A - physical metallurgy and materials science*, Accepted.

HOSFORD, W. F. (1993), *The Mechanics of crystals and textured polycrystals*, New York, NY, USA: Oxford University Press.

HUGHES, D. J. *et al.* (2006), "Scientific Review: First Impressions of SALSA: The New Engineering Instrument at ILL", *Neutron News* **17** (3), pp. 28–32.

HULL, D (1961), "Effect of grain size and temperature on slip, twinning and fracture in 3% silicon iron", *Acta Metallurgica* **9**, pp. 191–204.

ICE, G. E. and BARABASH, R. I. (2007), "White Beam Microdiffraction and Dislocations Gradients", in: *Dislocations in Solids*, ed. by NABARRO, F. R. N. and HIRTH, J. P., vol. 13, Elsevier B.V., chap. 79, pp. 499–601.

KERR, M *et al.* (2010), "Mapping of crack tip strains and twinned zone in a hexagonal close packed zirconium alloy", *Acta Materialia* **58** (5), pp. 1578–1588.

KOCKS, U. F. (1970), "The relation between polycrystal deformation and single-crystal deformation", *Metallurgical and Materials Transactions* **1** (5), pp. 1121–1143.

KOCKS, U. F., TOMÉ, C. N., and WENK, H. R. (1998), *Texture and Anisotropy: Preferred Orientations in Polycrystals and Their Effect on Materials Properties*, New York, NY, USA: Cambridge University Press.

KORSUNSKY, A. M., JAMES, K. E., and DAYMOND, M. R. (2004), "Intergranular stresses in polycrystalline fatigue: Diffraction measurement and self-consistent modelling", *Engineering Fracture Mechanics* **71**, pp. 805–812.

LABICHE, J.-C. *et al.* (2007), "The fast readout low noise camera as a versatile x-ray detector for time resolved dispersive extended x-ray absorption fine structure and diffraction studies of dynamic problems in materials science, chemistry, and catalysis", *Review of Scientific Instruments* **78** (9), p. 91301.

LAHAIE, D *et al.* (1992), "A note on the deformation of fine grained magnesium alloys", *Scripta Metallurgica et Materialia* **27** (2), pp. 139–142.

LARSON, B. C. *et al.* (2002), "Three-dimensional X-ray structural microscopy with submicrometre resolution.", *Nature* **415** (6874), pp. 887–890.

LAURIDSEN, E. M. *et al.* (2001), "Tracking: a method for structural characterization of grains in powders or polycrystals", *Journal of Applied Crystallography* **34** (6), pp. 744–750.

LEYENS, C. and PETERS, M., eds. (2003), *Titanium and Titanium Alloys, Fundamentals and Applications*, Weinheim, Germany: WILEY-VCH Verlag GmbH and Co. KGaA.

LIU, W. and DUPONT, J. N. (2004), "Fabrication of carbide-particle-reinforced titanium aluminide-matrix composites by laser-engineered net shaping", *Metallurgical and Materials Transactions A* **35** (3), pp. 1133–1140.

LIU, W. *et al.* (2005), "Nondestructive three-dimensional characterization of grain boundaries by X-ray crystal microscopy.", *Ultramicroscopy* **103** (3), pp. 199–204.

LUDWIG, W. *et al.* (2009b), "Three-dimensional grain mapping by x-ray diffraction contrast tomography and the use of Friedel pairs in diffraction data analysis", *Review of Scientific Instruments* **80** (3), p. 033905.

LUSTER, J and MORRIS, M. A. (1995), "Compatibility of deformation in two-phase Ti-Al alloys: Dependence on microstructure and orientation relationships", *Metallurgical and Materials Transactions A* **26** (7), pp. 1745–1756.

MCCABE, R. J. *et al.* (2009), "Quantitative analysis of deformation twinning in zirconium", *International Journal of Plasticity* **25** (3), pp. 454–472.

MEYERS, M. A., VÖHRINGER, O, and LUBARDA, V. A. (2001), "The onset of twinning in metals: a constitutive description", *Acta Materialia* **49** (19), pp. 4025–4039.

NERVO, L. *et al.* (2015), "A study of deformation twinning in a Titanium alloy by X-ray Diffraction Contrast Tomography.", *Acta Materialia*, In progress.

OKAZAKI, K and CONRAD, H (1973), "Effects of interstitial content and grain size on the strength of titanium at low temperatures", *Acta Metallurgica* **21**, pp. 1117–1129.

PALENSTIJN, W. J., BATENBURG, K. J., and SIJBERS, J (2011), "Performance improvements for iterative electron tomography reconstruction using graphics processing units (GPUs).", *Journal of structural biology* **176** (2), pp. 250–253.

— (2013), "The ASTRA Tomography Toolbox", in: *13th International Conference on Computational and Mathematical Methods in Science and Engineering*, pp. 1–7.

PIRLING, T., BRUNO, G., and WITHERS, P. J. (2006), "SALSA-A new instrument for strain imaging in engineering materials and components", *Materials Science and Engineering A* **437**, pp. 139–144.

POULSEN, H. F. (2004), *Three-Dimensional X-Ray Diffraction Microscopy: Mapping Polycrystals and Their Dynamics*, Springer.

— (2012), "An introduction to three-dimensional X-ray diffraction microscopy", *Journal of Applied Crystallography* **45** (6), pp. 1084–1097.

POULSEN, H. F. *et al.* (1997), "Applications of high-energy synchrotron radiation for structural studies of polycrystalline materials.", *Journal of synchrotron radiation* **4** (3), pp. 147–54.

POULSEN, H. F. *et al.* (2001), "Three-dimensional maps of grain boundaries and the stress state of individual grains in polycrystals and powders", *Journal of Applied Crystallography* **34** (6), pp. 751–756.

PRAKASH, D. G. L. *et al.* (2010), "Deformation twinning in Ti-6Al-4V during low strain rate deformation to moderate strains at room temperature", *Materials Science and Engineering: A* **527** (21–22), pp. 5734–5744.

PREUSS, M. *et al.* (2010), "Twinning in structural material with a hexagonal close-packed crystal structure", *The Journal of Strain Analysis for Engineering Design* **45** (5), pp. 377–390.

REISCHIG, P. *et al.* (2013), "Advances in X-ray diffraction contrast tomography: flexibility in the setup geometry and application to multiphase materials", *Journal of Applied Crystallography* **46** (2), pp. 297–311.

SALEM, A. A., KALIDINDI, S. R., and DOHERTY, R. D. (2003), "Strain hardening of titanium: role of deformation twinning", *Acta Materialia* **51** (14), pp. 4225–4237.

SERRA, A. and BACON, D. J. (1996), "A new model for {10 1 2} twin growth in hcp metals", *Philosophical Magazine A* **73** (2), pp. 333–343.

SONG, S. G. and GRAY III, G. T. (1995a), "Structural interpretation of the nucleation and growth of deformation twins in Zr and Ti. I. Application of the coincidence site lattice (CSL) theory to twinning problems in h.c.p. structures", *Acta Metallurgica et Materialia* **43** (6), pp. 2325–2337.

— (1995b), "Structural interpretation of the nucleation and growth of deformation twins in Zr and Ti. II. Tem study of twin morphology and defect reactions during twinning", *Acta Metallurgica et Materialia* **43** (6), pp. 2339–2350.

STANFORD, N, CARLSON, U, and BARNETT, M. R. (2008), "Deformation Twinning and the HallPetch Relation in Commercial Purity Ti", *Metallurgical and Materials Transactions A* **39** (4), pp. 934–944.

STAROSELSKY, A and ANAND, L (2003), "A constitutive model for hcp materials deforming by slip and twinning", *International Journal of Plasticity* **19** (10), pp. 1843–1864.

THOMPSON, N and MILLARD, D. J. (1952), "XXXVIII. Twin formation, in cadmium", *The London, Edinburgh, and Dublin Philosophical Magazine and Journal of Science: Series 7* **43** (339), pp. 422–440.

TIMÁR, G. and QUINTA DA FONSECA, J. A. (2014), "Modeling Twin Clustering and Strain Localization in Hexagonal Close-Packed Metals", *Metallurgical and Materials Transactions A* **45**, pp. 5883–5890.

TOMÉ, C. N. *et al.* (2011), "A multi-scale statistical study of twinning in magnesium", *JOM* **63** (3), pp. 19–23.

VON MISES, R (1928), "Mechanik der plastischen Formänderung von Kristallen", *Zeitschrift für Angewandte Mathematik und Mechanik* **8** (3), pp. 161–185.

WANG, L. *et al.* (2010a), "Nucleation of paired twins at grain boundaries in titanium", *Scripta Materialia* **63** (8), pp. 827–830.

WANG, L. *et al.* (2010b), "Twin Nucleation by Slip Transfer across Grain Boundaries in Commercial Purity Titanium", *Metallurgical and Materials Transactions A* **41** (2), pp. 421–430.

WANG, L. *et al.* (2011), "Experimental Characterization and Crystal Plasticity Modeling of Heterogeneous Deformation in Polycrystalline α-Ti", *Metallurgical and Materials Transactions A* **42** (3), pp. 626–635.

WANG, L. *et al.* (2013), "Study of $${11\bar{2}1}$$ Twinning in α-Ti by EBSD and Laue Microdiffraction", *Metallurgical and Materials Transactions A* **44** (8), pp. 3664–3674.

XIN, R. *et al.* (2014), "Characteristics of long {10-12} twin bands in sheet rolling of a magnesium alloy", *Scripta Materialia* **74**, pp. 96–99.

XU, F. *et al.* (2008), "Development of internal strains in textured Zircaloy-2 during uni-axial deformation", *Materials Science and Engineering A* **488**, pp. 172–185.

YOO, M. H. (1981), "Slip, twinning, and fracture in hexagonal close-packed metals", *Metallurgical Transactions A* **12** (3), pp. 409–418.

YOO, M. H. *et al.* (2002), "Nonbasal Deformation Modes of HCP Metals and Alloys : Role of Dislocation Source and Mobility", *Metallurgical and Materials Transactions A* **33**, pp. 813–822.

ZAEFFERER, S (2003), "A study of active deformation systems in titanium alloys: dependence on alloy composition and correlation with deformation texture", *Materials Science and Engineering: A* **344** (1–2), pp. 20–30.

Chapter 8

Results III: Section topography on AZ31 Mg alloy

Abstract

A combination of X-ray diffraction contrast tomography with X-ray section and pinhole topography for studying the microstructure in polycrystalline materials at the sub-grain level has been carried out by acquiring two sets of diffraction data with two different scattering geometries: in-line detector with horizontal rotation axis for the X-ray diffraction contrast tomography (DCT) technique and vertical detector with additional absorption masks for section topography. The 3D grain map of the sample volume produced with the X-ray DCT methodology provided position and orientation of the grains in the sample. This information was then used to predict rotation angles and diffraction spot positions on the vertical detector, for three Friedel pairs of diffraction spots from one selected grain. X-ray section and pinhole topography were used to study the selected grain in more detail. The studied material was a AZ31 Mg alloy, which has a hexagonal close packed crystal structure. The combination of the two techniques allows revealing the presence of lattice curvature, twins and small angle boundaries with improved sensitivity. Advantages of using the vertical detector have been analysed and perspectives and limitations of this approach discussed.

8.1 Introduction

The study of polycrystalline engineering materials on the length scale of individual grains is important for understanding their properties and behaviour. It is clear that grains are not homogeneous, and that a complete understanding of material behaviour requires in-situ characterisation techniques capable of analysing sub-structures within individual grains.

The X-ray DCT (JOHNSON *et al.*, 2008; KING *et al.*, 2008, 2011; LUDWIG *et al.*, 2008, 2009a,b; REISCHIG *et al.*, 2013) is a variant of the 3D X-ray diffraction (3DXRD) microscopy technique (LI and SUTER, 2013; ODDERSHEDE *et al.*, 2010, 2012; POULSEN, 2004, 2012; SCHMIDT, 2010; SØRENSEN *et al.*, 2012; SUTER *et al.*, 2006) enabling simultaneous reconstruction of the 3D microstructure (shape and orientation) in suitable polycrystalline materials, along with the absorption map of the specimen. However, the reconstruction unit of DCT is individual grains, which are described by average values of orientation and elastic strain state of the individual grains from polycrystalline sample volumes containing up to thousands grains. The goal of the current work is the development of combined tomographic and topographic diffraction imaging techniques that spatially resolve "topographic detail", as well as local orientations and strains inside bulk grains in a non-destructive way.

Over the recent years at modern synchrotron radiation facilities, LÜBBERT *et al.* (2000) and MIKULÍK *et al.* (2006) have developed the rocking curve imaging (RCI) technique, which is a digitised version of monochromatic beam X-ray diffraction topography, applying to flat, single crystal line specimen. Up to now RCI provides a quantitative picture of the features present in a several-micrometre-thick subsurface layer. A 3D Bragg-diffraction imaging technique (3DRCI), applicable to individual grains in a polycrystalline specimen, has been successfully implemented by KLUENDER *et al.* (2011), which combines RCI with X-ray pinhole and section topography in the transmission case. LANG and MAKEPEACE (1996) have developed another technique, called reticulography, for analysing misorientations in single crystals, where an X-ray absorbing grid structure is placed between the sample and the detector, close to the sample (LANG and MAKEPEACE, 1999). Variations in the directions of the diffracted beams from the sample are caused by distortions in the crystal lattice, which distort the image of the grid on the detector. By analysing these distortions, the misorientations in the crystal can be determined quantitatively, as studied in polycrystalline aluminium combining the reticulography with X-ray DCT (KING *et al.*, 2010). Recently, SIMONS *et al.* (2015) used dark-field X-ray microscopy, a non-destructive microscopy technique, for the three-dimensional mapping of orientations and stresses within individual grains approaching a spatial resolution of the order of 100 nm.

In section (pinhole) topography, the incident beam is restricted in size to a line (point), and the diffracted intensity studied. The aim of reducing the illumination is to simplify the interpretation of the projection images. The interest of combining DCT with section topography is to take advantage of the characteristics of the two techniques: a 3D vision of the grain microstructure from DCT, and more detailed sub-grain information from section topography. This combination offers new

possibilities for observation of deformation and damage mechanisms in the bulk of polycrystalline materials. One can obtain a comprehensive description of the materials' microstructure at the micrometre length scale, providing topographic detail (slip bands, twins) and local orientation measurements inside the bulk of selected grains.

8.1.1 Section topography combined with DCT

In X-ray diffraction imaging topography, one has the choice between different illumination modes ("full" beam versus "line" beam versus "pencil" beam) and detector positions. Normally the forward scattering geometry with the detector normal to the incident beam direction is used (see in-line detector in figure 8.1). The choice of this standard acquisition geometry is natural for experiments on macroscopic, absorbing samples, where the use of high X-ray energies is mandatory and scattering at high 2θ angles is weak.
Using a configuration with scattering angles and a detector position close to $2\theta = 90^\circ$ offers improved orientation and strain sensitivity (LUDWIG *et al.*, 2010). Using this configuration, it is possible to look into single grains in more detail, resolving topographic details originating from sub-grain structures like slip bands, twins, etc. In the absence of intragranular orientation spread, one observes 2D sections of the grain and one may construct 3D volumes without tomographic reconstruction by stacking slices (section topography) (KVARDAKOV *et al.*, 2007). "Pencil" beams illuminate lines within the slice. The lines are projected onto the diffraction image, and distortions in the lines reveal lattice rotations.

Due to the decay of the scattering signal for reflections with large Miller indices, working at scattering angles close to 90° is typically restricted to beam energies below 20 keV. Many structural materials of technological relevance have grain sizes below 50 µm and therefore require ultimate detector resolution when characterised with full field imaging techniques. In order to limit the probability of spot overlap the sample dimensions need to be scaled accordingly (typically less than 10–20 grains through the diameter of the sample). For lightweight materials like Al and Mg alloys, it is therefore possible to perform this kind of diffraction imaging experiments at energies below 20 keV and to take advantage of the above-mentioned configuration with high scattering angles.
Magnesium is a hexagonal close-packed (HCP) metal at room temperature and it is the third most commonly used structural metal, following steel and aluminium. Its application ranges from agricultural, chemical and construction industries, to automotive and manufacturing of housing of electronic devices. Among its several attractive engineering properties, its alloys can endure high temperature conditions up

to 400 °C. Thus, magnesium is an ideal candidate for the section topography technique because of its low absorption coefficient ($\mu/\rho \approx 6.358$ cm^2/g at 15 keV) if compared to other structural metals.

In this work we investigated twinning mechanisms operational during plastic deformation in AZ31 Mg alloys, using a combination of the X-ray DCT technique and X-ray section and pinhole topography, using "line" and "pencil" beam illumination modes. From the DCT data, the information of grain position, shape and orientation from the reconstructed sample volume were used together with the fitted geometry (detector position, detector tilts, sample-detector distance), in order to observe X-ray pinhole and section topography of a selected grain on a vertical detector positioned at high two-theta angles ($2\theta \approx 90°$).
In section 8.2 we describe the sample preparation and experimental setup. In section 8.3 we illustrate the results from X-ray DCT and section topography techniques applied to a sample made of AZ31 Mg alloy. In section 8.4 we discuss the interest of combining both techniques for the characterisation of deformation in polycrystalline materials. Finally, we highlight some of the limitations of the section and pinhole topography approaches and directives for future experiments are proposed.

8.2 Experimental procedure

8.2.1 Sample preparation and mounting

The material studied in this work is an extruded Mg-3% Al-1% Zn (AZ31) alloy, which has been annealed for 8 hours at 500 °C, yielding an average grain size of about 300 µm. A cylindrical sample with diameter of 600 µm and a length of about 1 mm long was prepared by electro-discharge machining (EDM), then inserted into a loading rig for deformation measurements. We present the analysis about the undeformed state.

8.2.2 Experimental setup

The experiment was performed at the beam line ID18F of the European Synchrotron Radiation Facility (ESRF) (SOMOGYI *et al.*, 2001) using a monochromatic beam produced by a Si (111) Bragg-Bragg double-crystal monochromator (14.4 keV, relative energy bandwidth $\Delta\lambda/\lambda \approx 10^{-4}$).
The experimental setup is represented schematically in figure 8.1. The coordinate system is defined such that the X-ray beam is along the laboratory X direction [100], the Z direction is vertical, upwards from the origin [001], and the Y direction [010] is

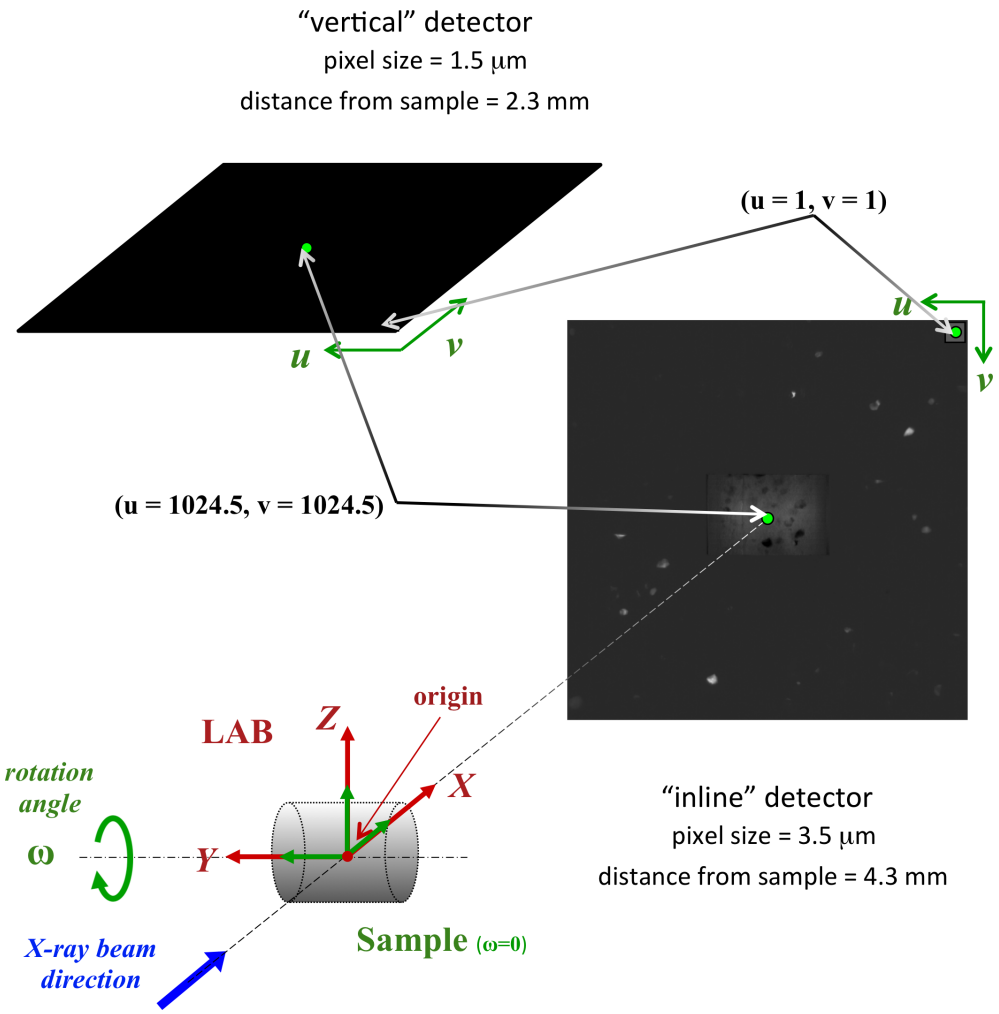

Figure 8.1: Experimental setup with two detectors (in-line and vertical) at beam line ID18F, ESRF, Grenoble, France.

consistent with a right-handed system. A compression rig hosting the cylinder shaped sample was mounted on the rotation stage such that the sample and the loading axis were aligned with the rotation axis.

The experiment was divided into two parts: (i) a DCT scan of the entire sample volume and, after the analysis of the 3D grain map, (ii) section and pinhole topography scans of the biggest grain were acquired. The DCT and section topography acquisitions were carried out consecutively, without changing the sample mounting in between.

In the first part, the sample was illuminated by a "full" beam with dimensions 1.04×0.85 mm^2 (horizontal $\times$ vertical) defined by slits. The detector was an ATMEL Fast Readout Low Noise (FReLoN) charge-coupled device (CCD) camera containing 2048×2048 pixels with exposure time of 0.15 seconds. The detector is light optically coupled to a transparent luminescent screen, yielding an effective pixel size of 3.5 μm/pixel. It was mounted centred in the direct beam and at a sample-detector

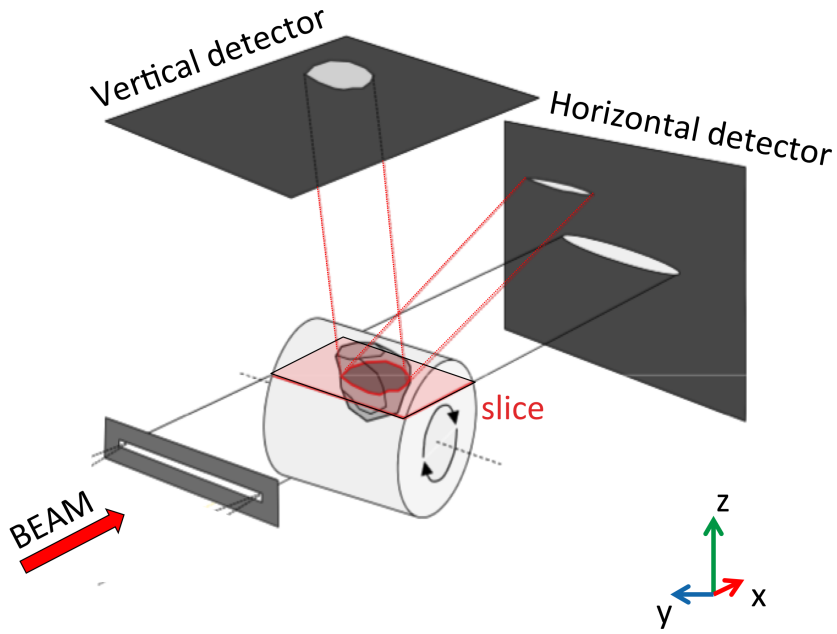

(a) "Line" beam illumination

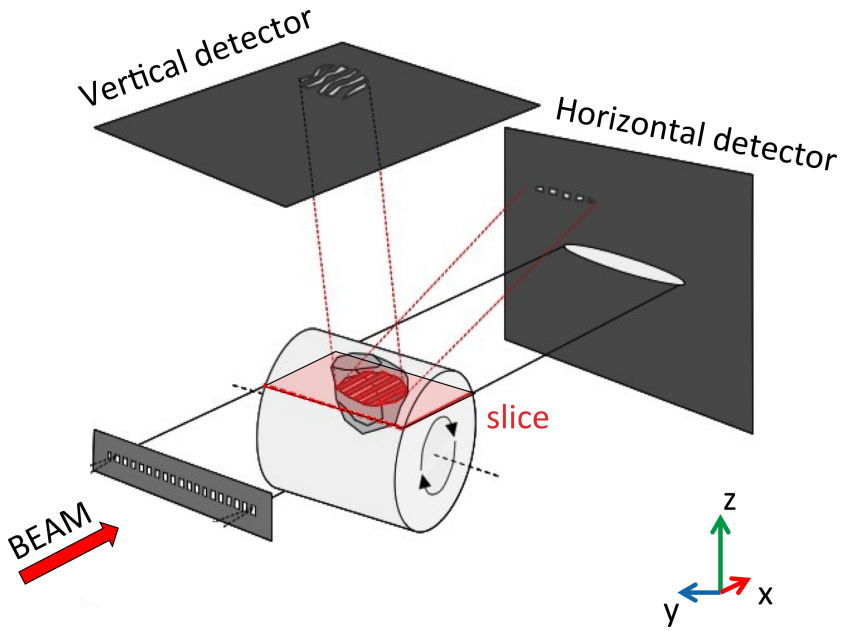

(b) "Pencil" beam illumination

Figure 8.2: Experimental setup with two detectors (in-line and vertical) with an absorption mask that provides (a) the "line" beam illumination mode or (b) the "pencil" beam illumination mode. The irradiated section of the grain is projected almost perpendicularly ($2\theta \approx 90^\circ$) onto the detector plane. An in-line detector on which the section appears compressed as it diffracts is also shown for comparison (REISCHIG *et al.*, 2013).

distance of 4.3 mm. The term 'in-line detector' will be used to refer to this camera, used with the X-ray DCT technique. The scan was performed over a 360° continuous rotation with 0.05° rotation increments.

For the second part, absorption masks (Au deposited on Si substrate produced by electron beam lithography techniques, (RUTISHAUSER *et al.*, 2012)) were placed in the incoming beam, in order to produce two configurations (figure 8.2): (i) the "line" beam profile illuminating a 7 µm-thick slice of the entire sample, parallel to the rotation axis; (ii) an array of "pencil" beams with period 50 µm and individual sections of about 7×7 µm^2. The diffraction images were recorded on a second detector system, based on a back illuminated E2V FReLoN camera system, placed vertically above the sample at about 2.3 mm distance, containing 2048×2048 pixels with exposure time of 0.7 seconds and an effective pixel size of 1.5 µm/pixel. The term 'vertical detector' will be used to refer to this camera. Prior to this experiment, two DCT scans of a Ge single crystal were used to calibrate the position of the in-line and vertical detectors.
Three reflections of the biggest grain, intersecting the vertical detector close to the centre, were selected and seven "pencil" beam scans were performed for each reflection and its corresponding Friedel pair. Each image was integrated over a ω range of 1.5°, covering the angular range of the reflection curve with an integration time of 7.5 seconds. The seven "pencil" beam scans were needed to illuminate the whole slice by shifting the grid along the rotation axis direction (1:6 duty cycle).

8.3 Results

8.3.1 DCT scan on the in-line detector

The 3D grain map of the reconstructed sample volume from the X-ray DCT data taken on the in-line detector is shown in figure 8.3. Colours represent crystallographic orientations of the grains according to the inverse pole figure (IPF) of the sample z-axis.
A slice through the reconstructed DCT volume close to the position of the rotation axis is shown in figure 8.4. Colours represent crystallographic orientations of the grains according to the IPF of the sample z-axis. The image shown is a section parallel to the rotation axis through the sample at $\omega = 129.15°$. The misorientation angles quoted are with respect to the biggest grain (grain 1), representing almost 64% of the illuminated sample volume. The sample contains only 5 grains, of which two could be identified as parents (grains 1 and 2) and three as twins (grains 4, 5 and 6). The misorientation angles and axes of the three magenta twins (grains 4, 5 and 6) with respect to the parent grain (grain 1) were calculated: they are respectively of 85.97°, 86.17° and 87.01°, close to the typical misorientation angle of the $\{10\bar{1}2\}$ $\langle\bar{1}011\rangle$ tensile twin (BOZZOLO *et al.*, 2010; BROWN *et al.*, 2007). The grain boundary planes in the Miller-Bravais notation for the twins (grains 4, 5 and 6) are respectively

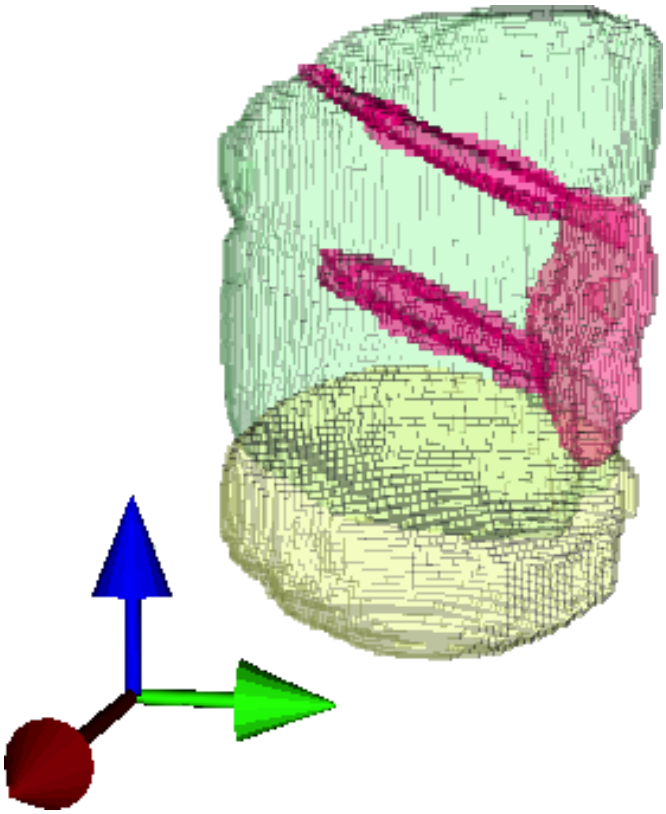

Figure 8.3: 3D grain map of the reconstructed sample volume coloured according to the IPF colour code for HCP materials of the sample z-axis. The red, green and blue arrows represent respectively the laboratory the X, Y and Z axes.

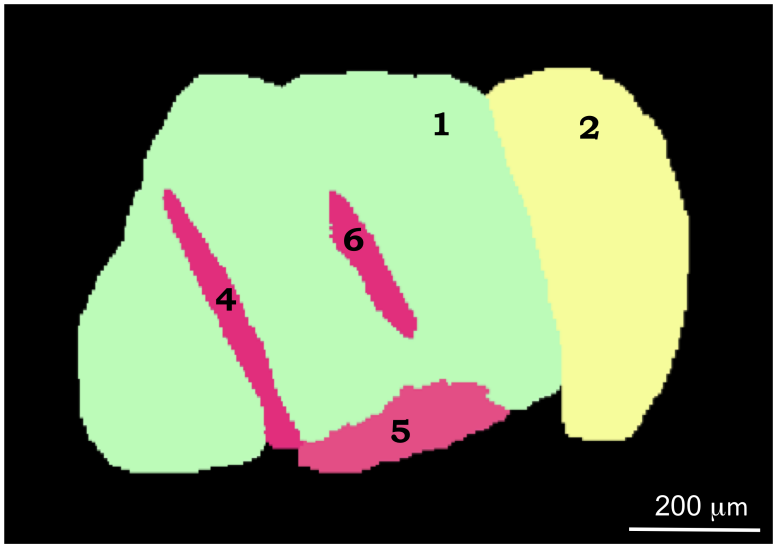

Figure 8.4: Slice of the reconstructed sample volume of a AZ31 Mg alloy specimen, showing misorientation angles of the three reconstructed twins with respect to the grain 1.

$(1.8871\ -1.8473\ -0.0398\ 3.8420)$, $(2.0915\ -1.8744\ -0.2170\ 3.6155)$ and $(-1.8535\ 2.3654\ -0.5119\ 3.2682)$. Given the ambiguity of the average orientations

reconstructed by DCT (resulting from the non-negligible intragranular orientation spread), these values are sufficiently close to indicate $\{10\bar{1}2\}\ \langle\bar{1}011\rangle$ twins. The misorientation angle between grains 1 and 2 is only 15.47°, indicating the presence of a low angle boundary.

8.3.2 Section topography on the vertical detector

In figure 8.5 a Friedel pair on the vertical detector is shown. The pair image has been flipped vertically so the two images (left and right) appear identical. The depicted section topograph corresponds roughly to the grain cross section shown in figure 8.4. The presence of twins in the bulk of the parent grain (grain 1) is evident, as revealed by the dark straight lines in the bright spot. The asymmetry between the Friedel pair of the diffraction spots in each row of figure 8.5, which indicates a slight misorientation of the parent grain on each side of a twin. Note that the dark lines due to the twins appear to taper from top to bottom (left) and from bottom to top in the pair image (right).

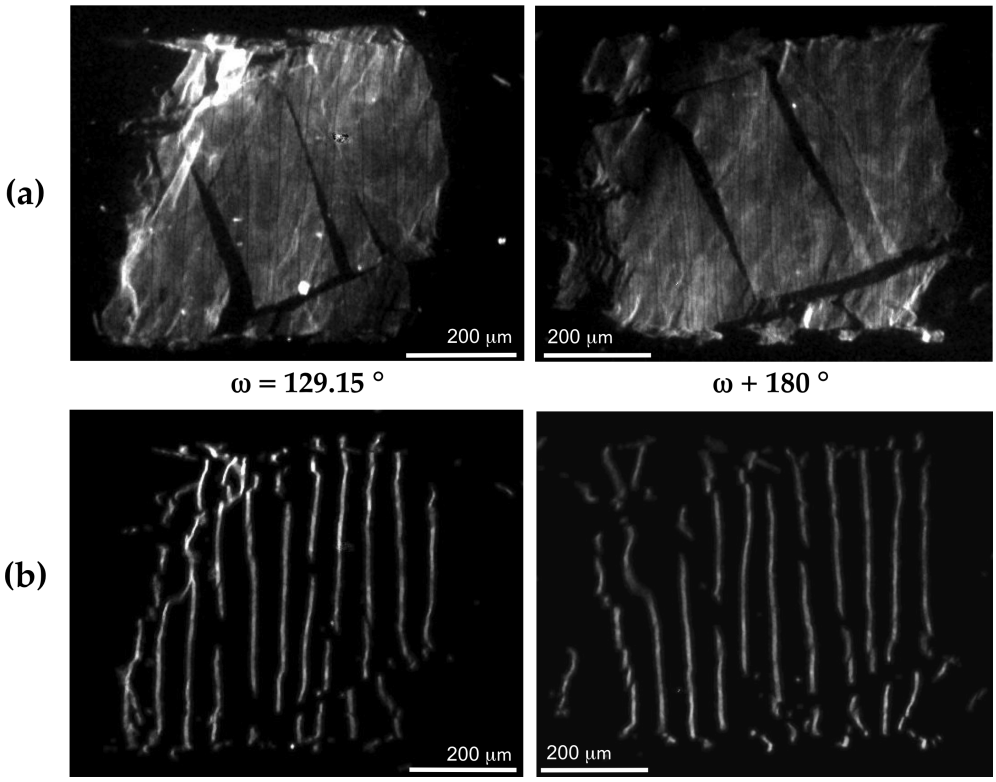

Figure 8.5: Friedel pair from (a) "line" beam illumination (see figure 8.2(a)) and (b) "pencil" beam illumination (see figure 8.2(b)) for the undeformed state.

Two different images are shown: figure 8.5(a) a pair of diffracted spots from the "line" beam illumination; figure 8.5(b) the same Friedel pair is seen with the "pencil" beam illumination. In the left column the diffraction spots correspond to $\omega = 129.15°$

and in the right column at $\omega \pm 180°$. The two section topography methodologies allowed to illuminate the sample slice by slice and characterise the full 3D sample volume by repeated acquisition of projection images at different vertical positions of the absorbing masks.

From figure 8.5(a), a big distorted area is visible in the top-left corner of the diffraction spot. Note both the difference in shape and intensity between the pair of images. This is due to converging or diverging diffracted rays. Violating the parallel beam assumption, this region is very difficult to reconstruct with the conventional (3D) DCT reconstruction algorithm. Moreover, an extra thin twin parallel to the existing twins (i.e. grains 4 and 6 of figure 8.4) was detected in both diffraction images using this approach, figure 8.6(a).

With the "line" beam, although the projections are still distorted, they contain less overlapping information and are hence easier to interpret. The twins can be located, and variations in intensity understood in terms of converging or diverging rays, and hence local orientation, figure 8.6(a). With the "pencil" beam illumination mode, figure 8.5(b), we can start to use the distorted lines to quantify local rotations (η) of the diffracted beam (and hence scattering vectors and lattice plane normals) around the axis defined by the beam. Knowing the position of the illuminated sample volume for each of the projection images in a "pencil" beam scan, the local deviation of the scattering vector from the grain average direction can be determined in all three dimensions of real space. In the present case, an estimate of the local lattice rotation corresponding to 1 pixel shift of the line images is about 0.7 mrad (0.04°), given the pixel size of 1.5 µm/pixel and the sample-detector distance of 2.3 mm. Note that some of the lines deviate by more than the inter-line spacing of 50 µm (≈20 pixels) over distances of a few tens of microns.

An example and some basic analysis of the deformation gradients observed in the Mg grain under investigation is shown in figure 8.6(b). As illustrated, one can measure the distance between two different pairs of lines in both images of a Friedel pair and calculate the local rotation ($\Delta\eta/\Delta d$) using equation (8.1). A description of the detector geometry using the "pencil" beam illumination mode is given in appendix B.9.

$$\Delta\eta = \frac{L_1 - L_2}{2D} \qquad \Delta d = \frac{L_1 + L_2}{2} \qquad \frac{\Delta\eta}{\Delta d} = \frac{\frac{L_1 - L_2}{2D}}{\frac{L_1 + L_2}{2}} \tag{8.1}$$

where L_1 and L_2 are the distances between a selected pair of lines in each image and D is the sample-detector distance. The distances between two selected lines in each image was calculated in two cases: $L_1 = 175$ µm and $L_2 = 155$ µm for the top example (in red), and $L_1 = 85$ µm and $L_2 = 135$ µm for the bottom example (in blue).

The distorted lines give $\Delta\eta/\Delta d$ in the two cases of 0.026 mrad/µm (0.001 degree/µm) and -0.099 mrad/µm (0.006 degree/µm), respectively.

In the red case of figure 8.6(b), over an average lateral distance (perpendicular to the beam) of 165 µm one observes a difference of 0.026 mrad in η (lattice rotation). This in turn can be expressed as a gradient (lattice rotation over a given distance). In the blue case of figure 8.6(b) one would observe a difference of 0.099 mrad in η over an average lateral distance (perpendicular to the beam) of 110 µm. This can in principle be linked to geometrically necessary dislocation (GND) density in the material. Another way to quantify these rotations would be along the beam direction, where one would have direct access to the gradient information at the micrometre scale.

Topographic data are difficult to interpret since image formation and local contrast (intensity in the images) are typically function of various parameters and change with size (shape) of the crystal, level of perfection of the crystal (dynamic versus kinematic diffraction), illumination mode (pinhole and section topography, projection topography, divergence of beam, ...) and type of radiation (monochromatic versus polychromatic beam). Dynamic diffraction effects dominate in close to perfect crystals, in which case even the presence of elastic strain may give rise to significant changes in diffracted intensities and individual dislocations may give rise to weird interference patterns.

A more quantitative analysis yielding access to the local lattice orientations within the sample will require an automated image analysis procedure extracting the direction of at least two independent scattering vectors for each of the voxels in the sample volume. In the present case such an analysis would have been complicated by the fact that the “line” images from neighbouring “pencils” beams interpenetrate, rendering the establishment of a fully automated assignment procedure problematic and has not been further pursued.

8.4 Discussion

The aim of using section topography is a description of the materials’ microstructure at the micrometre length scale, providing access to topographic detail like slip bands and/or twins, and local orientation measurements. The presented acquisition geometry with close to 90° scattering angles requires beam energies below 20 keV because the form factor drops off quickly for reflections with higher Miller indices.

The use of a vertical detector leads to the advantages listed below.

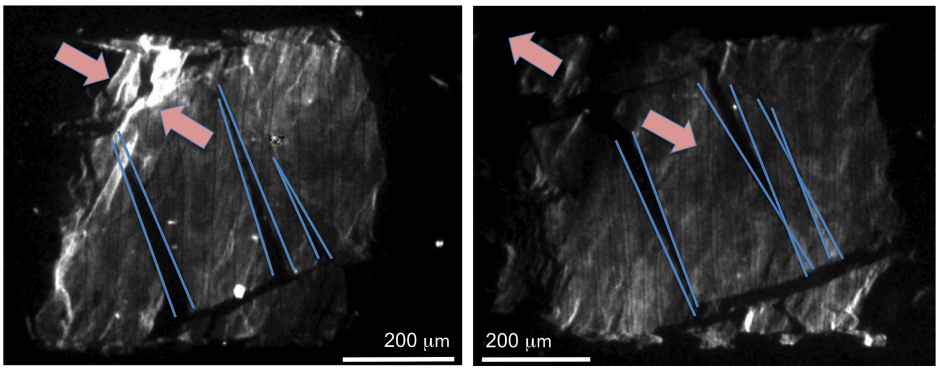

(a) "Line" beam illumination

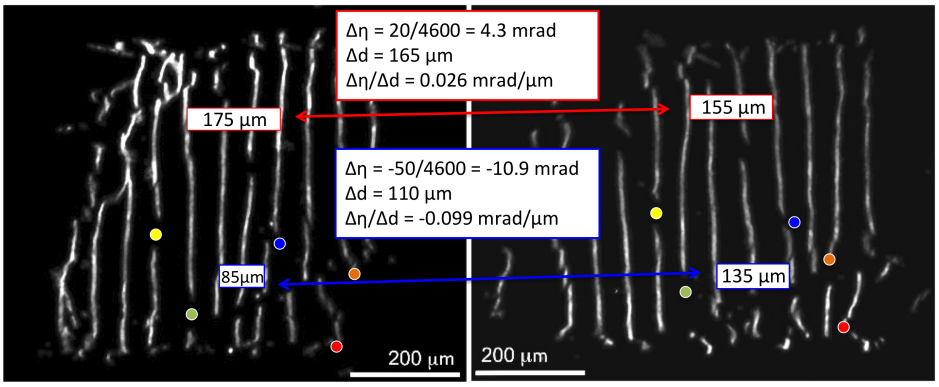

(b) "Pencil" beam illumination

Figure 8.6: (a) Some more guides for the eye were added to show asymmetric features: blue lines indicate twin edges and red arrows indicate that the diffracted intensity converges or diverges; (b) Coloured spots are guides identifying common features in the two images. Numbers in rectangular boxes represent lengths on the images defined by the boxes themselves.

- Background is reduced: only the diffracted beams reach the detector surface, avoiding the interactions of the direct beam with the scintillator screen.
- Optimised spatial resolution: the horizontal cross section of the grains are directly projected on the detector, without suffering from the compression of the vertical direction as observed in the forward scattering geometry, i.e. on the in-line detector. In the case of negligible intragranular orientation gradients, the three-dimensional grain volume is obtained by stacking the individually recorded section topographs, which allows skipping the reconstruction process.
- Improved azimuthal angle sensitivity: the distortion of projection images due to orientation gradients inside a grain is more pronounced at high diffraction angles. If D is the sample-detector distance, a change in the azimuthal angle $\Delta\eta$ of the diffracted beam will result in a displacement of about $D\Delta\eta\tan(2\theta)$ on the in-line detector and about $D\Delta\eta$ on the vertical detector. A typical value for the maximum 2θ scattering angle intercepted by the in-line detector is about 20°,

resulting in a factor $\gtrsim 1/\tan(20^\circ) \approx 3$ improvement in angular resolution for the vertical detector. See the geometry notation illustrated in appendix B.9.

- Friedel pairs of diffraction spots can still be collected.

Note that complete characterisation of an unknown sample would require a long acquisition procedure because the "pencil" beam scans would have to be acquired for a large number of rotation angles (in order to capture all grains) and for a number of steps covering the dimension of the sample. However, if the indexing procedure from a previous X-ray DCT scan is used to determine grain position and orientation of the grains, as in the present case, it is sufficient to select three independent reflections and their corresponding Friedel pairs in order to determine the local orientation changes in one single grain. This principle could be used in a future work where the analysis of the local ω and η diffraction angles will allow for determination of the orientation of each voxel of the grain volume. As the diffraction angles giving rise to reflections on the vertical detector can be simulated, the scanning procedure can be speeded up, without the need to scan the full sample.

The analysis of the lateral displacement of diffracted beams recorded on a 90° (vertical) detector provides access to local variations in η angle, as illustrated in figure 8.6. Last but not least, the observed line patterns may be used to validate advanced reconstruction algorithms (VIGANÒ *et al.*, 2014), applicable to measurements of local diffraction vectors from isolated diffraction volumes. This will serve as a test case for advanced reconstruction algorithms applicable to fast 2D acquisition schemes (DCT).
A change in 2θ angle (lattice spacing) will give rise to intensity variations along the lines. These variations are currently hard to analyse automatically and would require an important development of software tools for this kind of analysis. Working close to a three-beam case, KLUENDER *et al.* (2011) have managed to reconstruct local orientation for a ice single crystal combining pinhole topography of two reflections.

8.5 Conclusions

The described procedure combining X-ray DCT and subsequent pinhole topography allows a very promising characterisation of intragranular lattice distortions inside the grains. The observed deviations of the lines in pinhole topographs clearly indicate that intensity variations in section topographs arise from "orientation contrast" caused by local misorientations of the crystal lattice. A better visibility of twins and a visualisation of small angle boundaries ($\leq 1^\circ$) are possible in this combined imaging mode. However, the very high orientation gradients cause some problems, i.e. it is not obvious to detect continuity of "lines". Using focused beam (micro-scanning)

diffraction or the compound Fresnel refractive lenses (POULSEN and POULSEN, 2014) might be a better solution in this case.

8.6 Acknowledgements

The authors are grateful to Gulliermo Requena (former TU Vienna) for providing the samples and ESRF and its support staff are acknowledged for beam time on the beam line ID18F. The project was supported financially by the Engineering and Physical Science Research Council (EPSRC) in the UK (EP/F020910/1) and the ESRF in Grenoble, France.

8.7 References

BOZZOLO, N., CHAN, L., and ROLLETT, A. D. (2010), "Misorientations induced by deformation twinning in titanium", *Journal of Applied Crystallography* **43**, pp. 596–602.

BROWN, D. W. *et al.* (2007), "Twinning and detwinning during cyclic deformation of Mg alloy AZ31B", *Materials Science Forum* **539–543**, pp. 3407–3413.

JOHNSON, G. *et al.* (2008), "X-ray diffraction contrast tomography: a novel technique for three-dimensional grain mapping of polycrystals. II. The combined case", *Journal of Applied Crystallography* **41** (2), pp. 310–318.

KING, A. *et al.* (2008), "Observations of Intergranular Stress Corrosion Cracking in a Grain-Mapped Polycrystal", *Science* **321** (5887), pp. 382–385.

KING, A. *et al.* (2010), "Grain mapping by diffraction contrast tomography: extending the technique to sub-grain information", in: *Risoe International Symposium on Materials Science: Challenges in materials science and possibilities in 3D and 4D characterization techniques*.

KING, A. *et al.* (2011), "Three-dimensional in situ observations of short fatigue crack growth in magnesium", *Acta Materialia* **59** (17), pp. 6761–6771.

KLUENDER, R. T. *et al.* (2011), "Three-dimensional distortion measurements by section rocking curve imaging: Application to ice crystals", *physica status solidi (a)* **208** (11), pp. 2505–2510.

KVARDAKOV, V. *et al.* (2007), "Study of the three-dimensional distribution of defects in crystals by synchrotron radiation diffraction tomography", *Nuclear Instruments and Methods in Physics Research Section A: Accelerators, Spectrometers, Detectors and Associated Equipment* **575** (1–2), pp. 140–143.

LANG, A. R. and MAKEPEACE, A. P. W. (1996), "Reticulography: a simple and sensitive technique for mapping misorientations in single crystals.", *Journal of synchrotron radiation* **3** (6), pp. 313–315.

— (1999), "Synchrotron x-ray reticulography: principles and applications", *Journal of Physics D: Applied Physics* **32** (10A), A97–A103.

LI, S. F. and SUTER, R. M. (2013), "Adaptive reconstruction method for three-dimensional orientation imaging", *Journal of Applied Crystallography* **46** (2), pp. 512–524.

LÜBBERT, D *et al.* (2000), "μm-resolved high resolution X-ray diffraction imaging for semiconductor quality control", *Nuclear Instruments and Methods in Physics Research Section B: Beam Interactions with Materials and Atoms* **160** (4), pp. 521–527.

LUDWIG, W. *et al.* (2008), "X-ray diffraction contrast tomography: a novel technique for three-dimensional grain mapping of polycrystals. I. Direct beam case", *Journal of Applied Crystallography* **41** (2), pp. 302–309.

LUDWIG, W. *et al.* (2009a), "New opportunities for 3D materials science of polycrystalline materials at the micrometre lengthscale by combined use of X-ray diffraction and X-ray imaging", *Materials Science and Engineering: A* **524** (1–2), pp. 69–76.

LUDWIG, W. *et al.* (2009b), "Three-dimensional grain mapping by x-ray diffraction contrast tomography and the use of Friedel pairs in diffraction data analysis", *Review of Scientific Instruments* **80** (3), p. 033905.

LUDWIG, W. *et al.* (2010), "Characterization of Polycrystalline Materials Using Synchrotron X-ray Imaging and Diffraction Techniques", *JOM: the journal of the Minerals, Metals & Materials Society* **62** (12), pp. 22–28.

MIKULÍK, P *et al.* (2006), "Crystallite misorientation analysis in semiconductor wafers and ELO samples by rocking curve imaging", *Applied Surface Science* **253** (1), pp. 188–193.

ODDERSHEDE, J. *et al.* (2010), "Determining grain resolved stresses in polycrystalline materials using three-dimensional X-ray diffraction", *Journal of Applied Crystallography* **43** (3), pp. 539–549.

ODDERSHEDE, J. *et al.* (2012), "Measuring the stress field around an evolving crack in tensile deformed Mg AZ31 using three-dimensional X-ray diffraction", *Acta Materialia* **60** (8), pp. 3570–3580.

POULSEN, H. F. (2004), *Three-Dimensional X-Ray Diffraction Microscopy: Mapping Polycrystals and Their Dynamics*, Springer.

— (2012), "An introduction to three-dimensional X-ray diffraction microscopy", *Journal of Applied Crystallography* **45** (6), pp. 1084–1097.

POULSEN, S. O. and POULSEN, H. F. (2014), "Efficient Analytical Approaches to the Optics of Compound Refractive Lenses for Use with Synchrotron X-rays", *Metallurgical and Materials Transactions A* **45**, pp. 4772–4779.

REISCHIG, P. *et al.* (2013), "Advances in X-ray diffraction contrast tomography: flexibility in the setup geometry and application to multiphase materials", *Journal of Applied Crystallography* **46** (2), pp. 297–311.

RUTISHAUSER, S. *et al.* (2012), "Fabrication of two-dimensional hard X-ray diffraction gratings", *Microelectronic Engineering*, Preprint.

SCHMIDT, S. (2010), GrainSpotter v. 0.82, http://fable.svn.sourceforge.net/svnroot/fable/GrainSpotter.

SIMONS, H *et al.* (2015), "Dark-field X-ray microscopy for multiscale structural characterization.", *Nature communications* **6**, p. 6098.

SOMOGYI, A *et al.* (2001), "ID18F: A new micro-x-ray fluorescence end-station at the European Synchrotron Radiation Facility (ESRF): Preliminary results", *X-Ray Spectrometry* **30** (4), pp. 242–252.

SØRENSEN, H. O. *et al.* (2012), "Multigrain crystallography", *Zeitschrift für Kristallographie* **227** (1), pp. 63–78.

SUTER, R. M. *et al.* (2006), "Forward modeling method for microstructure reconstruction using x-ray diffraction microscopy: Single-crystal verification", *Review of Scientific Instruments* **77** (12), p. 123905.

VIGANÒ, N., LUDWIG, W., and BATENBURG, K. J. (2014), "Reconstruction of local orientation in grains using a discrete representation of orientation space", *Journal of Applied Crystallography* **47**, pp. 1826–1840.

Chapter 9

Conclusions

This thesis presents the results of the characterisation of deformation mechanisms in HCP metals. Deformation twinning during compression has been studied in commercially pure titanium and Ti-4Al alloys, as well as in AZ31 magnesium alloy, using X-ray diffraction imaging techniques, like X-ray diffraction contrast tomography (DCT) and X-ray section and pinhole topography. Whereas X-ray DCT can produce a spatially resolved 3D grain map of sample volumes containing several hundreds up to thousands of grains, X-ray section and pinhole topography apply to individual grains inside such a polycrystalline sample. Other techniques have been used for the cross-validation of the results, such as neutron diffraction, for the in-situ loading of a Ti-4Al alloy, and two-dimensional electron backscatter diffraction (EBSD), for the characterisation of the initial microstructure of the materials used in this work.

The first part of this thesis presented an analysis of the indexing procedure of a polycrystalline commercially pure titanium sample containing about 1750 grains. A comparison of indexing results obtained with the DCT and ImageD11 software packages, representing near-field and far-field approaches of the 3DXRD technique respectively, has been carried out. The measurements of grain position, size and crystallographic orientation have been analysed. An important aspect of the analysis was "matching" (cross-validation of indexing results), whereby the indexed grains from the near-field scan have been associated with the respective indexed grains from the far-field scan. The two techniques provide access to similar information (position, size, orientation) describing a polycrystalline aggregate and there was a good but not perfect agreement between the results from the two techniques.
The principle difference between the two techniques was the spatial resolution and the quantum efficiency of the detector systems employed. Consequently, near-field acquisition schemes are more accurate in spatial resolution and can be used for reconstruction of spatially resolved grain maps, whereas far-field acquisition schemes

are faster and provide more reliable angular resolution for scattering vectors.

Discrepancies between both approaches were mainly observed in the lower tail of the grain size distribution. For the far-field data, the finite dynamic range of the diffraction detector limited the minimum detected grain size with a single exposure in the current study to about 20 μm. A comparable value was obtained for the near-field diffraction data, but the limitation in this case was rather related to the poor quantum efficiency of the high resolution imaging system. Both algorithms can be used for fast indexing of datasets containing up to a few thousand grains.

The second part of this thesis was focused on the analysis of a Ti-4Al alloy compressed along the former rolling direction to 0.7% plastic strain. The work has been carried out first by using in-situ loading and neutron diffraction, followed by X-ray DCT. The main purpose of this work was to study the onset of deformation twinning and consider the 3D grain neighbourhood in this 3D analysis in order to elucidate possible twin nucleation criteria. A detailed comparison of the family of twinned grains with a family of similarly orientated grains that had not twinned has been carried out.

The neutron diffraction enabled the early detection of $\{10\bar{1}2\}\ \langle\bar{1}011\rangle$ tensile twinning, which has occurred after less than 1% plastic strain. A subsequent X-ray DCT analysis has confirmed the dominance of $\{10\bar{1}2\}\ \langle\bar{1}011\rangle$ twins. With the X-ray DCT methodology, almost 60 twinned grains were identified within the sample volume of about 400 grains, with a few cases of multiple twins per grain.

The detailed 3D analysis of the neighbourhood has revealed the importance of grain size on twin formation, looking at the distribution of grain size/volume of the two compared families of grains: the twinned grains and the similar oriented grains that had not twinned. A clear shift towards a higher mean value of the grain size/volume has been observed in the case of the twinned grains family. Conversely, an initial statistical analysis of the neighbourhood comparing Schmid factor, slip transfer parameter and crystallographic orientation distribution for the two families of grains has not revealed any significant differences.

Since the studied material was made by hundreds of grains, and those grains are confined into a limited volume, the neighbouring grains played an important role also in terms of slip and twinning shear transfer across grain boundaries. The 3D analysis of the neighbourhood has revealed the presence of chains/clusters of twins that have also developed an imperfect twin network. This clustering has been found related to the favourable conditions for prismatic $\langle a\rangle$ slip transfer between the parent grains that form the chains/clusters. This result has been obtained by performing a Luster-Morris parameter analysis in respect of prismatic $\langle a\rangle$ slip and twin shear within chains/clusters and in comparison to the neighbourhood of the non-twinned grain

family. The results are in good agreement with the prediction of twin clusters and the role of $\langle a \rangle$ slip strain localisation in Mg by TIMÁR and QUINTA DA FONSECA (2014). In contrast, easy shear transfer from $\{10\bar{1}2\}\ \langle\bar{1}011\rangle$ twins has not been identified to be relevant within the chains/clusters. This suggested that twin nucleation by stress concentration from a neighbouring grain that has twinned was not a main driving force for twin formation in Ti alloy.
It has to be noted that the presented observations are relevant for a compression experiment and that tensile loading would lead to different results. In the latter case the twinning grain has a 'hard' orientation while during compression loading the twinning grain would be in a 'soft' orientation in respect of slip.

The third part of this thesis concerned the characterisation of deformation mechanisms in magnesium alloys using X-ray section and pinhole topography and X-ray DCT. The combination of such procedures allowed a very promising characterisation of intragranular lattice distortions at the sub-grain level. Compared to the reconstruction of the sample from a standard X-ray DCT scan, it was possible to visualise slip bands and twins inside the bulk of grains in more detail. The variations in the patterns clearly indicate that intensity variations in section topographs arise from local misorientations.

9.1 Perspectives

Many possibilities for the continuation of this work can be considered:

- The X-ray DCT acquisition time went down from about 5 hours to nowadays 2 hours (using transfocators), whereas the saturation of the direct beam became 5 times bigger, yielding a much improved signal to noise ratio, crucial for detection of twins. Moreover, with the future upgrade of the ESRF storage ring, another factor of 20–50 in flux density will be expected, opening the possibility of in-situ observations of deformation twinning.

- The next generation of reconstruction algorithms results in much improved accuracy for moderately deformed materials. Moreover, this framework can be extended in a way such that parent and twin orientations are included in the reconstruction process, leading to a better shape reconstruction of twins.

- In order to study deformations inside the bulk of grains, one could "zoom" on individual grains/clusters using X-ray dark-field microscopy, topotomography or diffraction tomography (scanning micro-diffraction). These methods would allow the visualisation and identification of active slip systems, and early

detection of deformation twinning, i.e. a much more detailed view of the deformation mechanisms in a local neighbourhood.

- Attempts for identification of twins in the CP Ti and Ti-4Al alloy were initially done using as starting point the average orientation computed for the parent grain and the theoretical values of misorientation angle/axis relative to the twin mode, followed by the simulation of the twin variants on the detector and looking for intensity at the predicted spot positions. These attempts of automated twin detection failed because of the non-negligible orientation spread inside the grains, and deviations from the theoretical values. Thus, the calculation of the twin variants using only one value for the misorientation angle/axis was not successful. A search over a sub-volume in orientation space might solve this problem presumably, and lead to an improved ratio of detected versus existing twins.

Given these improvements, one can expect a new exciting era in the field of X-ray diffraction imaging techniques applied to studies of deformation and damage in structural materials.

Appendix A

Schmid factor and slip transfer calculation

Here below are listed the tables relative to the calculation of the slip transfer parameter *m'* and Schmid factor *m* along the chains/clusters formed by the twinned grains of the Ti-4Al sample as described in chapter 7. The slip transfer parameter *m'* has been computed for the prismatic $\langle a \rangle$ slip to prismatic $\langle a \rangle$ slip (column 2) and for $\{10\bar{1}2\}\ \langle\bar{1}011\rangle$ tensile twin to $\{10\bar{1}2\}\ \langle\bar{1}011\rangle$ tensile twin (column 3). The Schmid factor *m* has been computed for prismatic $\langle a \rangle$ slip (column 4) and $\{10\bar{1}2\}\ \langle\bar{1}011\rangle$ tensile twin (column 5).

Table A.1: Slip transfer parameter *m'* and Schmid factor *m* for chain 1

grainID	*m'* (prism → prism)	*m'* (twin → twin)	*m* (prism)	*m* (twin)
454			0.467	0.409
↓	0.713	0.736		
498			0.476	0.468
↓	0.786	0.834		
374			0.476	0.444
↓	0.310	0.973		
415			0.409	0.332
↓	0.906	0.916		
370			0.498	0.458
↓	0.226	0.910		
420			0.475	0.494

Table A.2: Slip transfer parameter *m'* and Schmid factor *m* for chain 2

grainID	*m'* (prism → prism)	*m'* (twin → twin)	*m* (prism)	*m* (twin)
497			0.464	0.406
↓	0.860	0.859		
388			0.475	0.420
↓	0.909	0.949		
416			0.474	0.419
↓	0.968	0.971		
386			0.411	0.338
↓	0.803	0.828		
404			0.494	0.447
↓	0.688	0.736		
376			0.492	0.451
↓	0.822	0.908		
469			0.471	0.476
↓	0.715	0.822		
394			0.476	0.421
↓	0.431	0.756		
395			0.481	0.453
↓	0.263	0.905		
447			0.496	0.465

Table A.3: Slip transfer parameter *m'* and Schmid factor *m* for chain 3

grainID	*m'* (prism → prism)	*m'* (twin → twin)	*m* (prism)	*m* (twin)
241			0.487	0.436
↓	0.950	0.952		
181			0.442	0.383
↓	0.983	0.981		
268			0.462	0.405
↓	0.698	0.690		
218			0.478	0.424
↓	0.589	0.628		
261			0.485	0.467
↓	0.947	0.965		
189			0.444	0.376
↓	0.696	0.706		
280			0.445	0.381
↓	0.792	0.787		
198			0.442	0.368
↓	0.282	0.940		
243			0.459	0.496
↓	0.398	0.791		
285			0.457	0.399
↓	0.276	0.871		
452			0.465	0.497

Table A.4: Slip transfer parameter *m'* and Schmid factor *m* for chain 4

grainID	*m'* (prism → prism)	*m'* (twin → twin)	*m* (prism)	*m* (twin)
32			0.495	0.472
↓	0.709	0.768		
8			0.446	0.374
↓	0.446	0.696		
55			0.475	0.421
↓	0.562	0.606		
28			0.442	0.430
↓	0.463	0.664		
50			0.490	0.479
↓	0.451	0.894		
4			0.430	0.348
↓	0.804	0.828		
16			0.450	0.389
↓	0.848	0.853		
110			0.487	0.439
↓	0.920	0.933		
15			0.437	0.378
↓	0.822	0.802		
17			0.409	0.325
↓	0.456	0.745		
67			0.394	0.284
↓	0.524	0.663		
42			0.444	0.384
↓	0.803	0.781		
61			0.460	0.402
↓	0.793	0.756		
111			0.470	0.413

Table A.5: Slip transfer parameter *m'* and Schmid factor *m* for chain 5

grainID	*m'* (prism → prism)	*m'* (twin → twin)	*m* (prism)	*m* (twin)
40			0.415	0.468
↓	0.534	0.617		
36			0.465	0.407
↓	0.399	0.817		
254			0.490	0.469
↓	0.780	0.880		
3			0.499	0.469
↓	0.264	0.965		
269			0.480	0.441
↓	0.590	0.739		
303			0.467	0.491
↓	0.799	0.848		
174			0.490	0.446
↓	0.857	0.926		
177			0.462	0.494
↓	0.884	0.881		
228			0.484	0.443
↓	0.930	0.941		
202			0.459	0.498
↓	0.979	0.977		
178			0.432	0.488
↓	0.670	0.675		
195			0.477	0.481
↓	0.458	0.868		
372			0.499	0.472
↓	0.686	0.677		
450			0.492	0.443
↓	0.917	0.956		
393			0.476	0.418
↓	0.988	0.987		
431			0.454	0.393

Appendix B

Crystallographic formulas

B.1 Symmetry operators

The symmetry operators for a given crystal system can be expressed by a rotation matrix (R) plus a translation vector ($\mathbf{t}$) as in equation (B.1).

$$\mathbf{X}' = R\mathbf{X} + \mathbf{t} \tag{B.1}$$

where $\mathbf{X}$ is the vector of components (x, y, z) of the generic position of an atom inside the unit cell and $\mathbf{X}'$ is the vector of components (x', y', z') of the position of the atom, obtained by applying the symmetry operator.
In this section only the rotation matrices for each crystal system used in FABLE are reported (http://sourceforge.net/projects/fable/).

triclinic:

$$\begin{pmatrix} 1 & 0 & 0 \\ 0 & 1 & 0 \\ 0 & 0 & 1 \end{pmatrix}$$

monoclinic:

$$\begin{pmatrix} 1 & 0 & 0 \\ 0 & 1 & 0 \\ 0 & 0 & 1 \end{pmatrix} \quad \begin{pmatrix} 1 & 0 & 0 \\ 0 & 1 & 0 \\ 0 & 0 & -1 \end{pmatrix}$$

orthorhombic:

$$\begin{pmatrix} 1 & 0 & 0 \\ 0 & 1 & 0 \\ 0 & 0 & 1 \end{pmatrix} \quad \begin{pmatrix} -1 & 0 & 0 \\ 0 & -1 & 0 \\ 0 & 0 & 1 \end{pmatrix} \quad \begin{pmatrix} -1 & 0 & 0 \\ 0 & 1 & 0 \\ 0 & 0 & -1 \end{pmatrix} \quad \begin{pmatrix} 1 & 0 & 0 \\ 0 & -1 & 0 \\ 0 & 0 & -1 \end{pmatrix}$$

tetragonal:

$$\begin{pmatrix} 1 & 0 & 0 \\ 0 & 1 & 0 \\ 0 & 0 & 1 \end{pmatrix} \quad \begin{pmatrix} -1 & 0 & 0 \\ 0 & -1 & 0 \\ 0 & 0 & 1 \end{pmatrix} \quad \begin{pmatrix} 0 & -1 & 0 \\ 1 & 0 & 0 \\ 0 & 0 & 1 \end{pmatrix}$$

$$\begin{pmatrix} 0 & 1 & 0 \\ -1 & 0 & 0 \\ 0 & 0 & 1 \end{pmatrix} \quad \begin{pmatrix} 1 & 0 & 0 \\ 0 & -1 & 0 \\ 0 & 0 & -1 \end{pmatrix} \quad \begin{pmatrix} 0 & -1 & 0 \\ -1 & 0 & 0 \\ 0 & 0 & -1 \end{pmatrix}$$
$$\begin{pmatrix} -1 & 0 & 0 \\ 0 & 1 & 0 \\ 0 & 0 & -1 \end{pmatrix} \quad \begin{pmatrix} 0 & 1 & 0 \\ 1 & 0 & 0 \\ 0 & 0 & -1 \end{pmatrix}$$

trigonal:

$$\begin{pmatrix} 1 & 0 & 0 \\ 0 & 1 & 0 \\ 0 & 0 & 1 \end{pmatrix} \quad \begin{pmatrix} -0.5 & 0.866 & 0 \\ -0.866 & -0.5 & 0 \\ 0 & 0 & 1 \end{pmatrix} \quad \begin{pmatrix} 0.5 & -0.866 & 0 \\ -0.866 & -0.5 & 0 \\ 0 & 0 & -1 \end{pmatrix}$$
$$\begin{pmatrix} -0.5 & -0.866 & 0 \\ 0.866 & -0.5 & 0 \\ 0 & 0 & 1 \end{pmatrix} \quad \begin{pmatrix} 0.5 & 0.866 & 0 \\ 0.866 & -0.5 & 0 \\ 0 & 0 & -1 \end{pmatrix} \quad \begin{pmatrix} -1 & 0 & 0 \\ 0 & 1 & 0 \\ 0 & 0 & -1 \end{pmatrix}$$

hexagonal:

$$\begin{pmatrix} 1 & 0 & 0 \\ 0 & 1 & 0 \\ 0 & 0 & 1 \end{pmatrix} \quad \begin{pmatrix} 0.5 & 0.866 & 0 \\ -0.866 & 0.5 & 0 \\ 0 & 0 & 1 \end{pmatrix} \quad \begin{pmatrix} -1 & 0 & 0 \\ 0 & 1 & 0 \\ 0 & 0 & -1 \end{pmatrix}$$
$$\begin{pmatrix} -0.5 & -0.866 & 0 \\ 0.866 & -0.5 & 0 \\ 0 & 0 & 1 \end{pmatrix} \quad \begin{pmatrix} 0.5 & -0.866 & 0 \\ 0.866 & 0.5 & 0 \\ 0 & 0 & 1 \end{pmatrix} \quad \begin{pmatrix} -0.5 & -0.866 & 0 \\ -0.866 & 0.5 & 0 \\ 0 & 0 & -1 \end{pmatrix}$$
$$\begin{pmatrix} -0.5 & 0.866 & 0 \\ -0.866 & -0.5 & 0 \\ 0 & 0 & 1 \end{pmatrix} \quad \begin{pmatrix} 0.5 & 0.866 & 0 \\ 0.866 & -0.5 & 0 \\ 0 & 0 & -1 \end{pmatrix} \quad \begin{pmatrix} -0.5 & 0.866 & 0 \\ 0.866 & 0.5 & 0 \\ 0 & 0 & -1 \end{pmatrix}$$
$$\begin{pmatrix} -1 & 0 & 0 \\ 0 & -1 & 0 \\ 0 & 0 & 1 \end{pmatrix} \quad \begin{pmatrix} 0.5 & -0.866 & 0 \\ -0.866 & -0.5 & 0 \\ 0 & 0 & -1 \end{pmatrix} \quad \begin{pmatrix} 1 & 0 & 0 \\ 0 & -1 & 0 \\ 0 & 0 & -1 \end{pmatrix}$$

cubic:

$$\begin{pmatrix} 1 & 0 & 0 \\ 0 & 1 & 0 \\ 0 & 0 & 1 \end{pmatrix} \quad \begin{pmatrix} 1 & 0 & 0 \\ 0 & -1 & 0 \\ 0 & 0 & -1 \end{pmatrix} \quad \begin{pmatrix} 1 & 0 & 0 \\ 0 & 0 & 1 \\ 0 & -1 & 0 \end{pmatrix}$$

$$\begin{pmatrix}1&0&0\\0&0&-1\\0&1&0\end{pmatrix} \quad \begin{pmatrix}0&1&0\\1&0&0\\0&0&-1\end{pmatrix} \quad \begin{pmatrix}0&1&0\\0&0&1\\1&0&0\end{pmatrix}$$
$$\begin{pmatrix}-1&0&0\\0&1&0\\0&0&-1\end{pmatrix} \quad \begin{pmatrix}0&0&1\\1&0&0\\0&1&0\end{pmatrix} \quad \begin{pmatrix}0&0&1\\0&-1&0\\1&0&0\end{pmatrix}$$
$$\begin{pmatrix}-1&0&0\\0&-1&0\\0&0&1\end{pmatrix} \quad \begin{pmatrix}0&1&0\\-1&0&0\\0&0&1\end{pmatrix} \quad \begin{pmatrix}0&-1&0\\0&0&-1\\1&0&0\end{pmatrix}$$
$$\begin{pmatrix}-1&0&0\\0&0&-1\\0&-1&0\end{pmatrix} \quad \begin{pmatrix}0&0&1\\-1&0&0\\0&-1&0\end{pmatrix} \quad \begin{pmatrix}0&0&1\\0&1&0\\-1&0&0\end{pmatrix}$$
$$\begin{pmatrix}-1&0&0\\0&0&1\\0&1&0\end{pmatrix} \quad \begin{pmatrix}0&-1&0\\-1&0&0\\0&0&-1\end{pmatrix} \quad \begin{pmatrix}0&-1&0\\0&0&1\\-1&0&0\end{pmatrix}$$
$$\begin{pmatrix}0&-1&0\\1&0&0\\0&0&1\end{pmatrix} \quad \begin{pmatrix}0&0&-1\\-1&0&0\\0&1&0\end{pmatrix} \quad \begin{pmatrix}0&0&-1\\0&-1&0\\-1&0&0\end{pmatrix}$$
$$\begin{pmatrix}0&0&-1\\1&0&0\\0&-1&0\end{pmatrix} \quad \begin{pmatrix}0&0&-1\\0&1&0\\1&0&0\end{pmatrix} \quad \begin{pmatrix}0&1&0\\0&0&-1\\-1&0&0\end{pmatrix}$$

B.2 Bravais lattices

In three-dimensions, the lattices are categorised into seven crystal lattice systems: triclinic, monoclinic, orthorhombic, tetragonal, trigonal, hexagonal and cubic. Within several of these, lattices supporting non-primitive unit cells can be defined. The classification scheme yields a total of 14 possible lattices, called Bravais lattices, figure B.1. The lattice symbols used for the classification are:

- Primitive (P): every lattice point contains an atom.
- Body-centered (I): an extra lattice point is centred in the exact middle of the cell.
- Face-centered (F): an extra lattice point is centred in every face of the cell.
- End-centered (A,B,C): an extra lattice point is centred in each of two opposing faces of the cell. A, B, C are the faces of the unit cell defined by lattice vectors b and c, a and c, and a and b respectively.
- Rhombohedral (R): rhombohedral primitive lattice.

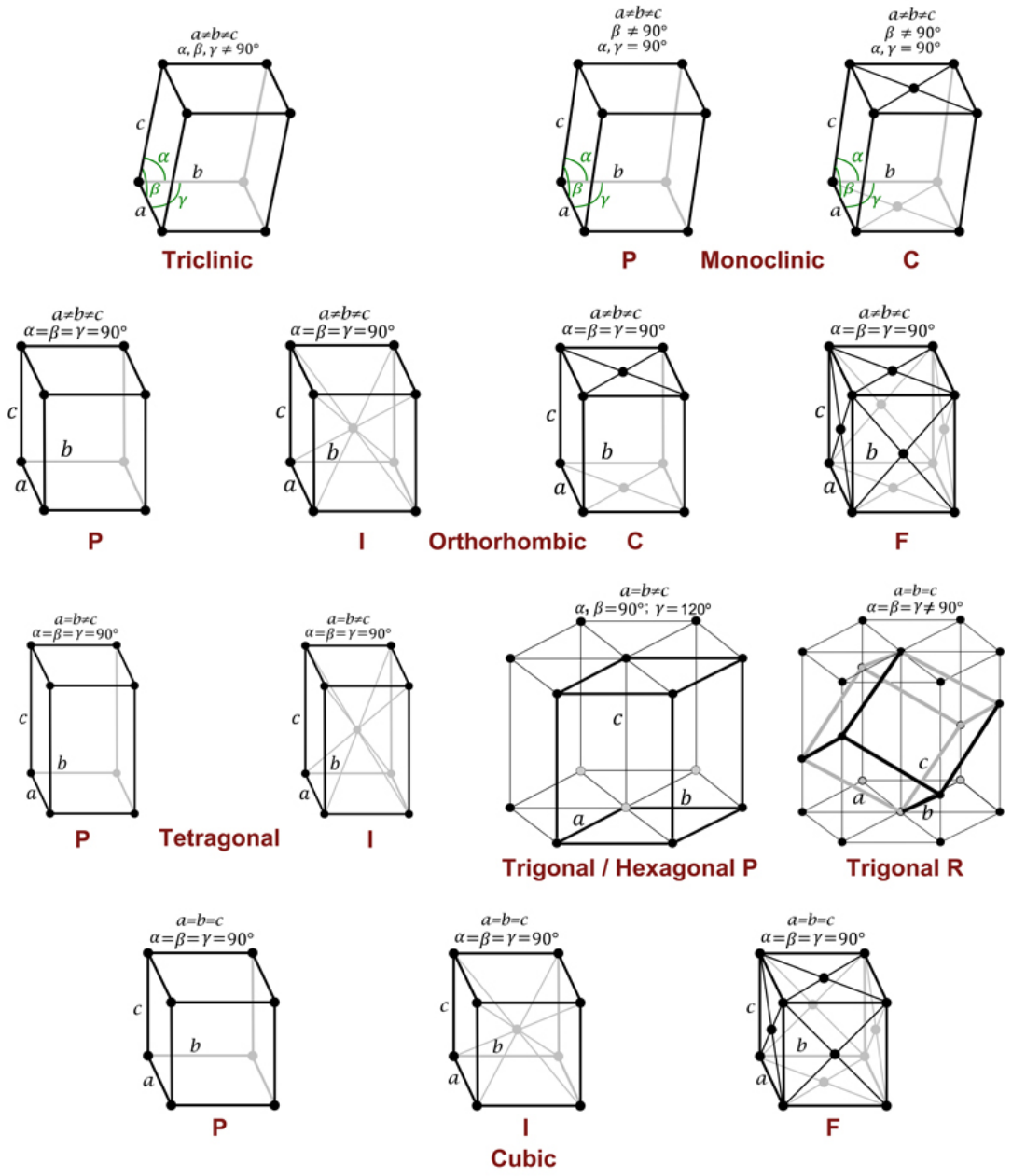

Figure B.1: The 14 Bravais lattices (http://www.xtal.iqfr.csic.es/Cristalografia/parte_03_4-en.html).

B.3 Lattice geometry: interplanar spacing

Let $a, b, c, \alpha, \beta, \gamma$ be the lattice parameters of the unit cell, the interplanar spacing (d) between adjacent planes in the *hkl* family can be derived from the following equations:

cubic:

$$\frac{1}{d_{hkl}^2} = \frac{h^2+k^2+l^2}{a^2} \tag{B.2}$$

tetragonal:

$$\frac{1}{d_{hkl}^2} = \frac{h^2+k^2}{a^2} + \frac{l^2}{c^2} \tag{B.3}$$

hexagonal / trigonal (P):

$$\frac{1}{d_{hkl}^2} = \frac{4}{3}\left(\frac{h^2+hk+k^2}{a^2}\right) + \frac{l^2}{c^2} \tag{B.4}$$

rhombohedral / trigonal (R):

$$\frac{1}{d_{hkl}^2} = \frac{(h^2+k^2+l^2)\sin^2\alpha + 2(hk+kl+hl)(\cos^2\alpha-\cos\alpha)}{a^2(1-3\cos^2\alpha+2\cos^3\alpha)} \tag{B.5}$$

orthorhombic:

$$\frac{1}{d_{hkl}^2} = \frac{h^2}{a^2} + \frac{k^2}{b^2} + \frac{l^2}{c^2} \tag{B.6}$$

monoclinic:

$$\frac{1}{d_{hkl}^2} = \frac{1}{\sin^2\beta}\left(\frac{h^2}{a^2} + \frac{k^2\sin^2\beta}{b^2} + \frac{l^2}{c^2} - \frac{2hl\cos\beta}{ac}\right) \tag{B.7}$$

triclinic:

$$\begin{aligned}\frac{1}{d_{hkl}^2} = \frac{1}{V^2}\Big(& b^2c^2\sin^2\alpha h^2 + a^2c^2\sin^2\beta k^2 + a^2b^2\sin^2\gamma l^2 \\ &+ 2abc^2(\cos\alpha\cos\beta-\cos\gamma)hk \\ &+ 2a^2bc(\cos\beta\cos\gamma-\cos\alpha)kl \\ &+ 2ab^2c(\cos\gamma\cos\alpha-\cos\beta)hl\Big)\end{aligned} \tag{B.8}$$

where

$$V = abc\sqrt{1-\cos^2\alpha-\cos^2\beta-\cos^2\gamma+2\cos\alpha\cos\beta\cos\gamma}$$

B.4 Cartesian coordinates

Sometimes it is convenient to transform from crystal coordinates to Cartesian coordinates. Let a, b, c be the real space lattice vectors and a^*, b^*, c^* the reciprocal space lattice vectors. The angles between those vectors are α, β, γ in the real space and $\alpha^*, \beta^*, \gamma^*$ in the reciprocal space. If the volume of the unit cell in the real space is V, the magnitudes of the reciprocal lattice vectors and the angles between them are written in equation (B.9).

$$\begin{aligned} a^* &= \frac{bc\sin\alpha}{V} \\ b^* &= \frac{ac\sin\beta}{V} \\ c^* &= \frac{ab\sin\gamma}{V} \\ \cos\alpha^* &= \frac{\cos\beta\cos\gamma - \cos\alpha}{\sin\beta\sin\gamma} \\ \cos\beta^* &= \frac{\cos\alpha\cos\gamma - \cos\beta}{\sin\alpha\sin\gamma} \\ \cos\gamma^* &= \frac{\cos\alpha\cos\beta - \cos\gamma}{\sin\alpha\sin\beta} \end{aligned} \tag{B.9}$$

The Cartesian coordinates x_c, y_c, z_c can be obtained from the crystal coordinates x, y, z using equation (B.10).

$$\begin{pmatrix} x_c \\ y_c \\ z_c \end{pmatrix} = \begin{pmatrix} \alpha & b\cos\gamma & c\cos\beta \\ 0 & b\sin\gamma & -c\cos\alpha^*\sin\beta \\ 0 & 0 & 1/c^* \end{pmatrix} \begin{pmatrix} x \\ y \\ z \end{pmatrix} \tag{B.10}$$

B.5 Sample and crystal axes definition

The sample reference system is defined by three unit vectors $\mathbf{X_S}$,$\mathbf{Y_S}$,$\mathbf{Z_S}$, identical to the laboratory reference system, and the Cartesian orthogonal basis for a crystal is defined by the three unit vectors $\mathbf{X_C}$,$\mathbf{Y_C}$,$\mathbf{Z_C}$, figure B.2.

B.6 Axes conventions for the hexagonal crystal systems

For hexagonal crystals there are two different axes conventions, depending on which lattice axis is parallel to the Cartesian $\mathbf{X_C}$ crystal axis. In both cases, the hexagonal

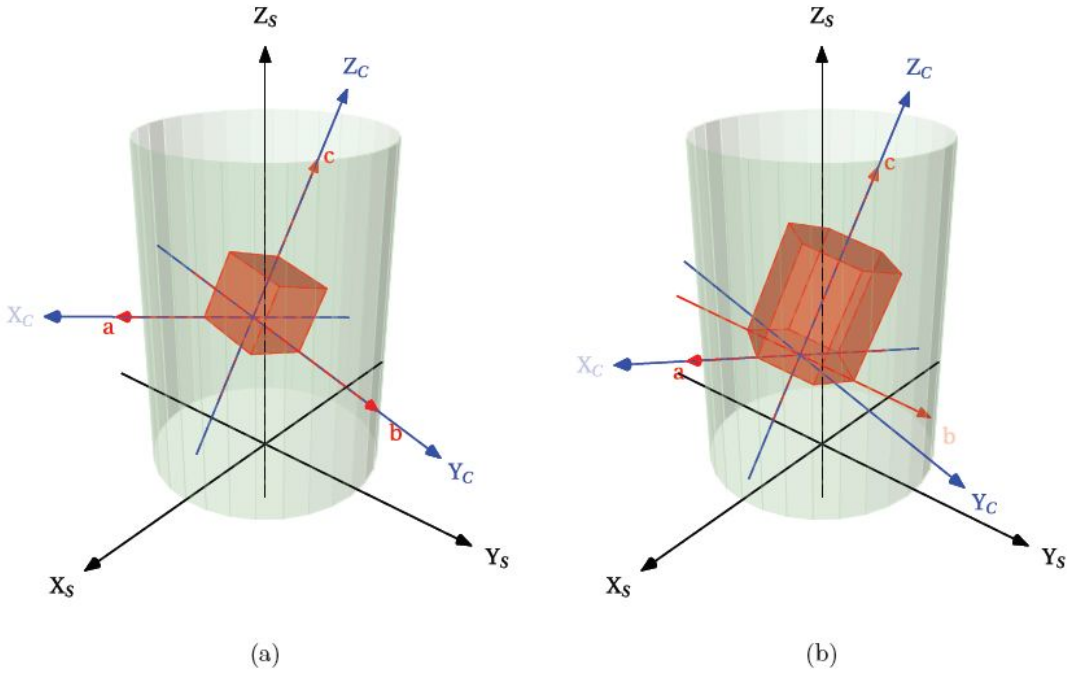

Figure B.2: Sample and crystal axes reference frames, as defined in the DCT code, for (a) cubic crystals and (b) hexagonal crystals. The sample is represented by the cylindric envelope and a, b, c are the unit cell lattice vectors.

crystal coordinates system follows a right-handed rotation and $\mathbf{Z_C}$ crystal axis is parallel to the $\langle c \rangle$ axis.

X axis convention

In the X axis convention the $\mathbf{X_C}$ crystal axis is aligned with the $\langle a \rangle$ axis and the $\mathbf{Y_C}$ crystal axis lies in the *ab* plane.

Y axis convention

In the Y axis convention the $\mathbf{Y_C}$ crystal axis is aligned with the $\langle b \rangle$ axis and the $\mathbf{X_C}$ crystal axis lies in the *ab* plane.

Both conventions are illustrated in figure B.3.

B.7 Axes notations for hexagonal crystal systems

For hexagonal crystal systems one can use two different axes notations: Miller notation (3 axes) and Miller-Bravais notation (4 axes).

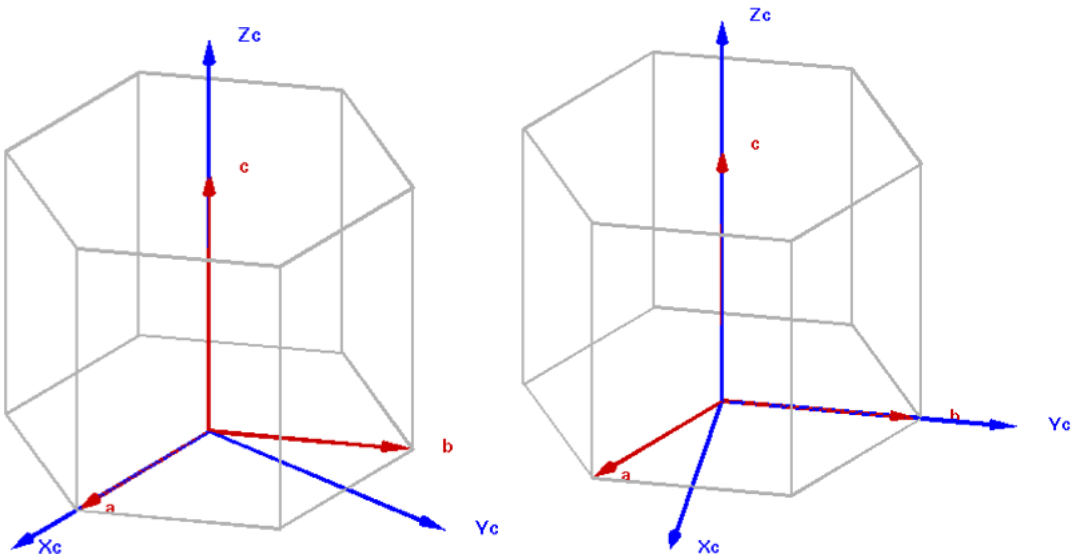

(a) X axis convention **(b)** Y axis convention

Figure B.3: Axes conventions for hexagonal crystal systems.

Miller notation

A plane in Miller notation is indicated with (hkl). A direction in Miller notation as $[uvw]$. In hexagonal crystals $\langle uvw \rangle$ directions in Miller notation are not perpendicular to $\{hkl\}$ planes, as in cubic system. For example, the $[210]$ is not perpendicular to (210), figure B.4.

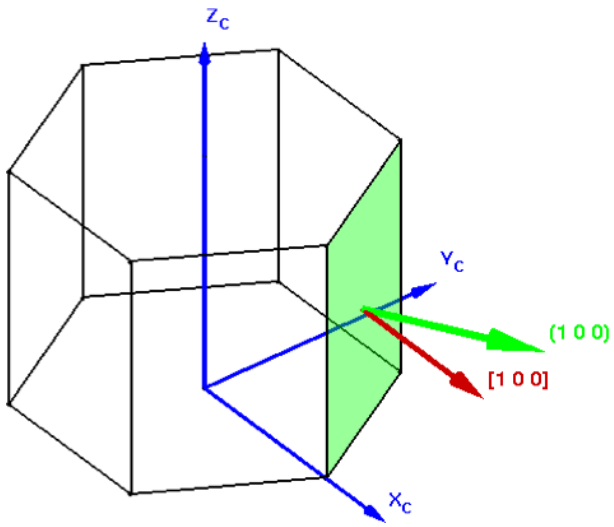

Figure B.4: Example of the non-perpendicularity of the $[210]$ direction to the (210) plane.

The three axes of hexagonal crystal systems using the Miller notation and the X axis convention are defined by equation (B.11).

$$\begin{aligned} a &= [100] = X_C \\ b &= [010] \\ c &= [001] = Z_C \end{aligned} \tag{B.11}$$

Miller-Bravais notation

A plane in Miller-Bravais notation is indicated with $(HKIL)$. A direction in Miller notation as $[UVTW]$. In hexagonal crystals $\langle UVTW \rangle$ directions in Miller-Bravais notation are perpendicular to $\{HKIL\}$ planes, as in cubic system. For example, the $[11\bar{2}0]$ is perpendicular to $(11\bar{2}0)$, figure B.5.

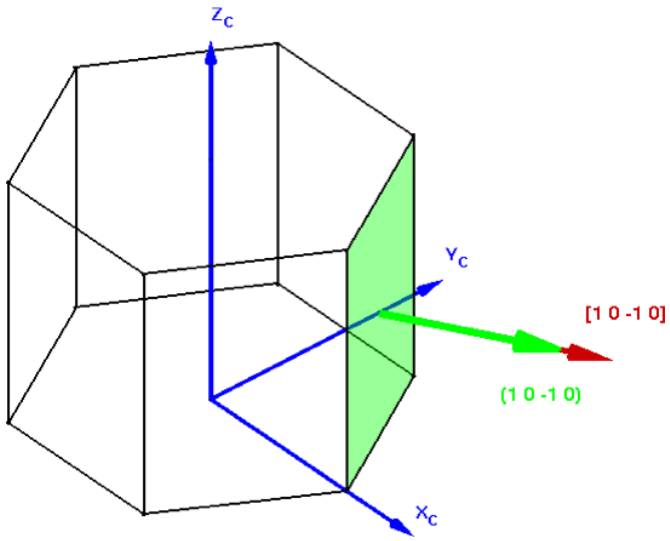

Figure B.5: Example of the perpendicularity of the $[11\bar{2}0]$ direction to the $(11\bar{2}0)$ plane.

The four axes of hexagonal crystal systems using the Miller-Bravais notation and the X axis convention are defined in equation (B.12).

$$\begin{aligned} a_1 &= [2\bar{1}\bar{1}0] = X_C \\ a_2 &= [\bar{1}2\bar{1}0] \\ a_3 &= [\bar{1}\bar{1}20] \\ c &= [0001] = Z_C \end{aligned} \tag{B.12}$$

Conversion from the two notations

There are simple relations to convert from Miller indices to Miller-Bravais indices and vice versa:

From Miller-Bravais to Miller indices:

$$\begin{aligned} u &= U - T \\ v &= V - T \\ w &= W \end{aligned} \qquad \text{(B.13)} \qquad\qquad \begin{aligned} u &= U \\ v &= V \\ w &= W \end{aligned} \qquad \text{(B.14)}$$

From Miller to Miller-Bravais indices:

$$\begin{aligned} U &= \frac{1}{3}(2u - v) \\ V &= \frac{1}{3}(2v - u) \\ T &= -\frac{1}{3}(u + v) \\ W &= w \end{aligned} \qquad \text{(B.15)} \qquad\qquad \begin{aligned} U &= u \\ V &= v \\ T &= -(u + w) \\ W &= w \end{aligned} \qquad \text{(B.16)}$$

B.8 $K - \eta$ notation for deformation twinning

The twinning elements in the $K - \eta$ notation are shown in figure B.6.

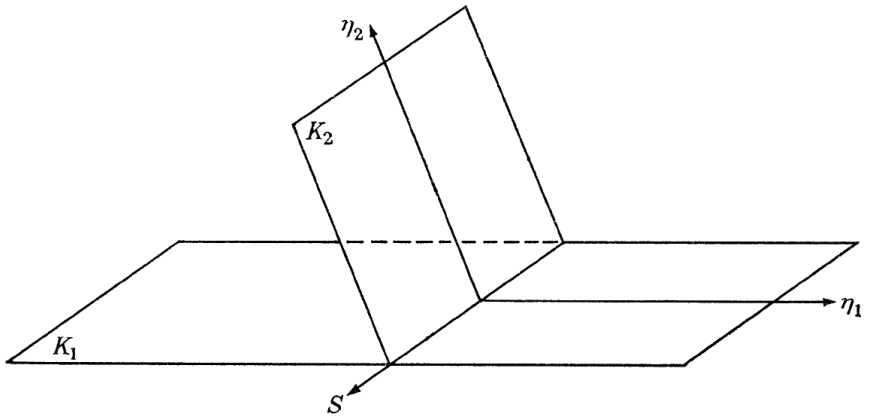

Figure B.6: $K - \eta$ notation for deformation twinning: the twinning plane K_1, the twinning direction η_1, the reciprocal twinning plane K_2 and the reciprocal twinning direction η_2. The normal to the shear plane S is contained in K_1 and K_2 and it is perpendicular to η_1 and η_2 (BILBY and CROCKER, 1965, p. 242).

B.9 "Pencil" beam illumination mode: geometry definition

In pinhole topography, diffraction spots using a 90° (vertical) detector look like the one shown in figure B.7. The nomenclature used to describe the geometry is here defined.

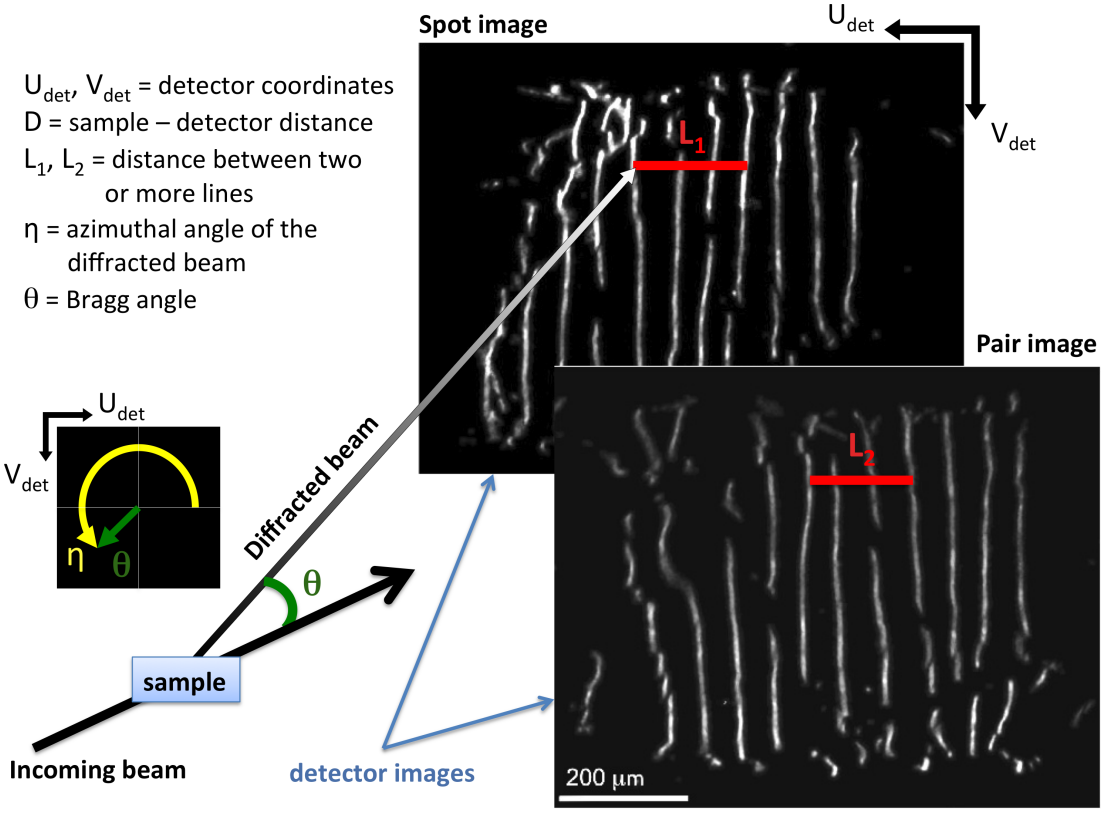

Figure B.7: Geometry of the detector used in the "pencil" beam illumination mode, with the typical "lines" pattern of the diffraction spots on the vertical detector.

Appendix C

Relevant Matlab Scripts

Due to the length of some functions and classes, headers of the methods/sub-functions are only included.

C.1 gtCrystCalculateReflecions.m

```
function list = gtCrystCalculateReflections(cryst, labgeo, energy, filename)
% GTCRYSTCALCULATEREFLECTIONS  Calculate the reflections list using python
%                              from xfab library in fable
%     list = gtCrystCalculateReflections(cryst, labgeo, energy, [filename])
%     ------------------------------------------------
%     List of theoretical reflections for a given crystal system and spacegroup
%
%     INPUT:
%       cryst    = <struct>     parameters.cryst(phaseid)
%       labgeo   = <struct>     parameters.labgeo
%       energy   = <double>     parameters.acq.energy (keV)
%       filename = <string>     filename for reflections list {'reflections_*.txt'}
%
%     OUTPUT:
%       list = structure with fields (the same with 'sp' for the full lists)
%            .hkl       = reflection list <double>
%            .theta     = theta value for each reflection <double>
%            .thetatype = theta type <double>
%            .sinthl    = sind(theta)/lambda <double>
%            .dspacing  = d-spacing <double>
%            .mult      = multiplicity of each reflections <double>
```

```
%
%
%      Version 002 12-12-2012 by LNervo
%        Compact output as a structure
%
%      Version 001 03-12-2012 by LNervo


latticepar = cryst.latticepar;
sg = cryst.spacegroup;

tmp = labgeo.detanglemin/2; % theta
minsintl = min(0.0001, sind(tmp)/gtConvEnergyToWavelength(energy));
tmp = labgeo.detanglemax/2;
maxsintl = sind(tmp)/gtConvEnergyToWavelength(energy);

if ~exist('filename','var') || isempty(filename)
    filename = 'reflections_';
end


latticepar_str = sprintf('%f ',latticepar);
latticepar_str = strtrim(latticepar_str);

% python script to be used
global GT_MATLAB_HOME;
script_file = fullfile(GT_MATLAB_HOME, 'zUtil_Python', '
    reflections_list.py');

% run the command for all the reflections
cmd = sprintf('%s %s %f %f %d %s %s', ...
              script_file,latticepar_str,minsintl,maxsintl,sg,'all',
    filename);
[~, msg] = gtPythonCommand(cmd, true); disp(msg);

% run the command for only the reflections unique
cmd = sprintf('%s %s %f %f %d %s %s', ...
              script_file,latticepar_str,minsintl,maxsintl,sg,'
    unique',filename);
[~, msg] = gtPythonCommand(cmd, true); disp(msg);

% read the full list of reflections
[~,Cmat] = gtReadTextFile([filename 'all.txt'],'%f %f %f %f',[1 3],
    true,'Delimiter','\n','CommentStyle','#');

% extracting information
hklsp = Cmat(:,1:3);
```

```
65 sinthlsp = Cmat(:,4);
66
67 % read the full list of reflections
68 [~,Cmat] = gtReadTextFile([filename 'unique.txt'],'%f %f %f %f',[1
       3],true,'Delimiter','\n','CommentStyle','#');
69
70 % extracting information
71 hkl = Cmat(:,1:3);
72 sinthl = Cmat(:,4);
73
74
75 if strcmp(cryst.crystal_system, 'hexagonal')
76     % getting 4-indexes notation
77     hklsp(:,4) = hklsp(:,3);
78     hklsp(:,3) = -hklsp(:,1)-hklsp(:,2);
79     hkl(:,4)   = hkl(:,3);
80     hkl(:,3)   = -hkl(:,1)-hkl(:,2);
81     disp('  h   k   i   l     theta   thetatype  mult    d-spacing')
       ;
82     disp('-------------------------------------');
83 else
84     disp('  h   k   l     theta   thetatype  mult    d-spacing');
85     disp('-------------------------------------------------------');
86 end
87
88 % extracting theta from sinthl = sin(theta)/lambda
89 thetasp = asind(sinthlsp*gtConvEnergyToWavelength(energy)); % fixed
       BUG !!!
90 theta = asind(sinthl*gtConvEnergyToWavelength(energy)); % fixed BUG
       !!!
91
92 [~, ind, thetatypesp] = unique(sinthlsp, 'stable');
93 thetatype = thetatypesp(ind);
94 mult = [ind(2:end)',length(thetatypesp)+1]-ind';
95
96 Bmat = gtCrystHKL2CartesianMatrix(latticepar);
97 dspacingsp = gtCrystDSpacing(hklsp', Bmat)';
98 dspacing = gtCrystDSpacing(hkl', Bmat)';
99
100
101 list.hklsp       = hklsp';
102 list.hkl         = hkl';
103 list.thetasp     = thetasp';
104 list.theta       = theta';
105 list.sinthlsp    = sinthlsp';
106 list.sinthl      = sinthl';
107 list.dspacingsp  = dspacingsp';
```

```
list.dspacing     = dspacing';
list.thetatypesp  = thetatypesp';
list.thetatype    = thetatype';
list.mult         = mult;
list.int          = ones(1,length(thetatype)); %dummy values
list.intsp        = ones(1,length(thetatypesp)); %dummy values
list.indfam       = ind';

for ii=1:length(list.thetatype)
    if ~strcmp(cryst.crystal_system, 'hexagonal')
        fprintf( '%3d %3d %3d %9.3f %5d %10d %10.3f\n',list.hkl(:,ii),list.theta(ii),list.thetatype(ii),list.mult(ii),list.dspacing(ii) );
    else
        fprintf( '%3d %3d %3d %3d %9.3f %5d %10d %10.3f\n',list.hkl(:,ii),list.theta(ii),list.thetatype(ii),list.mult(ii),list.dspacing(ii) );
    end
end

end % end of function
```

C.2 gtCrystCalculateSymmetryOperators.m

```
function [symm_unique, symm_all] = gtCrystCalculateSymmetryOperators(phaseid, sg, crystal_system)
% GTCRYSTCALCULATEREFLECTIONS  Calculate the symmetry operators list using python
%                              from xfab library in fable (sg.py)
%    [symm_unique, symm_all] = gtCrystCalculateSymmetryOperators(phaseid, [sg], [crystal_system])
%
% ------------------------------------------------------------------------

%    If spacegroup and crystal_system are not provided, they are read from
%    parameters.mat.
%
%    INPUT:
%      phaseid        = <double>   phase number {1}
%      sg             = <double>   spacegroup number
%      crystal_system = <string>   crystal system
%
%    OUTPUT:
%      symm_unique = <struct 1xN> contains :
%                .perm  = set of indistinguishable lattice permutations <double 3x3>
```

```
17 %               .g3    = set of unitary rotation matrices
   corresponding to the
18 %                        indistinguishable lattice permutations <
   double 3x3>
19 %       symm_all = <struct 1xM> contains :
20 %               .g3    = rotations (complete list using symmetry
   operators) <double 3x3>
21 %               .trans = translation values from symmetry operators
   <double 1x3>
22 %
23 %     Version 002 26-11-2013 by LNervo
24 %       Changed output names to 'symm_unique' and 'symm_all'
25 %       Changed symm_all.rot to symm_all.g3
26 %       Removed default value for phaseid
27 %
28 %     Version 001 10-12-2012 by LNervo
29
30
31 if ~exist('sg','var') || isempty(sg)
32     parameters = [];
33     load('parameters.mat');
34     sg = parameters.cryst(phaseid).spacegroup;
35 end
36
37 if ~exist('crystal_system','var') || isempty(crystal_system)
38     parameters = [];
39     load('parameters.mat');
40     crystal_system = parameters.cryst(phaseid).crystal_system;
41 end
42
43 global GT_MATLAB_HOME;
44 script_file = fullfile(GT_MATLAB_HOME, 'zUtil_Python', '
   symmetry_operators_list.py');
45 [~, msg] = gtPythonCommand([script_file ' ' num2str(sg) ' '
   crystal_system], true);
46 disp(msg);
47
48 % read produced files
49 permN     = gtReadTextFile(['perm_' crystal_system '.txt'],'%f %f %f
   ',[3 3],true,'Delimiter',' ','CommentStyle','#');
50 rotN      = gtReadTextFile(['rot_' crystal_system '.txt'],'%f %f %f'
   ,[3 3],true,'Delimiter',' ','CommentStyle','#');
51 all_rotN   = gtReadTextFile(['sg_rot_' crystal_system '.txt'],'%f %f
    %f',[3 3],true,'Delimiter',' ','CommentStyle','#');
52 all_transN = gtReadTextFile(['sg_trans_' crystal_system '.txt'],'%f
   %f %f',[1 3],true,'Delimiter',' ','CommentStyle','#');
53
```

```
symm_unique = struct('g3', rotN, 'perm', permN);
if nargout == 2
    symm_all = struct('g3', all_rotN, 'trans', all_transN);
end

end % end of function
```

C.3 GtAssembleVol3D.m::calculatePhaseVolumeTwins

```
    function volumeUpdate = calculatePhaseVolumeTwins(obj, volume,
    sampleInfo, phaseID, list)
    % GTASSEMBLEVOL3D/CALCULATEPHASEVOLUMETWINS
    % volume is zeros to build the new volume in
    % sample info includes bboxs and R vectors
    % list - grains to treat
    %
    % concept - place grain vol in a sample sized box
    % set undisputed voxels to the grainID
    % get a list of which grains overlap - test these for being
    twins
    % if they are twins, set the overlap to the grainID (principle
    of
    % largest first)

        obj.sigmas{phaseID} = gtCrystGetSigmas(obj.parameters.cryst(
    phaseID).crystal_system, ...
            obj.parameters.cryst(phaseID).latticepar, ...
            obj.localPar.convention);

        % check existence and validity of sigma_csl_twin parameter
        if (~isempty(obj.localPar.sigma_csl_twin) && ...
            ~ismember(obj.localPar.sigma_csl_twin, obj.sigmas{
    phaseID}(:, 1)))
            obj.localPar.sigma_csl_twin = [];
        end

        % how many grains to treat?
        grainsNum = length(list);

        index = obj.getGrainsSortedBySize(phaseID, list, 'descend');

        output     = cell(grainsNum, 1);
        twin_list  = zeros(grainsNum, 0);
        check_list = zeros(grainsNum, 0);
        merge_list = zeros(grainsNum, 0);
        desel_list = zeros(0, 1);
        fail_list  = zeros(0, 1);
```

```
34          hide_list   = zeros(grainsNum, 0);
35
36          gauge = GtGauge(grainsNum, sprintf('Phase %02d: ', phaseID))
    ;
37
38          % 1- twin
39          % 2- check possible twin
40          % 3- to be merged
41          % 4- deselected
42          % 5- failed
43          % 6- hidden twins
44          % 7- empty grain.seg volume
45          % 8- in conflict
46          foutput = cell(0, 8);
47
48          % loop through in descending size order
49          for kk = 1:length(list)
50              ii = index(kk);
51
52              gauge.setExtraText(sprintf('(grain %04d)', ii));
53              gauge.incrementAndDisplay();
54
55              % skip deselected grains
56              if (~sampleInfo.phases{phaseID}.getSelected(ii))
57                  foutput{end+1, 4} = sprintf('\nDeselected grainID %4
    d...', ii);
58                  desel_list(end+1, 1) = ii;
59                  continue;
60              end
61
62              % read the grain volume
63              try
64                  vol = obj.localPar.cache.get('grain', {phaseID, ii},
     'seg');
65                  volBBox = sampleInfo.phases{phaseID}.
    getBoundingBoxExtremes(ii);
66
67                  % Getting the intersecting volume of complete volume
     and
68                  % segmented volume
69                  if ~isempty(vol)
70                      [limsVolume, limsGrain] =
    gtGetVolsIntersectLimits(size(volume), size(vol), volBBox(1:3));
71                  else
72                      foutput{end+1, 7} = sprintf(['\nEmpty segmented
    volume for grainID %4d... '...
73                          'Please threshold it again!'], ii);
```

```
74                      continue
75                  end
76                  % Getting the subvolumes -> so we operate all the
    costy
77                  % operations on smaller volumes
78                  subVolume = volume( limsVolume(1, 1):limsVolume(2,
    1), ...
79                      limsVolume(1, 2):limsVolume(2, 2), ...
80                      limsVolume(1, 3):limsVolume(2, 3) );
81                  subGrain = vol( limsGrain(1, 1):limsGrain(2, 1), ...
82                      limsGrain(1, 2):limsGrain(2, 2), ...
83                      limsGrain(1, 3):limsGrain(2, 3) );
84
85                  % what grains overlap?
86                  disputes = subVolume(find(subGrain));
87                  disputes = unique(disputes);
88                  disputes(find(disputes == 0 | disputes == -1)) = [];
89
90                  if isempty(disputes)
91                      % Ok, no conflict or no twin case -> let's treat
     it as
92                      % normal case
93                      volume = gtPlaceSubVolume(volume, vol, volBBox
    (1:3), ...
94                          ii, obj.localPar.overlaps);
95                      continue
96                  end
97
98                  % first, assign the non disputed part
99                  indexes_notshared = find((subVolume == 0) & subGrain
    );
100                 subVolume(indexes_notshared) = ii;
101
102                 % now, go through the disputed grains checking
    orientations
103                 refRvector = sampleInfo.phases{phaseID}.getR_vector(
    ii);
104                 twincount  = 0;
105                 checkcount = 0;
106                 hidecount  = 0;
107                 info = {};
108                 for jj = 1:length(disputes)
109                     % test for being a twin
110                     testRvector = sampleInfo.phases{phaseID}.
    getR_vector(disputes(jj));
111                     [info{jj}, ~] = gtCrystTwinTest(refRvector,
    testRvector, phaseID, ...
```

```
112                         'symm', obj.symm{phaseID}, ...
113                         'sigmas', obj.sigmas{phaseID}, ...
114                         'merge_angle', obj.localPar.merge_angle, ...
115                         'convention', obj.localPar.convention);
116                     info{jj}.grainID_1 = ii;
117                     info{jj}.grainID_2 = disputes(jj);
118 
119                     % Test if it is twin of another grain
120                     indexes = find((subVolume == disputes(jj)) &
    subGrain);
121 
122                     info{jj}.indexes_shared = indexes;
123                     info{jj}.size_vol_free = length(
    indexes_notshared);
124                     info{jj}.size_vol      = length(
    indexes_notshared) + length(indexes);
125                     info{jj}.frac_shared   = length(indexes)/info{jj
    }.size_vol;
126 
127                     if (info{jj}.sigmaAnd == -1)
128                         if (info{jj}.frac_shared >= 0.5)
129                             % merge the two grains together; keep
    the parent
130                             %subVolume(indexes) = disputes(jj);
131                             foutput{end+1, 3} = sprintf(...
132                                 '\nGrains need merge (?): grain %4d
    and %4d - mis_angle %0.2f degrees (shared volume fraction %0.2f)'
    , ...
133                                 ii, disputes(jj), info{jj}.mis_angle
    , info{jj}.frac_shared);
134                             % record this in the merge list
135                             merge_list(ii, 1) = ii;
136                             merge_list(ii, 2) = disputes(jj);
137                         else
138                             % grains overlap
139                             foutput{end+1, 8} = sprintf(...
140                                 '\nGrains in conflict (?): grain %4d
     and %4d - mis_angle %0.2f degrees (shared volume fraction %0.2f)
    ', ...
141                                 ii, disputes(jj), info{jj}.mis_angle
    , info{jj}.frac_shared);
142                         end
143                     elseif ~isempty(info{jj}.sigmaAnd)
144                         if (info{jj}.frac_shared >= 0.5)
145                             % if no twin type specified or of twin
146                             % considered
```

```
147                             if (isempty(obj.localPar.sigma_csl_twin)
    || ...
148                                 (~isempty(obj.localPar.
    sigma_csl_twin) && ...
149                                 info{jj}.sigmaAnd(1) == obj.localPar
    .sigma_csl_twin))
150
151                                 % this is a twin. Allow the new
    grain (smaller)
152                                 % to overwrite the older grain
153                                 subVolume(indexes) = ii;
154                                 if (obj.localPar.use_parent_mask)
155                                     subVolume(indexes_notshared) =
    0;
156                                 end
157                                 foutput{end+1, 1} = sprintf(...
158                                     '\nFound twin %4d for grainID %4
    d with mis_angle %0.2f degrees (shared volume fraction %0.2f)',
    ...
159                                     ii, disputes(jj), info{jj}.
    mis_angle, info{jj}.frac_shared);
160                                 twin_list(ii, 1) = ii;
161                                 twin_list(ii, twincount+2) =
    disputes(jj);
162                                 twincount = twincount+1;
163                             elseif (~all(ismember([ii disputes(jj)],
     twin_list)))
164                                 % this is a twin, but we hide it.
165                                 %subVolume(indexes) = ii;
166                                 if (obj.localPar.use_parent_mask)
167                                     subVolume(indexes_notshared) =
    0;
168                                 end
169                                 foutput{end+1, 6} = sprintf(...
170                                     '\nHidden twin %4d for grainID
    %4d with mis_angle %0.2f degrees (shared volume fraction %0.2f)',
     ...
171                                     ii, disputes(jj), info{jj}.
    mis_angle, info{jj}.frac_shared);
172                                 hide_list(ii, 1) = ii;
173                                 hide_list(ii, hidecount+2) =
    disputes(jj);
174                                 hidecount = hidecount+1;
175                             end
176                         else
177                             % MAYBE this is a twin. Allow the new
    grain (smaller)
```

```
178                             % to overwrite the older grain: PROBLEM
179                             % WITH THE PARENT SEGMENTATION
180                             subVolume(indexes) = ii;
181                             if (obj.localPar.use_parent_mask)
182                                 subVolume(indexes_notshared) = 0;
183                             end
184                             foutput{end+1, 2} = sprintf(...
185                                 '\nCheck POSSIBLE twin %4d for
    grainID %4d with mis_angle %0.2f degrees (shared volume fraction
    %0.2f)', ...
186                                 ii, disputes(jj), info{jj}.mis_angle
    , info{jj}.frac_shared);
187                             check_list(ii, 1) = ii;
188                             check_list(ii, checkcount+2) = disputes(
    jj);
189                             checkcount = checkcount+1;
190                         end
191                     end
192                     if isempty(info{jj}.sigmaAnd)
193                         if (info{jj}.frac_shared < 0.5)
194                             % this is not a twin, so it is disputed
195                             switch (obj.localPar.overlaps)
196                                 case {'zero', 'conflict', 'adaptive'
    }
197                                     subVolume(indexes) = -1;
198                                 case 'summed'
199                                     subVolume(indexes) = subVolume(
    indexes) + ii;
200                                 case 'assign'
201                                     subVolume(indexes) = ii;
202                                 case 'parent'
203                                     subVolume(indexes) = disputes(jj
    );
204                             end
205                         end
206                     end
207                 end
208                 % Now let's get back the volume in the complete one
209                 volume = gtPlaceSubVolume(volume, subVolume, volBBox
    (1:3), ...
210                     0, 'assign');
211                 output{kk} = info;
212 
213             catch Mexc
214                 gtPrintException(Mexc, sprintf('\nGrain %d failed!!\
    n', ii));
```

```
215                 foutput{end+1, 5} = sprintf('\nFailed grainID %4d...
    Please check it!', ii);
216                 gauge.rePrint();
217                 fail_list(end+1, 1) = ii;
218             end % try catch loop
219         end % end for loop over kk
220 
221         gauge.delete();
222 
223         obj.redo = fail_list;
224 
225         % display on screen
226         for kk = 1:size(foutput, 2)
227             if (size(foutput(:, kk), 1) > 0)
228                 disp([foutput{:, kk}])
229             end
230         end
231 
232         % store twinInfo into object
233         obj.twinInfo{phaseID}.output     = output;
234         obj.twinInfo{phaseID}.foutput    = foutput;
235         obj.twinInfo{phaseID}.twin_list  = twin_list;
236         obj.twinInfo{phaseID}.check_list = check_list;
237         obj.twinInfo{phaseID}.merge_list = merge_list;
238         obj.twinInfo{phaseID}.desel_list = desel_list;
239         obj.twinInfo{phaseID}.fail_list  = fail_list;
240         obj.twinInfo{phaseID}.hide_list  = hide_list;
241 
242 
243         if (strcmpi(obj.localPar.overlaps, 'zero'))
244             % set overlapping regions to zero - this could be
    another label colour
245             volume(volume == -1) = 0;
246         end
247 
248         if (nargout > 0)
249             volumeUpdate = volume;
250         end
251     end % end function calculatePhaseVolumeTwins
```

C.4 gtTaperReadParFile.m

```
1 function parameters = gtTaperReadParFile(parfile)
2 % parameters = gtTaperReadParFile(parfile)
3 
4 fid = fopen(parfile);
5 C = textscan(fid, '%s %s');
```

```
fclose(fid);
index = [];
for ii=1:length(C{2})
    patt=regexp(C{2}{ii},'[0-9.e-]','match');
    C{3}{ii} = patt;
    if length(C{2}{ii})~=length(C{3}{ii})
        index(end+1) = ii;
    end
end

for ii=index
    C{1}(ii) = [];
    C{2}(ii) = [];
    C{3}(ii) = [];
end

for ii=1:length(C{2})
    C{4}{ii} = str2num(C{2}{ii});
end

final = [];

for ii=1:length(C{2})
    final.(C{1}{ii}) = C{4}{ii};
end

parameters = final;

end
```

C.5 gtTaperReadMapFile.m

```
function grain = gtTaperReadMapFile(pathtofiles,map_file,
   detector_par)
% grain = gtTaperReadMapFile(pathtofiles,map_file,detector_par)


if ~exist(pathtofiles,'dir') || isempty(pathtofiles)
    disp(['directory ' pathtofiles ' does not exist...'])
    return
end
if ~exist(fullfile(pathtofiles,map_file),'file')
    disp(['file ' map_file ' does not exist...'])
    return
end
if ~exist(fullfile(pathtofiles,detector_par),'file')
    disp(['file ' detector_par ' does not exist...'])
```

```
    return
end

output_gff = [map_file(1:end-4) '.gff'];
% to be run in the analsysis directory

%%%%%%%%%%%%%%%%%%%%%%%%%%%%%%%%%%%%%%%%%%%%%%%%%%
% convert ubi file into gff file
% grainno  x  y  z  rodx  rody  rodz
% ... U11  U12  U13  U21  U22  U23  U31  U32  U33
% ... eps11  eps22  eps33  eps23  eps13  eps12

cdir = pwd;
cd(pathtofiles);

cmd=['ubi_to_gff.py ' map_file ' ' detector_par ' ' output_gff];
[~,msg]=gtPythonCommand(cmd, true, false); disp(msg)

fid = fopen(output_gff);
C = textscan(fid, '%*d %f %f %f %f %f %f %f %f %f %f %f %f %f %f %f %f %f %f %f %f %f','Headerlines',1);
fclose(fid);
gff = cell2mat(C);

cen = gff(:,1:3); % x y z (mm)
rod = gff(:,4:6); % rx ry rz
U   = gff(:,7:15); % ... U11  U12  U13  U21  U22  U23  U31  U32  U33
eps = gff(:,16:end); % ... eps11  eps22  eps33  eps23  eps13  eps12

%%%%%%%%%%%%%%%%%%%%%%%%%%%%%%%%%%%%%%%%%%%%%%%%%%
% generate txt files from ubi file and save all into grain
bash_script = fullfile('/users',getenv('USER'),'matlabDCT','zUtil_Taper','script_generate_files.sh');
cmd = [bash_script ' ' map_file];
[~,msg]=unix(cmd); disp(msg)

cd(cdir);

fid = fopen(fullfile(pathtofiles,'translation.txt'));
C = textscan(fid, '%*s %d');
fclose(fid);
A0 = cell2mat(C);

fid = fopen(fullfile(pathtofiles,'rodrigues.txt'));
C = textscan(fid, '%*s %d');
fclose(fid);
A1 = cell2mat(C);
```

```
60
61 fid = fopen(fullfile(pathtofiles,'ids.txt'));
62 C = textscan(fid, '%*s %d');
63 fclose(fid);
64 A2 = cell2mat(C);
65
66 fid = fopen(fullfile(pathtofiles,'npeaks.txt'));
67 C = textscan(fid, '%*s %d');
68 fclose(fid);
69 A3 = cell2mat(C);
70
71 format longg
72 fid = fopen(fullfile(pathtofiles,'sum_of_all.txt'));
73 C = textscan(fid, '%f64');
74 fclose(fid);
75 A4 = cell2mat(C);
76
77 fid = fopen(fullfile(pathtofiles,'medians.txt'));
78 C = textscan(fid, '%f64');
79 fclose(fid);
80 A5 = cell2mat(C);
81
82 fid = fopen(fullfile(pathtofiles,'mins.txt'));
83 C = textscan(fid, '%f64');
84 fclose(fid);
85 A6 = cell2mat(C);
86
87 fid = fopen(fullfile(pathtofiles,'maxs.txt'));
88 C = textscan(fid, '%f64');
89 fclose(fid);
90 A7 = cell2mat(C);
91
92 fid = fopen(fullfile(pathtofiles,'means.txt'));
93 C = textscan(fid, '%f64');
94 fclose(fid);
95 A8 = cell2mat(C);
96
97 fid = fopen(fullfile(pathtofiles,'stds.txt'));
98 C = textscan(fid, '%f64');
99 fclose(fid);
100 A9 = cell2mat(C);
101
102 fid = fopen(fullfile(pathtofiles,'ns.txt'));
103 C = textscan(fid, '%d');
104 fclose(fid);
105 A10 = cell2mat(C);
106
```

```
grain = [];

for ii = 1:length(cen)

    grain{ii}.id        = ii;
    grain{ii}.center    = cen(ii,:);
    grain{ii}.R_vector  = rod(ii,:);
    grain{ii}.R_onedge  = false;
    grain{ii}.index     = A2(ii);
    grain{ii}.strain.strainT  = [eps(ii,1) eps(ii,6) eps(ii,5); ...
                                 eps(ii,6) eps(ii,2) eps(ii,4); ...
                                 eps(ii,5) eps(ii,4) eps(ii,3)];
    grain{ii}.strain.eps      = eps(ii,:);

    grain{ii}.stat.npeaks     = A3(ii);
    grain{ii}.stat.intmedian  = A5(ii);
    grain{ii}.stat.intmin     = A6(ii);
    grain{ii}.stat.intmax     = A7(ii);
    grain{ii}.stat.intmean    = A8(ii);
    grain{ii}.stat.intstd     = A9(ii);
    grain{ii}.stat.n          = A10(ii);
    grain{ii}.stat.sum_of_all = double(A4(ii));

    grain{ii}.stat.bbxsmean = 1;
    grain{ii}.stat.bbysmean = 1;

    grain{ii}.phaseid  = 1;

    grain{ii}.g        = [U(ii,1:3);U(ii,4:6);U(ii,7:9)];

end


end % end of function
```

C.6 gtTaperReadFltFile.m

```
function [data, data2] = gtTaperReadFltFile(fltfile)
% GTTAPERREADFLTFILE  Reads .flt file output from indexing ImageD11
%     [data, data2] = gtTaperReadFltFile(fltfile)
%     ------------------------------------------
%     INPUT:
%       fltfile  = <string>     name of the .flt file with peaks
    information
%
%     OUTPUT:
```

```
9  %       data      = <struct>     structure with column values for
   each field <double Nx1>
10 %       data2     = <cell Nx1>   cell structure for each peak with
   fields <struct>
11 %
12 %
13 %     Fields for each peak are:
14 %       sc                = distortion corrected centre of mass,
   slow index direction
15 %       fc                = distortion corrected centre of mass,
   fast index direction
16 %       omega             = omega (rotation sequence) centre of mass
17 %       Number_of_pixels  =  ... in the 3D connected object
18 %       avg_intensity     = average intensity of the pixels in the
   object
19 %       s_raw             = raw position (no spatial), slow
   direction
20 %       f_raw             = raw position (no spatial), fast
   direction
21 %       sigs              = second moment, slow direction
22 %       sigf              = second moment, fast direction
23 %       covsf             = covariance for fast/slow
24 %       sigo              = second moment, omega direction (out of
   plane of image)
25 %       covso             = covariance for slow/omega
26 %       covfo             = covariance for fast/omega
27 %       sum_intensity     = total intensity for pixels above
   threshold
28 %       sum_intensity^2   = summed intensity squared [not useful?]
29 %       IMax_int          = maximum pixel
30 %       IMax_s            = array index slow direction for maximum
   pixel
31 %       IMax_f            = array index fast direction for maximum
   pixel
32 %       IMax_o            = array index omega direction for maximum
   pixel
33 %       Min_s             = minimum pixel position in slow direction
34 %       Max_s             = maximum pixel position in slow direction
35 %       Min_f             = minimum pixel position in fast direction
36 %       Max_f             = maximum pixel position in fast direction
37 %       Min_o             = minimum pixel position in omega
   direction
38 %       Max_o             = maximum pixel position in omega
   direction
39 %       dety              = unlikely to be correct flipped direction
40 %       detz              = unlikely to be correct flipped direction
41 %       onfirst           = blob is present on first image
```

```
42 %       onlast             = blob is present on last image
43 %       spot3d_id          = line number - 1 (titles) in the file on
   creation by peaksearch.py
44 %       xl                 = x-component of scattering vector in the
   laboratory coordinate system (along the beam) with all angles at
   zero (units microns)
45 %       yl                 = y-component of scattering vector in the
   laboratory coordinate system (toward the door) with all angles at
    zero (units microns)
46 %       zl                 = z-component of scattering vector in the
   laboratory coordinate system (roughly up) with all angles at zero
    (units microns)
47 %       tth                = two theta angle (degrees)
48 %       eta                = azimuthal angle (degrees)
49 %       drlv2              =
50 %       labels             = grainID
51 %       tth_per_grain      =
52 %       eta_per_grain      =
53 %       gx                 = x-component of scattering vector (along
   the beam) with all angles at zero (units 1/  )
54 %       gy                 = y-component of scattering vector (toward
    the door) with all angles at zero (units 1/  )
55 %       gz                 = z-component of scattering vector (
   roughly up) with all angles at zero (units 1/  )
56 %       hr                 =
57 %       kr                 =
58 %       lr                 =
59 %       h                  =
60 %       k                  =
61 %       l                  =
62 %       Lorentz            =
63 %       Lorentz_per_grain  =
64 %
65 %
66 %     Version 001 11-06-2013 by LNervo
67
68
69 % read headers
70 fid = fopen(fltfile,'r');
71 titles = fgetl(fid);
72 if strfind(titles, 'filename') ~= 0
73     titles = fgetl(fid);
74 end
75 fclose(fid);
76 C = textscan(titles, '%s');
77 titles = C{1};
78 titles(1)=[];
```

```
79
80 ncols = length(titles);
81
82 titles = arrayfun(@(num) strrep(titles{num},'^','_'),1:ncols, '
   UniformOutput', false);
83
84 % read values
85 str_format = repmat('%f',1,ncols);
86 fid = fopen(fltfile,'r');
87 data_cell = textscan(fid,str_format,'CommentStyle','#','
   MultipleDelimsAsOne',true);
88 fclose(fid);
89
90 clear C fid
91 % take only existing columns
92
93 tmp = struct(titles{1},data_cell{1});
94 for ii=2:ncols
95     tmp.(titles{ii}) = data_cell{ii};
96 end
97
98 % add some useful columns
99 tmp.g_vec = [tmp.gx tmp.gy tmp.gz];
100 tmp.hkl   = [tmp.h  tmp.k  tmp.l];
101 tmp.hklr  = [tmp.hr tmp.kr tmp.lr];
102 tmp.xyzl  = [tmp.xl tmp.yl tmp.zl];
103
104
105 tmp.hklsp = tmp.hkl;
106
107 data = tmp;
108
109 if nargout > 1
110     tmp = cell(length(data_cell{1}),1);
111     for jj=1:length(data_cell{1})
112         for ii=1:ncols
113             tmp{jj}.(titles{ii}) = data_cell{ii}(jj);
114         end
115     end
116
117     data2 = tmp;
118 end
119
120 end % end of function
```

C.7 gtTaperUpdateGrains.m

```
function [grain, peaks_info] = gtTaperUpdateGrains(grain, peaks_info, cryst, saveFlag)
% [grain, peaks_info] = gtTaperUpdateGrains(grain, peaks_info, cryst, saveFlag)

if ~exist('saveFlag','var') || isempty(saveFlag)
    saveFlag = false;
end

if ~isfield(peaks_info, 'theta')
    [~, index] = sortrows([peaks_info.hkl peaks_info.tth/2],4);
    peaks_info.theta = peaks_info.tth/2;
    peaks_info.ind_sortByTheta = index;
end

% keep only families on detector
if ~isfield(peaks_info, 'thetatype')
    cryst.theta(cryst.theta > max(peaks_info.theta)) = [];

    for ii=1:length(peaks_info.theta)
        ind = find(abs(peaks_info.theta(ii) - cryst.theta) == min(abs(peaks_info.theta(ii) - cryst.theta)));
        peaks_info.thetatype(ii) = ind;
    end
end

if strcmp(cryst.crystal_system, 'hexagonal') && ~isfield(peaks_info, 'i')
    peaks_info.i = -(peaks_info.h+peaks_info.k);
    peaks_info.ir = -(peaks_info.hr+peaks_info.kr);
    peaks_info.hkl(:,4) = peaks_info.hkl(:,3);
    peaks_info.hkl(:,3) = -(peaks_info.hkl(:,1)+peaks_info.hkl(:,2));
    peaks_info.hklr(:,4) = peaks_info.hklr(:,3);
    peaks_info.hklr(:,3) = -(peaks_info.hklr(:,1)+peaks_info.hklr(:,2));
end

tocheck =[];
for jj=1:length(grain)
    fprintf('\b\b\b\b\b\b\b\b\b\b\b\b')

    index = jj-1;
    indGrain = find(peaks_info.labels == index);
    if grain{jj}.index ~= index
        tocheck = [tocheck; jj];
    end
```

```
42      grain{jj}.refind     = indGrain';
43      grain{jj}.npeaks     = length(indGrain);
44      grain{jj}.difspotID = peaks_info.spot3d_id(indGrain)';
45      grain{jj}.theta      = peaks_info.theta(indGrain)';
46      grain{jj}.thetatype = peaks_info.thetatype(indGrain)';
47      grain{jj}.eta        = peaks_info.eta(indGrain)';
48      grain{jj}.hklsp      = peaks_info.hkl(indGrain,:)';
49      grain{jj}.fc         = peaks_info.fc(indGrain)';
50      grain{jj}.sc         = peaks_info.sc(indGrain)';
51      grain{jj}.omega      = peaks_info.omega(indGrain)';
52      grain{jj}.deltaf     = (peaks_info.Max_f(indGrain) - peaks_info.
    Min_f(indGrain))';
53      grain{jj}.deltas     = (peaks_info.Max_s(indGrain) - peaks_info.
    Min_s(indGrain))';
54      grain{jj}.deltao     = (peaks_info.Max_o(indGrain) - peaks_info.
    Min_o(indGrain))';
55      grain{jj}.sumint     = peaks_info.sum_intensity(indGrain)';
56      grain{jj}.g_vec      = peaks_info.g_vec(indGrain,:)'; %Angstron
    ^-1
57      grain{jj}.xyzl       = peaks_info.xyzl(indGrain,:)'; %um
58      grain{jj}.drlv2      = peaks_info.drlv2(indGrain)';
59      grain{jj}.n_pixels   = peaks_info.Number_of_pixels(indGrain)';
60
61
62      list = gtCrystFindFamilies(grain{jj}.hklsp, cryst);
63      grain{jj} = gtAddMatFile(grain{jj}, list, true, true, false);
64
65      fprintf('grain # %04d',jj)
66  end
67
68  if saveFlag
69      save('peaks_info.mat','peaks_info','-v7.3');
70      disp('Saved peaks_info.mat')
71  end
72
73  end % end of function
```

C.8 gtDrawGrainUnitCells.m

```
1  function [f_handles, p_handles] = gtDrawGrainUnitCells(grains,
       varargin)
2  % GTDRAWGRAINUNITCELLS  Draws grain unit cells in the generalized
       case of more than one dataset
3  %     [f_handles, p_handles] = gtDrawGrainUnitCells(grains, varargin
       )
4  %
   ____________________________________________________________________
```

```
5  %     Draws grains by their unit cell representing grain size,
   location and
6  %     orientation by cubes or hexagonal prismes based on their
   Rodrigues vectors.
7  %
8  %     INPUT (- cell array -):
9  %       grains      = <cell>     grain cell-structure from indexing;
10 %                                one for each phase or one for each
   dataset
11 %
12 %     OPTIONAL INPUT (p/v pairs - cell arrays -): as in
   gtAppDrawGrainPars
13 %       ids         = <int>      list of grain IDs of interest; by
   default all
14 %                                the grains are drawn
15 %       cmap        = <double>   can be a component of the strain
   tensor
16 %                                {grain.strain.strainT(3, 3)} or a
   color map
17 %       hlight      = <int>      grain id-s to be highlighted {[]}
18 %       linecolor   = <double>   color for edges (1x3) {[0 0 0], [1
   0 0], ...}
19 %       strain      = <double>   scale factor for the strain values,
    if wanted. {0}
20 %                                (zero to use the unstrained unit
   cell)
21 %       alpha       = <double>   transparency value for patches {1}
22 %       phaseid     = <int>      phase number {1}
23 %       patch       = <logical>  true if drawing the patch of the
   unit cell <true>
24 %       pxsize      = <double>   pixel size (mm/px) {0.001}
25 %       ratio       = <double>   c/a ratio; if empty, taken from
   parameters.cryst {[]}
26 %       type        = <string>   unit cell type; if empty, taken
   from parameters.cryst {''}
27 %       label       = <string>   name for entry in the legend {''}
28 %       pars        = <struct>   Dataset parameters.mat:cryst,
   labgeo {[]}
29 %       shift       = <double>   Shift in Z for the current dataset
   with respect to the
30 %                                previous dataset (mm) {[]}
31 %       mrot        = <double>   matrix rotation for grains {[]}
32 %
33 %     OPTIONAL INPUT (p/v pairs): as in gtAppDrawGrainPars
34 %       orig        = <double>   sample reference (arrows) origin (
   same units as sampleenv)
35 %       caxis       = <logical>  flag to draw the c-axis {false}
```

```
36 %       pixels      = <logical>  flag to switch to pixels {false}
37 %       draw        = <logical>  Draw grain patches {true}
38 %       scale       = <logical>  Scale grain size {true}
39 %       size        = <double>   Factor to scale all the grains
   equally {[]}
40 %       translate   = <logical>  Translate grain centers {true}
41 %       stacked     = <logical>  Flag to draw a stack of datasets {
   false}
42 %       stack_dir   = <string>   Stack direction {'bot'} | 'top'
43 %       stack_order = <double>   Stack volumes order {1:numel(grains
   )}
44 %       tomo_setup  = <logical>  Use tomographic coordinates setup {
   false}
45 %
46 %       section     = <logical>  Draw a section for each grain {
   false}
47 %       secpos      = <double>   Section position {[]}
48 %       plane       = <string>   Section plane {'xy'}
49 %       paired      = <logical>  paired grains drawing useful for
   twins
50 %                                One figure for each pair {false}
51 %
52 %       figure      = <logical>  Display or not the figure {true}
53 %       figpos      = <double>   figure position in pixels (1x4)
   {[]}
54 %       figcolor    = <double>   figure background color {[0 0 0]}
55 %       legend      = <logical>  display or not the legend {false}
56 %       legendpos   = <double>   location of the legend box {'
   NorthEast'}
57 %       showaxes    = <logical>  Shows axes or not {true}
58 %       sampleaxes  = <logical>  Draw sample axes {true}
59 %       sampleenv   = <logical>  Draw sample envelope {true}
60 %       zoom        = <double>   zoom in of this quantity {[]}
61 %       view        = <double>   3D angular view (1x2) {[-45 20]}
62 %       verbose     = <logical>  print comments {false}
63 %
64 %       hf          = <handle>   existing figure handle {[]}
65 %       ha          = <handle>   existing axes handle {[]}
66 %
67 %    OUTPUT:
68 %       f_handles   = <struct>   figure handles
69 %       p_handles   = <handle>   patches handle
70 %
71 %    Usage:
72 %       For IPF-Z coloring for phase 1:
73 %         load parameters
74 %         load 4_grains/phase_01/index.mat grain
```

```
%         gtDrawGrainUnitCells({grain}, 'cmap', {gtIPFCmap(1, [0 0
    1])}, 'pxsize', {parameters.acq.pixelsize})
%
%       With random coloring and displaying only some grains:
%         gtDrawGrainUnitCells({grain}, 'ids', {1:10}, 'cmap', {
    gtRandCmap(10)}, 'pxsize', {parameters.acq.pixelsize})
%
%     Version 011 10-11-2014 by LNervo
%       Introduced the use of class 'GtUtilities' in place of sub-
    functions

%     Version 010 27-10-2014 by LNervo
%       Added 'pars', 'shift', 'stacked', 'stack_dir', 'stack_order
    ', 'tomo_setup' options for different datasets
%
%     Version 009 30-07-2014 by LNervo
%       Created gtAppDrawGrainPars
%     Version 008 20-01-2014 by LNervo
%
%     Version 007 17-10-2013 by LNervo
%       Added some options
%     Version 006 06-06-2013 by LNervo
%       Added function to compute unit cell vertices, modified
%       gtPlotGrainUnitCell
%     Version 005 11-03-2013 by LNervo
%       Use cell arrays to plot multiple datasets
%     Version 004 15-11-2012 by LNervo
%       Use gtDrawSampleGeometry(labgeo) to create the graphics with
     axis and reference
%       system
%     Version 003 23-10-2012 by LNervo
%       Add varargin


% default parameters
app = gtAppDrawGrainPars(grains);
[app, rej_pars] = parse_pv_pairs(app, varargin);

if (~app.pixels)
    app.sampleaxes = false;
end
if numel(grains) == 1 && all([app.ids{:}] <= length(grains{1}))
    app.stacked = false;
end
if ~ismember(app.stack_dir, {'bot', 'top'})
    disp('Option stack_dir not valid... not stacking')
    app.stacked = false;
```

```
117 end
118
119 % from parameters hipothesis : top = bot as abs value
120 % centered sample envelope
121 if isempty(app.pars{1})
122     tmpPar = load('parameters.mat');
123     app.pars{1} = GtUtilities.get_pars(tmpPar.parameters);
124     clear tmpPar
125 end
126 if isempty(app.pxsize{1})
127     app.pxsize{1} = GtUtilities.get_pxsize(app.pars{1});
128 end
129
130 % setting up variables
131 for ii = 1:numel(grains)
132     if (ii > 1)
133         if numel(app.type)    < ii, app.type{ii}    = app.type{1};
    end
134         if numel(app.ratio)   < ii, app.ratio{ii}   = app.ratio{1};
    end
135         if numel(app.hlight)  < ii, app.hlight{ii}  = app.hlight{1};
     end
136         if numel(app.label)   < ii, app.label{ii}   = app.label{1};
    end
137         if numel(app.phaseid) < ii, app.phaseid{ii} = app.phaseid
    {1}; end
138         if numel(app.strain)  < ii, app.strain{ii}  = app.strain{1};
     end
139         if numel(app.pars)    < ii, app.pars{ii}    = app.pars{1};
    end
140         if numel(app.pxsize)  < ii, app.pxsize{ii}  = app.pxsize{1};
     end
141         if numel(app.cmap)    < ii, app.cmap{ii}    = []; end
142         if numel(app.mrot)    < ii, app.mrot{ii}    = []; end
143         if numel(app.shift)   < ii, app.shift{ii}   = []; end
144     end
145     % update sample envelope
146     app.pars{ii}.labgeo = gtGeoSamEnvFromAcq(app.pars{ii}.labgeo,
    app.pars{ii}.acq);
147     if isempty(app.pxsize{ii}), app.pxsize{ii} = GtUtilities.
    get_pxsize(app.pars{ii}); end
148     % crystallographic data
149     cryst = app.pars{ii}.cryst(app.phaseid{ii});
150     if isempty(app.type{ii}),    app.type{ii}   = cryst.
    crystal_system; end
151     if isempty(app.ratio{ii}),   app.ratio{ii}  = cryst.latticepar(3)
    /cryst.latticepar(1); end
```

```
152     % IDs and cmap
153     if isempty(app.ids{ii}),    app.ids{ii}    = 1:length(grains{ii
    }); end
154     if isempty(app.cmap{ii}),   app.cmap{ii}   = app.linecolor{ii};
    end
155
156     % stack options
157     if (app.stacked)
158         if isempty(app.shift{ii})
159             if strcmpi(app.stack_dir, 'bot')
160                 app.shift{ii} = GtUtilities.get_stack_shift_bot( app
    .pars, ii );
161             elseif strcmpi(app.stack_dir, 'top')
162                 app.shift{ii} = GtUtilities.get_stack_shift_top( app
    .pars, ii );
163             end
164         end
165         app.pars{ii}.labgeo.samenvtop = app.pars{ii}.labgeo.
    samenvtop + app.shift{ii};
166         app.pars{ii}.labgeo.samenvbot = app.pars{ii}.labgeo.
    samenvbot + app.shift{ii};
167     end
168 end
169
170 % sample envelope and figure
171 if isempty(app.hf)
172     app.senv = [];
173     vars_in = {'orig', app.orig, 'centered', true, 'max', 100, ...
174                'axes', app.sampleaxes, 'sample', app.sampleenv};
175     if (app.stacked)
176         for ii = 1:numel(grains)
177             if ii > 1
178                 vars_in(end+1:end+4) = {'hf', h_tmp.fig, 'ha', get(
    h_tmp.fig, 'CurrentAxes')};
179             end
180             % stacked
181             h_tmp = gtDrawSampleGeometry(app.pars{ii}.labgeo, ...
182                 'pixels', app.pixels, 'pxsize', app.pxsize{ii},
    vars_in{:});
183             app.senv = [h_tmp.senv, app.senv];
184         end
185     else
186         disp('Sample envelope info from dataset 1')
187         h_tmp = gtDrawSampleGeometry(app.pars{1}.labgeo, ...
188             'pixels', app.pixels, 'pxsize', app.pxsize{1}, vars_in
    {:});
189         app.senv = h_tmp.senv;
```

```
190     end
191     h.fig = h_tmp.fig;
192     app.ha     = h_tmp.ax;
193     app.hf     = h_tmp.fig;
194     app.rot3d = h_tmp.rot3d;
195 else
196     h.fig = app.hf;
197     app.senv  = findobj(h.fig, 'tag', 'sampleenv');
198     app.rot3d = rotate3d(h.fig);
199     set(app.rot3d, 'RotateStyle', 'box', 'Enable', 'on');
200 end
201 % axes
202 if isempty(app.ha)
203     if ~isempty(gca)
204         app.ha = get(h.fig, 'CurrentAxes');
205     else
206         app.ha = axes('Parent', h.fig);
207     end
208 end
209
210 % create GUI
211 h.numData = length(grains);
212 h = GtUtilities.createGUI(h);
213 set(app.ha, 'Parent', h.axis_panel);
214 hold(app.ha, 'on');
215
216 % draw unit cells
217 hp = [];
218 % loop over datasets
219 for ii = 1:numel(grains)
220     if isrow(app.cmap{ii}) && all(app.linecolor{ii} == app.cmap{ii})
221         app.linecolor{ii} = app.linecolor{ii+1};
222     end
223     ids    = unique(app.ids{ii}, 'stable');
224     grain = grains{ii};
225     cmap  = app.cmap{ii};
226
227     % if single value (RGB), copy it for all the grains
228     if isrow(cmap) || (numel(cmap) == 3)
229         cmap = repmat(cmap, length(grain), 1);
230     end
231     % remove bkg color
232     if all(cmap(1, :) == [0 0 0]) && size(cmap, 1) == length(grain)
    + 1
233         cmap(1, :) = [];
234     end
235     app.cmap{ii} = cmap;
```

```
236
237     % get selected grains for current datasets
238     grain = grain(ids);
239     cmap  = cmap(ids, :);
240
241     % vertices and faces calculation
242     %%% TO DO LIST : unify in one function
243     if strcmpi(app.type{ii}, 'hexagonal')
244         data{ii} = gtHexagonalUnitCell('ratio', app.ratio{ii}, 'draw
    ', false, 'centered', true, 'caxis', app.caxis);
245     else
246         if ~strcmpi(app.type{ii}, 'cubic')
247             disp('Crystal unit cell not supported yet... Using cubic
    ')
248         end
249         data{ii} = gtCubicUnitCell('ratio', app.ratio{ii}, 'draw',
    false, 'centered', true, 'caxis', app.caxis);
250     end
251
252     % loop over grains
253     p = [];
254     for jj = 1:length(grain)
255         % grain size
256         %%% TO DO: add automatic normintmean calculation
257         if isfield(grain{jj}, 'stat')
258             if isfield(grain{jj}.stat, 'size_int') %px
259                 grain{jj}.radius = 0.5*app.pxsize{ii}*grain{jj}.stat
    .size_int; % mm
260             elseif isfield(grain{jj}.stat, 'bbxsmean') && isfield(
    grain{jj}.stat, 'bbysmean') %px
261                 grain{jj}.radius = 0.5*app.pxsize{ii}*(grain{jj}.
    stat.bbxsmean + grain{jj}.stat.bbysmean)/2; % mm
262             end
263         elseif isfiled(grain{jj}, 'size_int') %um
264             grain{jj}.radius = 0.5*grain{jj}.size_int/1000;%mm
265         else
266             grain{jj}.radius = 0.5*app.pxsize{ii}*10;%mm
267         end
268         if (app.scale == false && ~isempty(app.size) && isnumeric(
    app.size) && app.size > 0)
269             % it should be a multiplying factor
270             grain{jj}.radius = 0.5*app.pxsize{ii}*app.size;%mm
271         end
272         if (app.stacked && numel(grains) > 1)
273             grain{jj}.center(3) = grain{jj}.center(3) + app.shift{ii
    };%mm
274         end
```

```
275         if (app.pixels)
276             grain{jj}.radius = grain{jj}.radius/app.pxsize{ii};%px
277             grain{jj}.center = grain{jj}.center/app.pxsize{ii};%px
278         end
279         % translate
280         if (~app.translate && ~app.stacked)
281             grain{jj}.center = zeros(1, 3);
282         end
283         % grain strain
284         if ~isfield(grain{jj}, 'strain')
285             grain{jj}.strain.strainT = NaN(3);
286         end
287         % highlight grain?
288         if ismember(jj, app.hlight{ii}), hl = true; else hl = false;
    end
289
290         % computes vertices and caxis coordinates
291         vertices{jj} = gtComputeGrainUnitCell(grain{jj}.R_vector,
    data{ii}.vertices, ...
292             grain{jj}.radius, grain{jj}.center, grain{jj}.strain.
    strainT, app.strain{ii});
293         if (app.caxis)
294             caxis{jj} = gtComputeGrainUnitCell(grain{jj}.R_vector,
    data{ii}.c_axis, ...
295                 grain{jj}.radius, grain{jj}.center, grain{jj}.strain
    .strainT, app.strain{ii});
296         else
297             caxis{jj} = [];
298         end
299
300         % allow for the two coordinate systems.  Transform from
    instrument to
301         % reconstructed tomo coordinates: x-->y y-->x z-->-z
302         if (app.tomo_setup)
303             vertices{jj} = [vertices{jj}(:, 2) vertices{jj}(:, 1) -
    vertices{jj}(:, 3)];
304             if (app.caxis)
305                 caxis{jj} = [caxis{jj}(:, 2) caxis{jj}(:, 1) -caxis{
    jj}(:, 3)];
306             end
307         end
308         % do the rotate to follow the given global rotation
309         if numel(app.mrot) <= ii && ~isempty(app.mrot{ii})
310             vertices{jj} = rotateVectors(vertices{jj}, 'mrot', app.
    mrot{ii}, 'cell2mat', true);
311             if (app.caxis)
```

```
312                 caxis{jj} = rotateVectors(caxis{jj}, 'mrot', app.
    mrot{ii}, 'cell2mat', true);
313             end
314         end
315
316         % save the settings
317         grain{jj}.shift        = app.shift{ii};
318         grain{jj}.cmap         = cmap(jj, :);
319         grain{jj}.caxis        = caxis{jj};
320         grain{jj}.vertices     = vertices{jj};
321         grain{jj}.strain.scale = app.strain{ii};
322         grain{jj}.linecolor    = app.linecolor{ii};
323         grain{jj}.faces        = data{ii}.faces;
324         grain{jj}.alpha        = app.alpha{ii};
325         grain{jj}.patch        = app.patch{ii};
326         grain{jj}.dataset      = ii;
327         if (ii > 1 && app.patch{ii-1} == false && app.patch{ii} ==
    true)
328             app.linecolor{ii} = [0 0 0];
329         end
330         % draw the patch
331         if (app.draw)
332             % draws patches for prismatic planes
333             p{end+1} = gtPlotGrainUnitCell(vertices{jj}, caxis{jj},
    data{ii}.faces, ...
334                 cmap(jj, :), hl, app.linecolor{ii}, app.alpha{ii},
    app.patch{ii});
335
336             set(p{end}, 'UserData', [ii ids(jj)]);
337             set(p{end}, 'Parent', app.ha);
338             set(p{end}, 'Tag', sprintf('data_%02d_grain_%04d', ii,
    grain{jj}.id));
339             set(p{end}, 'ButtonDownFcn', @(src, evt)GtUtilities.
    displayTag(src, evt, h))
340             GtUtilities.patchMenu(p{end}, grain{jj})
341         end
342
343     end % end for jj % loop over grains
344
345     % update cmap and data
346     %app.cmap{ii} = cmap;
347     app.data{ii} = data{ii};
348     % save the settings
349     plotdata{ii} = grain;
350     hp{ii} = p;
351
352     % set the labels if empty
```

```
353     if isempty(app.label{ii})
354         if (app.stacked)
355             app.label{ii} = app.pars{ii}.acq.name;
356         elseif unique([app.phaseid{:}]) == numel(grains)
357             app.label{ii} = app.pars{ii}.cryst(app.phaseid{ii}).name
    ;
358         else
359             app.label{ii} = app.type{ii};
360         end
361     end
362
363 end % end for ii % loop over datasets
364 % update plotted data
365 app.plotdata = plotdata;
366 app.linecolor = app.linecolor(1:numel(grains));
367
368 % draw a section if true
369 if (app.section)
370     pos = min(mean(data{1}.vertices(data{1}.faces_end(1, :), 1)),
    mean(data{1}.vertices(data{1}.faces_end(2, :), 1)));
371     if ~isempty(app.secpos)
372         pos = app.secpos;
373     end
374     section_plane_vertices = [pos 1 1; pos 1 -1; pos -1 1; pos -1
    -1];
375     if strcmpi(app.plane, 'xz')
376         section_plane_vertices = section_plane_vertices(:, [2 1 3]);
377     end
378     if strcmpi(app.plane, 'xy')
379         section_plane_vertices = section_plane_vertices(:, [2 3 1]);
380     end
381     app.hp_section = gtPlotGrainUnitCell(section_plane_vertices, [],
    [1 2 4 3], ...
382         [0 0 0], [], [0 0 0], 0.4, true);
383     set(app.hp_section, 'Parent', app.ha);
384 end
385
386 % paired grains
387 %%% TO DO: handle multiple twins
388 if (app.paired) && length(plotdata{1}) == length(plotdata{2})
389     N = ceil(length(plotdata{1})/5) + 1;
390
391     f = figure();
392     g = uiextras.Grid('Parent', f);
393     set(g, 'ColumnSizes', repmat(-1, 1, 5), 'RowSizes', repmat(-1,
    1, N));
394     ha = [];
```

```
395     for jj = 1:length(plotdata{1})
396         panel(jj) = uipanel('Parent', g, 'BackgroundColor', [1 1 1])
    ;
397         ha(jj) = axes('Parent', panel(jj), 'Position', [0 0 1 1]);
398         hh = gtPlotHexagon([plotdata{1}(jj); plotdata{2}(jj)], ...
399             'ids', [1 2], 'cmap', [plotdata{1}{jj}.cmap; plotdata
    {2}{jj}.cmap;], ...
400             'reference', false, 'overlap', true, 'caxis', true, '
    alpha', 0.4, ...
401             'hf', f, 'ha', ha(jj));
402     end
403     % activate rotating option
404     h_rot3d = rotate3d(f);
405     set(h_rot3d, 'RotateStyle', 'box', 'Enable', 'on');
406
407     axis(ha, 'vis3d');
408     axis(ha, 'equal');
409
410     % linked properties for axes
411     h_link = linkprop(ha, 'View');
412     setappdata(f, 'h_link', h_link);
413     h.h_fig_grid = f;
414     h.h_axes_grin = ha;
415 end
416
417 % draw the legend
418 if (app.legend)
419     h.obj = [];
420     for ii = 1:numel(grains)
421         tmp = hp{ii};
422         h.obj(ii) = tmp{end}(1);
423     end
424     [h.axes_leg, ~] = legend(h.obj, app.label, ...
425        'Location', app.legendpos, 'Box', 'off', ...
426        'EdgeColor', [1 1 1], 'Parent', h.fig);
427     h.patch_leg = findobj(get(h.axes_leg, 'Children'), 'Type', '
    patch');
428     % only for the legend patches
429     set(h.patch_leg, 'FaceColor', [1 1 1]);
430 end
431
432 % general settings axes and figure
433 if (~app.scale || ~app.translate)
434     axis(app.ha, 'auto')
435 end
436 if (app.pixels)
437     axis(app.ha, 'equal')
```

```
438     axis(app.ha, 'tight')
439 end
440 % if ~isempty(app.zoom)
441 %     zoom('out');
442 %     zoom(app.zoom)
443 %     zoom('off')
444 % end
445 view(app.ha, app.view);
446 axis(app.ha, 'equal')
447 set(app.ha, 'Visible', GtUtilities.sfConvertValueToStatus(app.
    showaxes, 0, 1));
448
449 if ~isempty(app.figpos)
450     set(h.fig, 'Position', app.figpos)
451 end
452 set(h.fig, 'Renderer', 'zbuffer')
453 set(h.fig, 'ToolBar', 'none')
454 set(h.fig, 'Color', app.figcolor);
455 set(h.fig, 'Visible', GtUtilities.sfConvertValueToStatus(app.figure,
    0, 1));
456
457
458 % update handles
459 app.hf = h.fig;
460 app.hp = hp;
461
462 h.patch = hp;
463 h.axes  = app.ha;
464 h.senv  = app.senv;
465 h.rot3d = app.rot3d;
466
467 % save application data
468 setappdata(h.fig, 'AppData', app);
469 setappdata(h.fig, 'hp', hp)
470
471 % set callbacks
472 h = GtUtilities.addUICallbacks(h);
473 % initialize GUI
474 h = GtUtilities.initializeGui(h, app);
475
476 print_structure(app, 'AppData', false, app.verbose)
477
478 % output arguments
479 if (nargout > 0)
480     f_handles = h;
481     if (nargout > 1)
482         p_handles = hp;
```

```
    end
end

end % end of function
```

C.9 gtShowFsim.m

```
function grainOut = gtShowFsim(grain, phaseid, varargin)
% GTSHOWFSIM  Shows the forward simulation result for one grain
%     grainOut = gtShowFsim(grain, phaseid, varargin)
%     ------------------------------------------------
%     Usage:
%       gtShowFsim(grain.id, grain.phaseid)
%       gtShowFsim(grain{grain.id}, [], 'clims', [-200 500])
%           (in this case,phase ID is taken from grain)
%
%     INPUT:
%       grain      = <cell>/<double> grain info
%       phaseid    = <double>   phase number {1}
%
%     OPTIONAL INPUT (as in gtAppFsimDefaultPars()):
%       clims      = <double>   image color limits {0}
%       conflicts  = <logical>  true if check difspots in conflict {true}
%                               (needs 4_grains/grains_conflicts.mat)
%       fsimtype   = <string>   forward simulation structure name {'allblobs'}|'fwdsim'
%       fsimID     = <double>   number of fsim structure in grain
%                               It is related to the number of geometries
%                               you use and you have stored in the
%                               parameters file if needed {1}
%       replace    = <logical>  true to replace grain.full {true}
%       addspot    = <logical>  add new spots to full image {true}
%       viewblob   = <logical>  view difblob after checking raw images
%                               {false}
%       save_grain = <logical>  update 4_grains/phase_##/grain_####.mat
%                               {false}
%       verbose    = <logical>  true if printing comments {true}
%       resize     = <logical>  resize figure {false}
%       f_title    = <string>   Figure title {''}
%
%     OUTPUT:
%       grainOut   = <cell>     grain info updated
```

```
35 %
36 %       Version 004 12-05-2014 by LNervo
37
38 %       Version 003 16-01-2014 by LNervo
39 %
40 %       Version 002 13-12-2013 by LNervo
41 %         Added checkboxes for HKL families,spot flags;
42 %         Added conflicts box info
43
44 %%
45 %%%%%%%%%%%%%%%%%%%%%
46 % sub-functions %
47 %%%%%%%%%%%%%%%%%%%%%
48
49 %%%%%%%%%%%%%%%
50 % CALLBACKS %
51 %%%%%%%%%%%%%%%
52
53 function sfSetAppData(hObj,~,field,varname)
54 % GTSHOWFSIM/sfSETAPPDATA
55 %    sfSetAppData(hObj,~,field,varname)
56 %
57 % hObj      : popmenu h_cmap handle
58 % event     : ~
59 % field     :
60 % varname   :
61
62 function value = sfGetAppData(hObj,field,varname)
63 % GTSHOWFSIM/sfGETAPPDATA
64 %    value = sfGetAppData(hObj,~,field,varname)
65 %
66 % hObj      :
67 % event     : ~
68 % field     :
69 % varname   :
70 %
71 % value     :
72
73 function sfShowFlag(hObj,~,flagID,tagname)
74 % GTSHOWFSIM/sfSHOWFLAG
75 %    sfShowFlag(hObj,~,flagID,tagname)
76 %
77 % hObj     : single checkbox handle
78 % event    : ~
79 % h        : markers handles for flags
80 % flagID   : flag number
81 % tagname  : tag for hObj
```

```
82
83 function sfChooseMap(hObj,~,h_l)
84 % GTSHOWFSIM/sfCHOOSEMAP
85 %   sfChooseMap(hObj,~,hp)
86 %
87 % hObj      : popmenu h_cmap handle
88 % event     : ~
89 % h_l       : markers handles legend {h_l_flag,h_l_fam}
90
91 function sfDisplayUVWinfo(hObj,~)
92 % GTSHOWFSIM/sfDISPLAYUVWINFO
93 %   sfDisplayUVWinfo(hObj,~)
94 %
95 % hObj          : patch single handle
96 % event         : ~
97
98 function point = sfGetPointInfo(hObj,~)
99 % GTSHOWFSIM/sfGETPOINTINFO
100 %   point = sfGetPointInfo(hObj,~)
101 %
102 % hObj  : figure handle
103 % event : ~
104 %
105 % point :
106
107 function sfGetCandidates(hObj,~,omstep)
108 % GTSHOWFSIM/sfGETCANDIDATES
109 %   sfGetCandidates(hObj,~,omstep)
110 %
111 % hObj   : figure handle
112 % event  : ~
113 % omstep : omega step
114
115 function sfCheckRawImages(hObj,~)
116 % GTSHOWFSIM/sfCHECKRAWIMAGES
117 %   sfCheckRawImages(hObj,~)
118 %
119 % hObj    : uimenu handle of uicontextmenu parent
120 % event   : ~
121 % uvw_vec : UVW coordinates for fsim flags
122
123 function sfDisplaySpot(hObj,~)
124 % GTSHOWFSIM/sfVIEWSPOTIMAGE
125 %   sfDisplaySpot(hObj,~)
126 %
127 % hObj  : uimenu handle of uicontextmenu parent
128 % event : ~
```

```
129
130 %%
131 %%%%%%%%%%%%%%%%%%%
132 % WITH HANDLES %
133 %%%%%%%%%%%%%%%%%%%
134
135 function sfRowSelection(hObj,spotID)
136 % GTSHOWFSIM/sfROWSELECTION
137 %    sfRowSelection(hObj,spotID)
138 %
139 % hObj    :
140 % spotID  :
141
142 function hJTable = sfAutoResizeTable(hObj)
143 % GTSHOWFSIM/sfAUTORESIZETABLE
144 %    hJTable = sfAutoResizeTable(hObj)
145 %
146 % hObj    :
147 %
148 % hTable  :
149
150 function status = sfGetStatus(hObj)
151 % GTSHOWFSIM/sfGETSTATUS
152 %    status = sfGetStatus(hObj)
153 %
154 % hObj    :
155 %
156 % status  :
157
158 function val = sfGetValue(hObj)
159 % GTSHOWFSIM/sfGETVALUE
160 %    val = sfGetValue(hObj)
161 %
162 % hObj  :
163 %
164 % val   :
165
166 function sfSetStatus(hObj,val)
167 % GTSHOWFSIM/sfSETSTATUS
168 %    sfSetStatus(hObj,val)
169 %
170 % hObj  :
171 % val   :
172
173 function sfSetValue(hObj,status)
174 % GTSHOWFSIM/sfSETVALUE
175 %    sfSetValue(hObj,status)
```

```
176 %
177 % hObj    :
178 % status  :
179
180 function sfUpdateText(hObj,header,UV,conflicts)
181 % GTSHOWFSIM/sfUPDATETEXT
182 %    sfUpdateText(hObj,header,UV,conflicts)
183 %
184 % hObj       : UV coordinate label handle
185 % header     : columns names
186 % UV         : UVinfo stored in the axis 'omega'
187 %              UV = {UV;candidateID;indexes;dexp';dfsim';ddist_';
    ddistom_'};
188 % conflicts :
189
190 function sfAddSpotToFullImage(hObj,spot,bb)
191 % GTSHOWFSIM/sfADDSPOTTOFULLIMAGE
192 %    sfAddSpotToFullImage(hObj,spot,bb)
193 %
194 % hObj :
195 % spot :
196 % bb   :
197
198 function sfShowMontage(hObj,~,varargin)
199 % GTSHOWFSIM/sfUPDATEFULLIMAGE
200 %    sfShowMontage(hObj,~,varargin)
201 %
202 % hObj      :
203 % event     : ~
204 % varargin  :
205
206
207 function index = sfGetActiveMarkers(grain,flags_on,fams_on,h_child,
    tagname)
208 % GTSHOWFSIM/sfGETACTIVEMARKERS
209 %    index = sfGetActiveMarkers(grain,flags_on,fams_on,h_child,
    tagname)
210 % grain     :
211 % flags_on  :
212 % fams_on   :
213 % h_child   :
214 % tagname   :
215 %
216 % index     :
217
218 function sfUpdateFullImage(hObj,~)
219 % GTSHOWFSIM/sfUPDATEFULLIMAGE
```

```
220 %    full = sfUpdateFullImage(hObj,~)
221 %
222 % hObj   :
223 % event : ~
224
225 function sfChangeStyle(h_vec,markers,cmap,info_vec)
226 % GTSHOFSIM/sfCHANGESTYLE
227 %    sfChangeStyle(h_vec,markers,cmap,info_vec)
228 %
229 % h_vec     : scattergroup handles for flags
230 % markers   : marker(s) in cell
231 % cmap      : color map table
232 % info_vec  : current extra info values in cell (omega,thetatype,...)
233
234 %%
235 %%%%%%%%%%%%%%%%%%%%%%%%%
236 % WITHOUT HANDLES %
237 %%%%%%%%%%%%%%%%%%%%%%%%%
238
239 function val = sfConvertStatusToValue(status)
240 % GTSHOWFSIM/sfCONVERTSTATUSTOVALUE
241 %    val = sfConvertStatusToValue(status)
242 %
243 % status :
244 %
245 % val    :
246
247 function status = sfConvertValueToStatus(val,minV,maxV)
248 % GTSHOWFSIM/sfCONVERTVALUETOSTATUS
249 %    status = sfConvertValueToStatus(val,minV,maxV)
250 %
251 % val    :
252 % minV   :
253 % maxV   :
254 %
255 % status :
256
257 function ids = sfGetActiveSpots(grain,flags_on,fams_on)
258 % GTSHOWFSIM/sfGETACTIVESPOTS
259 %    ids = sfGetActiveSpots(grain,flags_on,fams_on)
260 %
261 % grain    :
262 % flags_on :
263 % fams_on  :
264 %
265 % ids      :
266
```

```
267 function full = sfBuildFull(spotid,parameters,spotsCommProps,bb)
268 % GTSHOWFSIM/sfBUILDFULL
269 %   full = sfBuildFull(spotid,parameters,spotsCommProps,bb)
270 %
271 % spotid          : spotid from grain
272 % parameters      : parameters.mat
273 % spotsCommProps : spots common properties
274 % bb              : bounding boxes from DB
275 %
276 % full            :
277
278 function structOut = sfStructArrayFromMatrix(data,fields)
279 % GTSHOWFSIM/sfSTRUCTARRAYFROMMATRIX
280 %   structOut = sfStructArrayFromMatrix(data,fields)
281 %
282 % data      : matrix with columns properties
283 % fields    : cell list of fields to put in the struct array
284 %
285 % structOut :
286
287 function [structData,fields] = sfGetSubFields(structData,fields)
288 % GTSHOWFSIM/sfGETSUBFIELDS
289 %   structData = sfGetSubFields(structData,fields)
290 %
291 % structData : original structure
292 % fields     : cell list of fields to get (row vector)
293 %
294 % structData :
295 % fields     :
296
297 function db_info = sfGetColumnIndexes(db_info,ids)
298 % GTSHOWFSIM/sfGETCOLUMNINDEXES
299 %   db_info = sfGetColumnIndexes(db_info,ids)
300 %
301 % db_info : structure with field content of same length
302 % ids     : column indexes to get
303 %
304 % db_info :
305
306 function db_info = sfGetRowIndexes(db_info,ids)
307 % GTSHOWFSIM/sfGETROWINDEXES
308 %   db_info = sfGetRowIndexes(db_info,ids)
309 %
310 % db_info : structure with field content of same length
311 % ids     : rows indexes to get
312 %
313 % db_info :
```

```

function omstep = sfGetOmegaStepSize(parameters)
% GTSHOWFSIM/sfGETOMEGASTEPSIZE
%   omstep = sfGetOmegaStepSize(parameters)
%
% parameters :
%
% omstep     :

function out = sfGetLengthMatrixFromCell(cellValues,indexes,repeat)
% GTSHOWFSIM/sfGETLENGTHMATRIXFROMCELL
%   out = sfGetLengthMatrixFromCell(cellValues,indexes,repeat)
%
% cellValues :
% indexes    :
% repeat     :
%
% out        :

function indexes = sfGetIndexesFromTagname(tagname)
% GTSHOWFSIM/sfGETINDEXESFROMTAGNAME
%   indexes = sfGetIndexesFromTagname(tagname)
%
% tagname :
%
% indexes :
```

C.10 GtTwinAnalysis.m

```
classdef GtTwinAnalysis < GtGrainsManager
% GtTwinAnalysis class
%   Twin identification and manipulation
%   3D visualization of grains
%   Texture analysis
%   Schmid factor calculation, slip transfer parameter calculation
%   Multiple colormaps
%
% Version 005 11-2014 by LNervo
% ...
% Version 001 08-2013 by LNervo

%%%%%%%%%%%%%%%%%%%%%%%%%%%%%%%%%%%%%%%%%%%%%%%
%% PUBLIC METHODS
methods (Access = public)

    function obj = GtTwinAnalysis(varargin)
    % GTTWINANALYSIS/GTTWINANALYSIS Constructor
```

```
19      %
20      % obj = GtTwinAnalysis(varargin)
21      %
22      %   OPTIONAL INPUT (parse by pairs): for GtGrainsManager
23      %       f_title          = <string>  object name
24      %                                    {'GtTwinAnalysis : <
    datasetname>'}
25      %       verflip          = <logical> volume vertical flip {false}
26      %       plane            = <string>  volume visualized plane {'yz'}
27      %       loadDir          = <double>  sample loading direction (1x3)
28      %                                    {[0 0 -1]}
29      %       crystDir         = <double>  crystal reference direction (1
    x3)
30      %                                    {[0 0 1]}
31      %
32      %   DEFAULT OPTIONS for GtAssembleVol3D:
33      %       deal_with_twins = true
34      %       use_parent_mask = false
35      %       sigma_csl_twin  = 11.2 (TT1)
36
37
38      function initialize(obj, varargin)
39      % GTTWINANALYSIS/INITIALIZE  Initializes colormap,
    crystallographic
40      % phase info, grain and phase IDs, load volume and database
    tables
41      % (difspot and pairs), set colormap to 'ID'
42      %
43      % initialize(obj, varargin)
44      %
45      % NB. varargin not used yet
46
47      function setCmap(obj)
48      % GTTWINANALYSIS/SETCMAP  Initializes the colormap
49      %
50      % setCmap(obj)
51
52      function setPhasesCrystalInfo(obj)
53      % GTTWINANALYSIS/SETPHASESCRYSTALINFO  Sets the crystal info for
     each
54      % phase together with the slip planes and directions for the
    current
55      % crystal system
56      %
57      % setPhasesCrystalInfo(obj)
58
59      function loadGrainsVolume(obj, volume, voxelSize)
```

```
60      % GTTWINANALYSIS/LOADGRAINSVOLUME  Loads the grains volume
        containing
61      % the grains ID
62      %
63      % loadGrainsVolume(obj, [volume], [voxelSize])
64      %
65      %   INPUT:
66      %     volume    = <string>  Name of volume to load
67      %                           {'complete'} | 'phase' | 'dilated'
68      %     voxelSize = <double>  Voxel size (um) {from parameters.
        labgeo}
69
70      function loadGrainsInfo(obj)
71      % GTTWINANALYSIS/LOADGRAINSINFO  Loads the list of all the R
        vectors,
72      % compute orientation matrices and load completeness values
73      %
74      % loadGrainsInfo(obj)
75
76      function setPhasesGrainID(obj)
77      % GTTWINANALYSIS/SETPHASESGRAINID  Sets grain IDs of each phases
        and
78      % updates the twinInfo for the current phase
79      %
80      % setPhasesGrainID(obj)
81
82      function setPhaseTwinInfo(obj, maxID)
83      % GTTWINANALYSIS/SETPHASETWININFO
84      %
85      % setPhaseTwinInfo(obj, maxID)
86
87      function loadDifspotTable(obj)
88      % GTTWINANALYSIS/LOADDIFSPOTTABLE  Loads difspot table data
89      %
90      % loadDifspotTable(obj)
91
92      function loadPairTable(obj)
93      % GTTWINANALYSIS/LOADPAIRTABLE  Loads pairs table data
94      %
95      % loadPairTable(obj)
96
97      function setGrainVolumes(obj, varargin)
98      % GTTWINANALYSIS/SETGRAINVOLUMES  Set grain volumes from grain.
        Area
99      % variable (if available)
100     %
101     % setGrainVolumes(obj, varargin)
```

```
102     %
103     % varargin not used yet
104
105     function resetAllGrainVars(obj)
106     % GTTWINANALYSIS/RESETALLGRAINVARS  Resets the variables
107     % 'flag', 'difspot', 'allblobs' to the original content saved
    into
108     % grain_%04d.mat files
109     %
110     % resetAllGrainVars(obj)
111
112     function updatePhaseInfo(obj, newdir, dirtype, phaseID)
113     % GTGRAINSMANAGER/UPDATEPHASEINFO  Updates phase info as phaseID
    ,
114     % direction for a specific direction type (sampleDir, crystDir,
115     % loadDir)
116     %
117     % updatePhaseInfo(obj, [newdir], [dirtype], [phaseID])
118     %
119     %   INPUT:
120     %     newdir  = <double>/<string>  New direction (1x3)/<name>
121     %     dirtype = <string>  Name of property to update
122     %                         {'sampleDir'} | 'loadDir'
123     %     phaseid = <double>  Phase id {1}
124
125     function updateGrainsInfoIndexes(obj, selectedFlag, fields)
126     % GTTWINANALYSIS/UPDATEGRAINSINFOINDEXES  Gets the same indexes
127     % for all the grain variables listed in 'fields', depending on
128     % the 'selectedFlag' value
129     %
130     % updateGrainsInfoIndexes(obj, [selectedFlag], [fields])
131     %
132     %   INPUT:
133     %     selectedFlag = <double>  Forward simulation flag to
    include spots
134     %     fields       = <cell>    Fields to add to table
135     %                              {'g_difspots', 'g_flags', '
    g_mosaicity'}
136
137     function setGrainInfoTable(obj, varargin)
138     % GTTWINANALYSIS/SETGRAININFOTABLE  Prepares a table for
    gtShowFsim
139     % using difspotID, mosaicity, flag and varargin
140     %
141     % setGrainInfoTable(obj, varargin)
142     %
143     %   OPTIONAL INPUT:
```

```
144     %       varargin = <cell>   List of fields from allblobs
145
146     function updateMosaicity(obj, varargin)
147     % GTTWINANALYSIS/UPDATEMOSAICITY
148     %
149     % updateMosaicity(obj, varargin)
150     %
151     %   OPTIONAL INPUT (parse by pairs):
152     %     extend  = <logical> compute also ext-extend mosaicity {
        false}
153     %     etacorr = <logical> eta correction (if true, using indexed
        pairs)
154     %                         (ExtEndImage - ExtStartImage) {true}
155
156     function computeGrainsMosaicity(obj, varargin)
157     % GTTWINANALYSIS/COMPUTEGRAINSMOSAICITY  Computes omega spread
        for each
158     % segmented spot
159     %
160     % computeGrainsMosaicity(obj, varargin)
161     %
162     %   OPTIONAL INPUT (parse by pairs):
163     %     extend  = <logical> compute also ext-extend mosaicity {
        false}
164     %     etacorr = <logical> eta correction (if true, using indexed
        pairs)
165     %                         (ExtEndImage - ExtStartImage) {true}
166     %
167     % It uses gtMosaicityCmaps
168
169     function updateSchmidFactors(obj, varargin)
170     % GTTWINANALYSIS/UPDATESCHMIDFACTORS
171     %
172     % updateSchmidFactors(obj, varargin)
173     %
174     %   OPTIONAL INPUT (parse by pairs):
175     %     useMTex     = <logical> Flag to use MTex toolbox
        calculation {true}
176     %     loadDir     = <double>  sample CS loading direction (1x3)
177     %                             {obj.loadDir}
178     %     convention = <string>  hcp crystal axes convention {'X'} |
        'Y'
179
180     function computeSchmidF(obj, varargin)
181     % GTTWINANALYSIS/COMPUTESCHMIDF  Compute all the Schmid factors
182     % depending on the given loading direction
183     %
```

```
184     % computeSchmidF(obj, varargin)
185     %
186     %   OPTIONAL INPUT (parse by pairs):
187     %     loadDir     = <double>  sample CS loading direction (1x3)
188     %                             {obj.loadDir}
189     %     convention  = <string>  hcp crystal axes convention {'X'} |
        'Y'
190     %     orimat      = <double>  orientation matrices as
191     %                             gtMathsRod2OriMat output
192     %                             (3x3xN) {obj.orientations}
193     %     grainids    = <double>  specific grainIDs {[]}
194     %     phaseid     = <double>  Phase id for all the considered
        grains {1}
195     %     overwrite   = <logical> reset and redo the calculation {
        false}
196     %
197     %   HexaSchmid software:
198     %   https://www.tu-berlin.de/metallischewerkstoffe/menue/
        forschung/parameter/maxhilfe/
199
200     function computeMTexSchmidF(obj, varargin)
201     % GTTWINANALYSIS/COMPUTEMTEXSCHMIDF  Uses the MTex toolbox to
        compute
202     % the Schmid factor for all the grains, given an applied stress
        tensor
203     %
204     % It uses the gtCalcShearStress function
205     %
206     % computeMTexSchmidF(obj, varargin)
207     %
208     %   OPTIONAL INPUT (parse by pairs):
209     %     loadDir     = <double>  sample CS loading direction (1x3) {
        obj.loadDir}
210     %     convention  = <string>  hcp crystal axes convention {'X'} |
        'Y'
211     %     tensorM     = <double>  stress tensor (3x3)
212     %     orimat      = <double>  orientation matrices as
        gtMathsRod2OriMat output
213     %                             (3x3xN) {obj.orientations}
214     %     grainids    = <double>  specific grainIDs {[]}
215     %     phaseid     = <double>  Phase id for all the grains
        considered {1}
216     %     overwrite   = <logical> reset and redo the calculation {
        false}
217
218     function list = getNeighborhood(obj, gID, oversize)
```

```
219     % GTTWINANALYSIS/GETNEIGHBORHOOD  Gets the neighborhood list for
        a
220     % grain from GtPhase method and creates the figure title
221     %
222     % list = getNeighborhood(obj, gID, oversize)
223     %
224     %   INPUT:
225     %     gID       = <double>  Grain to be considered
226     %     oversize = <double>  Factor to oversize the bounding box
        for
227     %                          neighborhood search {1}
228     %
229     %   OUTPUT:
230     %     list      = <double>  List of neighbors
231
232     function [maxSlip, nfam, slip] = calculateSchmidFactor(obj, gID,
        varargin)
233     % GTTWINANALYSIS/CALCULATESCHMIDFACTOR  Calculates the Schmid
        factor
234     % for grain gID
235     %
236     % [maxSlip, nfam, slip] = calculateSchmidFactor(obj, gID,
        varargin)
237     %
238     %   INPUT:
239     %     gID       = <double>  Grain to be considered (1x1)
240     %
241     %   OPTIONAL INPUT (parse by pairs):
242     %     maxSystem = <logical> Flag to consider maximum values for
        each
243     %                           slip family among the equivalent
        systems {true}
244     %     fam       = <double>  Family number to be considered {[]}
245     %     phaseid   = <double>  Phase id for all the grains
        considered {1}
246     %     useMTex   = <logical> Flag to use MTex toolbox calculation
        {true}
247     %     verbose   = <logical> Verbosity {true}
248     %     overwrite = <logical> reset and redo the calculation for
        the starting grainid {false}
249
250     function computeSlipTransfer(obj, gID, varargin)
251     % GTTWINANALYSIS/COMPUTESLIPTRANSFER  Does the slip transfer
252     % calculation from grain gID to all the given 'grainids'
253     %
254     % computeSlipTransfer(obj, varargin)
255     %
```

```
256     %   INPUT:
257     %     gID         = <double>  Grain to be considered (1x1)
258     %
259     %   OPTIONAL INPUT (parse by pairs):
260     %     orimat      = <double>  orientation matrices as
    gtMathsRod2OriMat output
261     %                             (3x3xN) {obj.orientations}
262     %     grainids    = <double>  specific grainIDs to which compute
    the slip transfer {[]}
263     %     phaseid     = <double>  Phase id for all the grains
    considered {1}
264     %     overwrite   = <logical> reset and redo the calculation for
    the starting grainid {false}
265     %     verbose     = <logical> Verbosity {false}
266
267     function [maxSlip, nfam, slip] = calculateSlipTransfer(obj, mis1
    , mis2, varargin)
268     % GTTWINANALYSIS/CALCULATESLIPTRANSFER  Calculates slip transfer
     parameter
269     % from grain mis1 to grain mis2
270     %
271     % [maxSlip, nfam, slip] = calculateSlipTransfer(obj, mis1, mis2,
     varargin)
272     %
273     %   INPUT:
274     %     mis1        = <double>  GrainID 1
275     %     mis2        = <double>  GrainID 2
276     %
277     %   OPTIONAL INPUT (parse by pairs):
278     %     maxSystem   = <logical> Flag to consider maximum values
    among the
279     %                             slip families {true}
280     %     fam         = <double>  Family number to be considered {[]}
281     %     phaseid     = <double>  Phase id for all the grains
    considered {1}
282     %     verbose     = <logical> Verbosity {true}
283     %     overwrite   = <logical> reset and redo the calculation for
    the starting grainid {false}
284
285     function out = calculateMis(obj, mis1, mis2, varargin)
286     % GTTWINANALYSIS/CALCULATEMIS  Calculates the misorientation
    between
287     % two grains, giving the Hcp axes convention and the merging
    angle,
288     % within the rotation mode (See Rollet lectures)
289     %
290     % out = calculateMis(obj, mis1, mis2, varargin)
```

```
291     %
292     %   INPUT:
293     %       mis1         = <double>  GrainID 1
294     %       mis2         = <double>  GrainID 2
295     %
296     %   OPTIONAL INPUT (parse by pairs):
297     %       convention   = <string>  Hcp axes convention {'X'} | 'Y'
298     %       merge_angle  = <double>  Minimum angle to merge grains {5}
299     %       mode         = <string>  Rotation type {'passive'} | '
    active'
300     %       doSizeCalc   = <logical> Flag to compute grain sizes from
    volume (um) {false}
301     %
302     %   OUTPUT:
303     %       out          = <struct>  Misorientation structure output
304
305     function [parent, twins, IDs] = getTwinParentNeighbors(obj, gID,
     IDs, includeCheckList)
306     % GTTWINANALYSIS/GETTWINPARENTNEIGHBORS  Gets the twinned grains
     and
307     % relative neighbors for a grain and saves the list into
308     % obj.extras.selected.id (.twins) (.list)
309     %
310     % [parent, twins, IDs] = getTwinParentNeighbors(obj, gID, [IDs],
     [includeCheckList])
311     %
312     %   INPUT:
313     %       gID              = <double>  Grain to be considered (1x1)
314     %       IDs              = <double>  Neighbors list already
    computed (1xM)
315     %       includeCheckList = <logical> Flag to include check_list
    into
316     %                                    twin_list {false}
317     %
318     %   OUTPUT:
319     %       parent           = <double>  Grain to be considered (1x1)
320     %       twins            = <double>  List of twins if available (1
    xP)
321     %       IDs              = <double>  List of neighbors (1xM)
322
323     function [maxSlip, nFam, slip] = getListSlipTransfer(obj, gID,
    IDs, varargin)
324     % GTTWINANALYSIS/GETLISTSLIPTRANSFER
325     %
326     % [maxSlip, nFam, slip] = getListSlipTransfer(obj, gID, IDs,
    varargin)
327     %
```

```
328     %   INPUT:
329     %     gID      = <double>  Grain to be considered as starting
        point
330     %     IDs      = <double>  List of considered grains (1xN)
331     %
332     %   OPTIONAL INPUT (parse by pairs) from calculateSlipTransfer
333     %
334     %   OUTPUT:
335     %     maxSlip = <cell>    Slip transfer for each grainID in list
        IDs (1xN)
336     %     nFam     = <cell>    Family (row,col) corresponding to the
        maximum value (1xN)
337     %     slip     = <cell>    (all the equivalent)
338
339     function [maxSlip, nFam, slip] = getListSchmidFactors(obj, IDs,
        varargin)
340     % GTTWINANALYSIS/GETLISTSCHMIDFACTORS
341     %
342     % [maxSlip, nFam, slip] = getListSchmidFactors(obj, IDs,
        varargin)
343     %
344     %   INPUT:
345     %     IDs      = <double>  List of considered grains (1xN)
346     %
347     %   OPTIONAL INPUT (parse by pairs) from calculateSchmidFactor
348     %
349     %   OUTPUT:
350     %     maxSlip = <cell>    Schmid factors for each grainID in
        list IDs (1xN)
351     %     nFam     = <cell>    Family (row,col) corresponding to the
        maximum value (1xN)
352     %     slip     = <cell>    (all the equivalent)
353
354     function printValuesList(obj, gID, IDs, values, nFam, vars_pars,
        valueType)
355     % GTTWINANALYSIS/PRINTVALUESLIST  Prints mostly schmid factors
        and slip
356     % transfer values.
357     %
358     % printValuesList(obj, gID, IDs, values, nFam, vars_pars,
        valueType)
359     %
360     %   INPUT:
361     %     gID       = <double>  Grain to be considered (1x1)
362     %     IDs       = <double>  List of considered grains (1xN)
363     %     values    = <cell>    Values for each grainID in list IDs
        (1xN)
```

```
364     %       nFam       = <cell>    Maximum family number (1xN)
365     %       vars_pars  = <struct>  Options for saving the figure
366     %       valueType  = <string>  Flag for current values
367
368     function out = getListMisorientation(obj, ids, varargin)
369     % GTTWINANALYSIS/GETLISTMISORIENTATION  Gets the misorientation
370     % between a grain list and their neighborhood
371     %
372     % out = getListMisorientation(obj, ids, varargin)
373     %
374     %   INPUT:
375     %       ids   = <double>  List of considered grains (1xN)
376     %
377     %   OPTIONAL INPUT (parse by pairs) from calculateMis plus:
378     %       list = <cell>     Neighbors list if available to avoid
379     %                         recalculation (1xN)
380     %
381     %   OUTPUT:
382     %       out   = <cell>      Misorientation output (NxM)
383
384     function mis = getMisorientation(obj, ids, varargin)
385     % GTTWINANALYSIS/GETMISORIENTATION  Calculates the
        misorientation
386     % between a list of grains with respect to all the grains, using
        the
387     % symmetry operators relative to the first phase.
388     %
389     % mis = getMisorientation(obj, ids, varargin)
390     %
391     %   INPUT:
392     %       ids = <double>  List of considered grains (1xN)
393     %
394     %   OPTIONAL INPUT (parse by pairs) from gtMathsMisorientation
395     %
396     %   OUTPUT:
397     %       mis = <cell>/<struct> Misorientation output
398
399     function changeGrainCmap(obj, typemap, overwrite, varargin)
400     % GTTWINANALYSIS/CHANGEGRAINCMAP  Changes the color map for the
        current
401     % volume for all the grains
402     %
403     % changeGrainCmap(obj, typemap, [overwrite], varargin)
404     %
405     %   INPUT:
406     %       typemap    = <string>  Colormap to be calculated and used
```

```
407     %     overwrite = <logical> Flag to overwrite the specified
    colormap {true}
408     %
409     %   OPTIONAL INPUT (parse by pairs) relative to the specified
    colormap
410
411     function createAllColorMaps(obj, overwrite)
412     % GTTWINANALYSIS/CREATEALLCOLORMAPS  Generate all the color maps
     need for the study
413     %
414     % createAllColorMaps(obj, [overwrite])
415     %
416     %   INPUT:
417     %     overwrite = <logical> Flag to overwrite all the colormaps
    {false}
418
419     function vars_pars = setFigureName(obj, varargin)
420     % GTTWINANALYSIS/SETFIGURENAME  Creates a figure name based on
    varargin
421     %                               arguments
422     %
423     % vars_pars = setFigureName(obj, varargin)
424     %
425     %   OPTIONAL INPUT (parse by pairs):
426     %     paper_fig = <logical> true if paper figure format (.tif
    600dpi)
427     %     ws_path   = <logical> true to save it in the worksace
    directory
428     %     doFig     = <logical> true to save .fig file
429     %     GMgui     = <logical> true if it is the GrainsManager GUI
430     %     ids       = <double>  ID list
431     %     neighbors = <logical> true if considering only neighbors
432     %     rendering = <logical> true if it's a render plot
433     %     unitcells = <logical> true if it's a unit cells plot
434     %     ipf       = <logical> true if it is an Inverse Pole Figure
435     %     pf        = <logical> true if it is a Pole Figure
436     %
437     %   COMPUTED:
438     %     fname     = <cell>    figure name
439     %
440     %   OUTPUT:
441     %     vars_pars = <struct>  Options for saving the figure
442
443     function similar = getIPFSimilarOrientedList(obj, similar_list,
    offset, saveFig, varargin)
444     % GTTWINANALYSIS/GETIPFSIMILARORIENTEDLIST
445     %
```

```
446     % similar = getIPFSimilarOrientedList(obj, similar_list, [offset
        ], [saveFig], varargin)
447     %
448     %   INPUT:
449     %     similar_list = <double>  Similar oriented list (N,4)
450     %                              [similar_to parent
        similar_to_data parent_global]
451     %     offset       = <double>  Number of opened figures {1}
452     %     saveFig      = <logical> Flag to save on disk {false}
453     %
454     %   OPTIONAL INPUT (parse by pairs) from displayIPFgrainList
455     %
456     %   OUTPUT:
457     %     similar      = <struct>  Similar oriented output structure
458
459     function twins = getIPFTwinList(obj, twin_list, offset, saveFig,
        varargin)
460     % GTTwINANALYSIS/GETIPFTWINLIST
461     %
462     % twins = getIPFTwinList(obj, twin_list, [offset], [saveFig],
        varargin)
463     %
464     %   INPUT:
465     %     twin_list = <double>  Twin list [twins parents] (N,2)
466     %     offset    = <double>  Number of opened figures {1}
467     %     saveFig   = <logical> Flag to save on disk {false}
468     %
469     %   OPTIONAL INPUT (parse by pairs) from displayIPFgrainList
470     %
471     %   OUTPUT:
472     %     twins     = <struct>  Twin output structure
473
474     function hf = displayIPFgrainList(obj, ids, varargin)
475     % GTTWINANALYSIS/DISPLAYIPFGRAINLIST
476     %
477     % hf = displayIPFgrainList(obj, ids, varargin)
478     %
479     %   INPUT:
480     %     ids
481     %
482     %   OPTIONAL INPUT (parse by pairs):
483     %     list
484     %     phaseid
485     %     figure_grid
486     %     do_twins
487     %     similar
488     %     id
```

```
489     %       exportFig
490     %
491     %   OUTPUT:
492     %       hf
493
494     function hf = displayPFgrainList(obj, ids, varargin)
495     % GTTWINANALYSIS/DISPLAYPFGRAINLIST
496     %
497     % hf = displayPFgrainList(obj, ids, varargin)
498     %
499     %   INPUT:
500     %       ids
501     %
502     %   OPTIONAL INPUT (parse by pairs):
503     %       list
504     %       phaseid
505     %       figure_grid
506     %       do_twins
507     %       similar
508     %       id
509     %       exportFig
510     %
511     %   OUTPUT:
512     %       hf
513
514     function slipTr = displaySlipTransferGrainList(obj, ids,
    varargin)
515     % GTTWINANALYSIS/DISPLAYSLIPTRANSFERGRAINLIST
516     %
517     % slipTr = displaySlipTransferGrainList(obj, ids, varargin)
518     %
519     %   INPUT:
520     %       ids             = <double>  List of considered grains {}
521     %
522     %   OPTIONAL INPUT (parse by pairs):
523     %       list            = <cell>    List of neighbors for each
    grainID {}
524     %       phaseid         = <double>  Phase id for all the grains
    considered {1}
525     %       chain           = <logical> Flag to do chain analysis {false
    }
526     %       num_chain       = <double>  Number of chain {[]}
527     %       maxSystem       = <logical> Flag to consider maximum values
    for each
528     %                                   slip family among the equivalent
     systems {true}
```

```
529     %     fam            = <double>  Family number to be considered
        {[]}
530     %     verbose        = <logical> Verbosity {false}
531     %     overwrite      = <logical> reset and redo the calculation
        for the starting grainid {false}
532     %     thr_value      = <double>  Threshold value {0.6}
533     %     write_to_file = <logical> Flag to save output to file {
        true}
534     %
535     %   OUTPUT:
536     %     slipTr         = <struct>  Output structure with 'ids',
537     %                                'neighbors' and 'vars_pars'
        fields
538
539     function schmidF = displaySchmidFGrainList(obj, ids, varargin)
540     % GTTWINANALYSIS/DISPLAYSCHMIDFGRAINLIST
541     %
542     % schmidF = displaySchmidFGrainList(obj, ids, varargin)
543     %
544     %     ids            = <double>  List of considered grains {}
545     %
546     %   OPTIONAL INPUT (parse by pairs):
547     %     list           = <cell>    List of neighbors for each
        grainID {}
548     %     phaseid        = <double>  Phase id for all the grains
        considered {1}
549     %     chain          = <logical> Flag to do chain analysis {false
        }
550     %     num_chain      = <double>  Number of chain {[]}
551     %     maxSystem      = <logical> Flag to consider maximum values
        for each
552     %                                slip family among the equivalent
         systems {true}
553     %     fam            = <double>  Family number to be considered
        {[]}
554     %     useMTex        = <logical> Flag to use MTex toolbox
        calculation {true}
555     %     verbose        = <logical> Verbosity {false}
556     %     overwrite      = <logical> reset and redo the calculation
        for the starting grainid {false}
557     %     thr_value      = <double>  Threshold value {0.4}
558     %     write_to_file = <logical> Flag to save output to file {
        true}
559     %
560     %   OUTPUT:
561     %     schmidF        = <struct>  Output structure with 'ids',
```

```
562     %                                   'neighbors' and 'vars_pars'
    fields
563
564     function displayIPFNeighborhood(obj, point, varargin)
565     % GTTWINANALYSIS/DISPLAYIPFNEIGHBORHOOD
566     %
567     % displayIPFNeighborhood(obj, [point], varargin)
568     %
569     %   INPUT:
570     %     point
571     %
572     %   OPTIONAL INPUT (parse by pairs) from displayIPFGrainList
    plus:
573     %     gID
574
575     function displayPFNeighborhood(obj, point, varargin)
576     % GTTWINANALYSIS/DISPLAYPFNEIGHBORHOOD
577     %
578     % displayPFNeighborhood(obj, [point], varargin)
579     %
580     %   INPUT:
581     %     point
582     %
583     %   OPTIONAL INPUT (parse by pairs) from displayPFGrainList plus
    :
584     %     gID
585
586     function displaySlipTransferNeighborhood(obj, point, varargin)
587     % GTTWINANALYSIS/DISPLAYSLIPTRANSFERNEIGHBORHOOD
588     %
589     % displaySlipTransferNeighborhood(obj, [point], varargin)
590     %
591     %   INPUT:
592     %     point
593     %
594     %   OPTIONAL INPUT (parse by pairs) from
    displaySlipTransferGrainList plus:
595     %     gID
596
597     function displaySchmidFNeighborhood(obj, point, varargin)
598     % GTTWINANALYSIS/DISPLAYSCHMIDFNEIGHBORHOOD
599     %
600     % displaySchmidFNeighborhood(obj, [point], varargin)
601     %
602     %   INPUT:
603     %     point
604     %
```

```
605     %   OPTIONAL INPUT (parse by pairs) from displaySchmidFGrainList
        plus:
606     %       gID
607
608     function displayNeighborhood(obj, point, printValues)
609     % GTTWINANALYSIS/DISPLAYNEIGHBORHOOD  Displays the neighbors of
        a grain
610     %
611     % displayNeighborhood(obj, point, printValues)
612     %
613     %   INPUT:
614     %       point
615     %       printValues
616
617     function displayShowFsim(obj, point)
618     % GTTWINANALYSIS/DISPLAYSHOWFSIM  Displays the forward
        simulation
619     %
620     % displayShowFsim(obj, point)
621     %
622     %   INPUT:
623     %       point
624
625     function displayCmapEditor(obj, point, varargin)
626     % GTTWINANALYSIS/DISPLAYCMAPEDITOR  Plays with colormap on the
        current
627     % volume slice and exports it in a new figure
628     %
629     % displayCmapEditor(obj, [point], varargin)
630     %
631     %   INPUT:
632     %       point
633     %
634     %   OPTIONAL INPUT (parse by pairs) from getVolumeSlice plus:
635     %       cluster
636     %       oversize
637
638     function handles = displayRenderGrains(obj, point, varargin)
639     % GTTWINANALYSIS/DISPLAYRENDERGRAINS  Displays rendered grains
        with
640     %                                       colorbar
641     %
642     % handles = displayRenderGrains(obj, [point], varargin)
643     %
644     %   INPUT:
645     %       point
646     %
```

```
647     %   OPTIONAL INPUT (parse by pairs):
648     %     ids
649     %     unitcells
650     %     cluster
651     %     oversize
652     %     vol
653     %     cmap
654     %     pxsize
655     %     grain
656     %     labgeo
657     %     figtitle
658     %     cbar
659     %     view -> [viewaz viewel]
660     %     [hf]
661     %     [ha]
662     %
663     %   OUTPUT:
664     %     handles
665
666     function handles = displayUnitCells(obj, point, varargin)
667     % GTTWINANALYSIS/DISPLAYUNITCELLS
668     %
669     % handles = displayUnitCells(obj, [point], varargin)
670     %
671     %   INPUT:
672     %     point
673     %
674     %   OPTIONAL INPUT (parse by pairs):
675     %     ids
676     %     rendering
677     %     cluster
678     %     oversize
679     %     vol
680     %     cmap
681     %     pxsize
682     %     grain
683     %     labgeo
684     %     figtitle
685     %     hf
686     %     cbar
687     %
688     %   OUTPUT:
689     %     handles
690
691     function hf = displayPoleFigure(obj, varargin)
692     % GTTWINANALYSIS/DISPLAYPOLEFIGURE  Displays the pole figure for
        the
```

```
693     % selected grains and changes the colormap to Caxis color map
694     %
695     % hf = displayPoleFigure(obj, varargin)
696
697     function hf = displayInversePoleFigure(obj, varargin)
698     % GTTWINANALYSIS/DISPLAYINVERSEPOLEFIGURE  Displays the Inverse
        Pole
699     % Figure for the selected grains and changes the colormap to the
        IPF
700     % color map
701     %
702     % hf = displayInversePoleFigure(obj, varargin)
703
704     function selectGrainsToVisualize(hObj, ~, obj)
705     % GTTWINANALYSIS/SELECTGRAINSTOVISUALIZE  Grain selection based
        aon
706     % some criteria : parent which twinned, not twinned grains, only
        twins,
707     % parents and twins, none, all
708     %
709     % selectGrainsToVisualize(hObj, eventdata, obj)
710
711     function setMakemapOptions(obj)
712     % GTTWINANALYSIS/SETMAKEMAPOPTIONS  Sets some general colormap
        options
713     % used in makemap method
714     %
715     % setMakemapOptions(obj)
716     %
717     %   OPTIONAL INPUT (parse by pairs):
718     %      bkg
719     %      conflict
720     %      hasBkg
721     %      hasConflict
722     %      hideColor
723     %      maxSystem
724     %      scale
725
726     function updateCmap(obj)
727     % GTTWINANALYSIS/UPDATECMAP  Updates the current colormap
        letting us
728     % changing the parameters for that colormap, together with
729     %
730     % updateCmap(obj)
731
732     function selectCmapCallback(hObj, ~, obj)
733     % GTTWINANALYSIS/SELECTCMAPCALLBACK  Changes the colormap
```

```
734     %
735     % selectCmapCallback(hObj, eventdata, obj)
736
737     function saveCmapFigure(obj, h_fig, varargin)
738     % GTTWINANALYSIS/SAVECMAPFIGURE  Saves the figures using dataset
        name and slice
739     % number into the [home]/workspace/[datasetname] folder by
        default
740     %
741     % saveCmapFigure(obj, h_fig, varargin)
742
743     function h = createMovie(obj, h_fig, varargin)
744     % GTTWINANALYSIS/CREATEMOVIE  Creates a movie of the current
        figure by
745     % rotating the current axes
746     %
747     % h = createMovie(obj, h_fig, varargin)
748
749     function h = add_colorbar(obj, h, varargin)
750     % GTTWINANALYSIS/ADD_COLORBAR
751     % h = add_colorbar(obj, h, varargin)
752
753 end % end of public methods
754
755 %%%%%%%%%%%%%%%%%%%%%%%%%%%%%%%%%%%%%%%%%%%%%%%%%%%%%%%%%%%%%%%%%%%%%%%
756 %% PROTECTED METHODS
757 methods (Access = protected)
758
759     function initGui(obj)
760     % GTTWINANALYSIS/INITGUI  Inherited method that builds the
        interface
761     %
762     % initGui(obj)
763
764     function updateSidePanel(obj)
765     % GTTWINANALYSIS/UPDATESIDEPANEL  Updates the side panel from
766     % GrainsManager and the new left panel. Updates also the figure
        size
767     %
768     % updateSidePanel(obj)
769
770     function doUpdateDisplay(obj)
771     % GTTWINANALYSIS/DOUPDATEDISPLAY  Updates labels on main axes
772     %
773     % doUpdateDisplay(obj)
774
775     function addUICallbacks(obj)
```

```
776     % GTTWINANALYSIS/ADDUICALLBACKS  Adds the callbacks to the GUI
        elements
777     %
778     % addUICallbacks(obj)
779     %   setMakemapOptions
780     %   GtUtilities.showSupportedCmaps
781     %   displayCmapEditor
782     %   saveCmapFigure
783     %   updateCmap
784     %   selectCmapCallback
785     %   displaySchmidFGrainList
786     %   displaySlipTransferGrainList
787     %   displayPoleFigure
788     %   displayInversePoleFigure
789     %   selectGrainsToVisualize
790
791     function createAxesMenu(obj)
792     % GTTWINANALYSIS/CREATEAXESMENU  Updates the axes UIContextMenu
793     %
794     % createAxesMenu(obj)
795     %   copy3DPixInfoToClipboard
796     %   displayNeighborhood
797     %   displayNeighborhood
798     %   displayPFNeighborhood
799     %   displayIPFNeighborhood
800     %   displaySchmidFNeighborhood
801     %   displaySlipTransferNeighborhood
802     %   displayShowFsim
803     %   copy3DPixInfoToClipboard
804     %   displayRenderGrains
805     %   displayUnitCells
806
807     function resetUiComponents(obj)
808     % GTTWINANALYSIS/RESETUICOMPONENTS  Inherited method to reset
        the ui
809     % components
810     %
811     % resetUiComponents(obj)
812
813     function toggleCbarVisibility(obj)
814     % GTTWINANALYSIS/TOGGLECBARVISIBILITY  Triggers the colorbar
815     % visualization, otherwise shuts it down
816     %
817     % toggleCbarVisibility(obj)
818
819     function [list, gID, pID] = getIDlist(obj, point, cluster,
        oversize)
```

```
820     % GTTWINANALYSIS/GETIDLIST  Gets the ID list basing on a point
        into the
821     % volume of its neighborhood or, if deselected, gets the active
        grains
822     % list.
823     %
824     % [list, gID, pID] = getIDlist(obj, point, [cluster], [oversize
        ])
825     %
826     %   INPUT:
827     %     point
828     %     cluster
829     %     oversize
830     %
831     %   OUTPUT:
832     %     list
833     %     gID
834     %     pID
835
836     function [point, values] = getPhaseAndGrainInfoValue(obj, ~, ~)
837     % GTTWINANALYSIS/GETPHASEANDGRAININFOVALUE  Sets the text
        relative to
838     % the current colormap value of the selected grain
839     %
840     % [point, values] = getPhaseAndGrainInfoValue(obj, ~, ~)
841
842     function updateValue(obj, infoPattern)
843     % GTTWINANALYSIS/UPDATEVALUE  Updates the selected cmap value
        for the
844     % current grain
845     %
846     % updateValue(obj, infoPattern)
847
848     function [point, pID, gID] = get3DPixInfoFromClipboard(obj)
849     % GTTWINANALYSIS/GET3DPIXINFOFROMCLIPBOARD
850     %
851     % [point, pID, gID] = get3DPixInfoFromClipboard(obj)
852
853     function [list, rej_pars] = getVolumeSlice(obj, varargin)
854     % GTTWINANALYSIS/GETVOLUMESLICE  Gets the slice volume and
        copies it
855     %                               into a new figure, adding
        control
856     %                               buttons and the colorbar
857     %
858     % [list, rej_pars] = getVolumeSlice(obj, varargin)
859     %
```

```
860     %   OPTIONAL INPUT (parse by pairs):
861     %     list      = <double>  IDs to be hidden {[]}
862     %     hide      = <double>  Select control buttons {[]}
863     %     cbar      = <logical> Plots the colorbar {true}
864     %     draw      = <logical> Draws the figure {true}
865     %     figtitle  = <string>  Figure title {''}
866     %
867     %   OUTPUT:
868     %     list      = <double>  List of visualized IDs {[]}
869     %     rej_pars  = <cell>    Rejected parameter/value pairs
870
871     function closeCmapFigure(hObj, ~, obj, reload)
872     % GTTWINANALYSIS/CLOSECMAPFIGURE  Closes the colormap figure, exporting
873     % the cmap properties and reloading the volume using this cmap if
874     % reload is true
875     %
876     % closeCmapFigure(hObj, eventdata, obj, reload)
877
878     function closeSelectGrains(hObj, ~, obj, h)
879     % GTTWINANALYSIS/CLOSESELECTGRAINS  Close the figure relative to the
880     % grain selection and save the IDs in the sample.mat; update the figure
881     % title and also save the flag into obj.extras
882     %
883     % closeSelectGrains(hObj, eventdata, obj, h)
884
885 end % end methods (Access = procected)
886
887 %%%%%%%%%%%%%%%%%%%%%%%%%%%%%%%%%%%%%%%%%%%%%%%%%%%%%%%%%%%%%%%%%%%%%%%
888 %% PRIVATE METHODS
889 methods(Access = private)
890
891     function getGrainVars(obj, igrain)
892     % GTTWINANALYSIS/GETGRAINVARS  Get variables for model 'grain'
893     % if Id > Ngrains{iphase}, it is calculated from
894     % Id - Ngrains{iphase} = newId
895     %
896     % getGrainVars(obj, igrain)
897
898     function setAllblobsFieldIndexes(obj, igrain, indexes)
899     % GTTWINANALYSIS/SETALLBLOBSFIELDINDEXES  Updates 'allblobs' structure
900     % fields taking only some indexes for igrain
901     %
```

```
902     % setAllblobsFieldIndexes(obj, igrain, indexes)
903
904     function indexes = getIndexesFromFlag(obj, flag)
905     % GTTWINANALYSIS/GETINDEXESFROMFLAG  Uses fsim flag to keep only
        some
906     % indexes over the reflection indexes on the detector
907     %
908     % indexes = getIndexesFromFlag(obj, flag)
909
910     function setGrainFieldIndexes(obj, variable, indexes)
911     % GTTWINANALYSIS/SETGRAINFIELDINDEXES  Keeps 'indexes' for the
912     % given property 'variable'
913     %
914     % setGrainFieldIndexes(obj, variable, indexes)
915
916     function map = makeColorMap(obj, varargin)
917     % GTTWINANALYSIS/MAKECOLORMAP  Compute color map given a list of
        values
918     %
919     % map = makeColorMap(obj, varargin)
920
921     function createGrainIDColorMap(obj, varargin)
922     % GTTWINANALYSIS/CREATEGRAINIDCOLORMAP  Creates a color map for
      grain labels
923     %
924     % createGrainIDColorMap(obj, varargin)
925     %   OPTIONAL INPUT (parse by pairs): from makeColorMap
926     %
927
928     function createGrainRandColorMap(obj)
929     % GTTWINANALYSIS/CREATEGRAINRANDCOLORMAP  Creates a random color
        map
930     % for grain labels
931     %
932     % createGrainRandColorMap(obj)
933
934     function createGrainVolumeColorMap(obj, varargin)
935     % GTTWINANALYSIS/CREATEGRAINVOLUMECOLORMAP  Creates a color map
      for grain volume
936     %
937     % createGrainVolumeColorMap(obj, varargin)
938     %   OPTIONAL INPUT (parse by pairs): from makeColorMap
939     %
940
941     function createGrainCompletenessColorMap(obj, varargin)
942     % GTTWINANALYSIS/CREATEGRAINCOMPLETENESSCOLORMAP  Creates a
      color map for grain completeness
```

```
943     %
944     % createGrainCompletenessColorMap(obj, varargin)
945     %   OPTIONAL INPUT (parse by pairs): from makeColorMap
946     %
947
948     function createGrainCaxisColorMap(obj, varargin)
949     % GTTWINANALYSIS/CREATEGRAINCAXISCOLORMAP  Creates a color map
        for
950     % grains given a crystallographic direction
951     %
952     % createGrainCaxisColorMap(obj, varargin)
953     %   OPTIONAL INPUT (parse by pairs):
954     %     crystDir
955     %     phaseid
956     %     axesRot
957     %     background
958     %     save
959     %     convention
960
961     function createGrainIPFColorMap(obj, varargin)
962     % GTTWINANALYSIS/CREATEGRAINIPFCOLORMAP  Creates a color map for
        grain
963     % inverse pole figure for LD direction
964     %
965     % createGrainIPFColorMap(obj, varargin)
966     %   OPTIONAL INPUT (parse by pairs):
967     %     sampleDir
968     %     phaseid
969     %     saturate
970     %     save
971     %     background
972
973     function createGrainRvecColorMap(obj)
974     % GTTWINANALYSIS/CREATEGRAINRVECCOLORMAP  Creates a color map
        for
975     % rvectors
976     %
977     % createGrainRvecColorMap(obj)
978
979     function createGrainSchmidFColorMap(obj, varargin)
980     % GTTWINANALYSIS/CREATEGRAINSCHMIDFCOLORMAP  Creates a color map
        for grain schmid factor for LD direction.
981     % By default use MTex computation if possible and find the
        maximum Schmid factor
982     % value for each slip family (among the symmetry equivalents)
983     %
984     % createGrainSchmidFColorMap(obj, varargin)
```

```
985     %   OPTIONAL INPUT (parse by pairs):
986     %       fam
987     %       syst
988     %       phaseid
989     %       useMTex
990     %       maxSystem
991
992     function createGrainMosaicityColorMap(obj, varargin)
993     % GTTWINANALYSIS/CREATEGRAINMOSAICITYCOLORMAP  Create a color
        map for
994     % each grain omega spread as average of each difspot assigned to
        it
995     %
996     % createGrainMosaicityColorMap(obj, varargin)
997     %   OPTIONAL INPUT (parse by pairs):
998     %       func
999     %       etacorr
1000    %       pairs
1001
1002    end
1003
1004    end % end of class
```

Bibliography

http://people.physics.anu.edu.au/~web107/research/highpage4.php.

http://en.wikipedia.org/wiki/Synchrotron_radiation.

http://pubs.usgs.gov/of/2001/of01-041/htmldocs/images/xrdtube.jpg.

http://www.ptable.com/#Property/State.

http://www.xtal.iqfr.csic.es/Cristalografia/parte_03_4-en.html.

AGHION, E and BRONFIN, B. (2000), "Magnesium Alloys Development towards the 21st Century", *Materials Science Forum* **350–351**, pp. 19–30.

AGNEW, S. R. *et al.* (2003), "Study of slip mechanisms in a magnesium alloy by neutron diffraction and modeling", *Scripta Materialia* **48**, pp. 1003–1008.

AGNEW, S. R., BROWN, D. W., and TOMÉ, C. N. (2006), "Validating a polycrystal model for the elastoplastic response of magnesium alloy AZ31 using in situ neutron diffraction", *Acta Materialia* **54**, pp. 4841–4852.

AMUNDSEN, K. *et al.* (2002), "Magnesium", in: *Ullmann's Encyclopedia of Industrial Chemistry*, Weinheim, Germany: Wiley-VCH Verlag GmbH & Co. KGaA.

ARMSTRONG, R. W. and WORTHINGTON, P. J. (1973), "A Constitutive Relation for Deformation Twinning in Body Centered Cubic Metals", in: *Metallurgical Effects at High Strain Rates*, ed. by ROHDE, R. W. *et al.*, Boston, MA, USA: Springer US, pp. 401–414.

ARMSTRONG, R *et al.* (1962), "The plastic deformation of polycrystalline aggregates", *Philosophical Magazine* **7** (73), pp. 45–58.

AVEDESIAN, M. and BAKER, H. D. R. (1999), *Magnesium and Magnesium Alloys*, Materials Park, OH, USA: ASM International, p. 314.

AYDINER, C *et al.* (2009), "Evolution of stress in individual grains and twins in a magnesium alloy aggregate", *Physical Review B* **80** (2), p. 024113.

BALASUBRAMANIAN, S and ANAND, L (2002), "Plasticity of initially textured hexagonal polycrystals at high homologous temperatures: application to titanium", *Acta Materialia* **50** (1), pp. 133–148.

BALL, C. J. P. (1956), "The History of Magnesium", *J. Inst. Met.* **84**, p. 399.

BARKSDALE, J. (1968), "Titanium", in: *The Encyclopedia of the Chemical Elements*, ed. by HAMPEL, C. A.

BARNETT, M. R. (2008), "A rationale for the strong dependence of mechanical twinning on grain size", *Scripta Materialia* **59** (7), pp. 696–698.

BARNETT, M. R. *et al.* (2004), "Influence of grain size on the compressive deformation of wrought Mg-3Al-1Zn", *Acta Materialia* **52**, pp. 5093–5103.

BARNETT, M. R. *et al.* (2008), "Non-Schmid behaviour during secondary twinning in a polycrystalline magnesium alloy", *Acta Materialia* **56** (1), pp. 5–15.

BARNETT, M. R., NAVE, M. D., and GHADERI, A. (2012), "Yield point elongation due to twinning in a magnesium alloy", *Acta Materialia* **60** (4), pp. 1433–1443.

BARRETT, C. D., EL KADIRI, H., and TSCHOPP, M. A. (2012), "Breakdown of the Schmid law in homogeneous and heterogeneous nucleation events of slip and twinning in magnesium", *Journal of the Mechanics and Physics of Solids* **60** (12), pp. 2084–2099.

BARUCHEL, J. *et al.* (2000), *X-ray Tomography in Material Science: Microtomography at a third generation synchrotron radiation facility*, Hermes Science Publications.

BERNIER, J. V. *et al.* (2011), "Far-field high-energy diffraction microscopy: a tool for intergranular orientation and strain analysis", *Journal of Strain Analysis for Engineering Design* **46** (7), pp. 527–547.

BEYERLEIN, I. J. and TOMÉ, C. N. (2010), "A probabilistic twin nucleation model for HCP polycrystalline metals", in: *Proceedings of the Royal Society A: Mathematical, Physical and Engineering Sciences*, vol. 466, pp. 2517–2544.

BEYERLEIN, I. J. *et al.* (2010), "Statistical analyses of deformation twinning in magnesium", *Philosophical Magazine* **90** (16), pp. 2161–2190.

BHATTACHARYYA, D *et al.* (2009), "Origin of dislocations within tensile and compressive twins in pure textured Zr", *Acta Materialia* **57** (2), pp. 305–315.

BIELER, T. R. *et al.* (2014a), "Grain boundaries and interfaces in slip transfer", *Current Opinion in Solid State and Materials Science* **18** (4), pp. 212–226.

BIELER, T. R. *et al.* (2014b), "In Situ Characterization of Twin Nucleation in Pure Ti Using 3D-XRD", *Metallurgical and Materials Transactions A* **45** (1), pp. 109–122.

BILBY, B. A. and CROCKER, A. G. (1965), "The Theory of the Crystallography of Deformation Twinning", in: *Proceedings of the Royal Society of London. Series A: Mathematical, Physical and Engineering Sciences*, vol. 288, pp. 240–255.

BLEUET, P. *et al.* (2009), "Towards synchrotron-based nanocharacterization", *Frontiers of Characterization and Metrology For Nanoelectronics* **1173**, ed. by SEILER, D. G. *et al.*, pp. 181–187.

BONNET, R, COUSINEAU, R, and WARRINGTON, D. H. (1981), "Determination of near-coincident cells for hexagonal crystals. Related DSC lattices", *Acta Crystallographica Section A Foundations of Crystallography* **37** (2), pp. 184–189.

BOZZOLO, N., CHAN, L., and ROLLETT, A. D. (2010), "Misorientations induced by deformation twinning in titanium", *Journal of Applied Crystallography* **43**, pp. 596–602.

BRANDES, E. A. and BROOK, G. B., eds. (1992), *Smithells Metals Reference Book*, 7th ed., Oxford, UK: Butterworth-Heinemann.

BRIDIER, F, VILLECHAISE, P, and MENDEZ, J (2005), "Analysis of the different slip systems activated by tension in a α/β titanium alloy in relation with local crystallographic orientation", *Acta Materialia* **53** (3), pp. 555–567.

BRITTON, T. B. *et al.* (2010), "Electron backscatter diffraction study of dislocation content of a macrozone in hot-rolled Ti-6Al-4V alloy", *Scripta Materialia* **62** (9), pp. 639–642.

BRONFIN, B. (2007), "Elektron 21 specification", in: *Magnesium: Proceedings of the 7th International Conference on Magnesium Alloys and Their Applications*, ed. by KAINER, K., Weinheim, Germany: Wiley.

BROWN, D. W. *et al.* (2005), "Internal strain and texture evolution during deformation twinning in magnesium", *Materials Science and Engineering: A* **399** (1–2), pp. 1–12.

BROWN, D. W. *et al.* (2007), "Twinning and detwinning during cyclic deformation of Mg alloy AZ31B", *Materials Science Forum* **539–543**, pp. 3407–3413.

BRYANT, P. J. (1996), "Neutron spallation sources in Europe", *Nuclear Physics B - Proceedings Supplements* **51** (1), pp. 125–134.

CAI, S *et al.* (2009), "Evolution of interphase and intergranular stresses in Zr2.5Nb during room temperature deformation", *Materials Science and Engineering: A* **501** (1–2), pp. 166–181.

CALLISTER JR, W. D. (2007), *Materials Science and Engineering: An Introduction*, 7th ed., New York, NY, USA: John Wiley & Sons, Incorporated.

CAPOLUNGO, L. and BEYERLEIN, I. J. (2008), "Nucleation and stability of twins in hcp metals", *Physical Review B* **78** (2), p. 024117.

CAPOLUNGO, L. *et al.* (2009), "Nucleation and growth of twins in Zr: A statistical study", *Acta Materialia* **57** (20), pp. 6047–6056.

Carpenter Technology Corporation, http://www.cartech.com/dynamet/.

CHICHILI, D. R., RAMESH, K. T., and HEMKER, K. J. (1998), "The high-strain-rate response of alpha-titanium: experiments, deformation mechanisms and modeling", *Acta Materialia* **46** (3), pp. 1025–1043.

CHRISTIAN, J. W. and MAHAJAN, S (1995), "Deformation Twinning", *Progress in Materials Science* **39** (1–2), pp. 1–157.

CHUN, Y. B. *et al.* (2005), "Effect of deformation twinning on microstructure and texture evolution during cold rolling of CP-titanium", *Materials Science and Engineering: A* **398** (1–2), pp. 209–219.

CLARK, W. A. T. *et al.* (1992), "On the criteria for slip transmission across interfaces in polycrystals", *Scripta Metallurgica et Materialia* **26** (2), pp. 203–206.

CLAUSEN, B *et al.* (2008), "Reorientation and stress relaxation due to twinning: Modeling and experimental characterization for Mg", *Acta Materialia* **56** (11), pp. 2456–2468.

CLOW, B. B. (1992), "No Title", in: *Magnesium Alloys and Their Applications*, vol. 13, Oberursel, Germany: Deutsche Gesellschaft fur Materialkunde E.V.

COAN, P. *et al.* (2006), "Evaluation of imaging performance of a taper optics CCD 'FReLoN' camera designed for medical imaging", *Journal of Synchrotron Radiation* **13** (3), pp. 260–270.

COGHE, F *et al.* (2012), "Importance of twinning in static and dynamic compression of a Ti6Al4V titanium alloy with an equiaxed microstructure", *Materials Science and Engineering: A* **537**, pp. 1–10.

CULLITY, B. D. and STOCK, S. R. (2001), *Elements of X-ray diffraction*, 3rd ed., Upper Saddle River, NJ, USA: Prentice Hall.

DCT code, http://sourceforge.net/projects/dct/.

DAVY, H. (1808), "Electro-Chemical Researches, on the Decomposition of the Earths; With Observations on the Metals Obtained from the Alkaline Earths, and on the Amalgam Procured from Ammonia", *Philosophical Transactions of the Royal Society of London* **98**, pp. 333–370.

DAYMOND, M. R. and PRIESMEYER, H. G. (2002), "Elastoplastic deformation of ferritic steel and cementite studied by neutron diffraction and self-consistent modelling", *Acta Materialia* **50**, pp. 1613–1626.

DAYMOND, M. R., PREUSS, M., and CLAUSEN, B (2007), "Evidence of variation in slip mode in a polycrystalline nickel-base superalloy with change in temperature from neutron diffraction strain measurements", *Acta Materialia* **55**, pp. 3089–3102.

DONACHIE, M. J. (1988), *Titanium: A Technical Guide*, ASM International, p. 469.

DREIZIN, E. L., BERMAN, C. H., and VICENZI, E. P. (2000), "Condensed-phase modifications in magnesium particle combustion in air", *Combustion and Flame* **122** (1–2), pp. 30–42.

EL KADIRI, H. and OPPEDAL, A. L. (2010), "A crystal plasticity theory for latent hardening by glide twinning through dislocation transmutation and twin accommodation effects", *Journal of the Mechanics and Physics of Solids* **58** (4), pp. 613–624.

EMSLEY, J. (2001), *Nature's Building Blocks: An A-Z Guide to the Elements*, p. 538.

EUSER, A. G. and CIPOLLA, M. J. (2009), "Magnesium Sulfate for the Treatment of Eclampsia: A Brief Review", *Stroke* **40** (4), pp. 1169–1175.

FABLE, http://sourceforge.net/projects/fable/.

FERNÁNDEZ, A *et al.* (2013), "Three-dimensional investigation of grain boundarytwin interactions in a Mg AZ31 alloy by electron backscatter diffraction and continuum modeling", *Acta Materialia* **61** (20), pp. 7679–7692.

FINNEY, J. L. and TOMKINSON, J (1990), "ISIS: a new powerful tool for hydrogen bonding studies", *Journal of Molecular Structure* **237**, pp. 249–264.

FITZNER, A. *et al.* (2014), "The effect of Aluminium on twin activity in binary α-Ti", *Acta Materialia*, Submitted.

FLOOR, A. J. (2006), The chemical composition of seawater, http://www.seafriends.org.nz/.

FORREST, A. L. (1981), *Effects of Metal Chemistry on Behavior of Titanium in Industrial Applications*, ASTM International.

GONG, J. and WILKINSON, A. J. (2011), "A microcantilever investigation of size effect, solid-solution strengthening and second-phase strengthening fora prism slip in alpha-Ti", *Acta Materialia* **59** (15), pp. 5970–5981.

GORDON, R., BENDER, R., and HERMAN, G. T. (1970), "Algebraic Reconstruction Techniques (ART) for three-dimensional electron microscopy and X-ray photography", *Journal of Theoretical Biology* **29** (3), pp. 471–481.

GRAFF, S. (2008), "Micromechanical Modeling of the Deformation of HCP Metals", PhD Thesis, Technical University of Berlin, p. 119.

GUO, C. *et al.* (2014a), "Understanding of variant selection and twin patterns in compressed Mg alloy sheets via combined analysis of Schmid factor and strain compatibility factor", *Materials Science and Engineering: A* **609**, pp. 92–101.

GUO, Y, BRITTON, T. B., and WILKINSON, A. J. (2014b), "Slip bandgrain boundary interactions in commercial-purity titanium", *Acta Materialia* **76**, pp. 1–12.

GUY, A. G. (1976), *Essentials of Materials Science*, New York, NY, USA: McGraw-Hill Kogakusha.

HAMPEL, C. A. (1968), *The Encyclopedia of the Chemical Elements*, Van Nostrand Reinhold, p. 849.

HARAN, B. (2011), Magnesium Video, http://www.periodicvideos.com/videos/012.htm.

HÄRTWIG, J *et al.* (2002), "X-ray diffraction topography at a synchrotron radiation source applied to the study of bonded silicon on insulator material", *Crystal Research and Technology* **37**, pp. 705–715.

HENDEE, W. R. and RITENOUR, E. R. (2003), *Medical Imaging Physics*, John Wiley & Sons, p. 536.

HOLDEN, T. M. (1999), "Intergranular stresses", *Journal of Neutron Research* **7** (3–4), pp. 291–317.

HOLT, J. M. T., MINDLIN, H., and HO, C. Y. (1996), *Structural alloys handbook*, West Lafayette, IN, USA: CINDAS/Purdue University.

HONNIBALL, P. *et al.* (2015), "Grain break-up during elevated temperature deformation of an HCP metal", *Metallurgical and materials transactions A - physical metallurgy and materials science*, Accepted.

HOSFORD, W. F. (1993), *The Mechanics of crystals and textured polycrystals*, New York, NY, USA: Oxford University Press.

HOUSECROFT, C. E. and SHARPE, A. G. (2008), *Inorganic Chemistry*, 3rd ed., Pearson Prentice Hall, pp. 305–306.

HOY-PETERSEN, N (1990), "From Past to Future", in: *47th World Magnesium Conference, I.M.A.* Cannes, France, pp. 18–23.

HUGHES, D. J. *et al.* (2006), "Scientific Review: First Impressions of SALSA: The New Engineering Instrument at ILL", *Neutron News* **17** (3), pp. 28–32.

HULL, D (1961), "Effect of grain size and temperature on slip, twinning and fracture in 3% silicon iron", *Acta Metallurgica* **9**, pp. 191–204.

ISIS Neutron and Muon Source, Harwell Oxford, Chilton, UK, http://www.isis.stfc.ac.uk/.

ICE, G. E. and BARABASH, R. I. (2007), "White Beam Microdiffraction and Dislocations Gradients", in: *Dislocations in Solids*, ed. by NABARRO, F. R. N. and HIRTH, J. P., vol. 13, Elsevier B.V., chap. 79, pp. 499–601.

JOHNSON, G. *et al.* (2008), "X-ray diffraction contrast tomography: a novel technique for three-dimensional grain mapping of polycrystals. II. The combined case", *Journal of Applied Crystallography* **41** (2), pp. 310–318.

JOHNSON, M. W. and DAYMOND, M. R. (2003), "Neutron Pulsed Source Instrumentation", in: *Analysis of Residual Stress by Diffraction using Neutron and Synchrotron Radiation*, ed. by FITZPATRICK, M. E. and LODINI, A, Taylor & Francis Group.

KERR, M *et al.* (2010), "Mapping of crack tip strains and twinned zone in a hexagonal close packed zirconium alloy", *Acta Materialia* **58** (5), pp. 1578–1588.

KING, A. (2005), "Residual stress and damage characterisation in wide chord fan blades", PhD Thesis, Manchester, UK: Materials Science Center, University of Manchester, p. 415.

KING, A. *et al.* (2008), "Observations of Intergranular Stress Corrosion Cracking in a Grain-Mapped Polycrystal", *Science* **321** (5887), pp. 382–385.

KING, A. *et al.* (2010), "Grain mapping by diffraction contrast tomography: extending the technique to sub-grain information", in: *Risoe International Symposium on Materials Science: Challenges in materials science and possibilities in 3D and 4D characterization techniques*.

KING, A. *et al.* (2011), "Three-dimensional in situ observations of short fatigue crack growth in magnesium", *Acta Materialia* **59** (17), pp. 6761–6771.

KITTEL, C. (2005), *Introduction to Solid State Physics*, 8th ed., Berkeley, CA, USA: John Wiley & Sons, p. 688.

KLUENDER, R. T. *et al.* (2011), "Three-dimensional distortion measurements by section rocking curve imaging: Application to ice crystals", *physica status solidi (a)* **208** (11), pp. 2505–2510.

KOCKS, U. F. (1970), "The relation between polycrystal deformation and single-crystal deformation", *Metallurgical and Materials Transactions* **1** (5), pp. 1121–1143.

KOCKS, U. F., TOMÉ, C. N., and WENK, H. R. (1998), *Texture and Anisotropy: Preferred Orientations in Polycrystals and Their Effect on Materials Properties*, New York, NY, USA: Cambridge University Press.

KORSUNSKY, A. M., JAMES, K. E., and DAYMOND, M. R. (2004), "Intergranular stresses in polycrystalline fatigue: Diffraction measurement and self-consistent modelling", *Engineering Fracture Mechanics* **71**, pp. 805–812.

KRAWITZ, A. D. (2001), *Introduction to Diffraction in Materials Science and Engineering*, WILEY-VCH.

KREBS, R. E. (2006), *The History and Use of Our Earth's Chemical Elements: A Reference Guide*, Greenwood Publishing Group, p. 422.

KVARDAKOV, V. *et al.* (2007), "Study of the three-dimensional distribution of defects in crystals by synchrotron radiation diffraction tomography", *Nuclear Instruments and Methods in Physics Research Section A: Accelerators, Spectrometers, Detectors and Associated Equipment* **575** (1–2), pp. 140–143.

LABICHE, J.-C. *et al.* (2007), "The fast readout low noise camera as a versatile x-ray detector for time resolved dispersive extended x-ray absorption fine structure and diffraction studies of dynamic problems in materials science, chemistry, and catalysis", *Review of Scientific Instruments* **78** (9), p. 91301.

LAHAIE, D *et al.* (1992), "A note on the deformation of fine grained magnesium alloys", *Scripta Metallurgica et Materialia* **27** (2), pp. 139–142.

LANG, A. R. and MAKEPEACE, A. P. W. (1996), "Reticulography: a simple and sensitive technique for mapping misorientations in single crystals.", *Journal of synchrotron radiation* **3** (6), pp. 313–315.

— (1999), "Synchrotron x-ray reticulography: principles and applications", *Journal of Physics D: Applied Physics* **32** (10A), A97–A103.

LARSON, B. C. *et al.* (2002), "Three-dimensional X-ray structural microscopy with submicrometre resolution.", *Nature* **415** (6874), pp. 887–890.

LAURIDSEN, E. M. *et al.* (2001), "Tracking: a method for structural characterization of grains in powders or polycrystals", *Journal of Applied Crystallography* **34** (6), pp. 744–750.

LE PAGE, Y and GABE, E. J. (1979), "Application of a segment description of the unique set of reflections to data collection and data reduction", *Journal of Applied Crystallography* **12** (5), pp. 464–466.

LEYENS, C. and PETERS, M., eds. (2003), *Titanium and Titanium Alloys, Fundamentals and Applications*, Weinheim, Germany: WILEY-VCH Verlag GmbH and Co. KGaA.

LI, S. F. and SUTER, R. M. (2013), "Adaptive reconstruction method for three-dimensional orientation imaging", *Journal of Applied Crystallography* **46** (2), pp. 512–524.

LI, S. F. *et al.* (2012), "Three-dimensional plastic response in polycrystalline copper via near-field high-energy X-ray diffraction microscopy", *Journal of Applied Crystallography* **45** (6), pp. 1098–1108.

LIDE, D. R., ed. (2005), *CRC Handbook of Chemistry and Physics, 86th Edition*, Boca Raton, FL, USA: CRC Press.

LINSLEY, T. (2011), "Properties of conductors and insulators", in: *Basic Electrical Installation Work*.

LIU, W. and DUPONT, J. N. (2004), "Fabrication of carbide-particle-reinforced titanium aluminide-matrix composites by laser-engineered net shaping", *Metallurgical and Materials Transactions A* **35** (3), pp. 1133–1140.

LIU, W. *et al.* (2005), "Nondestructive three-dimensional characterization of grain boundaries by X-ray crystal microscopy.", *Ultramicroscopy* **103** (3), pp. 199–204.

LÜBBERT, D *et al.* (2000), "μm-resolved high resolution X-ray diffraction imaging for semiconductor quality control", *Nuclear Instruments and Methods in Physics Research Section B: Beam Interactions with Materials and Atoms* **160** (4), pp. 521–527.

LUDWIG, W. *et al.* (2008), "X-ray diffraction contrast tomography: a novel technique for three-dimensional grain mapping of polycrystals. I. Direct beam case", *Journal of Applied Crystallography* **41** (2), pp. 302–309.

LUDWIG, W. *et al.* (2009a), "New opportunities for 3D materials science of polycrystalline materials at the micrometre lengthscale by combined use of X-ray diffraction and X-ray imaging", *Materials Science and Engineering: A* **524** (1–2), pp. 69–76.

LUDWIG, W. *et al.* (2009b), "Three-dimensional grain mapping by x-ray diffraction contrast tomography and the use of Friedel pairs in diffraction data analysis", *Review of Scientific Instruments* **80** (3), p. 033905.

LUDWIG, W. *et al.* (2010), "Characterization of Polycrystalline Materials Using Synchrotron X-ray Imaging and Diffraction Techniques", *JOM: the journal of the Minerals, Metals & Materials Society* **62** (12), pp. 22–28.

LUSTER, J and MORRIS, M. A. (1995), "Compatibility of deformation in two-phase Ti-Al alloys: Dependence on microstructure and orientation relationships", *Metallurgical and Materials Transactions A* **26** (7), pp. 1745–1756.

LYCKEGAARD, A. *et al.* (2011), "On the Use of Laguerre Tessellations for Representations of 3D Grain Structures", *Advanced Engineering Materials* **13** (3), pp. 165–170.

"Magnesium Overview", (2013), *China magnesium Corporation*.

Magnesium in health, (2013), http://www.mg12.info/.

MAINPRICE, D., LLOYD, G. E., and CASEY, M. (1993), "Individual orientation measurements in quartz polycrystals: advantages and limitations for texture and petrophysical property determinations", *Journal of Structural Geology* **15** (9–10), pp. 1169–1187.

MARIN, E. B. and DAWSON, P. R. (1998), "Elastoplastic finite element analyses of metal deformations using polycrystal constitutive models", *Computer Methods in Applied Mechanics and Engineering* **165** (1–4), pp. 23–41.

MCCABE, R. J. *et al.* (2009), "Quantitative analysis of deformation twinning in zirconium", *International Journal of Plasticity* **25** (3), pp. 454–472.

"Medical Devices - Emergency Medical Services", (1998), *Annual Book of ASTM Standards*, vol. 13, chap. 1, West Conshohocken, PA, USA: ASTM International.

MEISEL, A (1985), "E.-E. Koch (Hrsg.). Handbook on Synchrotron Radiation. Bände 1 A und 1 B", *Crystal Research and Technology* **20** (9), ed. by EASTMAN, D. E. and FARGE, Y.

MEYERS, M. A., VÖHRINGER, O, and LUBARDA, V. A. (2001), "The onset of twinning in metals: a constitutive description", *Acta Materialia* **49** (19), pp. 4025–4039.

MIKULÍK, P *et al.* (2006), "Crystallite misorientation analysis in semiconductor wafers and ELO samples by rocking curve imaging", *Applied Surface Science* **253** (1), pp. 188–193.

"Minerals Information: Titanium", (2012), *United States Geological survey*, http://minerals.usgs.gov/minerals/pubs/commodity/titanium/.

MOSCICKI, M *et al.* (2009), "Friedel-pair based indexing method for characterization of single grains with hard X-rays", *Materials Science and Engineering: A* **524** (12), pp. 64–68.

NERVO, L. *et al.* (2014), "Comparison between a near-field and a far-field indexing approach for characterization of a polycrystalline sample volume containing more than 1500 grains", *Journal of Applied Crystallography* **47** (4), pp. 1402–1416.

NERVO, L. *et al.* (2015), "A study of deformation twinning in a Titanium alloy by X-ray Diffraction Contrast Tomography.", *Acta Materialia*, In progress.

"Non-ferrous Metals", (2006), *Annual Book of ASTM Standards*, vol. 2, chap. 4, West Conshohocken, PA, USA: ASTM International.

ODDERSHEDE, J. *et al.* (2010), "Determining grain resolved stresses in polycrystalline materials using three-dimensional X-ray diffraction", *Journal of Applied Crystallography* **43** (3), pp. 539–549.

ODDERSHEDE, J. *et al.* (2012), "Measuring the stress field around an evolving crack in tensile deformed Mg AZ31 using three-dimensional X-ray diffraction", *Acta Materialia* **60** (8), pp. 3570–3580.

OKAZAKI, K and CONRAD, H (1973), "Effects of interstitial content and grain size on the strength of titanium at low temperatures", *Acta Metallurgica* **21**, pp. 1117–1129.

OLSEN, U. L. *et al.* (2009), "Structured scintillators for X-ray imaging with micrometre resolution", *Nuclear Instruments and Methods in Physics Research Section A: Accelerators, Spectrometers, Detectors and Associated Equipment* **607** (1), pp. 141–144.

PALENSTIJN, W. J., BATENBURG, K. J., and SIJBERS, J (2011), "Performance improvements for iterative electron tomography reconstruction using graphics processing units (GPUs).", *Journal of structural biology* **176** (2), pp. 250–253.

— (2013), "The ASTRA Tomography Toolbox", in: *13th International Conference on Computational and Mathematical Methods in Science and Engineering*, pp. 1–7.

PARTRIDGE, P. G. (1967), "The crystallography and deformation modes of hexagonal close-packed metals", *Metallurgical Reviews* **12** (1), pp. 169–194.

PIEHLER, H. R. (2009), "Crystal-Plasticity Fundamentals", in: *ASM Handbook Volume 22A: Fundamentals of Modeling for Metals Processing*, vol. 22, ASM International, pp. 232–238.

PIRLING, T. (2000), "Neutron Strain Scanning at Interfaces: An Optimised Beam Optics to Reduce the Surface Effect", in: *Materials Science Forum*, vol. 347–349, pp. 107–112.

PIRLING, T., BRUNO, G., and WITHERS, P. J. (2006), "SALSA-A new instrument for strain imaging in engineering materials and components", *Materials Science and Engineering A* **437**, pp. 139–144.

POULSEN, H. F. (2004), *Three-Dimensional X-Ray Diffraction Microscopy: Mapping Polycrystals and Their Dynamics*, Springer.

— (2012), "An introduction to three-dimensional X-ray diffraction microscopy", *Journal of Applied Crystallography* **45** (6), pp. 1084–1097.

POULSEN, H. F. *et al.* (1997), "Applications of high-energy synchrotron radiation for structural studies of polycrystalline materials.", *Journal of synchrotron radiation* **4** (3), pp. 147–54.

POULSEN, H. F. *et al.* (2001), "Three-dimensional maps of grain boundaries and the stress state of individual grains in polycrystals and powders", *Journal of Applied Crystallography* **34** (6), pp. 751–756.

POULSEN, S. O. and POULSEN, H. F. (2014), "Efficient Analytical Approaches to the Optics of Compound Refractive Lenses for Use with Synchrotron X-rays", *Metallurgical and Materials Transactions A* **45**, pp. 4772–4779.

PRAKASH, D. G. L. *et al.* (2010), "Deformation twinning in Ti-6Al-4V during low strain rate deformation to moderate strains at room temperature", *Materials Science and Engineering: A* **527** (21–22), pp. 5734–5744.

PREUSS, M. *et al.* (2010), "Twinning in structural material with a hexagonal close-packed crystal structure", *The Journal of Strain Analysis for Engineering Design* **45** (5), pp. 377–390.

RAILSBACK, B. (2008), Abundance and form of the most abundant elements in Earth's continental crust, http://www.gly.uga.edu/railsback/Fundamentals/ElementalAbundanceTableP.pdf.

RANDLE, V. (1992), *Microtexture Determination and Its Applications*, 1st ed., Institute of Materials.

REISCHIG, P. (2008), "Determination of elastic strain tensors of individual grains in polycrystals by means of diffraction contrast tomography", MSc Thesis, Delft University of Technology, p. 127.

REISCHIG, P. *et al.* (2013), "Advances in X-ray diffraction contrast tomography: flexibility in the setup geometry and application to multiphase materials", *Journal of Applied Crystallography* **46** (2), pp. 297–311.

ROTERS, F (2005), "Application of crystal plasticity FEM from single crystal to bulk polycrystal", *Computational Materials Science* **32** (3–4), pp. 509–517.

RUTISHAUSER, S. *et al.* (2012), "Fabrication of two-dimensional hard X-ray diffraction gratings", *Microelectronic Engineering*, Preprint.

SALEM, A. A., KALIDINDI, S. R., and DOHERTY, R. D. (2003), "Strain hardening of titanium: role of deformation twinning", *Acta Materialia* **51** (14), pp. 4225–4237.

SCHIOPPA, E. J. (2014), "The color of X-rays", PhD Thesis, University of Amsterdam, p. 179.

SCHMID, E. (1924), "'Yield Point' of Crystals. Critical Shear Stress Law", in: *Proc. Internat. Congr. Appl. Mech.* Pp. 342–352.

SCHMIDT, S. (2005), GrainSweeper, http://fable.svn.sourceforge.net/svnroot/fable/GrainSweeper.

— (2010), GrainSpotter v. 0.82, http://fable.svn.sourceforge.net/svnroot/fable/GrainSpotter.

— (2014), "GrainSpotter: a fast and robust polycrystalline indexing algorithm", *Journal of Applied Crystallography* **47** (1), pp. 276–284.

SERRA, A. and BACON, D. J. (1996), "A new model for {10 1 2} twin growth in hcp metals", *Philosophical Magazine A* **73** (2), pp. 333–343.

SHARMA, H., HUIZENGA, R. M., and OFFERMAN, S. E. (2012), "A fast methodology to determine the characteristics of thousands of grains using three-dimensional X-ray diffraction. II. Volume, centre-of-mass position, crystallographic orientation and strain state of grains", *Journal of Applied Crystallography* **45** (4), pp. 705–718.

SILLEKENS, W. H. and HORT, N. (2013), "Magnesium and Magnesium Alloys", in: *Structural Materials and Processes in Transportation*, pp. 113–150.

SIMONS, H *et al.* (2015), "Dark-field X-ray microscopy for multiscale structural characterization.", *Nature communications* **6**, p. 6098.

SOMOGYI, A *et al.* (2001), "ID18F: A new micro-x-ray fluorescence end-station at the European Synchrotron Radiation Facility (ESRF): Preliminary results", *X-Ray Spectrometry* **30** (4), pp. 242–252.

SONG, S. G. and GRAY III, G. T. (1995a), "Structural interpretation of the nucleation and growth of deformation twins in Zr and Ti. I. Application of the coincidence site lattice (CSL) theory to twinning problems in h.c.p. structures", *Acta Metallurgica et Materialia* **43** (6), pp. 2325–2337.

— (1995b), "Structural interpretation of the nucleation and growth of deformation twins in Zr and Ti. II. Tem study of twin morphology and defect reactions during twinning", *Acta Metallurgica et Materialia* **43** (6), pp. 2339–2350.

SØRENSEN, H. O. *et al.* (2012), "Multigrain crystallography", *Zeitschrift für Kristallographie* **227** (1), pp. 63–78.

STANFORD, N, CARLSON, U, and BARNETT, M. R. (2008), "Deformation Twinning and the HallPetch Relation in Commercial Purity Ti", *Metallurgical and Materials Transactions A* **39** (4), pp. 934–944.

STAROSELSKY, A and ANAND, L (2003), "A constitutive model for hcp materials deforming by slip and twinning", *International Journal of Plasticity* **19** (10), pp. 1843–1864.

STOCK, S. R. (2008), "Recent advances in X-ray microtomography applied to materials", *International Materials Reviews* **53** (3), pp. 129–181.

STWERTKA, A. (2002), *A guide to the elements*, New York: Oxford University Press.

SUTER, R. M. *et al.* (2006), "Forward modeling method for microstructure reconstruction using x-ray diffraction microscopy: Single-crystal verification", *Review of Scientific Instruments* **77** (12), p. 123905.

SYHA, M. *et al.* (2013), "Validation of three-dimensional diffraction contrast tomography reconstructions by means of electron backscatter diffraction characterization", *Journal of Applied Crystallography* **46** (4), pp. 1145–1150.

TIMET - Savoie, Ugine, France, http://www.timet.com.

TAYLOR, G. I. (1938), "Plastic strain in metals", *Twenty-eighth May Lecture to the Institute of Metals*, pp. 307–325.

THOMPSON, N and MILLARD, D. J. (1952), "XXXVIII. Twin formation, in cadmium", *The London, Edinburgh, and Dublin Philosophical Magazine and Journal of Science: Series 7* **43** (339), pp. 422–440.

TIMÁR, G. and QUINTA DA FONSECA, J. A. (2014), "Modeling Twin Clustering and Strain Localization in Hexagonal Close-Packed Metals", *Metallurgical and Materials Transactions A* **45**, pp. 5883–5890.

"Titanium", (2000), *Columbia Encyclopedia*, 6th ed., New York, NY, USA: Columbia University Press.

"Titanium", (2006), *Encyclopædia Britannica*, http://global.britannica.com/EBchecked/topic/597135/titanium-Ti.

TOMÉ, C. N. *et al.* (2011), "A multi-scale statistical study of twinning in magnesium", *JOM* **63** (3), pp. 19–23.

VAUGHAN, G. B. M. *et al.* (2010), "The extension of ID11 for nanoscale and hierarchical characterization", in: *RisøInternational Symposium on Materials Science*, vol. 31, Roskilde, Denmark, pp. 457–476.

VIGANÒ, N., LUDWIG, W., and BATENBURG, K. J. (2014), "Reconstruction of local orientation in grains using a discrete representation of orientation space", *Journal of Applied Crystallography* **47**, pp. 1826–1840.

VON MISES, R (1928), "Mechanik der plastischen Formänderung von Kristallen", *Zeitschrift für Angewandte Mathematik und Mechanik* **8** (3), pp. 161–185.

WANG, L. *et al.* (2010a), "Nucleation of paired twins at grain boundaries in titanium", *Scripta Materialia* **63** (8), pp. 827–830.

WANG, L. *et al.* (2010b), "Twin Nucleation by Slip Transfer across Grain Boundaries in Commercial Purity Titanium", *Metallurgical and Materials Transactions A* **41** (2), pp. 421–430.

WANG, L. *et al.* (2011), "Experimental Characterization and Crystal Plasticity Modeling of Heterogeneous Deformation in Polycrystalline α-Ti", *Metallurgical and Materials Transactions A* **42** (3), pp. 626–635.

WANG, L. *et al.* (2013), "Study of $${11\bar{2}1}$$ Twinning in α-Ti by EBSD and Laue Microdiffraction", *Metallurgical and Materials Transactions A* **44** (8), pp. 3664–3674.

WELSCH, G, BOYER, R, and COLLINGS, E. W. (1993), *Materials Properties Handbook: Titanium Alloys*, ASM International.

WEST, S. S. *et al.* (2009), "Direct non-destructive observation of bulk nucleation in 30% deformed aluminum", *Scripta Materialia* **61** (9), pp. 875–878.

WITHERS, P. J. (2001), "Residual stresses: Measurement by Diffraction", in: *Encyclopedia of Materials: Science and Technology*, Elsevier Science Ltd., pp. 8158–8170.

— (2003), "Use of synchrotron X-ray radiation for stress measurement", in: *Analysis of Residual Stress by Diffraction using Neutron and Synchrotron Radiation*, CRC Press, pp. 170–189.

WRIGHT, J. P. (2005), ImageD11, http://sourceforge.net/p/fable/wiki/imaged11/.

XIN, R. *et al.* (2014), "Characteristics of long {10-12} twin bands in sheet rolling of a magnesium alloy", *Scripta Materialia* **74**, pp. 96–99.

XU, F. *et al.* (2008), "Development of internal strains in textured Zircaloy-2 during uni-axial deformation", *Materials Science and Engineering A* **488**, pp. 172–185.

YOO, M. H. (1981), "Slip, twinning, and fracture in hexagonal close-packed metals", *Metallurgical Transactions A* **12** (3), pp. 409–418.

YOO, M. H. *et al.* (2002), "Nonbasal Deformation Modes of HCP Metals and Alloys : Role of Dislocation Source and Mobility", *Metallurgical and Materials Transactions A* **33**, pp. 813–822.

ZAEFFERER, S (2003), "A study of active deformation systems in titanium alloys: dependence on alloy composition and correlation with deformation texture", *Materials Science and Engineering: A* **344** (1–2), pp. 20–30.